Multi-Dimensional Modeling of Transient Transport Phenomena in Molten Carbonate Fuel Cells

By

MASOUD YOUSEF RAMANDI

A Thesis Submitted in Partial Fulfillment
of the Requirements for the degree of Doctor of Philosophy
in
Mechanical Engineering

Faculty of Engineering and Applied Science
University of Ontario Institute of Technology

Oshawa, Ontario, Canada, 2012

Multi-Dimensional Modeling of Transient Transport Phenomena in Molten Carbonate Fuel Cells

By

MASOUD YOUSEF RAMANDI

Supervisory Committee

1. **Dr. Ibrahim Dincer**, Supervisor (Faculty of Engineering and Applied Science, University of Ontario Institute of Technology)

2. **Dr. Peter Berg**, Supervisor (Faculty of Science, University of Ontario Institute of Technology)

3. **Dr. Tony Mazza**, External Member (Government of Canada)

4. **Dr. Greg Lewis**, External Member (Faculty of Science, University of Ontario Institute of Technology)

5. **Dr. Marc Rosen**, Faculty Member (Faculty of Engineering and Applied Science, University of Ontario Institute of Technology)

6. **Dr. Ghaus Rizvi**, Faculty Member (Faculty of Engineering and Applied Science, University of Ontario Institute of Technology)

7. **Dr. Greg Naterer**, Chair (Faculty of Engineering and Applied Science, University of Ontario Institute of Technology)

Abstract

Molten carbonate fuel cells (MCFCs) have become an attractive emerging technology for stationary co-generation of heat and power. From a technical perspective, dynamic operation has a significant effect on the fuel cell life cycle and, hence, economic viability of the device.

The scope of this thesis is to present an improved understanding of the system behaviour at transient operation that can be used to design a more robust control system in order to overcome the cost and the operating lifetime issues. Hence, a comprehensive multi-component multi-dimensional transient mathematical model is developed based on the conservation laws of mass, momentum, species, energy and electric charges coupled through the reaction kinetics. In essence, this model is a set of partial differential equations that are discretized and solved using the finite-volume based commercial software, ANSYS FLUENT 12.0.1. The model is validated with two sets of experimental results, available in open literature, and good agreements are obtained. The validated model is further engaged in an extensive study. First, the MCFC behaviour at high current densities or oxidant utilization, when the mass transfer becomes dominant, is investigated using peroxide and superoxide reaction mechanisms. In brief, both mechanisms predicted the linear region of the polarization curve accurately. However, none of these mechanisms showed a downward bent in the polarization curve. A positive exponent for the carbon-dioxide mole fraction is probably essential in obtaining the downward bent ("knee") at high current densities which is in contrast to what has been reported in the literature to date.

Next, a sinusoidal impedance approach is used to examine the dynamic response of the unit cell to inlet perturbations at various impedance frequencies. This analysis is further used to determine the phase shifts and time scales of the major dynamic processes within the fuel cell. Furthermore, numerical simulation is utilized in order to investigate the underlying electrochemical and transport phenomena without performing costly experiments. Results showed that the electrochemical reactions and the charge transport process occur under a millisecond. The mass transport process showed a comparatively larger time scale. The energy transport process is the slowest process in the cell and takes about an hour to reach its steady state condition.

Furthermore, the developed mathematical model is utilized as a predictive tool to provide a three-dimensional demonstration of the transient physical and chemical processes at system start-

up. The local distribution of field variables and quantities are presented. The results show that increasing the electrode thickness provides a higher reaction rate, but may lead to larger ohmic loss which is not desirable. The reversible heat generation and consumption mechanisms of the cathode and anode are dominant in the first 10 s while the heat conduction from the solid materials to the gas phase is not considerable. The activation and ohmic heating have the same impact within the anode and cathode because of their similar electric conductivity and voltage loss. Increasing the thermal conductivity of the cathode material will facilitate the process of heat transport throughout the cell. This can also be accomplished by lowering the effects of heat conduction by means of a cathode material with a smaller thickness.

In addition, a thermodynamic model is utilized to examine energy efficiency, exergy efficiency and entropy generation of a MCFC. By changing the operating temperature from 883 K to 963 K, the energy efficiency of the unit cell varies from 42.8 % to 50.5 % while the exergy efficiency remains in the range of 26.8% to 36.3%. Both efficiencies initially rise at lower current densities up to the point that they attain their maximum values and ultimately decrease with the increase of current density. With the increase of pressure, both energy and exergy efficiencies of the cell increase. An increase in this anode/cathode flow ratio lessens the energy and exergy efficiencies of the unit cell. Higher operating pressure and temperature decrease the unit cell entropy generation.

Acknowledgements

I would like to express my deep and sincere gratitude to my supervisors, Dr. Ibrahim Dincer and Dr. Peter Berg, for giving me this great opportunity to work on this fascinating subject in a pleasant environment. I am also grateful for their invaluable guidance, steady encouragement, inspiration and support throughout my PhD study.

I would like to thank all my committee members, Dr. Tony Mazza, Dr. Greg Lewis, Dr. Marc Rosen, Dr. Ghaus Rizvi and Dr. Greg Naterer for their valuable time in reading this thesis, and for making comments and constructive criticism.

I would also like to extend my thanks to Dr. Hao Wu and Dr. Kui Jiao from the University of Waterloo. Without their help, encouragement and fruitful discussions throughout these years, I would not have been able to complete this extensive research in just three years.

My special thanks to my dear friends, Sylvia and Dan La Fleur, for their valuable time in proof reading this thesis.

Furthermore, the financial support by Enbridge Inc. through the Natural Sciences and Engineering Research Council of Canada (NSERC) and the Ontario Research Fund (ORF) is acknowledged.

Last but not least, I would like to express my deep thanks to my wife, Rose. Her patience, devotion and understanding cannot be described in words.

Contents

List of Tables

List of Figures

List of Symbols

A_v	specific active surface area ($m^2\ m^{-3}$)
A	electrode-electrolyte interface area (m^2)
B	pre-exponential factor
C	molar concentration ($mol\ m^{-3}$)
c_p	specific heat capacity at constant pressure ($J\ kg^{-1}\ K^{-1}$)
D	mass diffusivity ($m^2\ s^{-1}$)
D_p	pore diameter (m)
E_{eq}	equilibrium electric potential (V)
E_κ	apparent activation energy (K^{-1})
F	Faraday's constant, 96485 ($C\ mol^{-1}$)
g	Gibbs free energy ($J\ mol^{-1}$)
i_0	exchange current density ($A\ m^{-2}$)
i_0^0	reference exchange current density ($A\ m^{-2}$)
J	local current density ($A\ m^{-2}$)
$\bar{J}$	average current density ($A\ m^{-2}$)

k	reaction rate constant; thermal conductivity (W m^{-1} K^{-1})
K	permeability (m^2)
L	length scale (m)
M	molecular weight (g mol^{-1})
$\dot{m}$	mass flow rate (kg s^{-1})
n	unit normal vector; number of electrons
$\dot{n}$	molar flow rate (mol h^{-1})
P	static pressure (Pa)
p_1, p_2, p_3	molar fraction exponents in the anode reaction rate
$\dot{Q}$	heat transfer rate (W)
q_1, q_2, q_3	molar fraction exponents in the cathode reaction rate
R	volumetric current density (A m^{-3})
S	molar entropy (J mol^{-1} K^{-1}); source term
t	time (s)
T	temperature (K)
u	gas velocity (m s^{-1})
V	control volume (m^3)
W	width scale (m)
$\dot{W}$	power output (W)

x	x-coordinate
X	molar fraction
y	y-coordinate
Y	mass fraction
z	z-coordinate

Greek letters

α	transfer coefficient; under-relaxation factor
β	general reaction order
λ_1, λ_2, λ_3	anode reaction order
γ_1, γ_2	cathode reaction order
τ	tortuosity
ε	porosity
θ	electrolyte filling degree
η	over-potential (V)
μ	dynamic viscosity (kg m^{-1} s^{-1})
ν	species stoichiometric coefficient of the reaction
$\Re$	universal gas constant (8.314 J mol^{-1} K^{-1})

ρ	density (kg m^{-3})
ϕ	electric potential (V)
σ	electric conductivity of the solid phase (S m^{-1})
κ	electric conductivity of the electrolyte phase (S m^{-1})
κ_0	pre-exponential factor for the electric conductivity of the electrolyte phase (S m^{-1})
ω''	rate of production (mol m^{-3} s^{-1})
Θ	unspecified variable

Subscripts and Superscripts

a	anode
agc	anode gas channel
b	backward reaction
c	cathode; carbonate ion
cgc	cathode gas channel
e	electrolyte phase ; electronic; equilibrium state
eff	effective
f	forward reaction
g	gas phase

in	inlet
i	i^{th} component
j	j^{th} species
m	mass equation
n	n^{th} iteration
nb	neighbouring cells
out	outlet
r	reversible
s	solid phase
T	energy equation
u	momentum equation
ϕ_s	electronic charge equation
ϕ_e	carbonate ion charge equation
eff	effective
ref	reference state
0	standard conditions

Acronyms

AFC	alkaline fuel cell
AGC	anode gas channel
AMG	algebraic multi-grid
APU	auxiliary power unit
CFD	computational fluid dynamics
CGC	cathode gas channel
CHP	combined heat and power
DFC-ERG	Direct Fuel Cell Energy Recovery Generation™
DIR	direct internal reforming, reformer
DMFC	direct methanol fuel cell
ER	external reforming, reformer
FCCS	fuel cell cogeneration system
FVM	finite volume method
HOR	hydrogen oxidation reaction
HPC	high performance computing
IEA	International Energy Agency
IIR	indirect internal reforming, reformer
LBM	Lattice Boltzmann method

MCFC	molten carbonate fuel cell
MSRR	methane steam reforming reaction
ORR	oxygen reduction reaction
PAFC	phosphoric acid fuel cell
PDE	partial differential equation
PEMFC	proton exchange membrane fuel cell
PSA	pressure swing absorption
SHARCNET	shared hierarchical academic research computing network
SOFC	solid oxide fuel cell
UDF	user defined function
UDS	user defined scalar
WETO	word energy technology and climate policy outlook
WGSR	water gas shift reaction

Chapter 1

Introduction

1.1 Motivation

Energy is a fundamental element in human life and is considered a key aspect for sustainable development [1]. Available conventional energy sources such as crude oil and natural gas have been exploited, extracted and refined to serve a dramatic growth in world population since the 1970s and earlier. Nevertheless, it is generally recognized that conventional energy sources are not sufficient to meet the constantly expanding needs of humanity. For instance, the European "World Energy Technology and Climate Policy Outlook" (WETO) has predicted an average growth rate of 1.8% per annum for the period 2000-2030 for primary energy worldwide [2]. Furthermore, referring to an International Energy Agency (IEA) report [3], world energy demand projection for the year 2030 is one and a half times the amount of current consumption which is estimated to be 700 Quadrillion BTU. This is equivalent to 31,500 million tons of coal, or 700 trillion cubic feet of natural gas, or 84,000 million barrels of crude oil.

Fossil fuels are non-renewable; they draw on finite resources that will eventually dwindle, becoming too expensive or too environmentally damaging to retrieve. In fact, at the present consumption rate, fossil fuels are reaching a natural discharge limitation with ongoing depletion. On the other hand, having relied merely on fossil fuels has resulted in several serious environmental consequences. Global warming, air pollution, acid precipitation, ozone depletion, forest destruction, and emission of radioactive substances are among the serious environmental concerns. Cleaner energy options with lower environmental impact can be achieved by considering all mentioned issues simultaneously [4].

Renewable energy comes from natural resources such as sunlight, wind, rain, tides, and geothermal heat, which are constantly replenished. They can be utilized to generate mechanical or thermal energy. However, renewable energy is tied to unpredictability and fluctuations; in other words, it has a lower reliability in comparison with the conventional energy sources. Clearly, renewable energy often relies on the weather for its source of power. Hydro generators need rain to fill dams to supply flowing water. Wind turbines need wind to turn the blades, and solar collectors need clear skies and sunshine to collect heat and light to make electricity. When these resources are unavailable so is the capacity to make energy from them. Their extremely large capital cost is another major obstacle to substitute the conventional energy sources with renewable energy.

In spite of these challenges and issues, there has been an increasing highlight on "quality of life" issues, such as air quality and the environment. The growing environmental concerns such as the greenhouse effect, regional acidification and climate change are driving research into cleaner and more efficient ways of producing energy. These concerns will demand much more work around the world in the hunt for new power sources and energy technologies. Hence, exploration of alternative energy sources seems to be one of the major concerns for the future.

In brief, hydrogen and electricity together constitute one of the most promising ways to realise sustainable energy, whilst fuel cells offer the most efficient conversion device for converting hydrogen, and possibly other fuels, into electricity. Hydrogen is a clean energy carrier, and can be produced from many kinds of energy sources (e.g. natural gas, renewable energies, biomass, etc) while gasoline is refined primarily from crude oil. In addition, fuel cells are far more energy-efficient than gasoline-fueled vehicles with double the efficiency of internal combustion engines, and are far less polluting. Fuel cells may be expected, in the long term, to replace a substantial part of combustion systems in all end use sectors, since they are intrinsically clean [5]. Table 1.1 compares fuel cells with other power generation technologies based on emissions.

One possibility of replacing the conventional energy conversion systems is fuel cells development. Among the various types of fuel cells, molten carbonate fuel cells (MCFCs) are suited for large-scale stationary co-generation of heat and power and are extensively studied in this thesis.

This thesis research is related to a MCFC-hybrid system installed at Enbridge Inc., Canada, that was commissioned in 2008. It was the world's first hybrid fuel cell power plant designed for gas utility pressure reduction stations. The plant converts unused pipeline energy, a by-product of distributing natural gas to customers, into ultra-clean electricity. The plant produces 2.2 MW of environmentally preferable, clean electricity, which is enough power for approximately 1,700 residences. It was the first multi-megawatt commercial fuel cell system to operate in Canada.

Table 1.1: Comparative emissions profiles of fuel cells versus distributed and central generation.

Generation Technology	NO_x (kg/MWh)	SO_2 (kg/MWh)	Particulate Matter (kg/MWh)	CO_2 (Tons/MWh)
Fuel Cells	0.005	0.0005	None	0.49*
Diesel Generators	2.68-7.76	0.14-0.23	0.34-0.14	0.75-0.9
Combined Cycle Natural Gas	0.05	0.01	0.03	0.5
Pulverized Coal	0.31	0.64	0.13	0.97

*Assumes internal conversion of natural gas to hydrogen within the fuel cell. CO_2-equivalent emissions would be reduced or eliminated if biogas or a renewable source of hydrogen were used. (Source: Adapted from Kubert [6]).

1.2 Scope of Research and Objectives

The overall aim of the ongoing MCFC studies is to overcome the barriers (cost and cell degradation) towards development and commercialization. Therefore, it is crucial to extend cell life with a stable performance and make the system more efficient in order to have reduced operating and maintenance costs. In this view, there is a necessity for multi-physics, multi-scale transient MCFC models, as most models in the literature do not consider the transport of mass, momentum, heat and charge, and chemical/electrochemical reactions simultaneously. Strong coupling involved in such a mathematical model between various phenomena, makes multi-physics MCFC modeling necessary for design, control and optimization which in turn can reduce the production cost. Therefore, the scope of this thesis is to present detailed information on MCFCs dynamic operation.

In view of that, an improved understanding of the underlying transport and electrochemical phenomena is essential. For instance, in start-up and shut-down processes, a step change voltage/current can have a large impact. The difference in time scales of different physical, chemical or electrochemical processes will result in a dynamic behaviour that can strongly affect the performance of the fuel cell. These transient and dynamic effects can eventually induce performance degradation. In practical operations, power sources have to be fast enough to respond to changes of operating conditions as well as duty loads. To prevail over this issue, it is indispensable to comprehend how and under what conditions the transients would be present. Based on this knowledge of the system behaviour, systematic elucidation and solutions can then be set up.

In essence, the specific objective of this thesis is to analyze fluid flow, chemical/electrochemical reactions and heat and mass transport processes in molten carbonate fuel cells, in order to enhance the understanding of complex physical, chemical and electrochemical phenomena occurring inside MCFCs. The sub-objectives may be formulated in more detail as given below:

- identify the limitation, weakness and effectiveness of the former mathematical models in electrode, unit cell, stack and hybrid system levels along with performance models;
- develop a comprehensive multi-phase transient mathematical model for molten carbonate fuel cells based on a literature survey;
- compare the resulting steady state polarization curves based on the most common electrochemical reaction mechanisms and their behaviour at high current densities;
- address the difficulties associated with the electrochemical reaction mechanisms;
- determine the corresponding phase shifts and time scales of various transport phenomena.
- examine the load-following capability of the MCFCs
- study the start-up process and find the transient three-dimensional distribution of temperature, reaction rates, molar fractions, over-potentials, and electric potentials;
- analyze the dynamic responses of the average current density, electrochemical reaction rates, heat and mass transfer, mass fractions and temperature, etc.

1.3 Summary of Approach and Rationale

The majority of the earlier studies have made several assumptions to simplify the highly coupled and complex governing equations. For instance, some researchers have considered one-dimensional models (e.g., [53, 54]), simplified the two-dimensional models by assuming x-direction flow for anode gas, y-direction flow for cathode gas [56], applied constant pressure [57], ignored the gradients of temperatures and concentrations in electrodes [59], used algebraic equations for potentials [59-61], or assumed no diffusion and no heat conduction [62]. Moreover, there is a lack of adequate research on the various heat loss processes when internal reforming is involved. The transient behaviour of the MCFC is usually overlooked. The transient modeling of MCFCs has been investigated only in some simplified cases (e.g., the simplified 2D model, while ignoring the diffusion and heat conduction [62]). A comprehensive literature review (Chapter 3) with respect to various aspects of MCFC models identifies the limitations, weaknesses and the effectiveness of the previous mathematical models.

The main objectives of this thesis are achieved by strictly applying balances of mass, energy, species and charges while avoiding highly algebraic empirical correlations. In order to serve as a basis for optimal control design, the developed transient mathematical model requires a certain level of understanding of the system behaviour. These objectives are approached through the following steps:

- The physical domain of a molten carbonate fuel cell (the schematic, thickness, width and length of the unit cell) and the material properties are specified;
- The governing equations along with the transport equations, initial and boundary conditions, are developed;
- The mathematical model is adapted to the employed commercial software, ANSYS FLUENT 12.0.1;
- The modeling capability of the ANSYS FLUENT 12.0.1 is enhanced by encountering the non-standard governing equations for electronic charge and carbonate ion charge through the User-Defined Scalar (UDS) concept;
- The programming language C is employed to customize various source terms, model parameters, material properties, boundary conditions, initial conditions, etc;

- The mathematical model is implemented into ANSYS FLUENT 12.0.1, with user coded sub-routines;
- The grid network is generated by a pre-processing software, ANSYS ICEM 12.0.1, as the input for the finite volume based solver, ANSYS FLUENT 12.0.1;
- An investigation is conducted to find the best controlling strategies and under-relaxation techniques for the present simulation;
- The grid independency test is carried out;
- The time independence tests are carried out;
- The model verification and validation are performed using the available experimental data, and previous numerical studies.

For the sake of time and computational expense, every step in the above pattern was first applied for the simplest case which is the two-dimensional, steady-state, isothermal model with no reforming reaction.

After achieving reasonable results, in the next steps, several simulations were carried out using the more complex models until the three-dimensional, transient, non-isothermal results were obtained. This comprehensive model is then validated with available experimental and numerical data in the open literature. The validated model provides the important details and serves as the foundation for the rest of the research.

The transient characteristics of MCFCs are analyzed by implementing the sinusoidal impedance frequency approach and linear step change. More details are presented in Chapter 6.

In this thesis, a CFD visualization software tool, Tecplot 360^{TM}, is employed to explore and analyze the numerical data, arrange multiple XY, 2D and 3D plots, and create vector and contour plots.

1.4 Thesis Outline

This thesis is organized in seven chapters and two appendices.

Chapter 2 presents the corresponding background, including an introduction to fuel cells, MCFC components, reforming processes, etc.

A comprehensive literature review on the existing steady state and transient models along with future prospects are included in Chapter 3.

Chapter 4 introduces the mathematical formulation of the current model comprising the governing equations, constitutive laws, boundary and initial conditions and the model input parameters.

The numerical procedure, incorporated to solve the system of partial differential equations, is illustrated in Chapter 5.

The numerical results based on the developed model are presented in Chapter 6.

Chapter 7 summarizes the conclusions and some recommendations for future work.

The code development along with a sample MCFC-Model code is presented in the appendices.

Chapter 2

Background

2.1 Introduction to Fuel Cells

A fuel cell is an energy conversion device that converts the chemical energy stored in fuels and oxidants into electricity through electrochemical reactions. It consists of an electrolyte material sandwiched between two thin electrodes, namely anode and cathode. Fuel and oxidant are continuously fed to the anode and cathode, respectively. Ions, which are produced through the electrochemical reactions at one electrode, are conducted to the other electrode through the electrolyte. Electrons are cycled via load and the electric current is generated by the flow of electrons. Figure 2.1 demonstrates the basic configuration of a typical fuel cell.

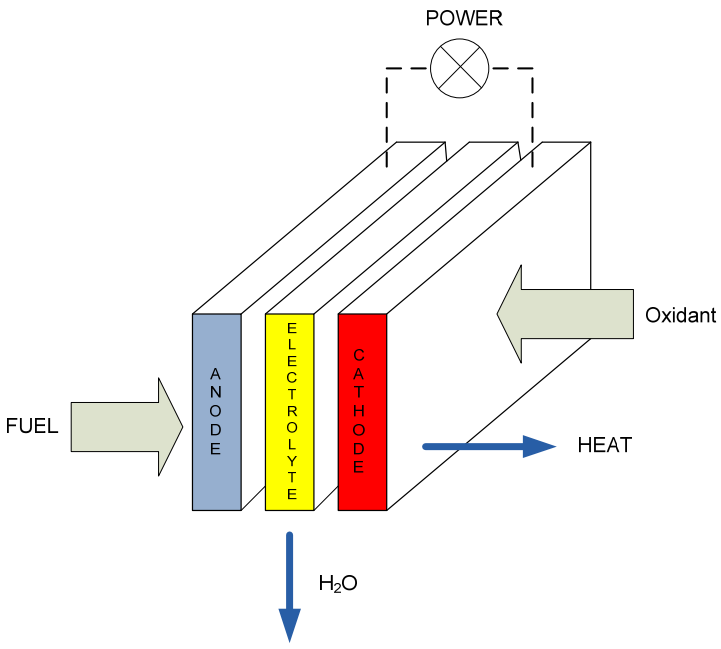

Figure 2.1: Basic configuration of a fuel cell.

Fuel cells work in the same manner as batteries, except they are not limited to the energy stored within the system since fuel may be continuously supplied. An important characteristic of fuel cells is their very low environmental impact. In addition, they have fewer moving or vibrating mechanical parts, and hence operate with minimal noise.

The promise of a more efficient and environmentally friendly means of generating power for mobile, portable and stationary applications has given rise to the development of several different types of fuel cells, typically requiring hydrogen as the ultimate fuel. Figure 2.2 summarizes the type, fuel and applications of fuel cells. They can be used for a wide variety of applications such as stationary power generation, cogeneration of heat and power units or even multi-megawatt central power plants and as auxiliary power in mobile applications.

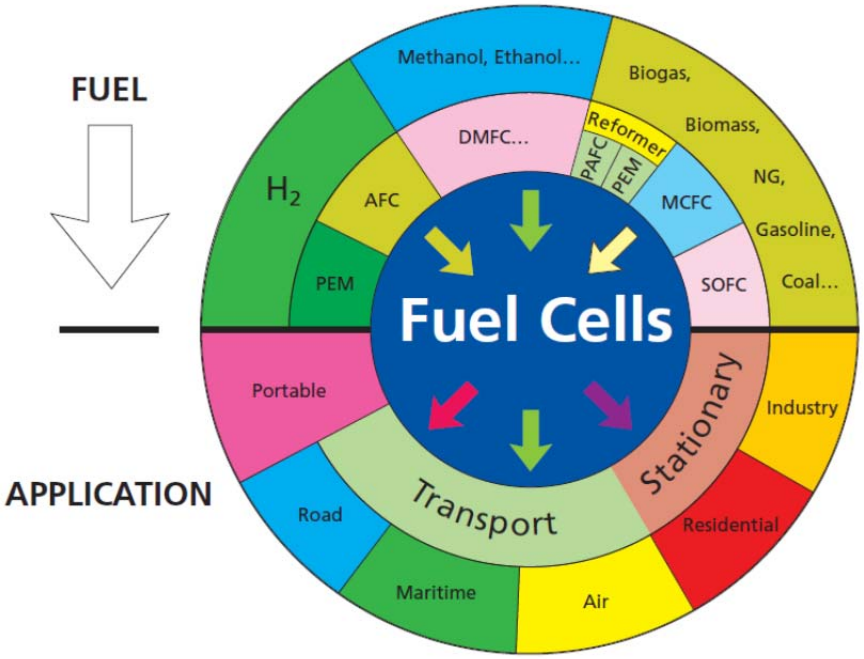

Figure 2.2: Fuel cells technologies, fuels and applications [2].

2.2 Classification of Fuel Cells

Although the very first fuel cell was demonstrated by Sir William Grove [7], in 1839, the renaissance of fuel cells began in 1950s when Bacon [8] introduced a fuel cell with dual porous electrodes made of Nickel and Lithiated Nickel Oxide. Afterwards, a modern version was successfully used in the 1960s, when a fuel cell provided onboard electric power for the Apollo space vehicle and Gemini program. It was a 1.5 kW alkaline fuel cell (AFC). Since 1839, when the first fuel cell was investigated, several different types have been developed and utilized for various applications. Considering the parameters related to the fuel cells operation or construction, they can be classified in different ways. Some of the major classifications are based on the type of electrolyte used, the type of ion transferred through the electrolyte, the type of reactants, operating temperature and pressure, direct or indirect use of primary fuels, and primary or regenerative systems [9].

Since the classification based on the type of electrolyte reflects the properties of fuel cell (operating principle, materials, design and construction), it is customary now to name them by their related electrolyte. Founded on this classification, there are five major fuel cells, namely; alkaline fuel cell (AFC), molten carbonate fuel cell (MCFC), phosphoric acid fuel cell (PAFC), proton exchange membrane (PEMFC) and solid oxide fuel cell (SOFC). Table 2.1 summarizes the characterizations of these fuel cell systems. Detailed specifications can be found in comprehensive references [9-11]. Fuel cells can also be categorized by their operating temperature. The alkaline fuel cell, phosphoric acid fuel cell and proton exchange membrane fuel cell are called low temperature fuel cells, while solid oxide fuel cells and molten carbonate fuel cells are named high temperature fuel cells.

Table 2.1: Summary of major characteristics and technological status of various fuel cells.

Type	**MCFC**	**PEMFC**	**SOFC**	**AFC**	**PAFC**
Electrodes	nickel and nickel oxide	carbon	perovskite and perovskite/metal cermet	transition metals	carbon
Electrolyte	immobilized liquid molten carbonate in $LiAlO_2$	hydrated polymeric ion exchange membranes	perovskites (ceramics)	mobilized/ immobilized potassium hydroxide in asbestos matrix	immobilized liquid phosphoric acid in SiC
Catalyst	electrode material	platinum	electrode material	platinum	platinum
Interconnect	stainless steel or nickel	carbon or metal	nickel, ceramic or steel	metal	graphite
Charge Carrier	CO_3^{2-}	H^+	O^{2-}	OH^-	H^+
Application	large-scale power generation, distributed power generation	mobile, portable, space, stationary, low power generation	medium- to large-scale power and CHP, vehicle APUs, off-grid power and micro-CHP	space, military, mobile	medium- to large-scale power and CHP
Operating Temperature (˚C)	600-700	50-80	800-1000	60-90	160-220
Projected Power Level (kW)	1000-100,000	0.01-1000	100-100,000	10-100	100-5000
Projected Power Density (mW/cm^2)	> 200	> 600	> 300	> 300	> 250
Projected Capital Cost (U.S. $/kW)	1000	> 200	1500	> 200	3000
Lifetime Projected (hr)	> 40,000	> 40,000	> 40,000	> 10,000	> 40,000
Fuel Efficiency % (Chemical to Electrical)	55-65	45-60	55-65	40-60	55

Source: adapted from [9-11].

2.3 Molten Carbonate Fuel Cells

2.3.1 Development and Commercialization History

Molten carbonate fuel cells were initially developed with the intention of operating directly on coal [9]. They have a history that can be traced back at least as far as the 1920s [12]. Baur et al. [13] developed the first molten carbonate fuel cell based on an equimolar mixture of sodium and potassium carbonate melt that operated at about 800-900 ˚C. The very first experimental progress of MCFCs on a laboratory scale was made by Ketelaar and Bores [14-15] in the Netherlands, Gorin and Recht [16-17] in the U.S.A., and Lurie [18] and Bannochie [19] in the U.K..

Subsequently, two major U.S. companies, MC Power Corporation (now Gas Technology Institute (GTI)) and Energy Research Corporation (now FuelCell Energy Corporation) developed MCFC systems for commercial and industrial applications. In 1997, the world's first cogeneration (heat and power) MCFC power plant, a 250 kW unit was installed by MC Power Corporation in California [20]. In 1996, FuelCell Energy Corporation installed a 2 MW pre-commercial test unit in Santa Clara, California. They signed agreements to build several MCFC systems in the United States and Japan [20]. After three decades, up to 2007, almost 40 FuelCell Energy power plants have been installed in the USA for a total of 11.5 MW; 15 in Asia amounting to 8.5 MW, and 12 in Europe corresponding to about 4.5 MW [22]. In late 2008, Enbridge Inc., installed the world's first hybrid MCFC into its natural gas pipeline infrastructure. The 2.2 MW project pairs a turbo-expander with a 1.2 MW Direct FuelCell unit manufactured by FuelCell Energy.

Despite the fact that MCFCs are currently being demonstrated in several sites around the world, only six companies are considered as major MCFC developers:

- FuelCell Energy (FCE, USA)
- CFC Solutions (Germany)
- Ansaldo Fuel Cells (AFCo, Italy)
- Ishikawajima-Harima Heavy Industries (IHI, Japan)
- POSCO/KEPCO consortium and Doosan Heavy Industries (Korea)
- GenCell Corportation (USA)

It is expected that MCFCs could generate more than 15 GWe in 2022 [22].

Although there are demonstration programs all around the world, a strong research and development (R&D) programme is also undertaken by R&D organizations, industrial companies, and universities. The technology of the molten carbonate fuel cells has already reached an advanced stage. However, for a commercial breakthrough there is still considerable financial commitment required by private and public contributors to continually support research advances.

2.3.2 Why Molten Carbonate Fuel Cells?

Molten carbonate fuel cells operate at high temperature. They are particularly suited for the stationary co-generation of electrical power and heat, and distributed energy supply (operating today with natural gas), which enables the development and use of this technology independently from the establishment of a hydrogen infrastructure [21]. In addition, as MCFCs generate electrical power and extremely hot exhaust gas, they are particularly well suited for combined heat and power cogeneration (CHP) applications. This type of fuel cell offers high electric energy conversion efficiency in a simple cycle configuration. Therefore, it can significantly reduce the exploitation of non-renewable and renewable energy sources [22]. They are also utilized in off-grid applications to replace small diesel generators. Furthermore, they can be used as auxiliary power units (APUs) for vehicles. Because of the very high operating temperature, MCFCs can operate without using an external reformer to convert hydrogen-rich fuels to hydrogen. Accordingly, from an economic point of view the system can be greatly simplified and consequently the cost will be reduced. In other words, the efficiency of the system is significantly increased. MCFCs operate at about 650°C. Therefore, unlike the low temperature fuel cells, no precious metal is required as the fuel catalyst. The reason is that the operating temperature is sufficiently high for the electrochemical conversion processes to take place at the electrodes without any precious metal catalysts [9]. Moreover, another consequence of the high operating temperature is that carbon monoxide (CO) is a welcomed fuel for the MCFCs in contrast to other fuel cells, where it is a catalyst poison. Therefore, a variety of CO-containing fuels can be used. Hydrocarbons, syngas derived from biomass or coal, landfill gas, gas obtained

from industrial or agricultural by-products are the major fuel resources of MCFCs. The other benefit of the high temperature MCFC system is the better utilization of the heat generated in the fuel cell. High temperature exhaust heat can not only be used in industrial processes of all kinds (e.g. as process steam) but also for further power generation in downstream turbine generators, especially in larger installations.

One of the disadvantages of current MCFC technology is durability. The high temperatures and corrosive electrolyte accelerate component breakdown and corrosion, which in turn decreases cell life.

Durability of materials is one of the main concerns in MCFC and SOFC technologies. However, there are two distinct characteristics that make MCFCs and SOFCs differ when it comes to positioning and integrating them in the gas turbine based system. The first feature is the operating temperature. Technically, MCFCs operate at 853-923 K while SOFCs operate at 1073-1273 K. The second difference is related to the carbon dioxide. Existence of CO_2 in the anode gas has a harmful effect on the performance of a SOFC, while it is a necessity for the MCFC. Furthermore, MCFCs are integrated downstream of the micro-turbine while SOFCs are almost constantly positioned upstream of the micro-turbine. Generally, for a system with the combustion chamber still present in the micro-turbine model, the MCFC is integrated such that the exhaust gas from the micro-turbine is utilized to feed the MCFC along with the anode exhaust.

2.3.3 Operating Principles of MCFCs

The basic operation principle of a typical MCFC is shown in Figure 2.3. At the anode gas channel (AGC) inlet, the fuel gas, which can be pure hydrogen or reformed hydrogen gas (or even gasified coal), enters the system and diffuses through the porous anode where hydrogen molecules get involved in the hydrogen oxidation reaction (HOR). During this electrochemical reaction, hydrogen combines with carbonate ions ($CO_3^=$), resulting in water vapour and carbon dioxide. Moreover, the released electrons migrate through an external circuit, create electricity, and return to the cell through the cathode.

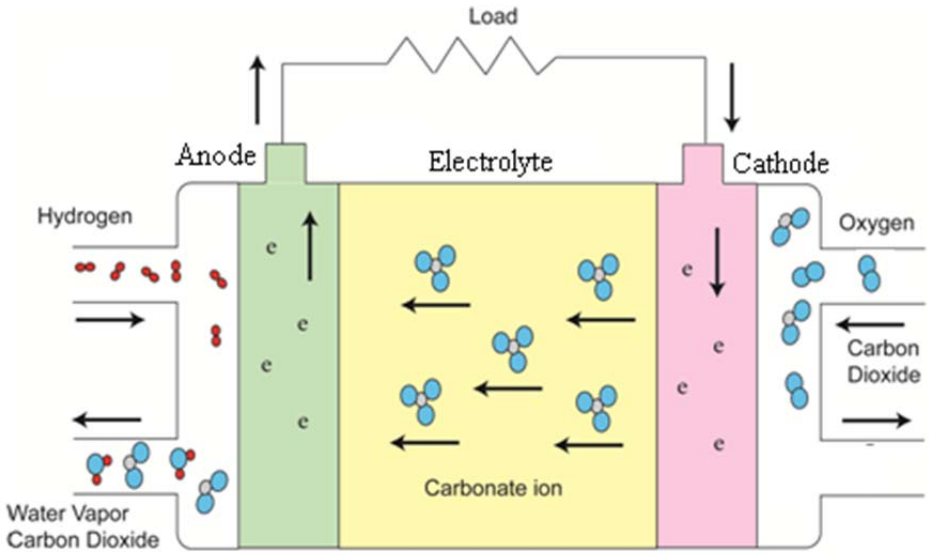

Figure 2.3: Schematic and operation principle of molten carbonate fuel cells.

Thereby, the overall electrochemical reaction at the anode is:

$$H_2 + CO_3^{=} \rightarrow H_2O + CO_2 + 2e^- \tag{2.1}$$

On the cathode side, pure oxygen or air along with carbon dioxide enter the cathode gas channel (CGC) and diffuse through the porous cathode, where the oxygen reduction reaction (ORR) takes place. Oxygen is reduced to carbonate ions by combining with carbon dioxide and the electrons coming from the external circuit. The carbonate ions formed at the cathode move through the electrolyte towards the anode, carrying the electric current, and completing the carbon dioxide circuit. Thus, the overall electrochemical reaction at the cathode can be summarized as follows:

$$\frac{1}{2}O_2 + CO_2 + 2e^- \rightarrow CO_3^{=} \tag{2.2}$$

Finally, the overall chemical reaction of the MCFC is:

$$H_2 + \frac{1}{2}O_2 \rightarrow H_2O + Heat + Electricity \tag{2.3}$$

This simple reaction indicates that an MCFC uses hydrogen and air to generate clean electrical energy besides a high temperature water vapour that can be used for heating systems. Although carbon dioxide could be supplied from an external source, it is the usual practice in an MCFC system that the carbon dioxide generated within the anode is recycled externally to the cathode where it is consumed [23]. The transfer of the carbon dioxide from the anode exhaust to the cathode inlet can be handled in two ways:

(i) burning the anode exhaust in a combustor (burner) in the presence of excess air and mixing it with cathode inlet gas after removing the water vapour or

(ii) utilizing a product exchange device to separate the carbon dioxide from the anode exhaust. The second way yields a higher cell voltage since it provides a richer oxidant [24].

Molten carbonate fuel cells operate approximately at 650 °C, current density of 100~200 mA/cm^2 (typically 160 mA/cm^2), cell potential of 0.7~0.95 V (typically 0.75 V), at atmospheric pressure and 75% fuel (hydrogen) utilization [9]. Although higher pressure may result in better performance, it increases the possibility of carbon particles formation according to the Boudouard reaction. They can deposit in the gas channels or even inside the cell structure:

$$2CO \quad \leftrightarrow \quad CO_2 + C \tag{2.4}$$

2.3.4 Components and Materials

Figure 2.4 shows the proportion of each material for a MCFC stack [26]. Although, there is a general standard of MCFC that serves as a baseline model, for efficient operation, it leaves room for further improvement [25]. The main materials of the standard MCFC are nickel (for electrodes), lithium aluminate (solid matrix), lithium-sodium or lithium-potassium carbonate (for electrolyte), stainless steel (for bipolar plate or gas manifolds) and chromium and/or aluminium for reinforcement and corrosion protection. Table 2.2 summarizes the state-of-the-art materials for MCFCs [26]. The following sections describe the main components of the MCFCs and their specifications.

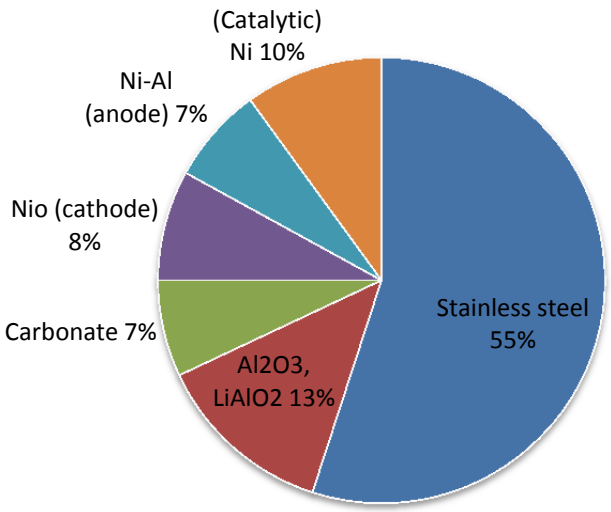

Figure 2.4: Material composition (wt. %) of an MCFC stack (adapted from [26]).

2.3.4.1 Anode

The anode is a porous electrode wherein the hydrogen is electrochemically oxidized. Unlike the low temperature fuel cells, in MCFCs, the anode can convert carbon monoxide and so it is not a poisoning gas anymore. Hence, biogas, syngas and coal gas, which contain carbon monoxide, can be utilized as fuel. Technically, the conversion of the carbon monoxide can occur through the water-gas shift reaction:

$$CO + H_2O \quad \leftrightarrow \quad H_2 + CO_2 \tag{2.5}$$

Thanks to the high operating temperature, there is no need for noble metals for the anode. It is worthwhile to mention that hydrogen molecules tend to insert themselves in gaps and vacancies which can lead to weakening the bonds of the metal's crystal structure, and consequently, fragility and brittleness of the material [26]. This process is known as the hydrogen attack or the hydrogen embrittlement. The anode material should have a good electrical conductivity in order to facilitate flow of the electrons to the external circuit. The thickness of the anode should be kept as low as possible to reduce resistance and hence the ohmic losses. Generally an ideal anode material has the properties which are tabulated in Table 2.3.

Table 2.2: Characteristics of state-of-the art cell components of MCFCs.

Component	Property	Current Status
Anode	Material	Ni with 2-20 % Cr/Ni-Al
	Thickness	0.5-1.5 mm
	Porosity	50-70 %
	Pore size	3-6 μm
	Surface area (BET)	0.1-1 m^2/g
Cathode	Material	Lithiated NiO (with 1-2 wt.% Li)
	Thickness	0.4-0.75 mm
	Porosity	70-80 %
	Pore size	7-15 μm
	Surface area (BET)	0.15/0.5 m^2/g (Ni pretest/post-test)
Electrolyte	Material	Alkali carbonate mixture
	Composition	62 % Li_2CO3–38% K_2CO_3 by mole
		50 % Li_2CO3–50% Na_2CO_3 by mole
		70 % Li_2CO3–30% K_2CO_3 by mole
Electrolyte-support	Material	γ-$LiAlO_2$
	Thickness	1.8 mm (hot pressed)
		0.5 mm (tape cast)
	Pore size	0.5-0.8 μm
	Surface area	0.1-12 m^2/g
Electrolyte-filled	Composition	40 % $LiAlO_2$–50% K_2CO_3 by wt.
		50-60 % carbonates
Current collector	Anode	Ni or Ni-plated steel 1-mm thick
	Cathode	Type 316 (perforated) 1-mm thick

Source: adapted from [9].

State-of-the-art MCFC anodes are made of a porous sintered nickel-chromium/nickel-aluminum alloy. The addition of Cr prevents the sintering of the porous anode, since it forms $LiCrO_2$ at the grain boundaries and prevents metal diffusion [23]. Moreover, small amounts of metal oxide (e.g. Al_2O_3, $LiAlO_2$, etc) prevent mechanical creep [27]. These are usually made with a thickness of 0.4 to 0.8 mm with a porosity between 55 and 75% [23].

Table 2.3: Some characteristics requiredfor the ideal anode of MCFCs.

Requirement	**Level**
High electrocatalytic activity for H_2 oxidation	-
Resistance to H_2 interstitial interference	100% H_2 for >40000 h
Enduring resistance to sulphur poisoning	> 10 ppm S
Good wetting properties (low wetting angle)	< 45˚
Porosity	45-70% 3-6 μm size
Conductivity	> 1 S/cm
Resistance to fracture, sintering, creep, thermal dilation	40000 h in full load operation
Low solubility in alkali carbonates	< 10 ppm
Low cost	-

Source: adapted from [26].

2.3.4.2 Cathode

The cathode is a porous electrode wherein the oxygen reduction reaction takes place. The cathode material has been lithiated nickel oxide (NiO) from the beginning of its development. This component is known to have small but finite solubility in the electrolyte [28]. Generally, the cathode material should have the following characteristics: high electronic conductivity to minimize resistance to ohmic polarization; chemical and physical stability at the operating conditions to maintain catalytic performance; low solubility in the cathode-electrolyte environment to avoid precipitation of metal in the electrolyte structure; high electrocatalytic activity for oxygen reduction; suitability for the fabrication of porous electrodes with high specific surface area; good wettability by the electrolyte in the oxidant environment [25]. Generally an ideal cathode material has the properties which are summarized in Table 2.4.

The major problem associated with a NiO cathode is its solubility in the electrolyte. At high carbon dioxide partial pressures, Ni^{2+} ions are formed according to the following reaction:

$$NiO + CO_2 \rightarrow Ni^{2+} + CO_3^{=} \tag{2.6}$$

The released Ni^{2+} ions are precipitated in the electrolyte and prepare a path for other nickel ions towards the anode. Consequently, the fuel cell performance is decreased because of the

electronic short-circuit caused by the metallic nickel ions. The optimal thickness of the electrode, which depends upon the gas composition and current density, ranges from 0.4-0.8 mm [9].

Table 2.4: Some characteristics required for the ideal cathode of MCFCs.

Requirement	**Level**
High electrocatalytic activity for O_2 reduction	-
High electronic conductivity	> 1 S/cm
Low solubility	< 5 ppm
or low dissolution rate in alkali carbonates	< 1 μg/cm^{2}h
Porosity	70-80% before (in situ) lithiation and oxidation, (60-70%) after 7-15 μm pore size
Good wettability	< 45˚
Congruous thermal expansion coefficient	with other cell components
Low cost	-

Source: adapted from [25].

2.3.4.3 Electrolyte

Generally, the role of the electrolyte is to conduct carbonate ions in the MCFC to facilitate the electrochemical reactions. In order to select a proper electrolyte for a MCFC, several criteria have to be considered:

(i) ionic conductivity,

(ii) solubility of the reactants and products,

(iii) diffusion coefficients of reactants and products,

(iv) the electrode kinetics of cathodic and anodic reactions,

(v) vapour pressure of the electrolyte,

(vi) stability of the cell components e.g., lithium-aluminate matrix and stainless steel current collector [27].

State-of-the-art MCFC electrolytes contain typically 60 wt% carbonate (Li_2CO_3 and K_2CO_3) constrained in a matrix of 40 wt% $LiOAlO_2$. The γ -form of $LiOAlO_2$ is the most stable in the MCFC electrolyte and is used in the form of fibres of less than 1 μm diameter [23]. The tape-casting fabrication method is commonly used for manufacturing of the matrix. This method is usually employed for other components also and provides a means of producing large-area components. Using tape casting, it is possible to produce a very thin electrolyte structure (0.25–0.5 mm), which has an advantage in reducing the ohmic resistance in MCFC. Capillary equilibrium is used as a means of controlling electrolyte distribution in the porous electrodes and stable electrolyte/gas interface in MCFC porous electrodes.

2.3.5 Three Phase Boundary

The reaction site of a molten carbonate fuel cell is the solid electrode surface wetted by the electrolyte where the electrochemical reactions (Equations (2.1) and (2.2)) take place. Hence, this zone is known as the three-phase boundary [9]. A typical three phase boundary of a porous cathode is illustrated in Figure 2.5.

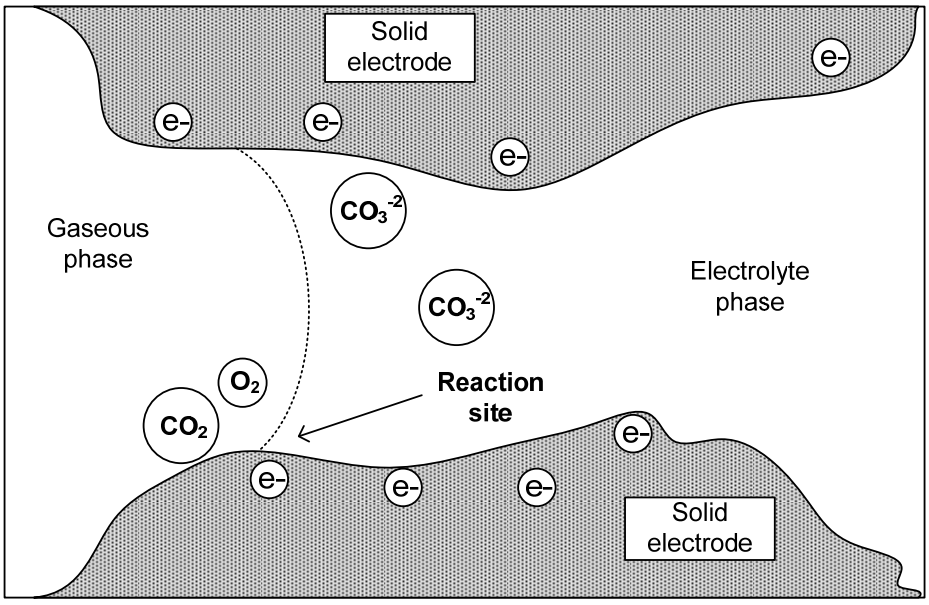

Figure 2.5: The schematic of the three-phase boundary in the cathode of an MCFC (adapted from [9, 54]).

As its name indicates, the three phases are present in this zone located at the electrode/ electrolyte interface: gaseous phase, liquid electrolyte and solid electrode. At this reaction site, the three-phase boundary, carbon dioxide and oxygen molecules react with the electrons and produce carbonate ions. On the other hand, in the anode three-phase boundaries, the hydrogen molecules react with the carbonate ions and generate carbon dioxide, water vapour and electrons.

2.3.6 Reforming Processes

One of the advantages of molten carbonate fuel cells is its fuel flexibility. In fact, carbonaceous fuels can be fed directly to the system due to the high operating temperature. However, having reforming units is necessary to convert the fuel to hydrogen that can be used for the electrochemical reaction occurring at the anode.

Figure 2.6 shows a demonstration of a typical MCFC with the reforming units. First, outside the fuel cell, in an adiabatic external reformer (ER), short chained hydrocarbons are reformed to methane using heat from the fuel gas, which was earlier heated by the off-gas from the fuel cell, thus transforming its thermal energy into heating value. The external reformer operating temperature is lower than the fuel cell temperature. The gaseous mixture is then fed to the indirect internal reformer (IIR) that is located between the cells in the cell stack. Because of the thermal coupling between the electrochemical processes in the cell and the IIR, waste heat from the cells is utilized, and the reforming takes place at approximately the cell temperature. This reforming step significantly increases the hydrogen content of the gas before it enters the anode gas channel. In the AGC zone, the direct internal reforming (DIR) continuously produces new hydrogen from the remaining methane as the electrochemical consumption of hydrogen proceeds and thereby obtains a nearly complete conversion of the reforming process. There are two main reforming processes that take place in the reforming units, namely the methane steam reforming reaction (MSRR) and the water gas shift reaction (WGSR). The former produces hydrogen and carbon monoxide according to Equation (2.7). Carbon monoxide undergoes the shift reaction and generates hydrogen and carbon dioxide (Equation (2.8)).

$$CH_4 + H_2O \quad \leftrightarrow \quad 3H_2 + CO \tag{2.7}$$

$$CO + H_2O \quad \leftrightarrow \quad H_2 + CO_2 \tag{2.8}$$

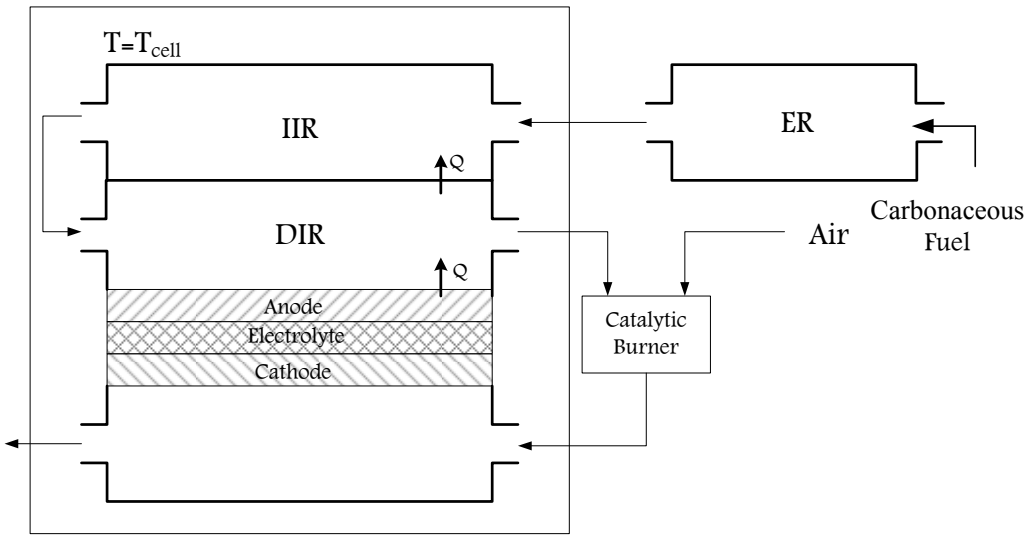

Figure 2.6: Schematic of the external reformer, indirect-internal reformer and direct-internal reformer units in MCFCs (adapted from [9, 54]).

Although, the water–gas shift reaction is slightly exothermic, the overall reforming process is endothermic. The advantage of MCFCs allows the endothermic process to be heated by waste heat generated from the electrochemical reactions at the electrodes. Conversion of methane to hydrogen during the reforming processes significantly increases the heating value of fuel. Furthermore, the endothermal character of this process is a form of chemical cooling for the heat-producing cell, which is important for thermal management of the system. The consumption of the reforming products shifts the chemical equilibrium of the reforming process toward high conversions. The anode exhaust gas consists of unreformed feed gas, reforming products and oxidation products. It is mixed with air and then fed into a catalytic combustion chamber, where all combustible species are completely oxidised. This mixture is then fed into the cathode channel. The cathode exhaust gas leaves the system.

Chapter 3

Literature Review

3.1 Introduction

The important advantages of fuel cells such as low emissions, flexibility in fuel choice and high energy conversion efficiency, initiated the research and development of fuel cells for applications in stationary and mobilized power generation units. By reviewing the previous efforts and accomplishments, it is an irrefutable conclusion that mathematical modeling and numerical analysis have played a key role. In order to investigate different aspects of any process or system without performing costly experiments, mathematical modeling helps to develop an enhanced understanding of the overall functionality of the system. Generally, the existing MCFCs numerical models in the published literature can be categorized in different ways as follows:

- Steady state or transient models
- Zero, one, two or three dimensional models
- Electrode, cell, stack or system level models

As observed in the existing literature, mathematical models of MCFCs can be as simple as a performance model (a set of empirically correlated equations) or as complicated as a system of partial differential equations (PDEs). The latter types of models can include several segregated or coupled PDEs that need to be solved using Computational Fluid Dynamics (CFD). Performance models deal with macroscopic (integral) level phenomena. In contrast, CFD models are formulated at a smaller (differential) level [29].

This chapter presents a comprehensive review of the past studies on MCFC models. The review will help to outline the current issues, problems or challenges that need to be resolved. Subsequently, in Chapter 4, the results of the review will be employed to develop a comprehensive model that can address the lack of details in the existing models.

3.2 CFD Models

Theoretically, a CFD model considers non-uniform distributions of the field variables (e.g. electric charges and concentration) within the porous components of the unit cell. These components are in direct contact with the bulk gas that has uniform composition and temperature. The microscopic structure of the electrodes (pore sizes and distribution) as well as the electrolyte distribution in the electrode pores is taken into account. As discussed in section 3.1, the CFD models can be divided into electrode, cell, stack and system level models.

3.2.1 Electrode and Cell Level Models

3.2.1.1 Steady State Models

Generally, adequate models of porous electrodes in steady-state mode would aim to enable researchers to illustrate precisely the relationship between the MCFC performance and the structure of pores. This has been a major subject of debate among researchers and several electrode level models have been developed to simulate the behaviour of porous gas-diffusion electrodes.

Simple Pore Models

The simplest electrode model, the so-called “Simple (or Flooded) Pore Model”, was introduced by Austin et al. [30] in 1965. The problem associated with this primitive model is the very poor performance prediction due to the severe mass transfer limitation in the system. This model shows an undesirable electrolyte-solid-gas distribution that in reality corresponds to a "flooded"

electrode (pores flooded with electrolyte). A practical gas-diffusion electrode should avoid flooded pores.

Following that model development, researchers have tried to introduce corrections to this model and introduced the "Thin Film Model" [31-32] and the "Finite-Contact-Angle Meniscus Model" [33]. These models provide some extensions to the simple pore model and consider the variations in the wetting tendency of the electrolyte. However, in a flooded pore with finite-angle meniscus, the current is assumed to be predominantly concentrated in a small portion of the pore wall. Also, in a film-covered pore, the electrochemical reaction still has a propensity to be concentrated in the part of the film that is closest to the bulk electrolyte. Iczkowski [34] then addressed these limiting assumptions and incorporated a model description of the migration of reactants on the surface of the electrode.

Dual-Porosity Models

Bearing in mind the above cited studies, a more realistic porous electrode model ought to consider a spectrum of pore sizes instead of simple single pore. Hence, several dual-porosity models were introduced [35-37]. For instance, the "Standard Agglomerate Model", presented by Giner and Hunter [38], presumes an idealized electrode in which the pores are divided into two forms. The micro-pores are assumed to be completely flooded with electrolyte, while the macro-pores are thought to enclose only gas. The model has been reasonably successful in predicting the performance of fuel cells. It is acknowledged that the agglomerate model characterizes electrode structure more satisfactorily than the thin film model [39]. However, the anode and cathode have different wetting characteristics and it is necessary to account for this. In fact, the nickel anode is not well wetted under reducing conditions, which would correspond reasonably well with the absence of an extended film ("Dry Agglomerate Model"). In contrast, the cathode is very well wetted (contact angle 0), and the agglomerates are probably covered by a film.

To address the different wetting issue, Wilemski [40] proposed individual porous electrode models for the anode and cathode of a molten carbonate fuel cell. In this model, all electrochemical activity is assumed to take place on film-covered walls of the larger gas filled pores. Smaller flooded pores were treated as electrochemically inert. The model showed good

agreement with experimental data. Nevertheless, it oversimplifies pore structure, and requires measured values for film areas and thicknesses, forcing these parameters to be treated empirically. In addition, the lack of experimentally measured values is always considered to be a drawback in numerical modeling.

In order to avoid using empirical values, Kunz et al. [41] used a theoretical approach and calculated the effective agglomerate diameter, porosity and tortuosity based on the electrode's pore spectrum and electrolyte content. By doing this, they modified the conventional agglomerate model and developed a homogeneous model.

Many researchers have used this theory and developed it further. For instance, Jewulski and Suski [42] proposed an isotropic steady state, one dimensional model for the porous anode of an MCFC, which required the thickness of the electrolyte film in the pores as the only adjustable parameter. Subsequently, Jewulski [43] applied this model for the porous cathode as well. Yuh and Selman [39] developed a steady state, two-dimensional dual-porosity agglomerate-type model for the porous electrodes. The proposed model involves a more complicated expression instead of the Ohm's law to include ionic migration in the melt.

Lee et al. [44] indicated that the resulting values of the fit parameters depend strongly on the choice of the agglomerate radius (or slab width), the film thickness, and the electrolyte conductivity which are very difficult to be meaningfully determined. Furthermore, because of its geometric restrictions, it is difficult to incorporate the electrolyte-filling degree into the agglomerate model. Another problem of the agglomerate model is that the model does not accurately predict the optimal degree of electrolyte filling [45].

Volume-Averaged Models

So far, all of the previous stated models are based on a continuum approach to modelling. Prins-Jansen et al. [46] chose to use a more fundamental approach named "Agglomerate-Like Model" which is based on an averaging technique that describes the processes on the micro-scale. This model eliminates the important drawback of the preceding agglomerate model caused by geometric assumptions and restrictions. Unlike the agglomerate model, the new model is suitable

for studying three dimensional and anisotropic problems, and incorporates the degree of electrolyte filling.

Later on, Fontes et al. [47] adopted this new approach and developed a steady-state two-dimensional pseudo-homogeneous model for the three-phase structure of the porous cathode (solid, gas and electrolyte). They published the results of subsequent work [48] and compared the homogeneous and heterogeneous agglomerate models in one and two-dimensional calculations, respectively.

Electrochemical-Potential Models

In the "Electrochemical-Potential Model" [49], the electrochemical potentials for individual species are combined to define component potentials which are separated by the slow chemical and/or electrochemical reactions. The reaction rates for the slow reactions are then assumed to be proportional to the differences in these component potentials. Fehribach et al. [49] employed this model for the peroxide mechanism describing the electrochemistry of a MCFC cathode. Fehribach and Hemmes [50] compared the polarization losses associated with the various diffusion-reaction-conduction processes in MCFC cathodes. They estimated each type of polarization loss in terms of component electrochemical potentials. The main advantage of the component-potential approach is that it simplifies both the analysis and the computations. However, it would be more difficult to approximate the current densities, if one had to think in terms of concentration [51].

Cell Level Models

In the 1980s and 1990s, MCFC modeling focussed on electrode level models. Over the past decade, researchers have employed the cell level models to investigate different aspects of the unit cells.

Subramanian et al. [52-53] employed the three-phase homogeneous model of Prins-Jansen et al. [46] and reported the performance analysis results based on a one-dimensional model.

Subsequently, Berg and Findlay [54] pointed out that the models presented by Subramanian et al. [52-53] are ill-posed. The problem arises when the authors neglect convection and assume that the two diffusive fluxes make up the mass transport of the two species within the cathode. However, these fluxes, which are meant to point in the same direction, must add up to zero by definition and cannot alone contribute to non-zero fluxes as can be found in such electrodes [54].

Despite all of these efforts in developing porous-electrode mathematical models, temperature variation effects have been overlooked. Moreover, hydrodynamics of the gas flow in the gas channels are disregarded. The effects of convective mass flux are overlooked. Specifically, three-dimensional studies based on a volume-averaging technique appears to be absent in the literature. Lastly, the unit cell behaviour at extreme gas utilization or high current density is rarely reported.

3.2.1.2 Transient Models

The cell corrosion and lifetime are still considered to be the greatest obstacles to commercialization. Technically, dynamic situations can cause non-uniform temperature and current density profile which have significant effects on the cell life cycle, and hence economic matters. The MCFC behaviour in dynamic situations still is not fully understood. Specifically, when the cell undergoes voltage/load variation or fluctuation, predicting the fuel cell dynamic performance becomes challenging. The transient situation at the MCFC start-up is another example of varying conditions.

Having an improved understanding of the system behaviour in dynamic situations helps to design a more robust control system in order to minimize the fuel consumption and maximize operating lifetime. In fact, in order to choose an optimal control system and operation parameters, an appropriate dynamic model of the MCFC consistent with other components of the hybrid system is ideal. This can be achieved by determination of time scales of the major dynamic processes in the MCFC and their analysis and comparison with time scales of other devices in the hybrid system. The developed dynamic model can be further employed to examine the quantitative response of the system to different inlet perturbations. In addition, phase shifts between variables' dynamic responses and the voltage perturbation will be identified.

By now, it has become clear that many studies have been performed in order to develop the most comprehensive mathematical model representing the various processes which occur in molten carbonate fuel cells operation [39-51]. Some authors have implemented these models to demonstrate steady state performance characteristics of MCFCs. However, implementation of these models in transient simulations have often encountered several simplifications. In other words, model reduction methods are widely used to establish a simple simulation model according to various operating conditions.

For instance, Hao et al. [55] developed a simplified dynamic model for a cross-flow molten carbonate fuel cell and solved the model using VC++. The model was two-dimensional with uniform voltage distribution. This model was developed based on identical heat characteristics for anode, cathode and electrolyte while they typically have an order of magnitude difference.

Another two-dimensional model was presented by Fermegila et al. [56] who employed this model to study the effects of step change and linear ramp for various inlet conditions. The authors neglected the enthalpy transport between the electrode pores and gas phase and also assumed an equally distributed current pattern in both electrodes. This is not always appropriate because of the different thermal characteristics of the gas and electrode materials.

There have been a few studies concerning transient behaviour at stack level models, as well. As an example, Lukas et al. [57] employed the lumped-parameter formulation of the first principle equations for a fuel cell stack with a simplifying assumption indicating that the solid mass temperature is equal to the exit stream temperature. In fact, this model does not provide sufficient information on the temperature profile in the electrodes and the electrolyte which is critical in MCFC lifetime and components degradation.

It was found that three-dimensional dynamic analysis is overlooked in the available literature. He and Chen [58] developed a three-dimensional transient stack model, implemented in a CFD commercial software (PHONICS), to demonstrate the heat transport at stack level. However, the processes of gas transport and chemical reactions were incorporated only at cell level.

The dynamic performance of fuel cell hybrid systems has also been investigated by some researchers. As an example, the investigation of the control performance of the internal

reforming MCFC systems was performed by Lukas et al. [57, 59, 60]. They used the actual data from a 2-MW demonstration project system. However, the focus of this study was primarily on the unit cell and the hybrid system was not considered. Zhang et al. [61] presented a dynamic model for a hybrid fuel cell-gas turbine system with some control loops applied to the system. A distributed power generation system was studied by Grillo et al. [62]. This hybrid system is based on pressurization and heat recovering of a 100 kW molten carbonate fuel cell. Au et al. [63] investigated the optimization of MCFC operating temperatures by presenting a case study in which the efficiency of a CHP plant was analyzed. Some authors have also used energy and exergy analysis to evaluate various system efficiencies for the integrated power generation systems [64].

A different approach to the dynamic performance modeling was implemented by Shen et al. [65] who used neural network structures to model transient cell behavior of a fuel cell. However, this model is not appropriate to other high-temperature fuel cell systems.

Recently, a transient mathematical model for a single counter-flow MCFC with an internal reformer was developed by Heidebrecht and Sundmacher [66]. Simplifications like plug flow and constant pressure in the gas phase along with a lumped solid phase for energy balance were used. Later on, they [67] presented a more detailed study based on a dimensionless mathematical model of a single cross-flow MCFC with spatially distributed simulation results for steady-state and dynamic scenarios. This model can be applied to any other high-temperature fuel cell such as SOFC but in two-dimensional simulation mode.

In brief, a considerable number of the present studies have been carried out by either performing the simulation for MCFC individual components or reducing the dimension to 0D, 1D or 2D. In addition, many of them have employed uniform distribution of the field variables, which significantly influences the accuracy of the dynamic results. The linear dynamic responses are overlooked. More importantly, no single study was found on the dynamic response of the MCFC under non-linear voltage perturbation.

3.2.2 Stack Level Models

Several unit cells can be combined to deliver the desired amount of energy. The unit fuel cells can be electronically in contact using the bipolar plates. Such a design is called a fuel cell stack. Temperature and current density are the two crucial parameters in a molten carbonate fuel cell stack which have a significant impact on its efficient and safe operation. It is important to accurately predict the temperature distribution of the MCFC stack because the local current density and temperature are strongly coupled. Moreover, the components corrosion, differential expansion and electrolyte evaporation losses due to the large temperature gradients, can be studied only when the temperature distribution is known. One of the engineering problems encountered in the design of fuel-cell stacks is the configuration of gas-flow manifolds and the overall pattern of gas-flow that would give uniform flow distribution and stable cell operation. The geometrical structure and size of the gas manifolds are the important parameters to be considered.

A stack model engages the physical and chemical phenomena at electrode, cell and stack levels. In other words, the stack model is the extension of the cell model by taking into account the heat transfer and gas transport processes with regard to the stack configuration. Not many studies are available on stack analysis in open literature.

A three dimensional simulation of a MCFC stack has been done by He and Chen [68] using CFD technique. Technically, their model can consider simultaneously the dominant processes of a stack, such as mass transport, chemical reactions, heat transfer and the voltage-current relation. It is also capable of calculating the mass distribution across the stack rather than assuming a uniform distribution but still uses a correlation for the cell current densities instead of solving the fundamental conservation equation.

An exploration of the parameters distribution in an MCFC stack under transient conditions was presented by He and Chen [69]. The three dimensional stack model implemented in CFD commercial software (the PHONICS) showed that the current density profile changes rapidly in the beginning and slowly in the following stage and that the temperature response is slow.

Yoshiba et al. [70-71] developed a three dimensional numerical analysis model and analyzed five gas flow type stack performances. They showed that in the case of uniform gas

distribution in the cell plane, the co-flow type stack has the highest net output power. In addition in the co-flow type stack, the temperature of cathode outlet gas is almost equivalent to the maximum temperature of the stack.

In order to investigate the effect of a change in the gas channel height on the gas-flow uniformity, pressure loss and the gas diffusion, a three-dimensional flow analysis in a plate heat exchanger type stack was conducted by Hirata et al. [72]. The effects of the gas channel height on the distribution of the reactive gas concentration in the direction perpendicular to the channel flow evaluated by an analytical solution of the two-dimensional concentration transport equation. The appropriate gas channel height in the molten carbonate fuel cell stack was investigated.

The effects of various stack parameters, numerical simulation parameters and internal/external gas manifolds of MCFC stacks have been investigated [73-75]. Bittani et al. [76] developed a dynamical model of a MCFC stack, describing both the thermo-fluid-dynamical and the electrochemical phenomena. Following a first-principle approach, a set of differential and algebraic equations is written, based on mass, momentum, energy, and charge balance referred to as small control volumes inside a cell. The outlined two-three-dimensional description took into account the strong point-to-point anode and cathode reaction coupling due to gas cross-flow.

Lee et al. [77] presented a mathematical model to simulate the performance of a molten carbonate fuel cell 5 kW class stack. They assumed identical average current densities for each cell of the stack.

3.2.3 Reforming Models

The reforming processes of molten carbonate fuel cells have been investigated in the open literature. Some authors have considered just the water gas shift reaction and others have employed both the methane steam reforming reaction and water gas shift reaction. Occurrence of these reactions only depends on the fuel type and its components. Most of the previous studies have considered several assumptions to simplify the complex mathematical models.

For instance, Park et al. [78] analyzed the conversion of methane, the temperature distribution and the composition of gases through a two-dimensional mathematical model for the reformer and the cell. The results showed that due to a temperature rise, the reactants concentration change rapidly at the entrance, and consequently the rate of reforming reaction increases.

Kim et al [79] simplified a two-dimensional steady state model by assuming x-direction flow for anode gas, y-direction flow for cathode gas and ignoring gas channels affects. They also assumed uniform concentration of gases in the direction of thickness. Using all these assumptions, they showed that when the shift reaction is excluded, the conversion of hydrogen is higher than that of a practical cell. At the same current density, the voltage calculated without the shift reaction would be higher than the real value but the effect of the shift reaction on the voltage distribution and cell performance is very small.

A transient mathematical model for a single counter-flow MCFC with an internal reformer was developed by Heidebrecht and Sundmacher [66]. Simplifications such as plug flow and constant pressure in the gas phase as well as a lumped solid phase for energy balance were used. In addition, the potential field was described by a set of algebraic equations allowing for the calculation of a spatially distributed potential field.

A steady state investigation was carried out by Ma et al. [80]. They presented the effect of non-uniform inlet flow rate from channel to channel on the fuel cell performance for both co-flow and cross-flow cell configurations. The results showed that the non-uniformity deteriorates the fuel cell performance for the co-flow configuration significantly. With a non-uniform fuel inlet flow through channels, the channel with higher fuel supply has a lower utilization, while others with poor fuel utilization will result in a lack of fuel. Non-isothermal performance with cross flow configuration was predicted for a variety of operating conditions.

Yoo et al. [81] performed a three-dimensional but steady state mathematical modeling of the butterfly-type unit MCFC. The presented model was not able to consider the gradient of temperature and concentrations in the direction of height. They found the local fuel conversions in the butterfly-type cell slightly higher than those in the co-flow type fuel cell. In addition, they

showed that the more uniform temperature distributions could be obtained by using the butterfly-type fuel cell.

Wee and Lee [82-83] used algebraic equations to model an MCFC with a direct internal reformer. The model was based on experimental data from a 5cm x 5cm sized unit cell operation. The results showed that the temperature increased steadily along with the direction of the anode gas flow. They also showed that electrochemical reaction rates at the anode gas entering position were almost two times faster than those at the anode gas outlet position. In addition, the water–gas shift reaction became faster from near the half position of the unit cell to the gas outlet position. Therefore, in the rear position of the unit cell, the steam reforming reaction played an important role as a supplementary reaction for providing the H_2 needed in the electrochemical reaction.

A dynamic two-dimensional model for a single, spatially distributed molten carbonate fuel cell involving the cross-flow configuration and direct internal reforming was presented by Heidebercht [67]. They found it a useful basis for system design, optimization, and control design of MCFC, applicable to any size of MCFC and transferable to other high-temperature fuel cells such as the solid oxide fuel cell.

Lee et al. [84] presented a two dimensional model for a parallel-flow molten carbonate fuel cell (10 x 10 cm^2) and observed the behaviour of the fuel cell at the beginning of the operation. The behaviour of the fuel cell such as changes in electrochemical reactions, in distributions of the current density and cell temperature and in mole fractions of gases at the beginning of the operation was examined. Their results showed that the current density decreases with time and reaches a steady-state value at 0.58 s for the chosen reference conditions. Furthermore, the time required reaching steady-state decreases as the inlet gas-flow rates or the hydrogen utilization are increased. With increased flow rates of the anode and cathode gases, the average current density showed to be high and the total concentration was low.

In the literature, there are two different approaches to model the indirect internal reforming process: either it is included as part of a lumped-parameter MCFC model [85] or is implemented as an additional layer in 2D simulations of an MCFC [78]. Recently, an article published by Pfafferodt et al. [86], claimed that the previous models do not have the level of detail needed for

a further optimization of the MCFC stack. In fact, while a flat 2D representation of the different components of a MCFC is a valid approach for a first spatially distributed simulation, a detailed simulation of each part is needed to further improve the model accuracy. Hence, they considered the complex 3D geometry of the reforming reactor as well as the spatial distribution of the catalyst pellets for the reforming reaction in steady state operation.

3.3 Performance and System Level Models

As discussed in section 3.1, a macroscopic model does not require knowledge of the complete potential and concentration distributions within the electrode pores. It uses only the local polarization (total over-potential), obtained by means of a microscopic model or an empirical correlation to calculate the current, temperature, and gas distributions at the macroscopic level. The existing macroscopic models for fuel cells employ co-flow, cross-flow, and counter-flow configurations for the gas feed streams. A macroscopic model is necessary to simulate the performance of a large-area cell which has high gas utilization and non-uniform temperature distribution.

The study of performance characteristics in MCFCs has always been one of major interest to researchers. Many studies can be found in the literature which have experimentally investigated performance of molten carbonate fuel cells (e.g., [87-89]). On the other hand, thermodynamic analysis has been used as a viable tool to investigate the energy and exergy aspects of the cogeneration systems. In fact, an MCFC permits the recovery of waste heat, which can be used in the production of steam, hot or cold water, or hot or cold air, depending on the associated recuperation equipment [90].

For instance, employing a bottoming cycle that includes a turbine will help to supply the necessary power required for the compressors. As an effort, Silveira et al. [90] implemented the energy and exergy analysis for a cogeneration system and accomplished a global efficiency or fuel utilization efficiency of 86%.

Varbanov et al. [91] offered a broader view of the concept of power generation combined cycle by combining an MCFC with a steam turbine instead of a gas turbine. Their results showed

that the inherently high power generation efficiency of the MCFC (46.38% in this case) can be significantly increased, up to nearly 70%.

Kang et al. [92] simulated an externally reformed MCFC system and analyzed the effects of system configuration and operating conditions on the system efficiency for a 100 kW MCFC system. Rashidi et al. [93] performed energy and exergy analyses of a molten carbonate fuel cell hybrid system. An overall energy efficiency of 57.4%, exergy efficiency of 56.2%, bottoming cycle energy efficiency of 24.7% and stack energy efficiency of 43.4%, respectively, were achieved.

Musa et al. [94] presented thermodynamic models for the internally and externally reformed MCFC and employed them in an ASPEN Customer Modeller. Their results indicated that the operating temperature has a larger effect on the cell voltage of an IR-MCFC system compared to an ER-MCFC system.

A multi-objective optimization of a poly-generation system for the production of electricity and hydrogen was performed by Verda et al. [95]. The system that was investigated was based on a MCFC stack integrated with a micro gas turbine for electricity generation, coupled with a pressure swing absorption (PSA) system for hydrogen production. They used a Pinch Analysis technique along with a general heat exchanger network in order to select the optimal configuration of the heat exchangers.

Campanari et al. [96] introduced an application of MCFCs in a system based on their potential in carbon dioxide separation when integrated into natural gas fired combined cycles.

Considering all previous studies, it is noticeable that the high cost of MCFCs is still an open challenge for commercialization. Operation at high current densities would be an option to lessen cell cost. Most of the previous studies have focused on the regular operating current densities (e.g. 0.1-0.25 A cm^{-2}). A potential research activity could be to provide a better insight into molten carbonate fuel cells operation and performance characteristics at very high current densities in order to reduce the molten carbonate fuel cells size weight and consequently cost. It is essential to develop fuel cells with higher power densities.

3.4 Present Study

Table 3.1 summarizes the weaknesses and effectiveness of the previous modeling approaches available in the open literature. This information is implemented to develop a rigorous transient, three-dimensional, non-isothermal model by employing the volume-averaged approach [46].

The previous studies have mostly used a single equation to describe the transport of electric charges. This research modifies the former approach and introduces two separate equations for the electronic and ionic charge transport processes. Hence, the presented model considers the potential and current density variation in both solid electrode and liquid electrolyte phases. In addition, gas channels are considered explicitly in the mathematical modeling and convection-diffusion mechanisms are taken into account. The developed model also incorporates the effect of electrolyte filling degree in solid electrodes.

This model is then used to predict unit cell behaviour at high cathode gas utilizations because the polarization curves of the porous lithiated NiO cathode, when the mass transfer becomes dominant, is mostly overlooked. To do this, the two most common cathode reaction mechanisms are used to describe the electrochemical reaction rates.

In addition, with the intention of determining the time scales of various transport phenomena, a sinusoidal impedance approach with varying impedance frequencies is integrated and the phase shifts for the non-linear dynamic responses of field variables are determined.

The developed mathematical model is also employed to analyze the system start-up. It is used as a predictive tool to provide a three-dimensional demonstration of the transient physical and chemical processes at system start-up. The local distribution of the species molar fraction, reaction rates, over-potentials, various form of current densities, electronic potential, ionic potential and temperature are presented.

Table 3.1: Highlights of weakness and effectiveness of previous MCFC electrode models.

Researcher	Model Name	Effectiveness / Corrections to Previous Models	Weaknesses / Simplifying Assumptions
Austin et al. [30]	Simple (or Flooded) Pore Model	The first model presented to study single electrodes of MCFCs	Very poor performance prediction, Undesirable electrolyte-solid-gas distribution, Pores flooded with electrolyte
Will et al. [31] Srinivas et al. [32]	Thin Film Model	Considers the variations in the wetting tendency of the electrolyte	The electrochemical reaction is concentrated in a small part of the film (close to the bulk electrolyte)
Albright [33]	Finite-Contact-Angle Meniscus Model	Considers the variations in the wetting tendency of the electrolyte	The current is predominantly concentrated in a small portion of the pore wall
Iczkowski [34]		Addressed previous limiting assumptions by incorporating of the migration of reactants on the surface of the electrode	
Giner and Hunter [38]	Standard Agglomerate Model (dual-porosity)	Instead of simple single pore, uses a spectrum of pore sizes, The pores are divided into two forms	Does not consider the different wetting characteristics of electrodes (the anode is not well wetted under reducing conditions while the cathode is very well wetted)
Wilemski [40]		Proposes individual porous electrode models for the anode and cathode	Oversimplifies pore structure, Requires measured values for film areas and thicknesses, Is empirical and the lack of experimentally measured values is always a problem
Kunz et al. [41]	A Homogeneous Model	Avoids using empirical values Uses a theoretical approach and calculates the effective agglomerate diameter, porosity and tortuosity based on the electrode's pore spectrum and electrolyte content	Strongly depends on the choice of the agglomerate radius, Has difficulties to incorporate the electrolyte-filling degree into the agglomerate model, Does not accurately predict the optimal degree of electrolyte filling
Prins-Jansen et al. [46]	Agglomerate-Like Model	Eliminates the important drawback of the preceding agglomerate model caused by geometric assumptions and restrictions, Suitable for studying three dimensional and anisotropic problems	

Chapter 4

Model Development

The proposed mathematical model for the molten carbonate fuel cell includes the conservation of mass, momentum, energy, chemical species and electric charges. To mathematically describe an MCFC, a comprehensive knowledge of physical and electrochemical processes is required. This chapter presents the MCFC model development process. First of all, the physical domain of the model is presented, followed by the assumptions. Next, the conservation equations governing the processes in the electrodes, electrolyte and gas channels along with the reaction kinetics are presented. Finally, the initial and boundary conditions required to complete the model formulation, are illustrated.

4.1 Physical Domain

The physical domain of the simulated MCFC is presented in Figure 4.1. As shown in this three-dimensional representation, it can be physically broken down into five distinct components: anode gas channel, anode, electrolyte, cathode and cathode gas channel.

As previously stated in chapter 2, the fuel gas which can be pure or reformed hydrogen gas along with water vapour and carbon-dioxide (also carbon monoxide and methane in the case of direct internal reforming), enter the anode gas channel. The hydrogen molecules diffuse through the porous anode wherein they are subjected to the hydrogen oxidation reaction (Equation (2.1)), through the combination with the carbonate ions. The electrochemical reaction of the anode produces water, carbon dioxide and electrons. The electrons are passed through an external circuit, generating electricity and eventually returning to the cathode. On the cathode side, a mixture of oxygen, carbon-dioxide and nitrogen enters the cathode gas channel and diffuses

through the porous cathode, where the oxygen reduction reaction (Equation (2.2)) takes place. Oxygen is reduced to carbonate ions by combining with carbon dioxide and the electrons coming from the external circuit.

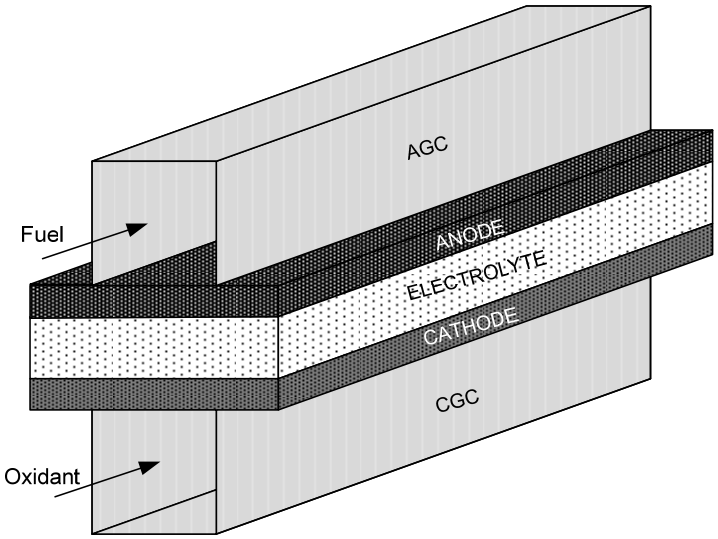

Figure 4.1: The physical domain of the simulated MCFC.

4.2 Assumptions

Making a theoretically rigorous fuel cell model which reflects the micro- and macro-scale transport processes is extremely challenging. Therefore, without losing the generic physical characteristics, every numerical simulation is conceived and developed based on a set of assumptions motivated by a lack of experimentally evaluated physical parameters. Likewise, the following assumptions are made for this model:

(i) the chemical species obey the ideal gas law and are ideally mixed;
(ii) the porous anode and cathode are homogeneous;
(iii) the effects of gravity are negligible;
(iv) the anodic and cathodic electrochemical reactions take place at the three-phase boundaries inside the electrodes;

(v) the gas mixture and solid components of the fuel cell are in a thermal equilibrium state;

(vi) both anodic and cathodic electrochemical reactions follow the Butler-Volmer equation;

(vii) any change in the concentration of carbonate ions inside the electrolyte is negligible;

(viii) water exists only in gaseous form;

(ix) the thermal conductivities of solid and liquid material are constant.

4.3 General Form of a Conservation Equation

This section exhibits the general form of the governing equations implemented to model the MCFC. In contrast to the approach that employs separate differential equations for different sub-domains, in this study, the 'single-domain approach' is utilized. This approach considers a single set of governing equations for all sub-domains. No interfacial conditions are required to be specified at internal boundaries between various sub-domains. However, for each sub-domain model input parameters (diffusivities, conductivities, etc) are specified separately. In fact, some adjustments are made in a way that the conductivities and diffusivities (of field variables) are set to extremely small values for the sub-domains in which no transport process occurs.

Prior to describing each specific governing equation, it is worthwhile to point out that each phenomenon can be described with a separate partial differential equation which comprises a transient term, diffusion term, convection term and a source term. By taking all these terms into account, a general equation can be derived in the following form:

$$\frac{\partial}{\partial t}\left(\rho\Theta\right)+\nabla\cdot\left(\rho\vec{u}\Theta-\Gamma_{\Theta}\nabla\Theta\right)=S_{\Theta} \tag{4.1}$$

where Θ is 1, u, Y, h, ϕ_s and ϕ_e in the continuity, momentum, species, energy, electronic charge and ionic charge equations, respectively. Γ_{Θ} and S_{Θ} are the diffusion coefficient (or conductivity) and source terms, respectively, which have consistent units. Other variables will be introduced shortly.

4.4 Governing Equations and Constitutive Laws

A comprehensive MCFC model needs to consider the transport of the multi-component gas species in gaseous and liquid phases, electrochemical and chemical reaction kinetics, heat generation, heat transfer, transport of the electrons and carbonate ions, and porous electrode effects. These processes occur in void volumes, liquid phase, solid phase and at triple-phase boundaries. The following sections demonstrate the governing equations that describe each phenomenon that occur within an MCFC.

An appropriate approach is needed to model the porous electrodes. In general, the agglomerate model divides the porous media into a number of micro-pores and macro-pores, followed by averaging the two-phase equations over the micro-porous regions which makes it difficult to justify the model rigorously. Essentially, in this approach a few assumptions concerning pore structure (agglomerate radius and electrolyte film thickness) are unavoidable. Hence, in this study a more realistic approach commonly used in porous media problems, the so-called 'volume averaging', is employed. However, according to porous-media theory, it must be feasible to define representative control volumes (unit cells) for the homogenization (averaging) process to be meaningful. The size of a unit cell must be chosen with the intention that a change in the size and/or position of the cell has an insignificant effect on the porosity of the cell. This implies that it must be considerably larger than the length scale of micro-porosity, but much smaller than the scale on which significant changes in macroscopic quantities arise. In this model, all three phases are taken into account. By doing so, a large enough unit cell can be defined, and this makes it possible for a unit cell to fulfill the requirements for averaging. In contrast to the agglomerate model, the new model is suitable for studying three-dimensional and anisotropic problems, and integrating the degree of electrolyte filling. In actual fact, this model is based on the basic mass and current balances at the micro-scale which, subsequently, are averaged (homogenized) across all three phases (solid/gas/liquid) of the electrode to yield the macro-scale level equations. In the following sections, the macro-scale governing equations are illustrated. Readers are referred to Prins-Jansen et al. [103] for more details on the volume averaging technique and derivation of the equations.

4.4.1 Transport of Gas Species

4.4.1.1 Conservation of Mass

To begin with, the transport of any gas species has to satisfy the conservation of mass and momentum. The total mass gain in the anode is equal to the mass loss in the cathode. This can be justified by considering the production and consumption of carbon-dioxide. Clearly, for each mole of CO_2 produced in the fuel flow, a mole of CO_2 is consumed in the oxidant flow due to conservation of electric charges (Equations (2.1) and (2.2)). Therefore, the conservation of mass is written as [104]:

$$\frac{\partial}{\partial t}\left(\varepsilon^{eff}\rho_g\right)+\nabla\cdot\left(\rho_g\vec{u}_g\right)=S_m \tag{4.2}$$

where ρ_g and $\vec{u}_g$ are the gas mixture density and velocity, respectively. S_m (kg m^3 s^{-1}) is the mass source term which has different values depending on the cell sub-domain. The gas mixture density (kg m^{-3}) is calculated based on the ideal gas law [104]:

$$\rho_g = P_g\left(\Re T\sum_i \frac{Y_i}{M_i}\right)^{-1} \tag{4.3}$$

where P_g is the gas pressure (Pa), T the temperature (K), $\Re$ the universal gas constant (J $kmol^{-1}$ K^{-1}). In addition, Y_i and M_i are mass fraction and molecular weight (kg $kmol^{-1}$) of species i, respectively.

It is crucial to indicate that the actual volume fractions of the gas in porous anode and cathode are less than the electrode porosity (ε). This is a result of the volume percentage occupied by the electrolyte, namely the electrolyte filling degree (θ), which is present in liquid form. Hence, an effective porosity (ε^{eff}) is defined and implemented in the governing equation as well as in constitutive laws

$$\varepsilon^{eff}=\varepsilon\left(1-\theta\right). \tag{4.4}$$

4.4.1.2 Conservation of Momentum

The general form of the conservation of momentum equation can be written as [104]:

$$\frac{\partial}{\partial t}\left(\frac{1}{\varepsilon^{eff}}\rho_g \vec{u}_g\right)+\nabla\cdot\left(\frac{1}{\left(\varepsilon^{eff}\right)^2}\rho_g \vec{u}_g \vec{u}_g\right)=-\nabla P_g+\nabla\cdot\left(\bar{\bar{\tau}}\right)+S_u \tag{4.5}$$

where S_u is the momentum volumetric sink term (Pa m^{-3}) which is zero in gas channels and is determined in the porous electrodes using Darcy's equation [104]. This momentum sink contributes to the pressure gradient in the porous electrodes, creating a pressure drop that is proportional to the fluid velocity. For homogeneous porous media:

$$S_u=-\frac{\mu_g}{K^{eff}}\vec{u}_g \quad . \tag{4.6}$$

Here, μ_g is the dynamic viscosity of the ideal gas mixture (kg m^{-1} s^{-1}) and it is calculated based on kinetic theory [104] as

$$\mu_g=\sum_i \frac{X_i\mu_i}{\sum_j X_i\psi_{ij}} \tag{4.7}$$

$$\psi_{ij}=\frac{\left[1+\left(\mu_i/\mu_j\right)^{0.5}\left(M_i/M_j\right)^{0.25}\right]^{0.5}}{\left[8\left(1+M_i/M_j\right)\right]^{0.5}} \tag{4.8}$$

where i and j represent different species. X_i is the mole fraction of species i. Furthermore, K^{eff} is the effective permeability of the porous media which depends on the relative permeability, K_r and the intrinsic permeability, K_i, through the following equation [105]:

$$K^{eff}=K_r K_i \quad . \tag{4.9}$$

The relative permeability is defined as a measure of the ability of the porous electrode to allow fluids to pass through it and determined by [105]:

$$K_r = \left(1-\theta\right)^{\gamma} \quad . \tag{4.10}$$

Here, different values are used for the exponent. The widely used cubic correlation is empirical and comes from sand/rock-type porous media with a typical porosity of 0.1–0.4. Nonetheless, it is suggested to be between 4.0 and 5.0 for porous materials with porosities over 0.6 [30]. For MCFCs, it is recommended to be 1 [106]. Perceptibly, a combination of Equations (4.9) and (4.10) depicts that if the local pore volume of the anode or cathode is fully saturated with liquid electrolyte, the gas permeability will become zero, resulting in an infinite (negative) value for the momentum source term. The intrinsic permeability is an intensive (bulk) property. It is a measure of the ability of the porous material to allow fluids to pass through it and is a function of the material structure only (and not of the fluid), and explicitly distinguishes the value from that of relative permeability. It is hard to find values for permeability in the literature for MCFCs. Findlay [107] utilized the values for the permeability in a proton exchange membrane fuel cell (PEMFC) which is 1.9E-12 m^2. On the other hand, the Carman-Kozeny relation for an aggregated bed of spheres [108-109] can be used to estimate the value of the permeability:

$$K = \frac{D_p^2}{150}\frac{\left(\varepsilon^{eff}\right)^3}{\left(1-\varepsilon^{eff}\right)^3} \tag{4.11}$$

where D_p is the pore diameter of the porous material which is normally between 8-12 μm for MCFC electrodes [107-108]. By substituting this value in Equation (4.11) and calculating the permeability, the value used by Findlay [107] can be justified. Also, in a CFD model developed by Jiao [110], the pore diameter of the catalyst layer is reported to be 24 μm and the permeability is estimated to be 6.2E-12 m^2. By considering the electrode pore diameter ratio of the MCFCs and the value used by Jiao [110], one can approximate the permeability to be 1.9E-12 m^2 for the simulated MCFC, which is also reported by Promislow et al. [111].

4.4.1.3 Conservation of Gaseous Species

To describe the chemical species transport, the general form of the conservation equation including both convection and diffusion terms, is considered:

$$\frac{\partial}{\partial t}\left(\varepsilon^{eff}\rho_g Y_i\right)+\nabla\cdot\left(-\rho_g D_{i,m}^{eff}\nabla Y_i\right)+\nabla\cdot\left(\rho_g \vec{u}_g Y_i\right)=S_i \tag{4.12}$$

where i represents the species H_2, H_2O and CO_2 at the anode and O_2, CO_2 and N_2 at the cathode. Therefore, there are mainly five species to be considered in this study. In order to facilitate the solution procedure, four independent variables can be numerically solved with the fifth one being dependent on the other four:

$$\sum_i Y_i = 1 \quad . \tag{4.13}$$

However, the mechanism of species transport in gas channels and porous electrodes are not identical. In gas channels, no electrochemical reaction exists and simple multi-component gas species transport occurs. Therefore, in Equation (4.12) the species mass source term, S_i, is zero. $D_{i,m}^{eff}$ is the effective mass diffusion coefficient of species i in the gas mixture and is determined by [104]:

$$D_{i,m}^{eff}=\frac{1-X_i}{\sum_{i,j\neq i}\left(X_j \Big/ D_{ij}^{eff}\right)} \tag{4.14}$$

where D_{ij}^{eff} is the effective binary mass diffusion coefficient of species i in species j which is calculated by

$$D_{ij}^{eff}=D_{ij}\frac{T}{T^{ref}}\frac{P^{ref}}{P}\frac{\varepsilon^{eff}}{\tau} \quad . \tag{4.15}$$

Here, D_{ij} is the bulk binary diffusivity at the reference temperature (T^{ref}) and reference pressure (P^{ref}). Also, τ is the tortuosity of the porous material which is frequently estimated by the following Bruggemann correlation in fuel cell modeling [105]:

$$\tau = \left(\varepsilon^{eff}\right)^{-0.5} \quad . \tag{4.16}$$

It is obvious that in gas channels the porosity is equal to one. The species transport mechanism of porous electrodes is a more complex scenario. Figure 4.2 demonstrates a closer view of the porous electrode morphology. According to this figure, each volume-averaging cell encloses the solid electrode, gas mixture and liquid electrolyte.

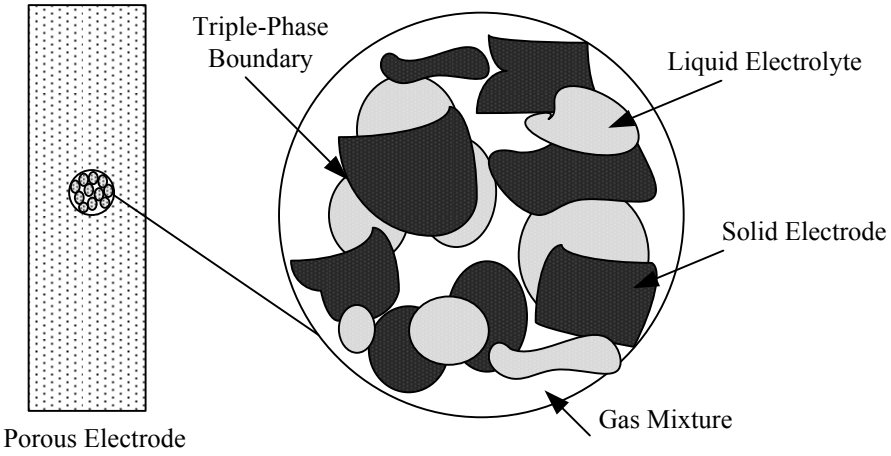

Figure 4.2: Schematic of porous electrode (left) and volume-averaging cell enclosing the triple-phase boundaries (right).

Mass transport occurs in the liquid and gas phases. Precisely, reactants diffuse through the gaseous mixture and then transfer to the molten electrolyte so as to reach the triple-phase boundary where the electrochemical reaction takes place. Hence, two equations can be written for species transport in gas and liquid phases at the micro-scale level, considering the fact that electrochemical reactions take place in the liquid phase only. Now, by defining a control volume resembling Figure 4.2, the two phases (the gas and the electrolyte) could be effectively combined. Clearly, the physically observable quantities of interest (concentration) occur on a much larger macro-scale where micro-scale equations are not practical. Rather, these micro-scale equations can be averaged using theorems from porous-media theory [112]. By doing so, it

introduces average concentrations defined across both phases, represented by Equation (4.12). Nevertheless, there is a major apprehension in regards to the diffusive flux terms which is related to the diffusion coefficients. It is said to be evaluated by a volume fraction-based average over the gas and liquid phase diffusivities [103]. In this study it is implemented as

$$D_{i,m}^{eff} = \left(\varepsilon(1-\theta) \Big/ \frac{1-X_i}{\sum_{i,j\neq i} \left(X_j / D_{ij}^{g} \right)} + \varepsilon\theta / D_i^{l} \right)^{-1} \tag{4.17}$$

where g and l correspond to the gas and liquid phases, respectively.

4.4.1.4 Electrochemical Reaction Kinetics

The source terms on the right hand side of Equations (4.2) and (4.12) are directly associated with the electrochemical reactions in anode and cathode. In this section, the general form of the electrochemical reactions rate will be derived. Afterwards, based on this equation, two specific correlations will be introduced for the anodic and cathodic reactions, employing the most common reaction mechanisms. Finally, these equations will be implemented to evaluate the various source terms corresponding to the conservation of mass and gaseous species.

Considering the forward and backward reactions, the general form of the electrochemical reactions is as follows [9]:

$$\underbrace{\sum_{i=1}^{N} \nu_i' M_i}_{Reactants} \quad \leftrightarrow \quad \underbrace{\sum_{i=1}^{N} \nu_i'' M_i}_{Products} \tag{4.18}$$

where M_i, ν_i' and ν_i'' represents the chemical formula of the ith reactant species, the number of moles for species i in the reactant and the number of moles for species i in the product mixture, respectively. N is the total number of species in the system.

The net rate of reaction can be calculated using a summation of forward and backward reaction rates. Therefore, the net rate of reaction for species i, ω_i'', can be defined as:

$$\omega_i'' = \omega_{i,f}'' - \omega_{i,b}'' \tag{4.19}$$

In addition, for the elementary reactions, the rate of reaction is proportional to the product of the concentration of the reactants present raised to a power, which is equal to the corresponding stoichiometric coefficient of the reaction [9]. This expression is known as the law of mass action;

$$\omega_{i,f}'' = \left(\nu_i'' - \nu_i'\right) k_f \prod_{i=1}^{N} \left[M_i\right]^{\nu_i'} \tag{4.20}$$

and

$$\omega_{i,b}'' = \left(\nu_i' - \nu_i''\right) k_b \prod_{i=1}^{N} \left[M_i\right]^{\nu_i''} \quad . \tag{4.21}$$

Replacing Equations (4.20) and (4.21) in Equation (4.19), we find

$$\omega_i'' = \left(\nu_i'' - \nu_i'\right) \left[k_f \prod_{i=1}^{N} \left[M_i\right]^{\nu_i'} - k_b \prod_{i=1}^{N} \left[M_i\right]^{\nu_i''} \right] \tag{4.22}$$

where k_f and k_b are the reaction rate constants for the forward and backward reactions, respectively. Moreover, $\left[M_i\right]$ is the molar concentration of species i which is equal to C_i in the species transport equation.

The current associated with the forward reaction is denoted by i_f and the backward reaction corresponds to i_b. In fact, i_f and i_b are normally called anodic current density and cathodic current density, respectively. The difference between the forward and backward current density is conventionally referred to as the net current density at the electrode, i. According to Faraday's law, the rate of electrochemical reaction is proportional to the current density as defined through the following equation:

$$i = i_f - i_b = k_f C_R - k_b C_P = -nF\omega_i'' \tag{4.23}$$

where C_R and C_P are the concentrations of reactant and product, respectively. F is Faraday's constant and has the value of 96,485 (C mol^{-1}) and n is the number of electrons transferred during the electrochemical reaction.

When a net current is withdrawn from the electrode reaction, it becomes irreversible which leads to different rates for forward and backward reaction. The net amount of current flow to the electrode depends on the difference between electrode potential, ϕ, and its equilibrium value, ϕ_r. This parameter is called the electrode over-potential:

$$\eta = \phi - \phi_r \quad . \tag{4.24}$$

According to transition state theory, despite the fact that the reaction is in forward or backward direction, there is an energy barrier to be overcome in order for the reaction to proceed successfully [9]. The magnitude of this barrier is equal to the Gibbs energy change between the activated complex and the reactant, R, or the product, P, respectively.

In the irreversible condition, similar to the electrode potential, the Gibbs energy of the reactant and product differ from their reversible values. The effect of this irreversibility, caused by the electrode over-potential, on the Gibbs energy of the reactant and product is shown in Figure 4.3. As shown in this figure, it is determined that the over-potential enhances the forward reaction by raising the energy level of the reactant while lowering the energy level of the product. This effect is not equally distributed between forward and backward reaction. This means that a proportion α is spent on promoting the Gibbs function of the reactant and the remaining proportion, $1-\alpha$, is on hindering the Gibbs function of the product. The parameter α is called the transfer coefficient or symmetry factor.

Therefore, the actual Gibbs function of activation for the forward and backward reactions, Δg_f and Δg_b, can be written as:

$$\Delta g_f = \Delta g_{f,r} - \alpha nF\eta \tag{4.25}$$

$$\Delta g_b = \Delta g_{b,r} - (1-\alpha) nF\eta \tag{4.26}$$

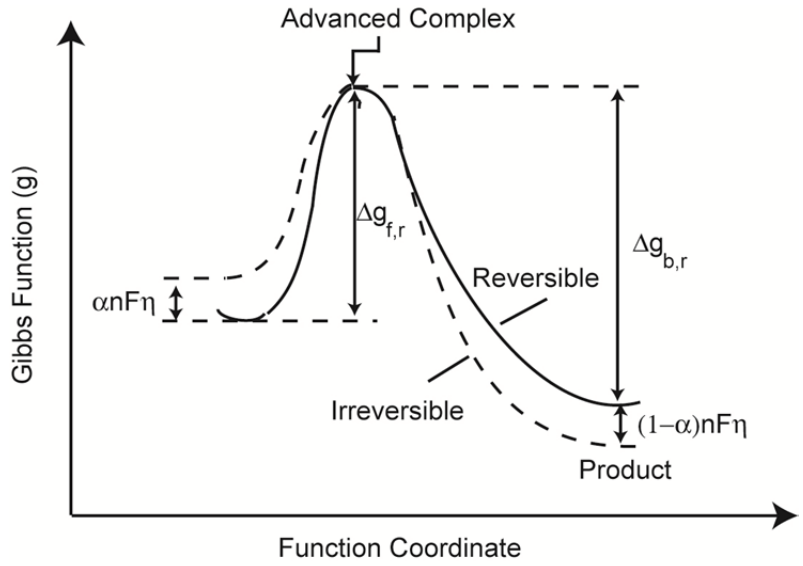

Figure 4.3: The typical effect of an electrode over-potential on the Gibbs function of the reactant and product (reproduced from [9]).

where $\Delta g_{f,r}$ and $\Delta g_{b,r}$ are the equilibrium Gibbs function of activation for forward and backward reaction, respectively. Moreover, according to transition state theory the reaction rates under irreversible conditions may be expressed as:

$$k_f = B_f T \, exp\left(-\frac{\Delta g_f}{\Re T}\right) \tag{4.27}$$

$$k_b = B_b T \, exp\left(-\frac{\Delta g_b}{\Re T}\right) . \tag{4.28}$$

Here, B is the pre-exponential factor. $\Re$ is the universal gas constant. Considering the Equation (4.18) to (4.28), we find

$$i = i_f - i_b = i_0 \left[exp\left(\frac{\alpha nF\eta}{\Re T}\right) - exp\left(-\frac{(1-\alpha) nF\eta}{\Re T}\right)\right] \tag{4.29}$$

which is called Butler-Volmer equation and it describes the relation between net current density and the activation over-potential. It may also be written as:

$$i = i_0 \left[exp\left(\frac{\alpha_a n F \eta}{\Re T} \right) - exp\left(-\frac{\alpha_c n F \eta}{\Re T} \right) \right] \tag{4.30}$$

$$\alpha_a + \alpha_c = 1 \tag{4.31}$$

where α_a is called the anodic transfer coefficient and α_c is the cathodic transfer coefficient. In addition, i_0 is the exchange current density (A m^{-2}):

$$i_0 = B_f C_R T \, exp\left(-\frac{\Delta g_{f,r}}{\Re T} \right) = B_b C_P T \, exp\left(-\frac{\Delta g_{b,r}}{\Re T} \right) \quad . \tag{4.32}$$

Unlike elementary reactions, real reactions take place due to several sequential elementary reactions. Therefore, for the real reactions the exchange current density can be modified as follows:

$$i_0 = i_0^0 \left(\frac{C_R}{C_R^{ref}} \right)^{\beta} \tag{4.33}$$

where i_0^0 is the reference or standard exchange current density and β is the reaction order with respect to the reactant R. Finally, the volumetric current density (A m^{-3}), R, can be expressed as:

$$R = A_v \cdot i_0^0 \left(\frac{C_R}{C_R^{ref}} \right)^{\beta} \left[exp\left(\frac{\alpha_a n F \eta}{\Re T} \right) - exp\left(-\frac{\alpha_c n F \eta}{\Re T} \right) \right] \quad . \tag{4.34}$$

The reactive surface area density, A_v, also known as the specific reactive surface area (m^2 m^{-3}), is defined by:

$$A_v = \frac{Actual\ reactive\ surface\ area}{Volume\ of\ electrode} \quad . \tag{4.35}$$

Now, the volumetric current density for both anode and cathode can be expressed as follows:

$$R_a = A_{v,a} i_{0,a}^{0} \left(\frac{C_{R,a}}{C_{R,a}^{ref}} \right)^{\beta_a} \left[exp\left(\frac{\alpha_{a,a} nF\eta_a}{\Re T} \right) - exp\left(-\frac{\alpha_{c,a} nF\eta_a}{\Re T} \right) \right] \tag{4.36}$$

$$R_c = A_{v,c} \cdot i_{0,c} \left(\frac{C_{R,c}}{C_{R,c}^{ref}} \right)^{\beta_c} \left[exp\left(\frac{\alpha_{a,c} nF\eta_c}{\Re T} \right) - exp\left(-\frac{\alpha_{c,c} nF\eta_c}{\Re T} \right) \right] \quad . \tag{4.37}$$

These equations are the general concentration form of the Butler-Volmer equation for anode and cathode. Over the past three decades, several studies have been carried out to find the reaction mechanisms that best represent the actual electrochemical reactions (e.g. [43]). The available proposed mechanisms are mostly based on the concept of rate-determining step.

The two most common reaction mechanisms for the anode were proposed by Ang and Sammels [113], and Jewulski and Suski [42]. The general form of the reaction rate for both of these mechanisms was presented based on the molar fractions as follows:

$$R_a = A_{v,a} \cdot i_{0,a} \left[\begin{array}{l} \left(\frac{X_{H_2}}{X_{H_2,in}} \right)^{p_1} exp\left(\frac{\alpha_{aa} F}{\Re T} \eta_a \right) - \\ \left(\frac{X_{H_2}}{X_{H_2,in}} \right)^{p_2} \left(\frac{X_{H_2O}}{X_{H_2O,in}} \right)^{p_3} \left(\frac{X_{CO_2}}{X_{CO_2,in}} \right)^{p_4} exp\left(-\frac{\alpha_{ca} F}{\Re T} \eta_a \right) \end{array} \right] \quad . \tag{4.38}$$

Boden et al. [106] incorporated both mechanisms in their mathematical modeling and achieved identical results. In this study, the former mechanism is employed. The corresponding exponents are summarized in Table 4.1.

Likewise, several mechanisms have been proposed for the cathode electrochemical reaction. However, there is uncertainty about the validity of the existing mechanisms. Therefore, the two most common reaction mechanisms, namely the peroxide and superoxide mechanisms [39, 41] are employed in this paper. They are named after their electro-active oxide species. The peroxide mechanism can be described in four steps:

$$O_2 + 2CO_3^{2-} \leftrightarrow 2O_2^{2-} + 2CO_2$$
$$O_2^{2-} + e^- \leftrightarrow O^{2-} + O^- \quad (R.D.S)$$
$$O^- + e^- \leftrightarrow O^{2-}$$
$$O^{2-} + CO_2 \leftrightarrow 2CO_3^{2-}$$

The term R.D.S stands for 'Rate Determining Step' and indicates the slowest step of the multi-step electrochemical reaction. The superoxide mechanism can be illustrated in six steps:

$$O_2 + 2CO_3^{2-} \leftrightarrow 2O_2^{2-} + 2CO_2$$
$$O_2 + O_2^{2-} \leftrightarrow 2O_2^-$$
$$O_2^- + e^- \leftrightarrow O_2^{2-} \quad (R.D.S)$$
$$O_2^{2-} + e^- \leftrightarrow O^{2-} + O^-$$
$$O^- + e^- \leftrightarrow O^{2-}$$
$$O^{2-} + CO_2 \leftrightarrow CO_3^{2-}$$

In any event, the general form of the cathode reaction equation reads

$$R_c = A_{v,c} \cdot i_{0,c} \left[\frac{\left(\frac{X_{CO_2}}{X_{CO_2,in}} \right)^{q_1} \left(\frac{X_{O_2}}{X_{O_2,in}} \right)^{q_2} exp\left(\frac{\alpha_{ac} F}{\Re T} \eta_c \right) -}{\left(\frac{X_{CO_2}}{X_{CO_2,in}} \right)^{q_3} \left(\frac{X_{O_2}}{X_{O_2,in}} \right)^{q_4} exp\left(-\frac{\alpha_{cc} F}{\Re T} \eta_c \right)} \right] . \tag{4.39}$$

The exchange current density, in Equations (4.38) and (4.39), is given by [106]:

$$i_{0,a} = i_{0,a}^0 \left(X_{H_2,in} \right)^{\lambda_1} \left(X_{H_2O,in} \right)^{\lambda_2} \left(X_{CO_2,in} \right)^{\lambda_3} \tag{4.40}$$

$$i_{0,c} = i_{0,c}^0 \left(X_{O_2,in} \right)^{\gamma_1} \left(X_{CO_2,in} \right)^{\gamma_2} \tag{4.41}$$

where "in" donates inlet. The reaction rates of the peroxide and superoxide mechanisms differ in the exponents, which are summarized in Table 4.1.

Table 4.1: Reaction orders and species exponents in the electrochemical reaction rates [117].

Reaction Mechanism	Reaction Orders	Concentration Exponents
Ang and Sammels (anode)	λ_1 =0.25, λ_2 = 0.25, λ_3 = 0.25	p_1 = 0.5, p_2 = -0.5, p_3 = 1, p_4 = 1
Peroxide (Cathode)	γ_1 = 0.375, γ_2 = -1.25	q_1 = -2, q_2 = 0, q_3 = -1, q_4 = 0.5
Superoxide (Cathode)	γ_1 = 0.625, γ_2 = -0.75	q_1 = -2, q_2 = 0, q_3 = -0.5, q_4 = 0.75

Furthermore, the over-potential parameter, η, is defined as

$$\eta_a = \phi_s - \phi_e \tag{4.42}$$

$$\eta_c = \phi_s - \phi_e - E_{eq} \tag{4.43}$$

where η_a and η_c represent anode over-potential and cathode over-potential, respectively. In these two equations, ϕ_s and ϕ_e are solid phase and electrolyte phase potentials. Moreover, E_{eq} is the potential difference between solid and electrolyte phase potentials in equilibrium, i.e. when no current is generated, and is defined using the Nernst equation [40]:

$$E_{eq} = E_0 + \left[\frac{RT}{nF} ln \left(\frac{P_{H_2,a} P_{CO_2,c} P_{O_2,c}^{0.5}}{P_{CO_2,a} P_{H_2O,a}} \right) \right] \tag{4.44}$$

$$E_0 = 1.2723 - 2.7645 \times 10^{-4} T \quad . \tag{4.45}$$

Source Terms Evaluation

Now, the production and consumption of various species involved in the anode and cathode reactions can be evaluated. Accordingly, in the anode sub-domain:

$$S_{H_2,a} = -\frac{R_a}{2F} M_i \tag{4.46}$$

$$S_{H_2O,a} = -\frac{R_a}{2F} M_{H_2O} \tag{4.47}$$

$$S_{CO_2,a} = -\frac{R_a}{2F} M_{CO_2} \tag{4.48}$$

$$S_{m,a} = S_{H_2,a} + S_{H_2O,a} + S_{CO_2,a} \tag{4.49}$$

and in the cathode sub-domain:

$$S_{O_2,a} = \frac{R_c}{4F} M_{O_2} \tag{4.50}$$

$$S_{CO_2,c} = \frac{R_c}{2F} M_{CO_2} \tag{4.51}$$

$$S_{m,c} = S_{O_2,c} + S_{CO_2,c} \,. \tag{4.52}$$

The source term of the species transport equation can be formulated in a general form as follows:

$$S_i = -\frac{\nu_i R_i}{nF} M_i \tag{4.53}$$

where ν_i denotes the stoichiometric coefficient of species i. Also, the mass equation source term reads

$$S_m = \sum_i S_i \quad . \tag{4.54}$$

4.4.2 Transport of Electric Charge

The charge conservation equations describe the electric current in electrically conductive components and ionic current in ionic conductive components. As illustrated in the assumptions, any change in concentration of carbonate ions is neglected which consequently means that the effect of migration can be neglected as well. Therefore, Ohms' law is valid in MCFC zones for both electronic charge and ionic charge.

4.4.2.1 Conservation of Electronic Charge

Considering J_s as the electronic current density through the anode and cathode, the conservation of electronic charge can be written as follows:

$$\nabla \cdot \left(\overrightarrow{J_s} \right) = S_{\phi_s} \quad . \tag{4.55}$$

The current density is a vector quantity, and only the transverse component (normal to the electrode surface) is useful and contributes to the power output of the cell; the lateral component only decreases the cell output. Therefore, the lateral component should be minimized through appropriate design [114].

Furthermore, Ohm's law can be utilized in order to demonstrate the relation between the electronic current density and the electric potential:

$$\overrightarrow{J_s} = -\sigma^{eff} \nabla \phi_s \tag{4.56}$$

where σ^{eff} is the effective electric conductivity of the solid material which is estimated based on the Bruggemann correlation. An exponent of 1.0 is used [106]:

$$\sigma^{eff} = \sigma \left(1 - \varepsilon \right)^{1.0} \quad . \tag{4.57}$$

Finally, a combination of equation (4.55) and (4.56) and (4.57) results in:

$$\nabla \cdot \left(-\sigma \left(1 - \varepsilon \right) \nabla \phi_s \right) = S_{\phi_s} \quad . \tag{4.58}$$

Additionally, S_{ϕ_s} denotes the electron generation or consumption in the electrodes.

In the anode, the electrons are generated, thus

$$S_{\phi_s} = R_a \quad . \tag{4.59}$$

In the cathode, the electrons are consumed, hence

$$S_{\phi_s} = R_c \quad . \tag{4.60}$$

Note that this source term is zero elsewhere.

4.4.2.2 Conservation of Ionic Charge

Similar to Equation (4.55), the same scenario is employed to describe conservation of carbonate ion charge as below:

$$\nabla \cdot \left(\overrightarrow{J_e} \right) = S_{\phi_e} \tag{4.61}$$

where J_e is the ionic current density. Furthermore, the Ohm's law for the carbonate charge can be written as

$$\overrightarrow{J_e} = \kappa^{eff} \nabla \phi_e \quad . \tag{4.62}$$

Here, κ^{eff} is the effective conductivity in the liquid phase which is approximated based on the following correlation for electrodes [106]

$$\kappa^{eff} = \kappa \left(\varepsilon \theta \right)^{1.5} \quad . \tag{4.63}$$

According to the study presented in [106], the effective conductivity of the pore electrolyte in the anode is 0.03-93 S m^{-1}, depending on the degree of electrolyte filling. However, the following correlation is used to estimate the ionic conductivity [115]

$$\kappa = \kappa_0 \, exp\left(-E_k / T \right) \quad . \tag{4.64}$$

Finally, a combination of equation (4.61) and (4.62) and (4.63) results in:

$$\nabla \cdot \left(\kappa \left(\varepsilon \theta \right)^{1.5} \nabla \phi_e \right) = S_{\phi_e} \quad . \tag{4.65}$$

Here, S_{ϕ_e} denotes the carbonate ion generation or consumption in the electrodes. The carbonate ions are consumed in the anode, thus

$$S_{\phi_e} = R_a \quad . \tag{4.66}$$

In the cathode, the carbonate ions are produced, hence

$$S_{\phi_e} = R_c \quad . \tag{4.67}$$

Note that this source term vanishes elsewhere.

4.4.3 Transport of Heat Energy

It is assumed that the gas mixture and solid components of the fuel cell are in a thermal equilibrium state [116] and, hence, have identical temperature. Thus, only one energy equation will be solved for each cell region. As such, the energy equation applying to each individual zone of the fuel cell can be written as [104]:

$$\frac{\partial}{\partial t}\left(\sum_{k=g,s,e}\left(\varepsilon\rho c_p\right)_k T\right)+\nabla\cdot\left(-k^{eff}\nabla T\right)+\nabla\cdot\left(\vec{u}_g\varepsilon\rho_g c_p T\right)=S_T \quad . \tag{4.68}$$

The first term on the left hand side accounts for all three phases available in each individual sub-domain which incorporates the volume-averaged values of material properties. k^{eff} is the effective thermal conductivity determined by

$$k^{eff} = \left(1-\varepsilon\right)k_s+\varepsilon\left(1-\theta\right)k_g+\varepsilon\theta k_e \quad , \tag{4.69}$$

where k_s, k_g and k_e are the thermal conductivity of solid material, gas mixture and liquid electrolyte, respectively. Similar to the dynamic viscosity, kinetic theory is used to determine the thermal conductivity of the gas mixture as follows:

$$k_g = \sum_i \frac{X_i k_i}{\sum_j X_j \psi_{ij}} \tag{4.70}$$

$$\varphi_{ij} = \frac{\left[1 + \left(\frac{\mu_i}{\mu_j}\right)^{1/2} \left(\frac{M_j}{M_i}\right)^{1/4}\right]^2}{\left[8\left(1 + \frac{M_i}{M_j}\right)\right]^{1/2}} \quad . \tag{4.71}$$

The heat generation or consumption is represented by the source term, S_T. Three kinds of heat sources exist within the cell components, namely the reversible heat release during the electrochemical reaction, irreversible or activation heat generation and ohmic heating. The only heat source in the electrolyte is due to the ohmic heating which is evaluated by:

$$S_T = \frac{J_e^2}{\kappa} \quad . \tag{4.72}$$

In the anode, all three types of heat generation mechanisms are present. Hence, we have

$$S_T = \frac{J_e^2}{\kappa_a} + \frac{J_s^2}{\sigma_a} + \left|\eta_a R_a\right| + \left|\frac{R_a}{2F}\right|\left(T\Delta S_a\right) \quad . \tag{4.73}$$

Likewise, the source term in the cathode is

$$S_T = \frac{J_e^2}{\kappa_c} + \frac{J_s^2}{\sigma_c} + \left|\eta_c R_c\right| + \left|\frac{R_c}{2F}\right|\left(T\Delta S_c\right) \quad . \tag{4.74}$$

In the gas flow channels no heat generation occurs. In the above equations, J_s and J_e are the magnitude of the electronic and ionic current density, respectively. These parameters are related to the potentials through Ohm's law (Equations (4.56) and (4.62)).

4.5 Boundary and Initial Conditions

4.5.1 Boundary Conditions

With the intention of completing the fuel cell model formulation, stating various boundary conditions at different positions is essential. A demonstration of the various internal and external boundaries is presented in Figure 4.4. Nevertheless, the boundary conditions are required only at the external surfaces of the computational domain due to the implemented single-domain formulation. This figure shows the boundaries at which conditions need to be specified.

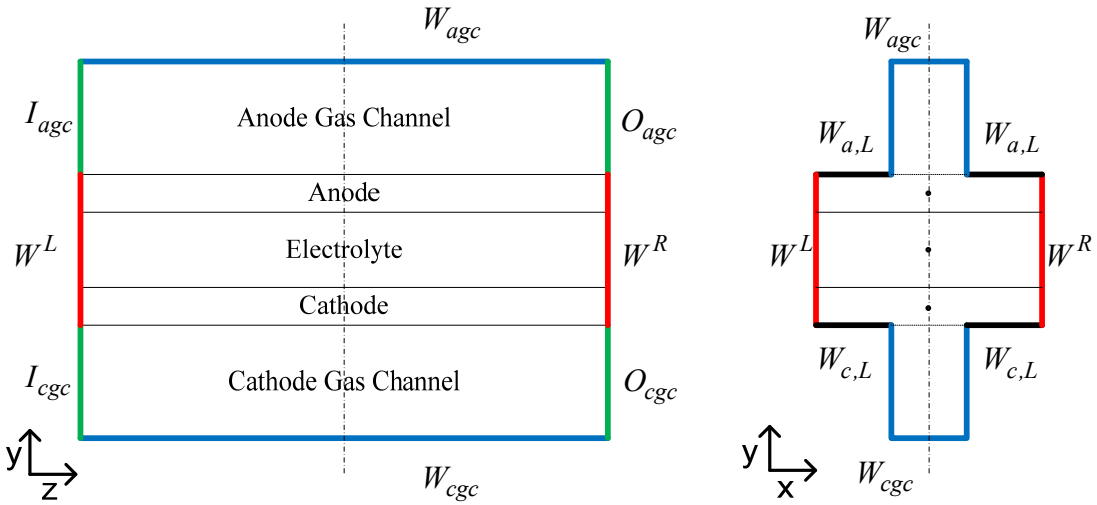

Figure 4.4: Boundary conditions for the MCFC model: (a) front view, (b) side view

The MCFC boundaries are classified into inlet, outlet, land, wall and no-flux boundaries. The boundary conditions for the computational domain, demonstrated in Figure 4.4, are specified as follows:

- At AGC inlet (I_{agc}) and CGC inlet (I_{cgc})

The gas species mass fraction, total mass flow rate and temperature of the entering gas flow are specified. Furthermore, the normal fluxes of all other variables are set to zero.

$$\left\{ \begin{array}{c} Y_i = Specified \\ \dot{m} = Specified \\ T = Specified \\ \dfrac{\partial \Theta}{\partial \vec{n}} = 0 \end{array} \right\} \tag{4.75}$$

Here, Θ represents any variable that is not explicitly specified.

- At AGC outlet (O_{agc}) and CGC outlet (O_{cgc})

Since the gas channels aspect ratio is very large, the flow is assumed to be fully developed. This means that none of the variables and respective fluxes varies in the normal direction. Accordingly, the gas pressure is specified.

$$\left\{ \begin{array}{c} P = Specified \\ \dfrac{\partial \Theta}{\partial \vec{n}} = 0 \end{array} \right\} \tag{4.76}$$

- At AGC walls (W_{agc}) and CGC walls (W_{cgc})

A no-slip boundary condition is applied to these walls along with the zero flux boundary condition for all other variables.

$$\left\{ \begin{array}{c} \vec{u}_g = 0 \\ \dfrac{\partial \Theta}{\partial \vec{n}} = 0 \end{array} \right\} \tag{4.77}$$

- At anode lands ($W_{a,L}$)

A no-slip boundary condition is employed. The electronic potential is set to zero. The flux of ionic charge and all remaining variables are set to zero.

$$\left\{ \begin{array}{l} \vec{u}_g = 0 \\ \phi_s = 0 \\ \dfrac{\partial \Theta}{\partial \vec{n}} = 0 \end{array} \right\} \tag{4.78}$$

- At cathode lands ($W_{c,L}$)

A no-slip boundary condition is employed. The electronic potential is set to the cell voltage. The flux of ionic charge and all remaining variables are set to zero.

$$\left\{ \begin{array}{l} \vec{u}_g = 0 \\ \phi_s = V \\ \dfrac{\partial \Theta}{\partial \vec{n}} = 0 \end{array} \right\} \tag{4.79}$$

- At no-flux boundaries (W^L and W^R)

The zero-flux condition is assumed for all variables.

$$\left\{ \frac{\partial \Theta}{\partial \vec{n}} = 0 \right\} \tag{4.80}$$

It is worthwhile to mention that the unit cell is fully insulated and, hence, the thermal energy exits only through the gas channel outlets.

4.5.2 Initial Conditions

The initial conditions for the case of linear and non-linear voltage perturbation are prescribed by the steady state pre-solutions. In other words, the solutions for the steady state simulation are pre-computed and then used as the initial conditions for the transient simulation. Furthermore,

the transient simulation can also start from an initialized flow field to simulate cell start-up processes for which the variable values are specified.

4.6 Model Input Parameters

The mathematical model described in the preceding sections accounts for all basic transport phenomena, so a proper choice of the modeling properties and parameters will make it possible to obtain good agreements with experimental results acquired from a real MCFC. The model input parameters and properties described in this chapter are taken from various books and studies available in the open literature. The corresponding references are indicated in the tables. Table 4.2 summarizes the structural parameters of the simulated molten carbonate fuel cell. These parameters are taken from previous experimental studies.

Table 4.2: The structural parameters of the simulated MCFC.

Parameter	**Value**
Anode gas channel height (mm)	2.0
Anode height (mm)	0.7
Electrolyte height (mm)	1.0
Cathode height (mm)	0.6
Cathode gas channel height (mm)	2.0
Cell length (mm)	50
Cell width (mm)	4.0
Porosity of anode, ε_a, [31]	0.52
Porosity of cathode, ε_c, [31]	0.62

In addition, Table 4.3 illustrates the electrochemical kinetic parameters that are experimentally determined and are available in the open literature (e.g. [106], [113]). The physical and thermal properties that are employed in the developed model are listed in Table 4.4. These parameters can be found in thermodynamic books ([9], [104]), handbooks ([118]), numerical and experimental studies (e.g. [80], [119]). The operating parameters are subject to different case studies and, hence, will be presented in Chapter 6.

Table 4.3: Electrochemical kinetic parameters.

Parameter	Value
Standard exchange current density of anode, $i_{0,a}^{0}$ (A m^{-2}) [113]	20-220
Standard exchange current density of cathode, $i_{0,c}^{0}$ (A m^{-2}) [103]	0.3-7.0
Active surface area of anode, $A_{v,a}$ (m^2 m^{-3}) [106]	2.7E5
Active surface area of cathode, $A_{v,c}$ (m^2 m^{-3}) [106]	3.0E5

4.7 Thermodynamic Analysis

Thermodynamics plays a critical role in the analysis of processes, systems and devices in which energy transfers and energy transformations take place [131]. In this regard, energy analysis is the traditional method of assessing the way energy is used. However, an energy balance provides no information on the degradation of energy or resources and does not quantify the usefulness or quality of the various energy and material streams flowing through a system and exiting as products and waste [131]. On the other hand, exergy analysis is a useful tool for furthering the goal of more efficient energy use, as it enables the determination of the location, type and true magnitude of energy waste and losses in a system [132]. Exergy is defined as the maximum amount of work which can be obtained from a system or a flow of matter when it is brought reversibly to equilibrium with the reference environment. Exergy analysis is based on second law of thermodynamics and the concept of irreversible entropy production. The exergy consumption during a process is proportional to the entropy production due to irreversibilities.

In order to investigate the performance of the MCFC in thermodynamics terms, the molten carbonate fuel cell is treated as a black box with two inputs and two output streams (Figure 4.5), and the energy and exergy balances are applied for the unit cell. In this fashion, energy and exergy efficiencies of the unit cell are defined accordingly.

It is worthwhile to mention that this research is to present performance characteristics of a ‘unit cell’. Generally, the inlet streams are taken from external devices as they are. Therefore, no calculation is performed beyond the unit cell boundaries, as estimating the parasitic losses is not within the scope of this study.

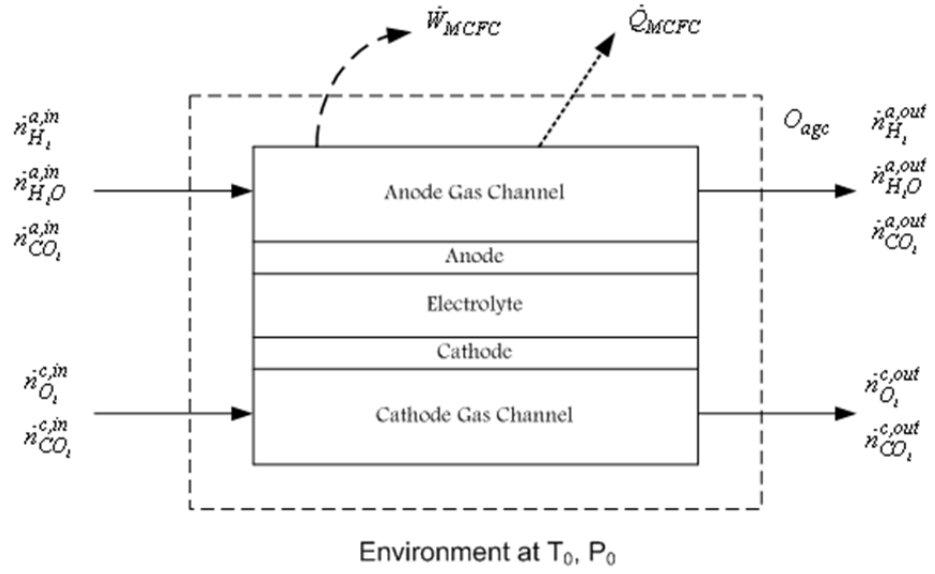

Figure 4.5: Schematic of the system boundaries studied in energy and exergy analysis

First of all, for a specified operating current density, the components' molar usage and production can be calculated. Therefore, a molar balance results in

$$\dot{n}_{H_2}^{a,in} = \dot{n}_{H_2}^{a,out} + \frac{i_{MCFC} A_{MCFC}}{nF} \tag{4.81}$$

$$\dot{n}_{H_2O}^{a,in} + \frac{i_{MCFC} A_{MCFC}}{nF} = \dot{n}_{H_2O}^{a,out} \tag{4.82}$$

$$\dot{n}_{CO_2}^{a,in} + \frac{i_{MCFC} A_{MCFC}}{nF} = \dot{n}_{CO_2}^{a,out} \tag{4.83}$$

$$\dot{n}_{O_2}^{c,in} = \dot{n}_{O_2}^{c,out} + \frac{i_{MCFC} A_{MCFC}}{2nF} \tag{4.84}$$

$$\dot{n}_{CO_2}^{c,in} = \dot{n}_{CO_2}^{c,out} + \frac{i_{MCFC} A_{MCFC}}{nF} . \tag{4.85}$$

The energy balance of the unit cell can be written as follows:

$$\sum_{i=1}^{N} \dot{n}_i^{a,in} h_i^{a,in} + \sum_{i=1}^{N} \dot{n}_i^{c,in} h_i^{c,in} = \sum_{i=1}^{N} \dot{n}_i^{a,out} h_i^{a,out} + \sum_{i=1}^{N} \dot{n}_i^{c,out} h_i^{c,out} + \dot{Q}_{MCFC} + \dot{W}_{MCFC} \quad . \tag{4.86}$$

Accordingly, the exergy balance reads

$$\sum_{i=1}^{N} \dot{n}_i^{a,in} \Xi_i^{a,in} + \sum_{i=1}^{N} \dot{n}_i^{c,in} \Xi_i^{c,in} = \sum_{i=1}^{N} \dot{n}_i^{a,out} \Xi_i^{a,out} + \sum_{i=1}^{N} \dot{n}_i^{c,out} \Xi_i^{c,out} + \left(1 - \frac{T_0}{T}\right) r\dot{Q}_{MCFC} + \dot{W}_{MCFC} + \Xi_{des} \tag{4.87}$$

where $\dot{Q}_{MCFC}$, $\dot{W}_{MCFC}$ and Ξ_d denote the heat transferred by MCFC walls, the output electrical power of the MCFC and the destroyed exergy ($T.\dot{s}_{gen}$), respectively.

The molar exergy term is evaluated by a summation over physical, thermal and chemical exergetic terms. Therefore, we obtain

$$\Xi_i = \left(\left[h_i(T) - h_i(T_0)\right] - T_0\left[s_i(T) - s_i(T_0)\right]\right) + RT_0 \ln(X_i) + \Xi_i^{chem} \tag{4.88}$$

where X_i is the molar fraction of component i and Ξ_i^{chem} is the chemical exergy which are found from [118]. With the purpose of evaluating molar enthalpy and entropy of each species, and assuming that the gasses in anode gas channel and cathode gas channel obey the ideal gas behaviour, the following polynomial equations are fitted to the data, taken from JANAF table used in [133]:

$$\frac{h}{RT} = \left(a_1 + \frac{a_2}{2}T + + \frac{a_3}{3}T^2 + \frac{a_4}{4}T^3 + \frac{a_5}{5}T^4 + \frac{a_6}{T}\right) \tag{4.89}$$

$$\frac{s}{RT} = \left(a_1 \ln(T) + a_2 T + + \frac{a_3}{2}T^2 + \frac{a_4}{3}T^3 + \frac{a_5}{4}T^4 + a_7\right) . \tag{4.90}$$

Furthermore, the output power of the unit cell is calculated as follows:

$$\dot{W}_{MCFC} = i_{MCFC}.A_{MCFC}.V_{MCFC} \tag{4.91}$$

where A_{MCFC} is the active surface area of MCFC and i_{MCFC} is the operating current density. The cell voltage is determined by

$$V_{MCFC} = E_r - i_{MCFC}\left(\eta_{act} + \eta_{conc} + \eta_{ohm}\right) . \tag{4.92}$$

Here, E_r is the reversible open circuit voltage. Likewise, η_{act} , η_{conc} and η_{ohm} are the activation, concentration and ohmic impedances, respectively. These parameters are estimated by the available empirical correlations in the literature [35]:

$$E_r = E_0 + \left[\frac{RT}{2F} ln \left(\frac{P_{H_2,a} P_{CO_2,c} P_{O_2,c}^{0.5}}{P_{CO_2,a} P_{H_2O,a}} \right) \right] \tag{4.93}$$

$$E_0 = 1.2723 - 2.7645 \times 10^{-4} T \tag{4.94}$$

$$\eta_{act} = 2.27 \times 10^{-9} \times exp\left(\frac{6435}{T} \right) \times P_{H_2}^{-0.42} \times P_{CO_2}^{-0.17} \times P_{H_2O}^{-1.0} \tag{4.95}$$

$$\eta_{conc} = 7.505 \times 10^{-10} \times exp\left(\frac{9298}{T} \right) \times P_{O_2}^{-0.43} \times P_{CO_2}^{-0.09} \tag{4.96}$$

$$\eta_{ohm} = 0.5 \times 10^{-4} \times exp\left[3016 \times \left(\frac{1}{T} - \frac{1}{923} \right) \right] \quad . \tag{4.97}$$

In addition, the heat transferred by MCFC walls is

$$\dot{Q}_{MCFC} = T\left(\Delta s - s_{gen} \right) \tag{4.98}$$

where s_{gen} is calculated by

$$s_{gen} = \frac{2F}{T} \left(\eta_{act} + \eta_{conc} + \eta_{ohm} \right) . \tag{4.99}$$

Finally, the energy and exergy efficiency of the molten carbonate fuel cell are evaluated by

$$\eta = \frac{\dot{W}_{MCFC}}{\sum_{i=1}^{N} \dot{n}_i^{a,in} h_i^{a,in} + \sum_{i=1}^{N} \dot{n}_i^{c,in} h_i^{c,in}} \tag{4.100}$$

$$\psi = \frac{\dot{W}_{MCFC}}{\sum_{i=1}^{N} \dot{n}_i^{a,in} \Xi_i^{a,in} + \sum_{i=1}^{N} \dot{n}_i^{c,in} \Xi_i^{c,in}} \quad . \tag{4.101}$$

4.8 Summary

In this chapter, a detailed three-dimensional, transient mathematical model of a molten carbonate fuel cell was developed by employing volume-averaged equations. Two different mechanisms were incorporated for the cathode electrochemical reaction rate. This model accounts for all transport phenomena occurring within MCFCs. The partial differential equations, describing the conservation of mass, momentum, species, electronic charge, ionic charge and energy are summarized as follows:

$$\frac{\partial}{\partial t}\left(\varepsilon^{eff}\rho_g\right) + \nabla\cdot\left(\rho_g \vec{u}_g\right) = S_m \tag{4.81}$$

$$\frac{\partial}{\partial t}\left(\frac{1}{\varepsilon^{eff}}\rho_g \vec{u}_g\right) + \nabla\cdot\left(\frac{1}{\left(\varepsilon^{eff}\right)^2}\rho_g \vec{u}_g \vec{u}_g\right) = -\nabla P_g + \nabla\cdot\left(\bar{\bar{\tau}}\right) + S_u \tag{4.82}$$

$$\frac{\partial}{\partial t}\left(\varepsilon^{eff}\rho_g Y_i\right) + \nabla\cdot\left(-\rho_g D_{i,m}^{eff}\nabla Y_i\right) + \nabla\cdot\left(\rho_g \vec{u}_g Y_i\right) = S_i \tag{4.83}$$

$$\nabla\cdot\left(-\sigma\left(1-\varepsilon\right)\nabla\phi_s\right) = S_{\phi_s} \tag{4.84}$$

$$\nabla\cdot\left(\kappa\left(\varepsilon\theta\right)^{1.5}\nabla\phi_e\right) = S_{\phi_e} \tag{4.85}$$

$$\frac{\partial}{\partial t}\left(\sum_{k=g,s,e}\left(\varepsilon\rho c_p\right)_k T\right) + \nabla\cdot\left(-k^{eff}\nabla T\right) + \nabla\cdot\left(\vec{u}_g \varepsilon\rho_g c_p T\right) = S_T \quad . \tag{4.86}$$

The associated source terms for various equations in each individual sub-domain are presented in Table 4.5. Based on the complete set of governing equations, there are 12 equations with 12 unknowns which need to be solved for: u, v, w, P, Y_{H_2}, Y_{H_2O}, Y_{CO_2}, Y_{O_2}, Y_{N_2}, T, ϕ_e, ϕ_s. In addition, the boundary and initial conditions, along with the model input parameters are stated.

Table 4.4: Physical and thermal properties of various materials

Parameter	Value
Thermal conductivity of anode, k_a (W m^{-1} K) [80, 82]	78
Thermal conductivity of cathode, k_c (W m^{-1} K) [80, 82]	0.9
Thermal conductivity of electrolyte, k_e (W m^{-1} K) [82]	2.0
Specific heat of anode, $c_{p,a}$ (J kg^{-1} K) [118]	444
Specific heat of cathode, $c_{p,c}$ (J kg^{-1} K) [118]	4435
Specific heat of electrolyte, $c_{p,e}$ (J kg^{-1} K) [118]	4000
Density of anode, ρ_a (kg m^{-3}) [118]	8220
Density of cathode, ρ_c (kg m^{-3}) [118]	6794
Density of electrolyte, ρ_e (kg m^{-3}) [118]	1914
Electric conductivity of anode, σ_a (S m^{-1}) [47, 102]	1300
Electric conductivity of cathode, σ_a (S m^{-1}) [47, 102]	1300
Free electrolyte conductivity: Pre-exponential factor, κ_0 (S m^{-1}) [40]	3637
Free electrolyte conductivity: Apparent activation energy, E_k (K^{-1}) [40]	3016
Hydrogen diffusivity in carbon-dioxide, $D_{H_2-CO_2}$ (m^2 s^{-1}) [118, 9]	5.5E-5
Hydrogen diffusivity in water vapour, $D_{H_2-H_2O}$ (m^2 s^{-1}) [118, 48]	9.15E-5
Oxygen diffusivity in carbon-dioxide, $D_{O_2-CO_2}$ (m^2 s^{-1}) [47, 9]	1.4E-5
Oxygen diffusivity in nitrogen, $D_{O_2-N_2}$ (m^2 s^{-1}) [118, 9]	1.8E-5
Carbon-dioxide diffusivity in water vapour, $D_{CO_2-H_2O}$ (m^2 s^{-1}) [118, 9]	1.62E-5
Carbon-dioxide diffusivity in nitrogen, $D_{CO_2-N_2}$ (m^2 s^{-1}) [118, 9]	1.6E-5
Hydrogen diffusivity in liquid electrolyte, $D^l_{H_2}$ (m^2 s^{-1}) [52]	1E-7
Oxygen diffusivity in liquid electrolyte, $D^l_{O_2}$ (m^2 s^{-1}) [52, 104]	3E-7
Carbon-dioxide diffusivity in liquid electrolyte, $D^l_{CO_2}$ (m^2 s^{-1}) [52, 104]	1E-7
Water vapour diffusivity in liquid electrolyte, $D^l_{H_2O}$ (m^2 s^{-1})	1E-7
Nitrogen diffusivity in liquid electrolyte, $D^l_{N_2}$ (m^2 s^{-1})	1E-7
Standard entropy change of anode, ΔS_a (J mol^{-1} K^{-1}) [119]	54.56
Standard entropy change of cathode, ΔS_c (J mol^{-1} K^{-1}) [119]	-216.2
Standard entropy change of generation reaction, ΔS_{tot} (J mol^{-1} K^{-1}) [119]	-161.64

Table 4.5: Source terms in various conservation equations.

	S_m	S_i	S_u	S_{ϕ_s}	S_{ϕ_e}	S_T
Gas Channels	0	0	0	0	0	0
Anode	$S_{H_2} + S_{H_2O} + S_{CO_2}$	$\begin{cases} S_{H_2} = -\frac{R_a}{2F} M_{H_2} \\ S_{H_2O} = \frac{R_a}{2F} M_{H_2O} \\ S_{CO_2} = \frac{R_a}{2F} M_{CO_2} \end{cases}$	$-\frac{\mu_g}{K^{eff}} \vec{u}_g$	R_a	R_a	$\frac{J_e^2}{\kappa_a} + \frac{J_s^2}{\sigma_a} + \lvert \eta_a R_a \rvert + \left\lvert \frac{R_a}{2F} \right\rvert (T \Delta S_a)$
Electrolyte	0	0	0	0	0	$\frac{J_e^2}{\kappa}$
Cathode	$S_{O_2} + S_{CO_2}$	$\begin{cases} S_{O_2} = \frac{R_c}{4F} M_{O_2} \\ S_{CO_2} = \frac{R_c}{2F} M_{CO_2} \end{cases}$	$-\frac{\mu_g}{K^{eff}} \vec{u}_g$	R_c	R_c	$\frac{J_e^2}{\kappa_c} + \frac{J_s^2}{\sigma_c} + \lvert \eta_c R_c \rvert + \left\lvert \frac{R_c}{2F} \right\rvert (T \Delta S_c)$

Chapter 5

Numerical Implementation

In this research, the Finite Volume Method (FVM) is employed to simulate the operation of the molten carbonate fuel cell. This method is one of the most versatile discretization techniques used in computational fluid dynamics. The first step in the FVM is to divide the computational domain into a number of control volumes where the variables are located at the centroid of the control volume. The next step is to integrate the differential form of the governing equations (very similar to the control volume approach) over each control volume. Interpolation profiles are then assumed in order to describe the variation of the variable in consideration between cell centroids. The resulting equations are called the discretized or discretization equations. In this manner, the discretization equations express the conservation principle for the variables inside the control volume [120]. This chapter describes the numerical implementation of the comprehensive three-dimensional mathematical model of the molten carbonate fuel cell. The solver solves a set of highly coupled non-linear conservation equations. Temperature-dependent coefficients (thermal conductivity, mass diffusivity, etc) of the conservation equations along with the exponential functions in the source terms make the system highly non-linear and stiff. A stiff equation refers to an equation for which certain numerical methods are numerically unstable, unless the step size is considerably reduced. Therefore, effective numerical techniques are developed to overcome the solution divergence issues. The overall solution methodology used to solve the governing equations, includes the generated mesh, the utilized commercial solver and the developed code, algorithms, discretization method, under-relaxation schemes and convergence criteria. These are all illustrated in some detail.

5.1 Mesh Generation

The first step in the finite volume method is to divide the computational domain into a number of non-overlapping control volumes such that there is one control volume enclosing each grid point. In this research, a pre-processing software, ANSYS ICEM CFD 12.0.1, was employed to generate a structured non-uniform grid network which is prepared to be imported into the finite volume based commercial software, ANSYS FLUENT 12.0.1, in order to solve the conservation equations. ANSYS ICEM CFD provides advanced geometry acquisition, mesh generation, mesh optimization, and post-processing tools to meet the requirement for integrated mesh generation [121]. A higher number of grid points in the computational domain, with a smaller grid size, can result in a more accurate solution. On the other hand, this will lead to considerable computational expense. Therefore, several numerical analyses were carried out in this study to find the optimum grid size and to ensure that the solutions are ultimately independent of grid size. For this 3D model, the effects of the number of grid points on the results for all three directions (x, y and z) were examined. The methodology and the resulting grid network will be presented in Chapter 6.

5.2 Available Solvers

As stated above, in this study, ANSYS FLUENT 12.0.1 is used for the numerical analysis. Generally, this software has a capability to use both pressure-based (Figure 5.1a) and density-based solvers (Figure 5.1b). Originally, the pressure-based approach was developed for low-speed incompressible flows, while the density-based approach was mainly used for high-speed compressible flows [122]. Recently, both methods have been modified and reformulated to solve and operate for a wide range of flow conditions beyond their traditional purpose.

5.2.1 Pressure-Based Solver

In this solver, the constraint of mass conservation of the velocity field is obtained by solving a pressure (or pressure correction) equation. The pressure equation is derived from the continuity and the momentum equations in such a way that the velocity field, corrected by the pressure,

satisfies the continuity. Since the governing equations are nonlinear and coupled to one another, the solution process involves iterations wherein the entire set of governing equations is solved repeatedly until the solution converges. Two pressure-based solver algorithms are available in ANSYS FLUENT 12.0.1.

The Pressure-Based Segregated Algorithm

This solver uses a solution algorithm where the governing equations are solved sequentially (i.e., segregated from one another). Because the governing equations are non-linear and coupled, the solution loop must be carried out iteratively in order to obtain a converged numerical solution. The individual governing equations for the solution variables are solved one after another. Each governing equation, while being solved, is "decoupled" or "segregated" from other equations, hence its name. With the segregated algorithm, each iteration consists of the steps illustrated in Figure 5.1a.

The Pressure-Based Coupled Algorithm

Unlike the segregated algorithm, the pressure-based coupled algorithm solves a coupled system of equations comprising the momentum equations and the pressure-based continuity equation. Thus, in the coupled algorithm, Steps 2 and 3 in the segregated solution algorithm are replaced by a single step in which the coupled system of equations are solved (Figure 5.1b). The remaining equations are solved in a decoupled fashion as in the segregated algorithm.

5.2.2 Density-Based Solver

The density-based solver solves the governing equations of continuity, momentum, energy and species transport simultaneously. Governing equations for additional scalars will be solved afterward and sequentially (i.e., segregated from one another and from the coupled set). Because the governing equations are non-linear (and coupled), several iterations of the solution loop must be performed before a converged solution is obtained. Each iteration consists of the steps illustrated in Figure 5.1c.

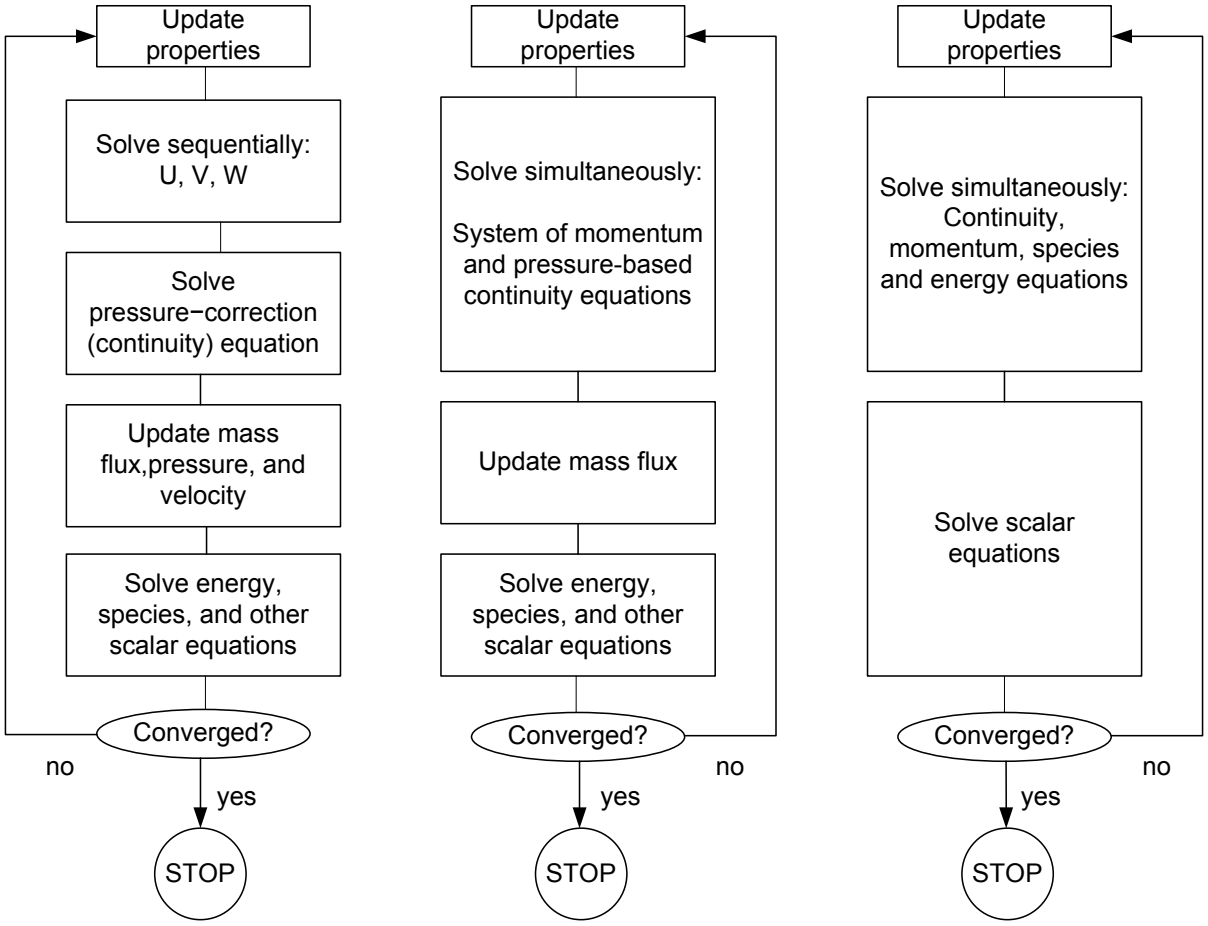

Figure 5.1: Overview of the available steady-state solvers in ANSYS FLUENT 12.01: (a) Pressure-Based Segregated Algorithm, (b) Pressure-Based Coupled Algorithm, (c) Density-Based Algorithm.

5.3 The Adapted Solver

Each algorithm has advantages and disadvantages. For instance, the pressure-based segregated algorithm is memory-efficient, since the discretized equations need only be stored in the memory one at a time. However, the solution convergence is relatively slow, because equations are solved in a decoupled manner. In the pressure-based coupled algorithm, the momentum and continuity equations are solved in a closely coupled manner. Therefore, the rate of solution convergence

significantly improves when compared to the segregated algorithm. However, the memory requirement (RAM) increases by 1.5 – 2 times that of the segregated algorithm since the discrete system of all momentum and pressure-based continuity equations needs to be stored in the memory when solving for the velocity and pressure fields (rather than just a single equation, as is the case with the segregated algorithm).

All three algorithms were implemented and examined for a few simple cases to find the best solver with consideration of computational speed and convergence. The pressure-based segregated solver was found to give accurate results with a balance of memory and speed. However, when all equations and source terms are involved in the simulation, ANSYS FLUENT does not allow using density-based and pressure-based coupled algorithms. This weakness might be removed in the newer versions in future. Thus, the pressure-based segregated solver was employed and adapted as shown in Figure 5.2 which describes the whole solution procedure based on the incorporated non-standard governing equations, so-called User-Defined-Scalars (UDS), properties modification and various imposed source terms.

In essence, in the segregated algorithm, the individual governing equations for the solution variables are solved one after another. Each governing equation, while being solved, is "decoupled" or "segregated" from other equations. Since the governing equations are nonlinear and coupled to one another, the solution process involves iterations wherein the entire set of governing equations is solved repeatedly until the solution converges. Furthermore, the pressure-velocity coupling as a constraint is achieved by solving a pressure correction equation which is derived from the continuity and the momentum equations in such a way that the velocity field, corrected by the pressure, satisfies the continuity. The SIMPLE and PISO algorithms are used for steady state and transient modelling, respectively. The PISO algorithm uses more CPU time per iteration than the SIMPLE algorithm, but the number of iterations for each time step can be significantly reduced for the transient simulations [122]. An algebraic multigrid (AMG) method with a Gauss-Seidel type smoother is used to accelerate the convergence [122]. The overall algorithm of the solution procedure after initialization is summarized in Figure 5.2. The FLUENT specific macros that are used in this figure will be introduced in Appendix A. Additionally, a sample code that was developed using the programming language C is presented in Appendix B.

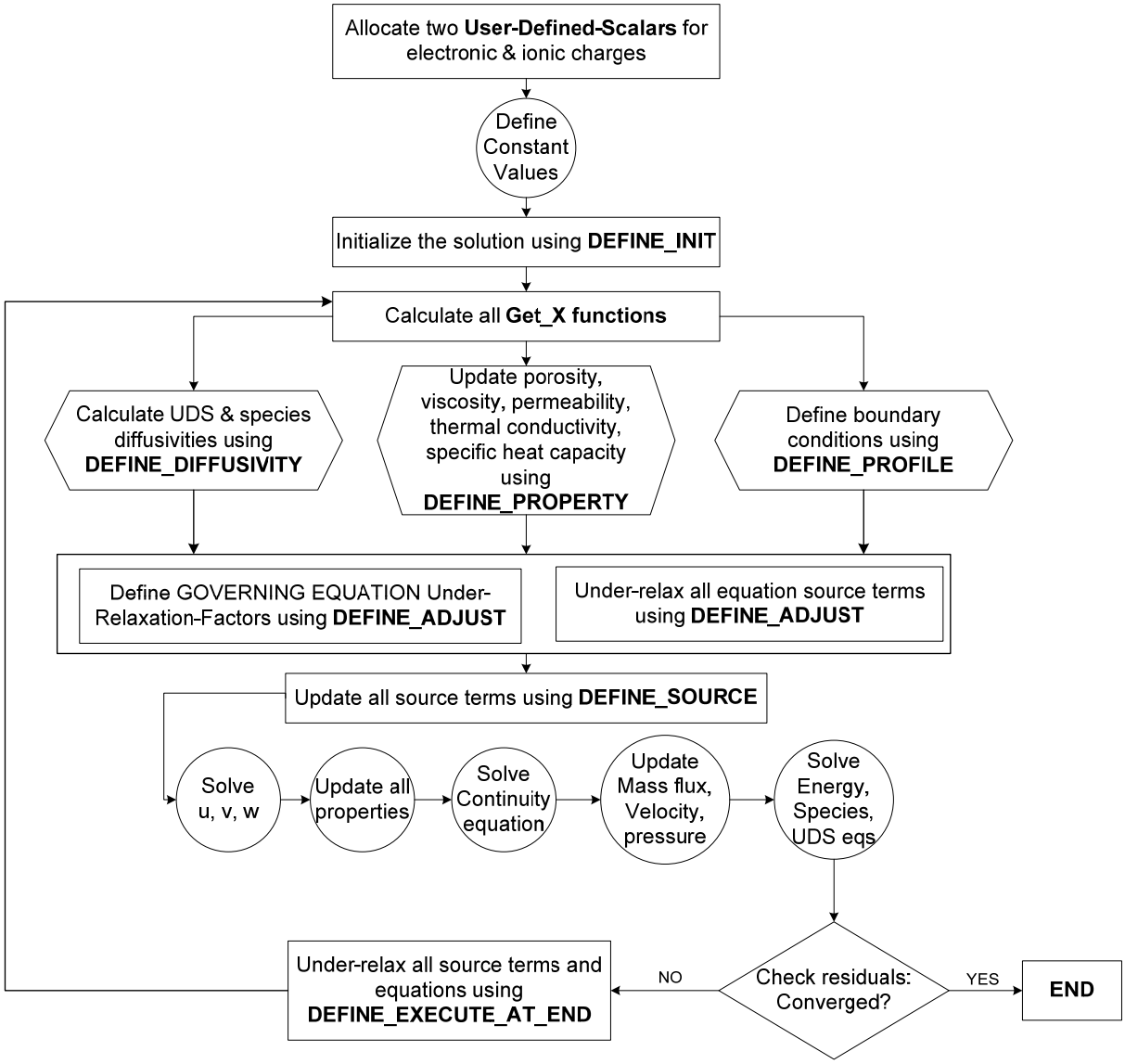

Figure 5.2: Illustration of the modified solution procedure based on the developed in-house code, employing the segregated pressure-based solver, implemented in ANSYS FLUENT.

5.4 Discretization Scheme

Discretization is a technique to convert the partial differential equation to an algebraic equation that can be solved numerically. The control volume technique consists of integrating the

transport equation over each control volume. This leads to a discrete equation that expresses the conservation law on a control-volume basis. Discretization of the general form of governing equations, including transient, convection, diffusion and source terms, can be demonstrated by the following equation written in integral form for an arbitrary control volume V as follows:

$$\int_V \frac{\partial \rho\theta}{\partial t} dV + \oint \rho\theta\vec{\upsilon} \cdot d\vec{A} = \oint \Gamma_\theta \nabla\theta \cdot d\vec{A} + \int_V S_\theta dV \tag{5.1}$$

where, ρ , $\vec{\upsilon}$, $\vec{A}$, Γ_θ , $\nabla\theta$, S_θ are density, velocity vector, surface area vector, diffusion coefficient, θ gradient and source of θ per unit volume, respectively. The above equation is applied to each control volume, or cell, in the computational domain. Discretization of Equation (5.1) on a given cell leads to:

$$\frac{\partial \rho\theta}{\partial t} V + \sum_f^{N_{faces}} \rho_f \vec{\upsilon}_f \theta_f . \vec{A}_f = \sum_f^{N_{faces}} \Gamma_\theta \nabla\theta_f \cdot \vec{A}_f + S_\theta V \tag{5.2}$$

Here, N_{faces} , θ_f , $\rho_f \vec{\upsilon}_f . \vec{A}_f$, $\vec{A}_f$, $\nabla\theta_f$, V are number of faces enclosing the cell, value of θ convected through face f , mass flux through the face, area of face f and gradient of θ at face f , respectively.

Equation (5.2) is the discretized form of the scalar transport equation and contains the unknown scalar variable θ at the cell center as well as the unknown values in surrounding neighbour cells. In general, this equation is non-linear with respect to the corresponding variable that needs to be solved. Therefore, an appropriate discretization scheme is selected to linearize this equation as follows:

$$a_p \theta = \sum_{nb} a_{nb} \theta_{nb} + b \tag{5.3}$$

where the subscript nb refers to neighbor cells, and a_p and a_{nb} are the linearized coefficients for θ and θ_{nb}. In addition, b is the general source term. The above equation is applied for each cell in the computational grid. Consequently, the linearized algebraic equations form a sparse

coefficient matrix which is solved using an implicit Gauss-Seidel linear equation solver in conjunction with an algebraic multigrid method.

5.4.1 Temporal Discretization

For the transient simulations, the governing equations must be discretized in both space and time. The temporal discretization needs to be done in addition to the spatial discretization. Temporal discretization involves the integration of every term in the differential equations over a time step. The integration of the transient terms is straightforward, as shown below. A generic expression for the time evolution of a variable θ is given by

$$\frac{\partial \theta}{\partial t} = F(\theta) \tag{5.4}$$

where the function F incorporates any spatial discretization. Here, the time derivative is discretized using backward differences, which is first-order accurate and given by

$$\frac{\theta^{n+1} - \theta^{n}}{\Delta t} = F(\theta) \quad . \tag{5.5}$$

Here, $n+1$, and n are referred to the next time level ($t + \Delta t$) and current time level (t), respectively. A first-order implicit time integration is used to evaluate $F(\theta)$ at the future time level:

$$\frac{\theta^{n+1} - \theta^{n}}{\Delta t} = F\left(\theta^{n+1}\right) \quad . \tag{5.6}$$

Rearranging the above equation results in

$$\theta^{n+1} = \theta^{n} + \Delta t F\left(\theta^{n+1}\right). \tag{5.7}$$

This implicit equation is solved iteratively at each time level before moving to the next time step. The advantage of the fully implicit scheme is that it is unconditionally stable with respect to time step size.

5.4.2 Spatial Discretization

Face values θ_f are required for the convection terms in Equation (5.2) in the discretization which is interpolated from the cell center values. This is accomplished using an upwind scheme. Upwinding means that the face value θ_f is derived from quantities in the cell upstream, or "upwind", relative to the direction of the normal velocity υ_n. A second-order upwind scheme is used for the discretization of density in the continuity equation, while for the face pressure which appears in the linearized momentum equation, it is evaluated based on a standard linear interpolation of the adjacent node values. For all other conservation equations (mass, momentum, heat, electronic charge and ionic charge), a second-order upwind scheme is chosen.

5.5 Under-Relaxation Scheme

Under-relaxation is a constraint on the change of a dependent or auxiliary variable from one solution iteration (at a particular time-step for transient simulation) to the next. It is required to maintain the stability of the coupled, non-linear system of equations. In other words, under-relaxation is a technique to stabilize the solution in order to achieve convergence. Usually, well-posed problems with proper boundary conditions and grid network usually do not require a high reduction of under-relaxation factors. But for a problem which is highly non-linear and stiff, a proper under-relaxation scheme is essential. When under-relaxation applies, the under-relaxed variable does not reach its next value (of the iteration) directly, but the process is divided into steps. Technically, under-relaxation factors make the solution take a lot longer to converge. By performing an under-relaxation scheme, the following steps were applied:

1. A high enough number of iterations were performed to allow the under-relaxed variable to reach its final value.
2. A convergence criterion (described in section 5.6) which is strict enough to avoid problems of false convergence was applied.

Therefore, three different under-relaxation schemes were developed and applied to the solver in order to overcome the stiffness and stabilize the solution.

5.5.1 Variable Under-Relaxation Scheme

Because of the nonlinearity of the equation set being solved by the solver, it is necessary to control the change of independent variables, θ. This is typically achieved by under-relaxation of variables (also referred to as explicit relaxation), which reduces the change of θ produced during each iteration. In a simple form, the new value of the variable θ within a cell depends upon the old value, θ_{old}, the computed change in θ, $\Delta\theta$, and the under-relaxation factor, α, as follows:

$$\theta = \theta_{old} + \alpha\Delta\theta \tag{5.8}$$

The under-relaxation factor, ranges from 0 to 1.

5.5.2 Source Term Under-Relaxation Scheme

Source terms contribute to the divergence issues in the solution procedure. They are evaluated based on the exponential Butler-Volmer equation and increase exponentially as the solution progresses. Therefore, another under-relaxation method is essential to avoid divergence. This kind of under-relaxation is similar to the variable under-relaxation scheme but applied to the source terms of the conservation equations. Here, the source terms that are evaluated by other equations are under-relaxed in an explicit manner:

$$S = S_{old} + \alpha\Delta S \tag{5.9}$$

5.5.3 Equation Under-Relaxation Scheme

The under-relaxation of equations, also known as implicit relaxation, is used in the pressure-based solver to stabilize the convergence behaviour of the outer non-linear iterations by introducing selective amounts of θ in the system of discretized equations. In other words, the main idea of this technique is to limit the change in each variable from one outer iteration to the next because a change in one variable changes the coefficients in the other equations, which may slow or prevent convergence. This is equivalent to a location-specific time step.

$$\frac{a_p\theta}{\alpha} = \sum_{nb} a_{nb}\theta_{nb} + b + \frac{1-\alpha}{\alpha} a_p\theta_{old} \tag{5.10}$$

The equation under-relaxation scheme was found to be more effective for this study. Finally, a few simulations were carried out to find the proper values of the under-relaxation factors.

A small under-relaxation factor was used at the beginning of iterations in order to overcome the divergence issue and stabilize the solution. As the solution progressed and achieved a certain level of stabilization, the under-relaxation factor was elevated to accelerate the convergence. By monitoring the stability of the solution, this parameter was gradually increased up to 1 or a value near 1 (for some variables 0.999 and for some others 0.9999). The solution was considered converged when the convergence criteria (described in section 5.6) were achieved.

5.6 Convergence Criteria

In general, having a criterion to judge the convergence of the solution is crucial. Therefore, a parameter called "residual" is defined to have a better insight into the convergence of the solution. By definition, the residual is the imbalance in Equation (5.3) summed over all the computational cells P.

$$R^{\theta} = \frac{\sum_{cell\ P} \left| \sum_{nb} a_{nb}\theta_{nb} + b - a_P\theta_P \right|}{\sum_{cells\ P} |a_P\theta_P|} \tag{5.11}$$

The residual sum for each of the conserved variables is computed at the end of each iteration. In this thesis, residuals of 1×10^{-12} are defined as the convergence criteria to ensure sufficient accuracy of the solution. Figure 5.3 exhibits a typical convergence history for a sample steady-state run which was carried out by employing the numerical implementation method described in this chapter.

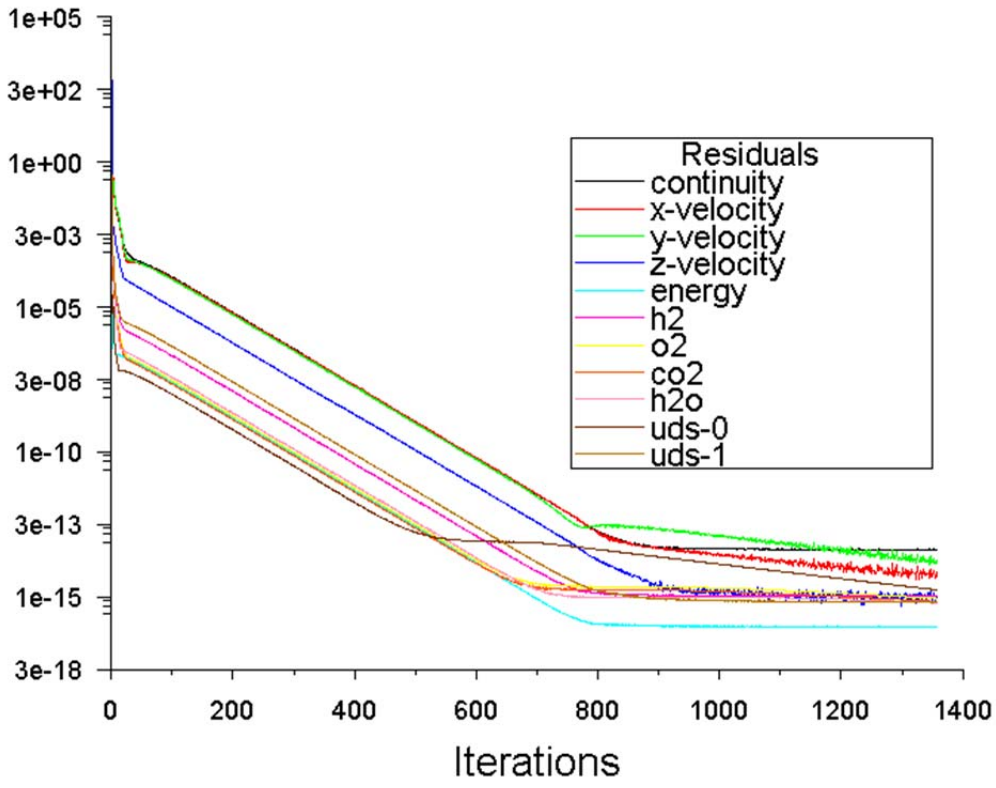

Figure 5.3: A typical convergence history for a sample steady-state run.

5.7 Hardware

In this thesis research, two laptops were used to conduct all steady-state and transient simulations, with the following specifications:

1. Intel(R) Core(TM) i3 CPU (M 370 @ 2.40 GHz) at 6.00 GB memory (RAM) on a 64-bit Operating System.
2. Intel(R) Core(TM) 2 Duo CPU (T6400 @ 2.00 GHz) at 3.00 GB memory (RAM) on a 32-bit Operating System.

The first machine was much faster than the second one. In fact, the required computational time for a specific case was almost three times higher for the second machine in comparison with the first one. Hence, the slower machine was mostly used for steady-state simulations while the

transient simulations were performed using the first machine. More details on computational time will be presented in section 6.2.

It is also worthwhile to mention that a super computing facility, SHARCNET, was employed to find if it can help to expedite the simulations. SHARCNET stands for Shared Hierarchical Academic Research Computing Network. Formally established in 2001, SHARCNET is the largest high performance computing consortium in Canada, including 17 universities, colleges and research institutes across southwestern, central and northern Ontario. SHARCNET provides a wide array of high performance computer systems (HPC) on a dedicated, private high speed wide area network. SHARCNET is a partner consortium in the Compute Canada national HPC platform.

It was found that if there is a case that takes days or weeks to run on desktops or laptops, using SHARCNET will be very helpful as it could probably run it within a few hours using hundreds of processors on the SHARCNET clusters. Therefore, it would be an asset for stack simulations were the number of grid points is extremely large. However, for unit cell simulations, there will not be notable difference considering the required time for upload and download to and from the parallel network.

Chapter 6

Results and Discussion

In this chapter, the computational domain of the simulated molten carbonate fuel cell is presented. Then a grid independence test is introduced and the resulting grid network is demonstrated. In addition, a verification and validation of the developed mathematical model is presented by implementing the two most common cathodic reaction mechanisms. Using the validated mathematical model and the computational mesh scheme, extensive numerical simulations have been conducted to investigate various aspects of the molten carbonate fuel cell. The validated model is utilized to compare the prediction capabilities of the peroxide and superoxide reaction mechanisms. Subsequently, a sinusoidal approach is introduced and implemented to identify the phase shifts and time scales of the physical and chemical transport phenomena occurring within different components of the MCFC. This is carried out by an analysis of the dynamic response of the field variables and parameters to an inlet perturbation. Based on these findings, the start-up process of the fuel cell is investigated. Furthermore, a detailed three-dimensional transient distribution of the field variables and parameters, including molar fractions, temperature, current density, electrochemical reaction rates, etc., is illustrated.

6.1 Physical Domain

Since the molten carbonate fuel cell, shown in Figure 4.4 is symmetric with respect to the y-z plane, only half of the physical domain needs to be modeled. This will help to reduce the computational expense. Therefore, in this research all simulations were conducted for half of the cell domain. This small change requires an adjustment of the boundary conditions that were presented in Chapter 4. Figure 6.1 shows the sketch of the modified computational domain. By

having this new domain, a symmetric boundary condition is applied to the symmetry plane. All other boundary conditions remain unchanged. There are also some points and planes included in Figure 6.1 that were utilized for post-processing of the local and surface-averaged values of various field variables and parameters.

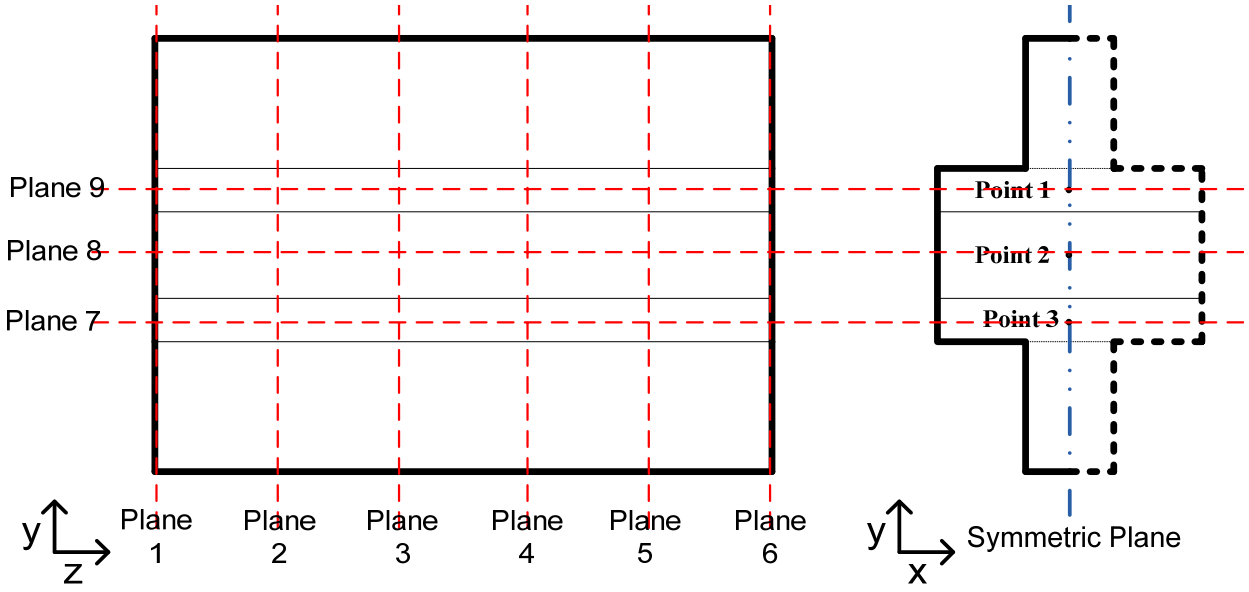

Figure 6.1: A demonstration of the computational domain schematic including the points and planes that are used for data post-processing.

6.2 Grid Independent Solution

In theory, increasing the number grid points improves the exactness, and hence an exact solution can be attained when the grid size is infinitely small. Nonetheless, finding the optimized number of grid points is crucial so as to reduce the computational time and expense and speed up the convergence process. Here, the procedure of the grid independence test for the three-dimensional model is illustrated which examines the effect of number of grids on computational time and accuracy. In this thesis, a procedure presented by Wu [123] is implemented to perform the grid independence study along all three directions (x, y, z). In other words, the effects of the number of grid points along the three directions are examined.

First of all, the model is expected to have larger gradients of field variables along the thickness (y-direction). The reason is that the length scale in that direction is much smaller than the other two directions (especially z-direction). Therefore, a double-sided non-uniform grid scheme is utilized for the y-direction so as to help reduce the computational expense and enhance the convergence process.

There are five layers (or sub-domains) in the y-direction, namely AGC, anode, electrolyte and CGC. The same number of grid points in the y direction is used to simplify the grid independence tests. Thus

$$N^{y}_{anode} = N^{y}_{cathode} = N^{y}_{electrolyte} = N^{y}_{AGC} = N^{y}_{CGC} \tag{6.1}$$

where N denotes the number of grid points. On the other hand, the same grid size along the width (x-direction) and the length (z-direction) of the fuel cell are used for all layers. In fact, a uniform grid scheme is utilized for x and z directions. It is worthwhile to mention that the width of the AGC and CGC are half that of the electrolyte and electrode layers, hence the number of grid points will be half too:

$$N^{x}_{anode} = N^{x}_{cathode} = N^{x}_{electrolyte} = 2N^{x}_{AGC} = 2N^{x}_{CGC} \tag{6.2}$$

$$N^{z}_{anode} = N^{z}_{cathode} = N^{z}_{electrolyte} = 2N^{z}_{AGC} = 2N^{z}_{CGC} \quad . \tag{6.3}$$

Now the total number of grid points in all three directions of the computational domain can be determined as follows:

$$N_{total} = \sum_{layers} N^{x}N^{y}N^{z} = 4N^{x}N^{y}N^{z} \quad . \tag{6.4}$$

The next step is to choose the actual number of grid points in each direction so as to calculate the total number of grid points. In order to find the optimized number of grids, grid independence tests must be carried out in each direction, separately. In order to perform this, the number of grid points was varied in one direction whilst the other directions were kept with the same number of grid points. For instance, in order to test the grid independency of the computational domain in the y-direction, the number of grid points in the y-direction was varied

while the number of grid points in the x and z directions were fixed. Table 6.1 shows the numbers in each case study, which were used for the corresponding grid independency test.

Table 6.1: Grid independent study in the y-direction (N_x = 25 and N_z = 50).

Case	1	2	3	4	5	6
N_y	6	8	10	15	20	25

When the N_y is less than 6, the residuals oscillate at the early stage of iterations and (after 20-30 iterations) the solution diverges. This divergence issue can be attributed to the discretization error which is increased when the grid size is enlarged. It was found that by increasing the N_y, the solution achieves convergence and the results find a more reasonable value. However, when the number of grid points is above 25 ($N_y > 25$), another kind of divergence occurs that is caused by the larger grid aspect ratios. Consequently, $N_y = 25$ is the finest grid possible and gives the most accurate solution that can be achieved (considering the solver limitations). The approximate errors of the other cases are judged by evaluating the corresponding error as follows:

$$Error_x(\%) \cong \left| \frac{\Theta|_{@\,N^y=25} - \Theta|_{@\,N^y}}{\Theta|_{@\,N^y=25}} \right| \times 100 \tag{6.5}$$

where Θ denotes the local field variable which is chosen to be judged.

Figure 6.2 shows the effect of N_y on the approximate error of the average current density in the y-direction. It may be understood that the approximate error of the solution decreases with the grid number. The approximate error for case 4 (N_y = 15) is about 1.7 %. This error is small enough and hence N_y = 15 is used as the optimum number of grid points in the y-direction.

To make a better decision, the computational expense needs to be examined also. Therefore, the effects of N_y on the computational expense are also investigated and the results are shown in Figures 6.3 and 6.4. Figure 6.3 exhibits the time required per 100 iterations and Figure 6.4 shows the number of iterations required for a steady-state simulation to converge.

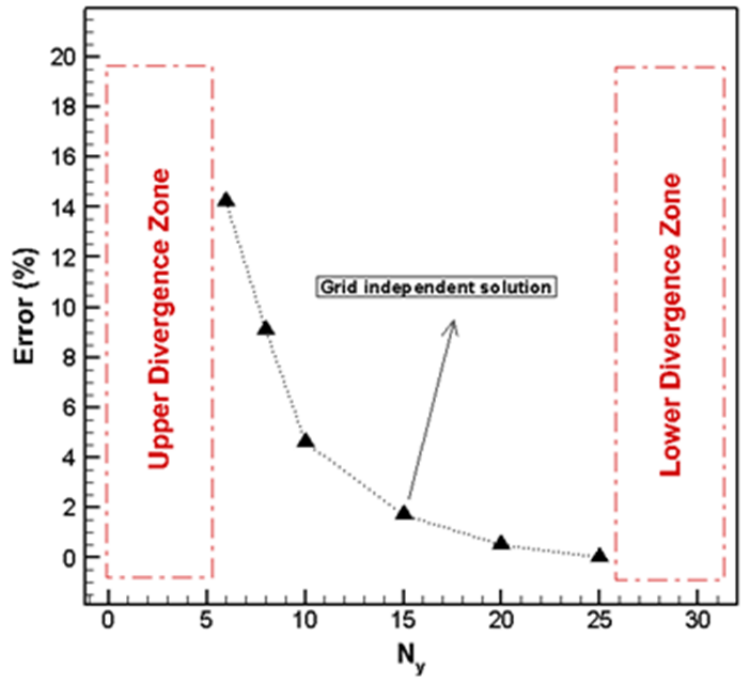

Figure 6.2: Grid Independent Study: effect of N_y on the approximate error of average current density.

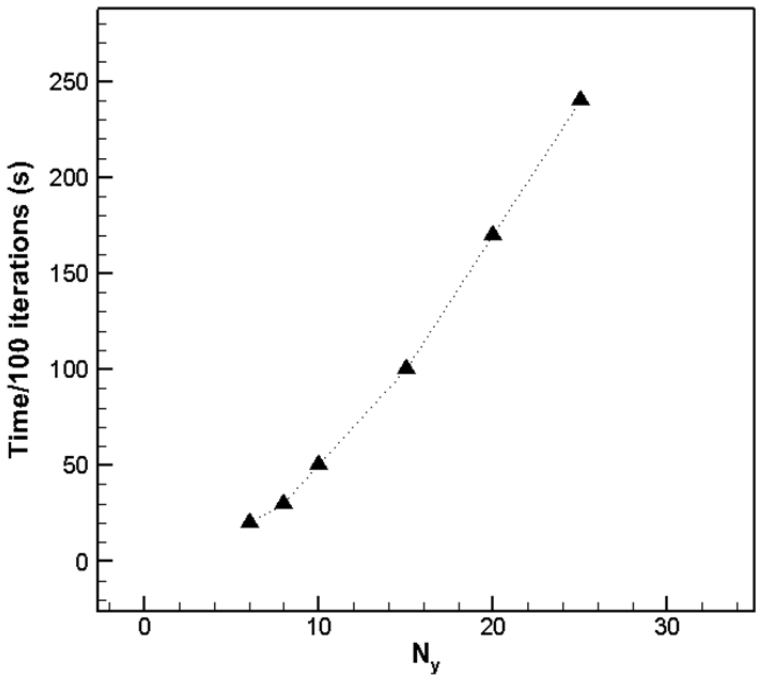

Figure 6.3: Grid Independent Study: effect of N_y on the computational time.

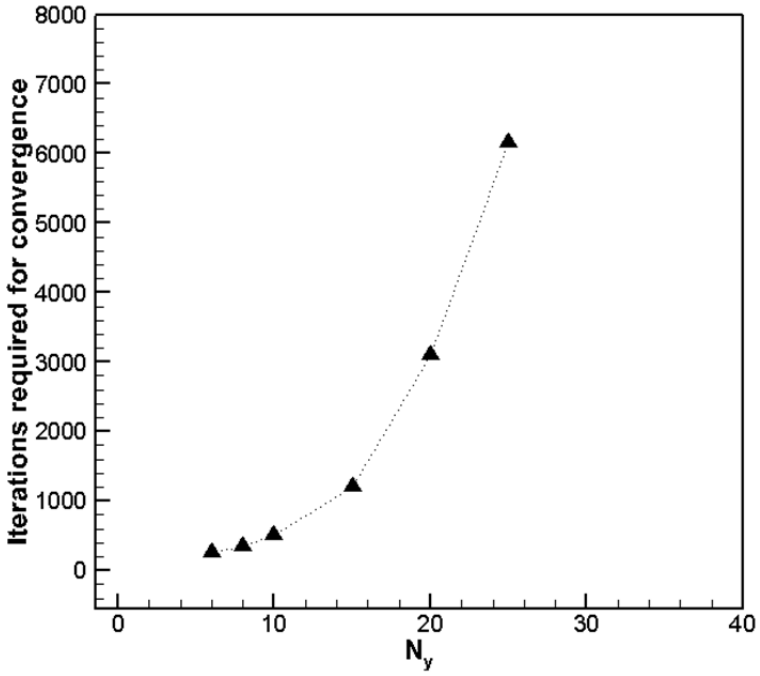

Figure 6.4: Grid Independent Study: effect of N_y on the number of iterations required for a converged steady state solution.

Considering all three figures, it becomes clear that case 4 (N_y = 15) gives a reasonably small error (1.7 %) and computational time (1 s per iteration) and also provides an acceptable stability (1200 iterations for a converged solution).

In general, as was stated previosuly, the model requires smaller grid size along the y-direction whilst x and z directions can use courser grid sizes. In essence, N_x = 25 and N_z = 50 were determined to be able to provide satisfactory results. Additionally, based on Equation 6.5, the corresponding errors are approximated as $Error_x$ = 0.31 % and $Error_z$ = 0.04 %, respectively. Now, the total number of gird points of the selected computational domain can be calculated as:

$$N_{total} = 4 \times 15 \times 25 \times 50 = 75{,}000 \tag{6.6}$$

and the total approximate error for the final mesh is roughly estimated as

$$Error = \left[\left| Error^x \right|^2 + \left| Error^y \right|^2 + \left| Error^z \right|^2 \right]^{0.5} = 1.72\% \tag{6.7}$$

Finally, the resulting grid network for the simulated MCFC is generated using ANSYS ICEM CFD 12.0.1 and a 2D demonstration of the front view and side views in x-y plane, y-z plane and x-z plane is presented in Figure 6.5. The final 3D computational domain is provided in Figure 6.6.

6.3 Time-independent Solution

For transient simulations, it is necessary to specify the time step size. Since the temporal discretization in the ANSYS FLUENT formulation is fully implicit, there is no stability criterion that needs to be met in determining the time step size. Nevertheless, to perform an accurate transient simulation, it is crucial to set this parameter at least one order of magnitude smaller than the smallest time scale in the system being modeled.

As will be seen in section 6.6, a time-dependent problem has a very fast "start-up" transient that decays rapidly. Therefore, it is wise to choose a conservatively small time step size to capture the initial variation of the variables and then increase it gradually as the calculation proceeds. It is possible to have the size of the time step change as the calculation proceeds, rather than specifying a fixed size for the entire calculation.

In this thesis, an adaptive time step method [122] is employed that automatically adjusts the time step size based on the estimation of the truncation error associated with the time integration scheme. If the truncation error is smaller than a specified tolerance, the size of the time step is increased; if the truncation error is greater, the time step size is decreased. The lower and upper limits of the time step size were set to 10^{-6} and 1 s, respectively. More details on the time scales of the various transport phenomena within the system will be presented in section 6.6.

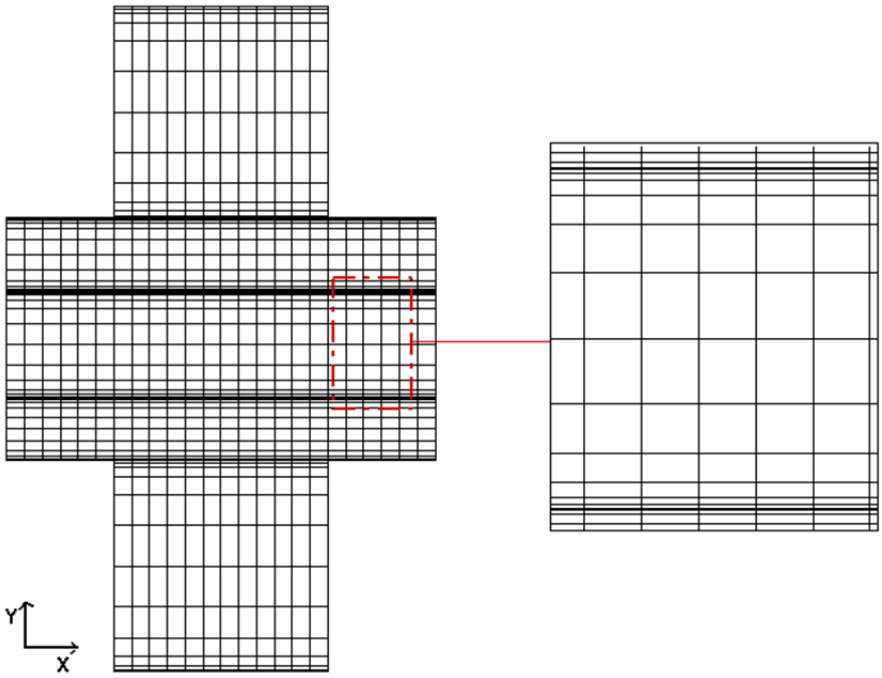

(a)

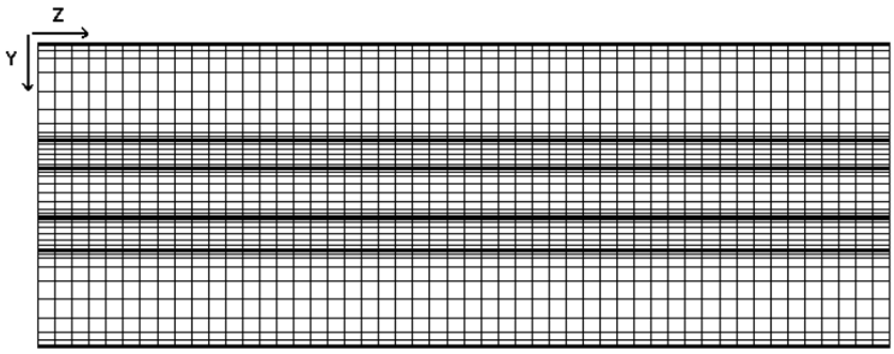

(b)

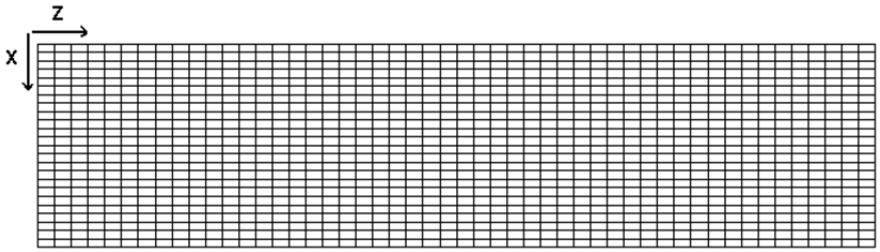

(c)

Figure 6.5: 2D illustration of the grid network for the: (a) front view, x-y plane, (b) side view, scaled y-z plane (y:z = 3:1), and (c) side view, scaled x-z plane (x:z = 3:1).

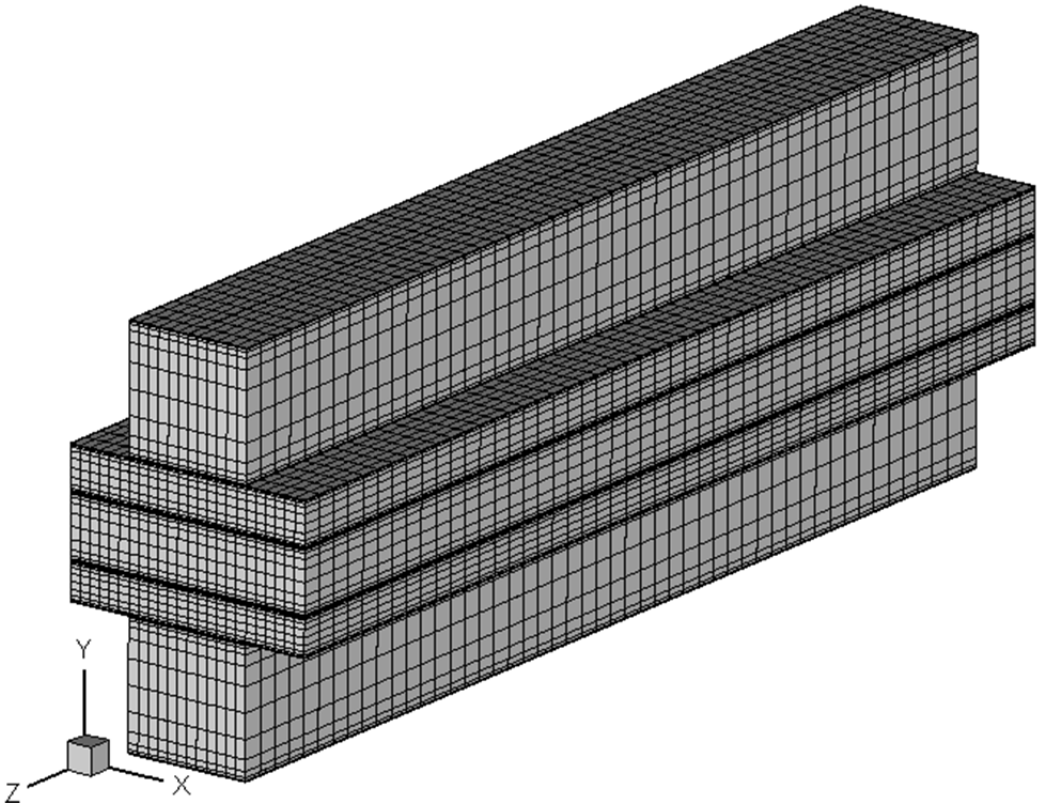

Figure 6.6: 3D demonstration of the grid network for the simulated MCFC.

6.4 Model Verification and Validation

It is generally acknowledged that model validation is the most significant step in the model building sequence of numerical simulations. It is also one of the most overlooked. Apparently, there is no universally reliable method for achieving absolute confidence regarding the verification and validation process. In this study, with the purpose of achieving highly accurate results, the experimental studies by Brouwer et al. [87] and Lee et al. [124] are selected to investigate the model trustworthiness. In fact, the mathematical model is validated by means of the most popular criterion, the polarization curve. In the first step, the model is built based on the reported geometry and operating conditions in Reference [124]. In brief, the authors conducted several experiments to examine the performance of a single MCFC. The electrode-electrolyte assembly consisted of a 0.77 mm Ni–Cr alloy anode and a 0.72 mm in situ oxidized NiO

cathode. A 62 mol % Li_2CO_3, 38 mol % K_2CO_3 eutectic carbonate was utilized as electrolyte, and $LiAlO_2$ with Al_2O_3 fiber was fabricated as matrix material. At the anode side, a gaseous mixture of H_2, H_2O and CO_2 with molar fractions of 0.69, 0.14 and 0.17 was used while in the cathode side, a mixture of O_2, CO_2 and N_2 with molar fractions of 0.15, 0.30 and 0.55 was fed into the system. Based on these conditions, the steady-state polarization curve at various operating condition was obtained [124].

In this study, the polarization curve at atmospheric pressure is initially used to verify and adjust the model input parameters (reference exchange current density and specific surface area). The two most common mechanisms for the cathode electrochemical reaction rate, namely the peroxide and superoxide mechanisms, are employed to investigate the validity of the model. Details of these mechanisms will be discussed in the following section. In the next step, the verified model is put into practice to predict the polarization curve for another MCFC, reported in [87]. This step serves as the validation process. In conclusion, the verification and validation outcome is summarized in Figures 6.7 and 6.8.

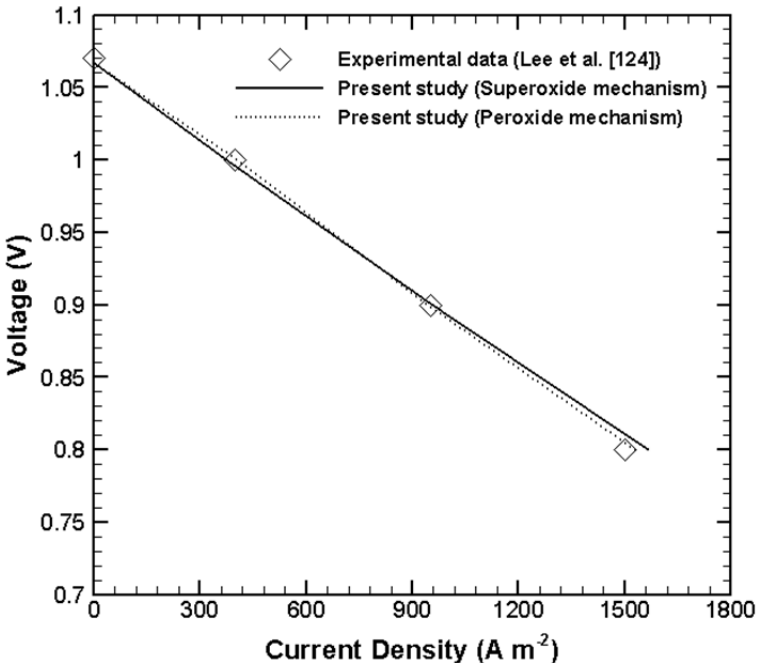

Figure 6.7: Model parameter verification: based on peroxide and superoxide mechanisms for cathode electrochemical reaction rate using the experimental study by Lee et al. [124].

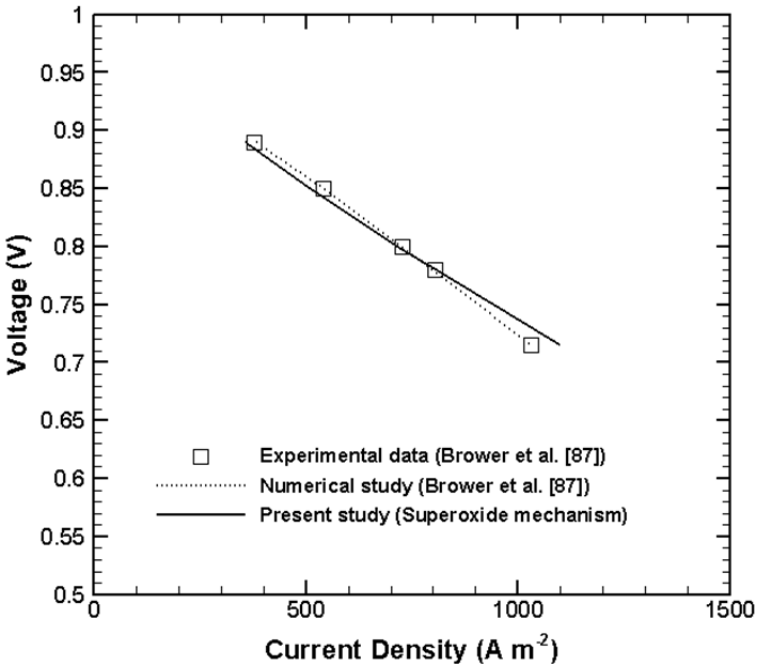

Figure 6.8: Model validation: based on superoxide mechanism for cathode electrochemical reaction rate using the experimental and numerical study by Brouwer et al. [87].

The former illustrates the measured [124] and verified values based on the model fine-tuning. In contrast, the latter demonstrates the accuracy of the verified model in comparison with another experimental study [87] and also a numerical study. It can be easily observed that the model prediction has matched the experimental data adequately. Based on these two strict steps of verification and validation processes, the developed mathematical model is deemed functional in the sense that the model addresses the right problem and presents accurate results. Thereafter, the validated model is engaged in several simulation cases to examine polarization characteristics of a unit cell at relatively high utilization of the cathode gas.

6.5 Peroxide versus Superoxide Reaction Mechanisms

Polarization curves for the porous lithiated NiO cathode are very often reported with a linear slope over a wide potential range. However, the MCFC behaviour at higher oxidant utilization, when the mass transfer becomes dominant, is mostly overlooked. Therefore, in this section, the

two most common cathode mechanisms are utilized to compare their prediction capabilities at higher current densities.

In general, the first region of a fuel cell polarization curve, the so-called activation polarization region, occurs due to the sluggishness of the electrochemical reaction at low current densities (or voltage losses) across the cell. Boosting the supplied gas temperature helps to overcome the activation barrier that is required to drive the electrochemical reaction. However, in molten carbonate fuel cells this region can become insignificant since the operating temperature is relatively high compared to lower temperature fuel cells. This could be observed both in Figures 6.7 and 6.8. Therefore, the polarization curve straight away starts with a linear behaviour which is due to the ohmic polarization. This is the practical and useful region of any fuel cell which is normally (for some fuel cells) followed by a more rapid voltage drop with increased operating current density. Conversely, opposite behaviour is observed in the simulated MCFC, shown in Figure 6.9. In fact, Figure 6.9 implies that using the prevailing reaction mechanisms, the linear behaviour could be achieved flawlessly but only for low and moderate current densities or cathode gas utilizations. It is worthwhile to mention that almost all previous experimental and numerical studies for MCFCs have only shown completely linear polarization curves. In Figure 6.9, first the experimental data [124], which were used for the verification process, are extrapolated linearly in order to estimate the MCFC polarization characteristics at higher current densities. Then the model predictions, based on the two most common cathode mechanisms, are included. It is observed that model predictions demonstrate an upwards bent. This has been rarely discussed in the literature.

This study reveals why the downwards curve is not reported in numerical studies. Noticeably, the issue was found to be in the porous cathode. In actual fact, it is expected that as the gaseous reactants are being consumed to produce current, the mass transfer process becomes dominant in controlling the fuel cell performance.

In other words, the availability of gas mixture components turns out to be crucial which should lead to a drop off in the amount of current generation. Nevertheless, Figures 6.10 and 6.11 show different trends. These graphs demonstrate the variation of local cathode volumetric current density (or carbonate ion generation rate) with carbon dioxide utilization for various over-potentials using peroxide and superoxide mechanisms.

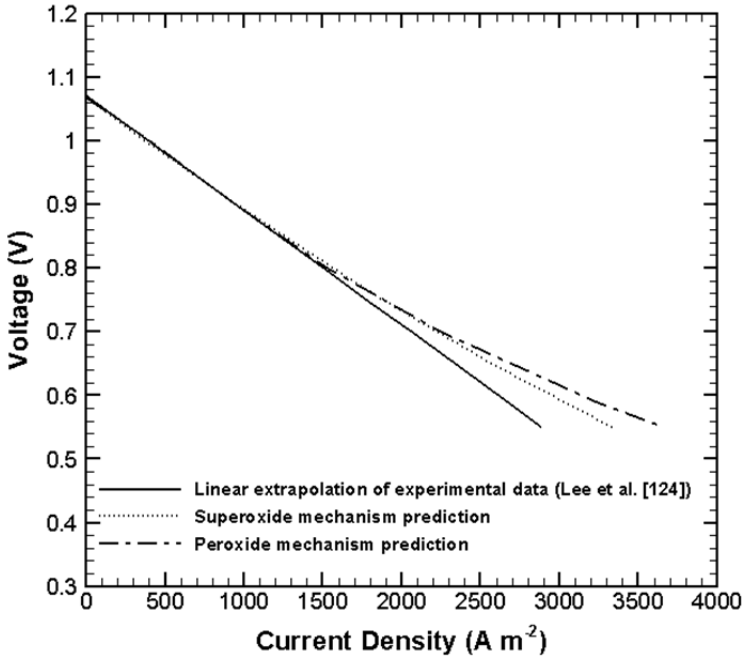

Figure 6.9: Evaluation of polarization curve linearity between the model predictions (superoxide and peroxide mechanisms) and a linear extrapolation of experimental data [124].

Both mechanisms show an exponentially rising tendency (for all over-potential values) as the carbon dioxide mole fraction is decreased. The peroxide mechanism (Figure 6.10) indicates the fact that the volumetric generation of current is increasing up to a point where there is almost no carbon dioxide left in the cathode. Higher over-potentials exacerbate the situation. The same growing trend may be observed from Figure 6.11 for the superoxide mechanism which is less utilized compared with the peroxide mechanism. However, for lower values of over-potentials, the rate of reaction decreases as the utilization reaches almost 80%. Therefore, because of the tendency in reaction rate (or volumetric current density) to increase with falling CO_2, it is obvious that these mechanisms will never predict a downwards bent in the polarization curve.

This could be justified by looking back at Equation (4.39) which describes the cathode electrochemical reaction rate or volumetric current density. It suggests that the negative exponent of the carbon-dioxide mole fraction causes larger values at lower mole fractions. According to Table 4.1, the magnitude of this negative value is greater for the peroxide mechanism which creates a bigger divergence from the linear curve in Figure 6.9.

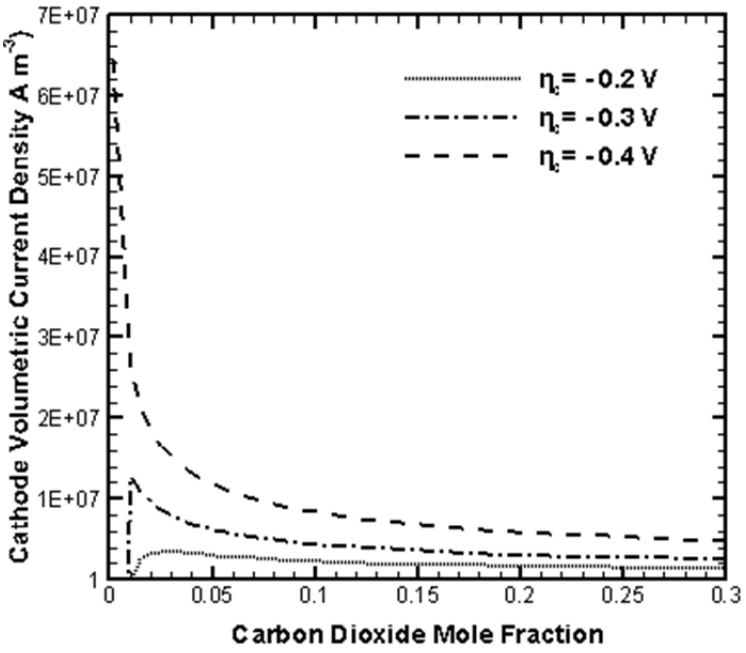

Figure 6.10: Variation of cathode volumetric current density with carbon dioxide utilization in various over-potentials using peroxide mechanism for cathode reaction rate.

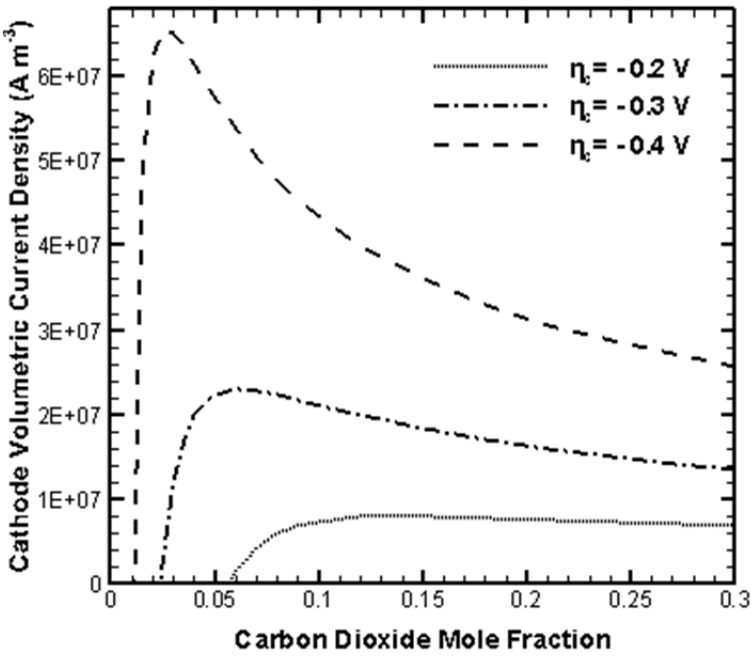

Figure 6.11: Variation of cathode volumetric current density with carbon dioxide utilization in various over-potentials using superoxide mechanism for cathode reaction rate.

At the microscopic level, these negative exponents could be interpreted as reactant molecules competing over reaction sites at the electrode surface, resulting in a saturation effect as the concentration increases.

In conclusion, the literature seems to lack experimental and numerical data at extremely high cathode gas utilizations, or high average current densities. Investigations have always been conducted at low and moderate current densities, namely the practical operating region. Basically, none of the theoretical mechanisms seems to be functional for high utilizations. More investigation is yet to be carried out to identify the realistic reaction rates and exchange current densities. The current correlations for cathode reaction rate [39, 41] may characterize only apparent values without considering the true kinetics. Perhaps, one way to obtain a good fit to the experimental data at high current densities is to assign a positive exponent to CO_2. Changing this exponent at very low concentration could be another alternative. In any case, conducting further experimental analysis would be helpful to check whether the prediction in Figure 6.12 is accurate.

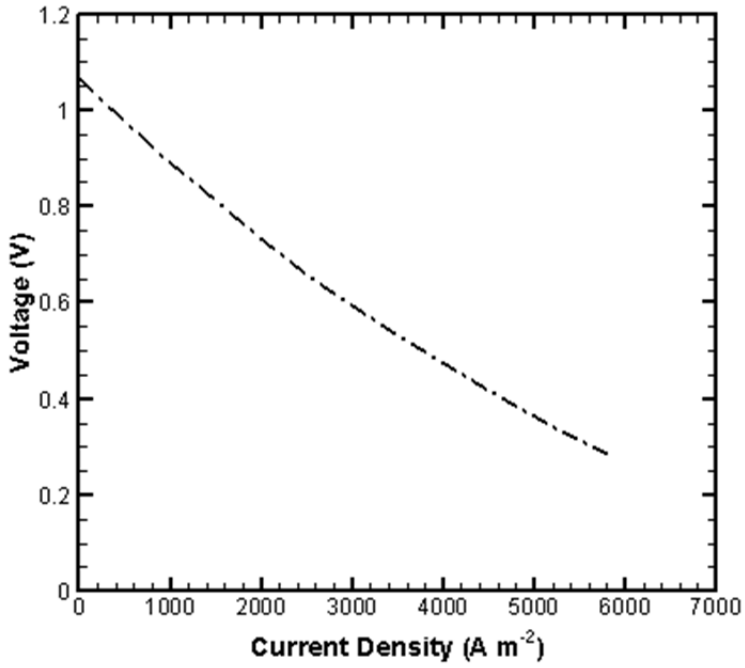

Figure 6.12: Polarization curve obtained by using superoxide mechanism for cathode reaction rate.

It is worth bringing up the fact that the downwards bent exists in the polarization curve of proton exchange membrane fuel cells [e.g. 125-126] and solid oxide fuel cells [e.g. 127-128] at higher current densities, wherein the mass transfer limitations become dominant. The reaction rates of PEMFCs and SOFCs are found to have positive exponents for reaction orders.

Figure 6.12 is obtained by running several cases for different cell voltages up to the point when the code did not converge. In general, at the end of the simulation, once the electrolyte phase and solid phase potentials (ϕ_s and ϕ_e) are determined in the anode, cathode and electrolyte, the transverse component of the local current densities (J_s^y and J_e^y) can be calculated. Then, the average current density of the cell is determined by

$$\overline{J} = \frac{1}{A}\left(\iint_A J_e dA \right) \tag{6.8}$$

where A is the electrode-electrolyte interface area, which should match for both anode and cathode. In the case that the simulation reaches convergence, the calculated average current density in anode and cathode are identical. As well, the local distribution of current density in anode and cathode are similar.

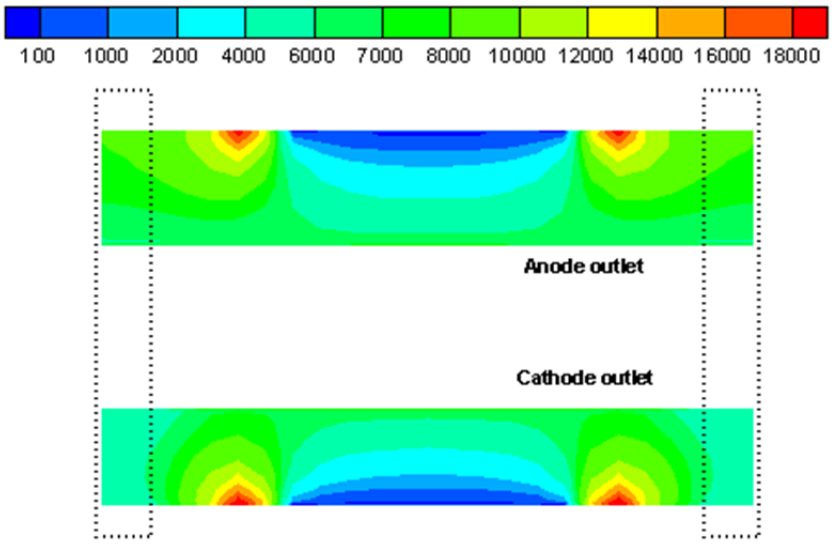

Figure 6.13: Local current density (A m^{-2}) distribution in anode and cathode outlet – Anode mechanism: Ang and Sammels, Cathode mechanism: Superoxide (operating voltage: 0.28 V).

In contrast, according to Figure 6.13, non-uniformity in local volumetric current density started to occur after V = 0.28 V and different values for average current density were obtained (Figure 6.14). Apparently, Figure 6.13 shows that by lowering the cell voltage right down to 0.28 V, which corresponds to a 0.79 V drop in cell voltage, the local current density at the cathode corners (shown in dotted-box) diminishes. In other words, it declines by a factor of 2 comparing to the anode local current density at the same spot. This could be explained by taking Figure 6.14 into consideration.

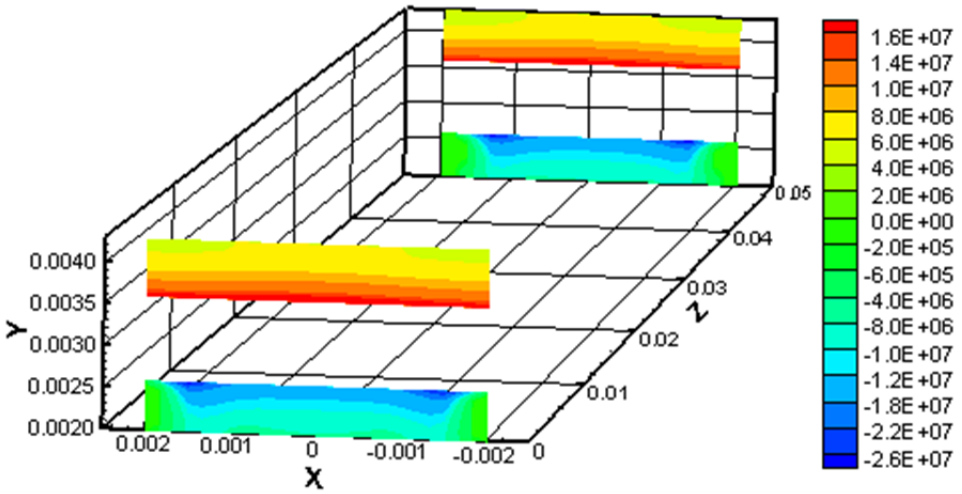

Figure 6.14: Local volumetric current density (A m^{-3}) distribution in anode and cathode inlet and outlet – Anode mechanism: Ang and Sammels, Cathode mechanism: Superoxide (operating voltage: 0.28 V).

It simply demonstrates the sluggishness of the reaction rate or volumetric current density at the corners. In fact, in this extreme condition, the cathode electrochemical reaction occurs mainly under the gas channel and partially in a small spot close to the gas channel. Since the rate of reaction is decreased, the amount of generated current is reduced. Consequently, non-uniformity of the local current density deteriorates the MCFC performance. In realistic operating conditions, the same current has to transfer through the electrode-electrolyte assembly. However, the local current density is not necessarily uniform. The surface area through which the current is transferred, determines the current density and its area-weighted surface integral identifies the cell total current density. Our mathematical model perfectly predicts this equality, hence this

value was used to generate the polarization curves up to V=0.28 V. At this voltage, the anode and cathode average current density are calculated as 6343 and 5740 A m^{-2} , respectively, which means they are not identical to any further extent. This is all due to the extremely small molar fraction of carbon dioxide in the cathode corners shown in Figure 6.15.

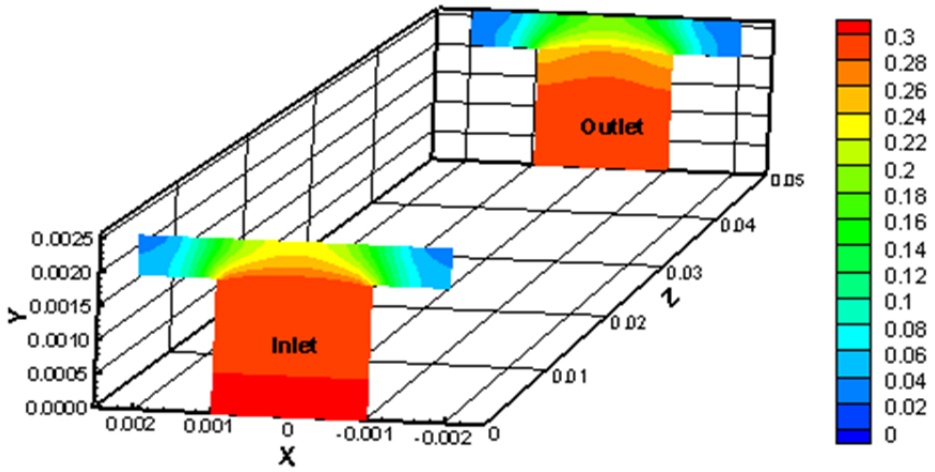

Figure 6.15: Superoxide mechanism prediction for carbon dioxide mole fraction at cathode and cathode gas channel (operating voltage: 0.28 V).

This figure shows the local molar fraction of carbon dioxide in cathode and cathode gas channel inlet and outlet. It is obvious that carbon dioxide utilization reaches its highest value at the cathode corners and the electrochemical reaction rate finds smaller values at these spots. Therefore, the lack of reactants in high current densities (or high utilizations) can result in non-uniformity and performance deterioration.

6.6 Non-Linear Dynamic Response

The various transport phenomena in a molten carbonate fuel cell have a broad range of time scales. It is acknowledged that the electrochemical reactions at the three-phase boundaries in the anode and cathode, heat conduction in solid electrodes and electrolyte, convective form of heat and mass transfer in gas channels, and charge transport processes at the electrodes and electrolyte are the foremost processes which take place inside an MCFC. To be able to elucidate the phase shifts and time scales for different processes occurring in the MCFC, a transient technique, a so-called sinusoidal impedance approach, is incorporated along with the developed mathematical model.

6.6.1 Sinusoidal Impedance Approach

In this approach, a sinusoidal voltage perturbation is applied to assess the resulting harmonic current density, outlet mass flow rates, heat transfer rates, mass fractions and temperature. The general form of the applied voltage is

$$V(t) = V_b + A\sin(2\pi ft) \quad . \tag{6.9}$$

This sinusoidal function serves as the boundary condition for the solid phase potential at the cathode land boundaries (in Equation (4.79)):

$$\varphi_s = V(t) \tag{6.10}$$

where V_b is the base voltage, A is the amplitude of the voltage perturbation, f is the frequency of the sine wave and t is the operating time.

Using the boundary condition described in Equations (4.79), (6.9) and (6.10) and keeping all other input quantities constant, several simulations were carried out in transient mode. The results demonstrate the non-linear dynamic responses of the unit cell variables.

Generally, if the amplitude of the applied perturbation is small enough, the dynamic responses are also sinusoidal (although this may not be applicable to the energy transport process in MCFCs). Accordingly, the dynamic response of the field variables, Θ, is

$$\Theta = \Theta_b + A_\Theta \sin\left(2\pi ft + \theta(f)\right) \quad . \tag{6.11}$$

Here, $\theta(f)$ is the phase difference between the voltage and the response function. Obviously, for a purely resistive behaviour θ is zero. In this study, the following parameters are utilized to analyze the non-linear dynamic responses:

$$V_b = 0.7\ V$$

$$A = 0.1\ V$$

$$f = 0.001,\quad 0.01,\quad 0.1,\quad 1.0,\quad 10.0\ Hz$$

Figure 6.16 demonstrates the sinusoidal perturbation for all frequencies over one periodic cycle. In this figure, the horizontal axis is the non-dimensional time which is defined as

$$Non-Dimensional\ Time = \frac{Time(s)}{One\ Periodic\ Cycle(s)} \tag{6.12}$$

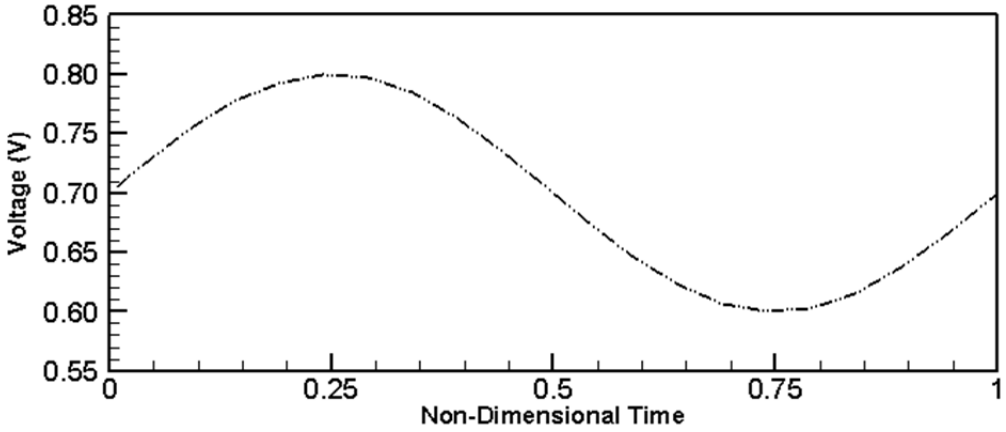

Figure 6.16: The applied sinusoidal voltage perturbation with amplitude of 0.1 V under different impedance frequencies (10.0-0.001 Hz) during one sinusoidal cycle. The horizontal axis is the dimensionless form of the time period.

By means of this definition, the applied sinusoidal voltage versus non-dimensional time finds an identical trend for all frequencies. Accordingly, 0.50 in the horizontal axis corresponds to 500 sec, 50 sec, 5 sec, 0.5 sec and 0.05 sec for the impedance frequencies of 0.001 Hz, 0.01 Hz, 0.1 Hz, 1 Hz and 10 Hz, respectively.

Hereafter, Figure 6.16 along with the resulting dynamic responses will be utilized to determine the phase shifts among the different variables and the applied perturbation. Nevertheless, the characteristic time scale of each process will also be roughly evaluated.

6.6.2 Dynamic Response of the Current Density

The most critical quantity in the dynamic response analysis of fuel cells is the cell average current density. The corresponding time scale characterizes the charge transport in both solid and electrolyte phase and can be evaluated by [129]:

$$\tau_{charge} = \delta^2 A_v C \left(\frac{1}{\sigma} + \frac{1}{\kappa} \right) \tag{6.13}$$

where δ is the electrode thickness and C is the electric capacitance, ranging from 1.5 to 55 F m^{-2} [130]. Using the model input parameters, the time scale of the charge transport process is evaluated to be 3.6E-06 to 1.5E-04 sec. These values imply that the charge transport in MCFCs is extremely fast and, hence, it is beyond the scope of this research to model the double-layer dynamics. Figure 6.17 shows the dynamic responses of the unit cell average current density during one sinusoidal cycle under four different frequencies (0.01-10 Hz).

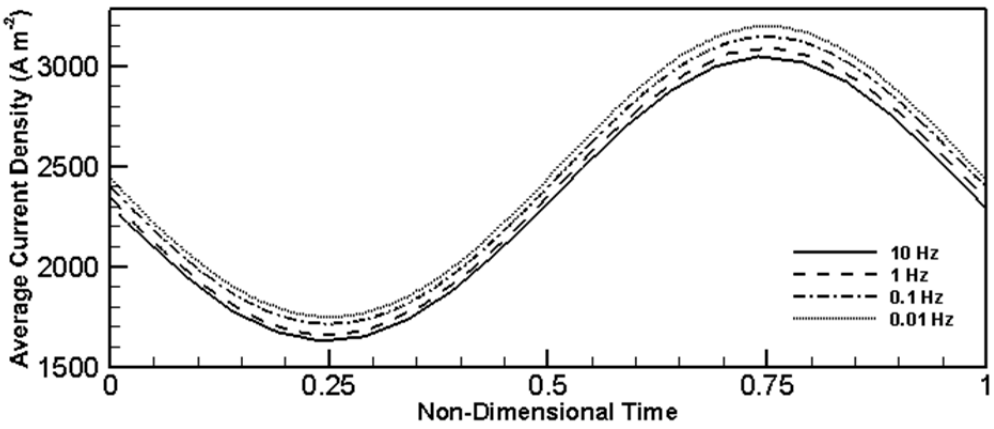

Figure 6.17: The applied sinusoidal voltage perturbation with amplitude of 0.1 V under different impedance frequencies (10.0-0.001 Hz) during one sinusoidal cycle. The horizontal axis is dimensionless form of the time period.

It may be observed that the resulting dynamic responses for all impedance frequencies follow a sinusoidal trend with no noticeable phase shifts. This simply entails that the dynamic response of the cell current density is independent of the perturbation frequency. Technically, this occurs only when the time scales are extremely small, as in Equation (6.13).

The next parameters of interest are the anode and cathode volumetric reaction rates which are demonstrated in Figure 6.18 for various frequencies. This figure exhibits a pattern similar to the average current density with no phase shift.

It seems as if the electrochemical reaction rates respond to the voltage change instantaneously. This is expected because the charge-transport process which showed an extremely small time scale, is coupled to the electrochemical reactions. In other words, the ionic and electronic charges are generated and consumed with the same time scales as the charge transport process.

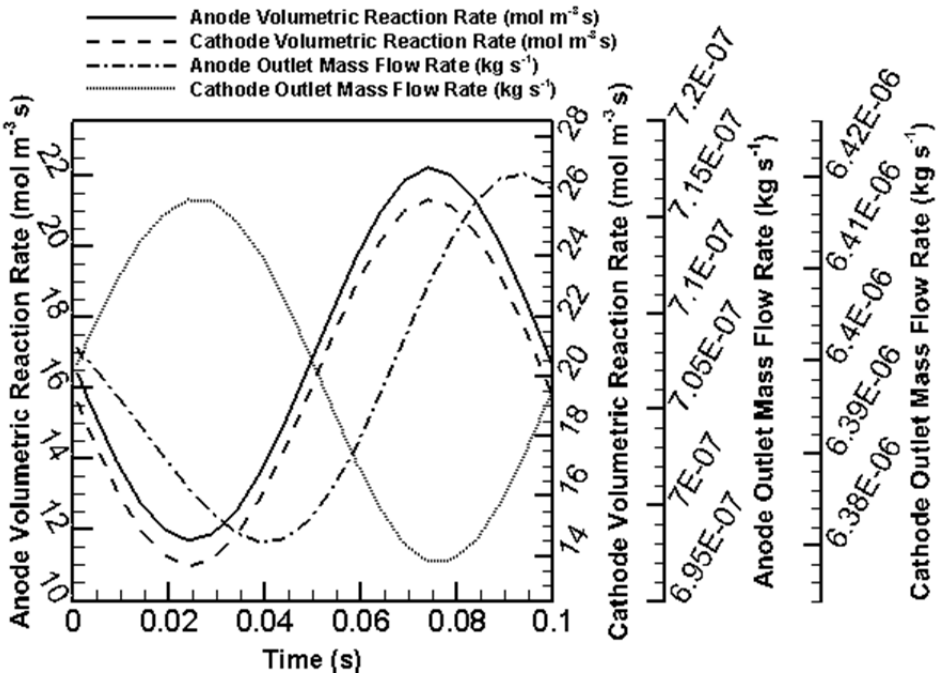
Anode Volumetric Reaction Rate (mol m-3 s)
Cathode Volumetric Reaction Rate (mol m-3 s)
Anode Outlet Mass Flow Rate (kg s-1)
Cathode Outlet Mass Flow Rate (kg s-1)
Anode Volumetric Reaction Rate (mol m-3 s)
Time (s)
Cathode Volumetric Reaction Rate (mol m-3 s)
Anode Outlet Mass Flow Rate (kg s-1)
Cathode Outlet Mass Flow Rate (kg s-1)

(a) 10 Hz

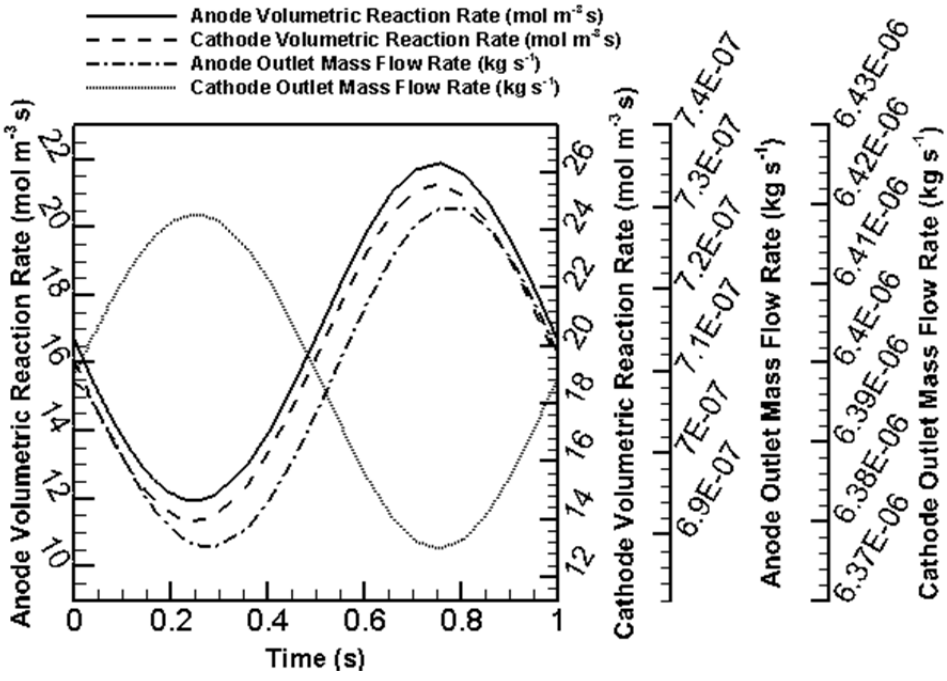
Anode Volumetric Reaction Rate (mol m-3 s)
Cathode Volumetric Reaction Rate (mol m-3 s)
Anode Outlet Mass Flow Rate (kg s-1)
Cathode Outlet Mass Flow Rate (kg s-1)
Anode Volumetric Reaction Rate (mol m-3 s)
Time (s)
Cathode Volumetric Reaction Rate (mol m-3 s)
Anode Outlet Mass Flow Rate (kg s-1)
Cathode Outlet Mass Flow Rate (kg s-1)

(b) 1 Hz

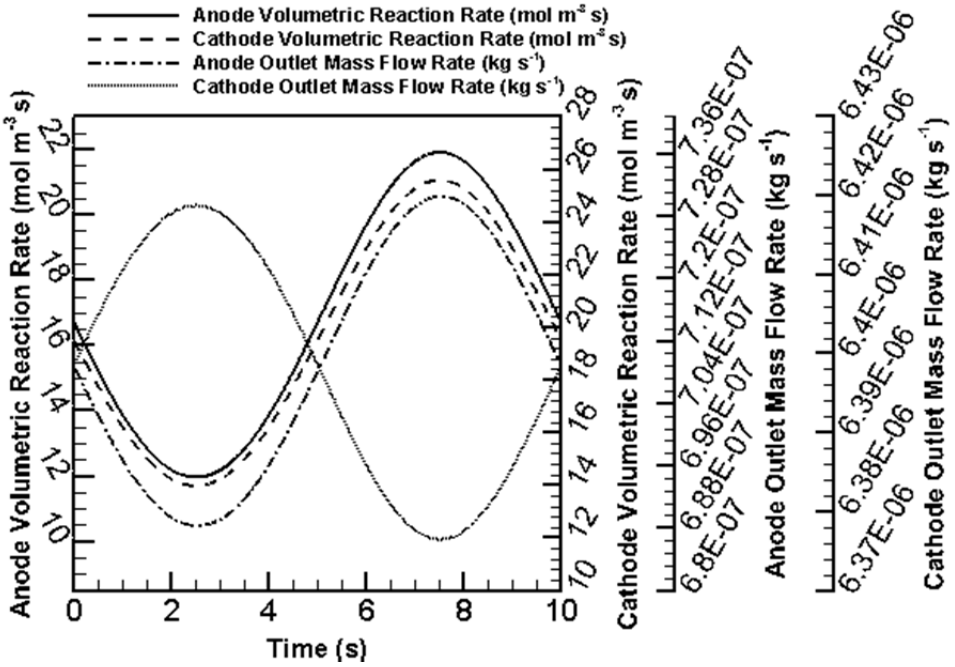

(c) 0.1 Hz

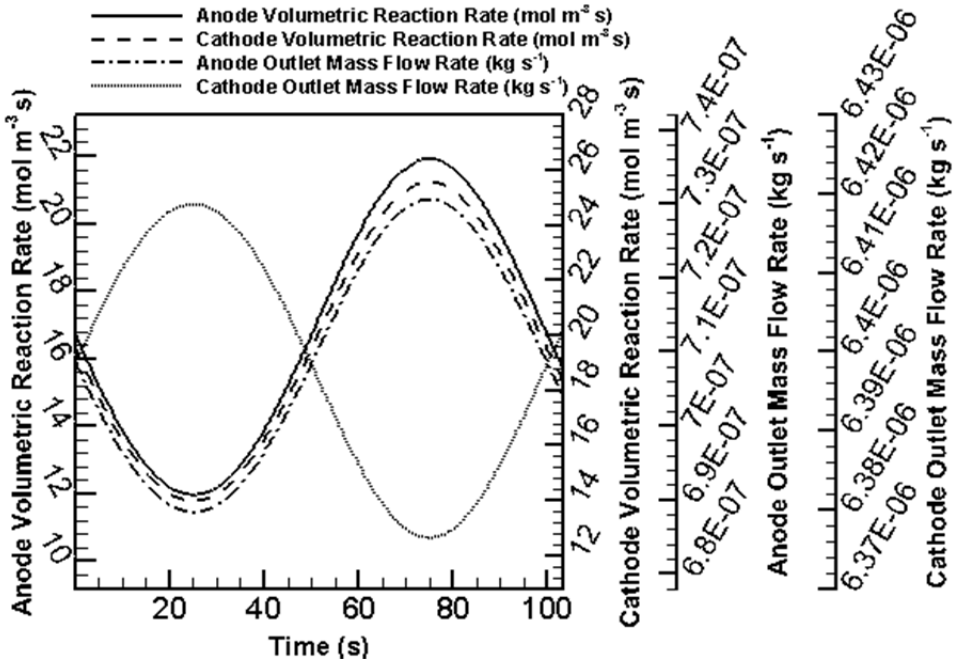

(d) 0.01 Hz

Figure 6.18: Dynamic response of the electrodes' volumetric reaction rates and gas flow rates in gas channels outlet corresponding to sinusoidal voltage perturbation during one sinusoidal cycle and over a wide range of impedance frequencies (10.0-0.001 Hz).

6.6.3 Dynamic Response of Mass Transfer Characteristics

In order to identify the dynamic behaviour of the mass transport process, two types of parameters are considered. One is the average bulk value of mass flow rates at gas channel outlets (shown in Figure 6.18), and the second is the local value of the gaseous species' mass fractions in the anode and cathode (at Points 1 and 3, shown in Figure 6.1). The approximate characteristic time scale can be evaluated as:

$$\tau_{mass} = \frac{\delta^2}{D_g^{eff}} \tag{6.14}$$

which is derived by assuming that diffusive mass transfer dominates the convective mass transfer. By substituting parameter values, the time scale of the gas transport process is evaluated to be about 0.2-1 sec. This value indicates that the gas transport process is relatively slower than the electrochemical reactions and charge transport process. Figure 6.18 confirms this conclusion by showing obvious phase shifts for both of AGC and CGC outlet mass flow rates at a frequency of 10 Hz. These phase shifts are then decreased and vanish at a frequency of 1 Hz. One can justify the fading of the phase shift by taking into account the sluggishness of the variation in the operating condition, when the oscillation frequency is small. In this situation, the unit cell has more time to reach its local equilibrium. Therefore, the phase shift disappears when the impedance frequency diminishes. Even though the AGC and CGC outlet mass flow rates (bulk variables) are reasonable parameters for an analysis of the mass transport characteristic time scales, a number of local variables are also selected to present an enhanced understanding of mass transport process. Results are summarized in Figure 6.19, and confirm the same time scale as that of the bulk variables.

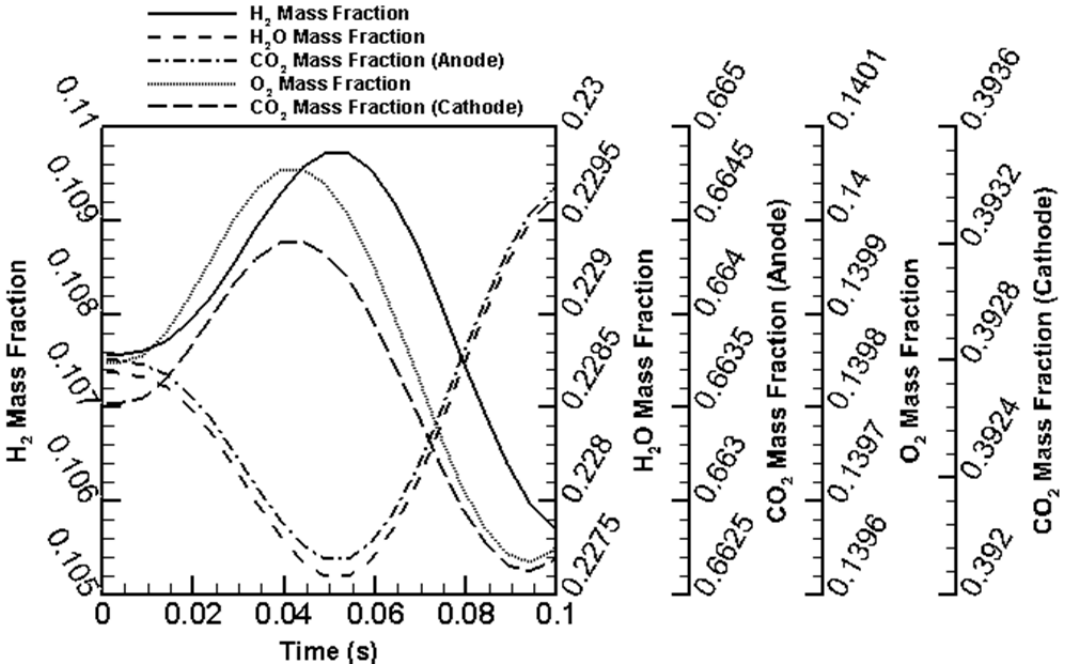
H2 Mass Fraction
H2O Mass Fraction
CO2 Mass Fraction (Anode)
O2 Mass Fraction
CO2 Mass Fraction (Cathode)
Time (s)

(a) 10 Hz

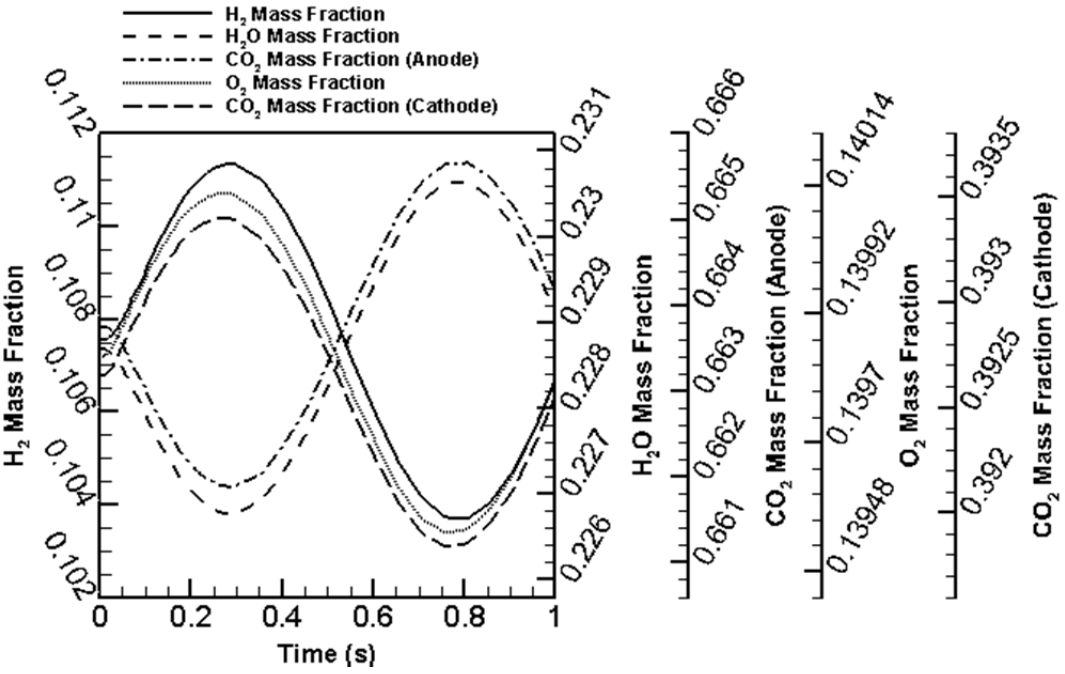
H2 Mass Fraction
H2O Mass Fraction
CO2 Mass Fraction (Anode)
O2 Mass Fraction
CO2 Mass Fraction (Cathode)
Time (s)

(b) 1 Hz

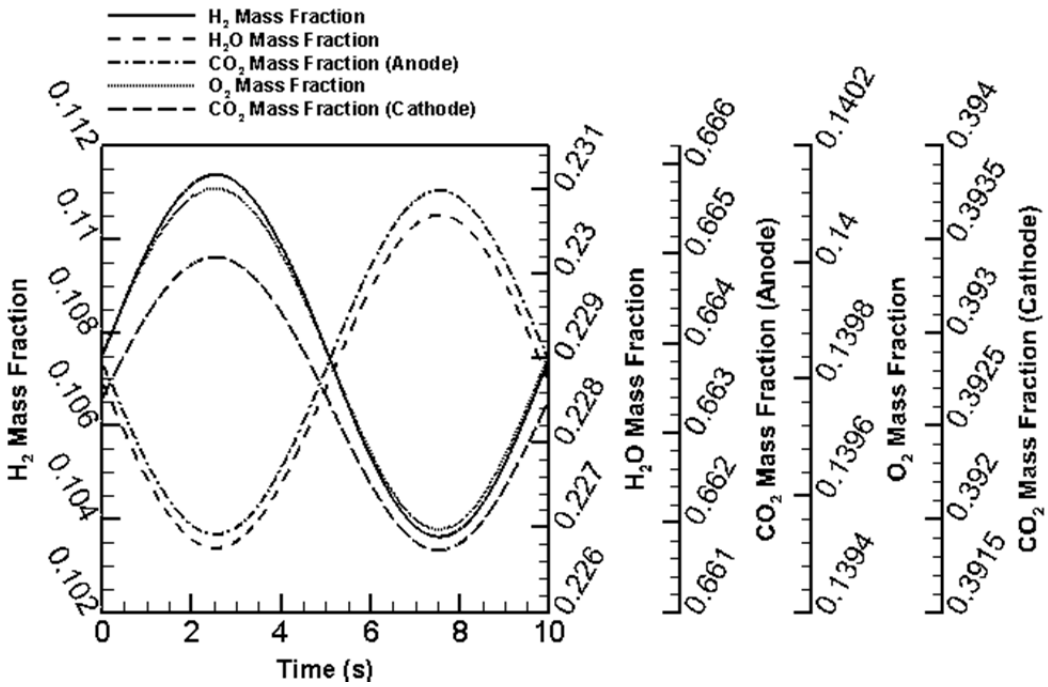

(c) 0.1 Hz

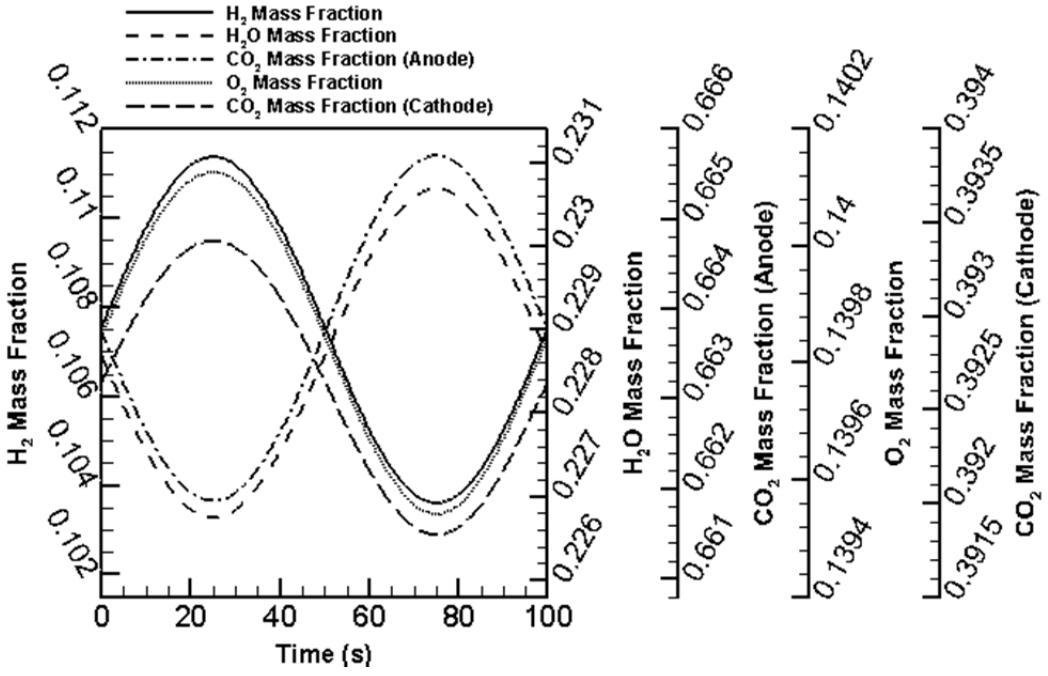

(d) 0.01 Hz

Figure 6.19: Dynamic response of the gas species' mass fractions corresponding to sinusoidal voltage perturbation during one sinusoidal cycle and over a wide range of impedance frequencies (10.0-0.001 Hz).

6.6.4 Dynamic Response of the Heat Transfer Characteristics

Finally, the characteristic time scales of the heat energy transport process are examined. The corresponding time scale can be evaluated as:

$$\tau_{energy} = \frac{\rho c_p \delta^2}{k} \quad . \tag{6.15}$$

It is worthwhile to mention that there are two major energy transport mechanisms in an MCFC. One is the convective heat transfer in gas channels, and the other is the heat conduction in electrodes and the electrolyte. The overall energy transport process is controlled by the slowest mechanism which has the largest time scale. Since the heat capacity of the solid material is much higher than the heat capacity of the gas mixture, the parameters in Equation (6.15) are replaced by the solid materials properties. Thus, the characteristic time scale is found to be on the order of 1.0E+3.0 sec. This value shows that the energy transport process is three orders of magnitude slower than the mass transport process. This notable conclusion facilitates the process of choosing the appropriate time step size. The simulation must be started with an extremely small time step size (1.0E-6.0 sec) which can be increased to 1 sec when the operating time passes the mass transport time scale. Subsequently, solution accuracy is secured along with the optimal computational expense.

Similar to the mass transport dynamic response, both local and bulk variables are chosen to analyze the phase shifts for energy transport characteristics. Figure 6.20 demonstrates the concluding dynamic response of the local temperature (at Points 1, 2 and 3) and the average bulk value of total energy at gas channels outlet.

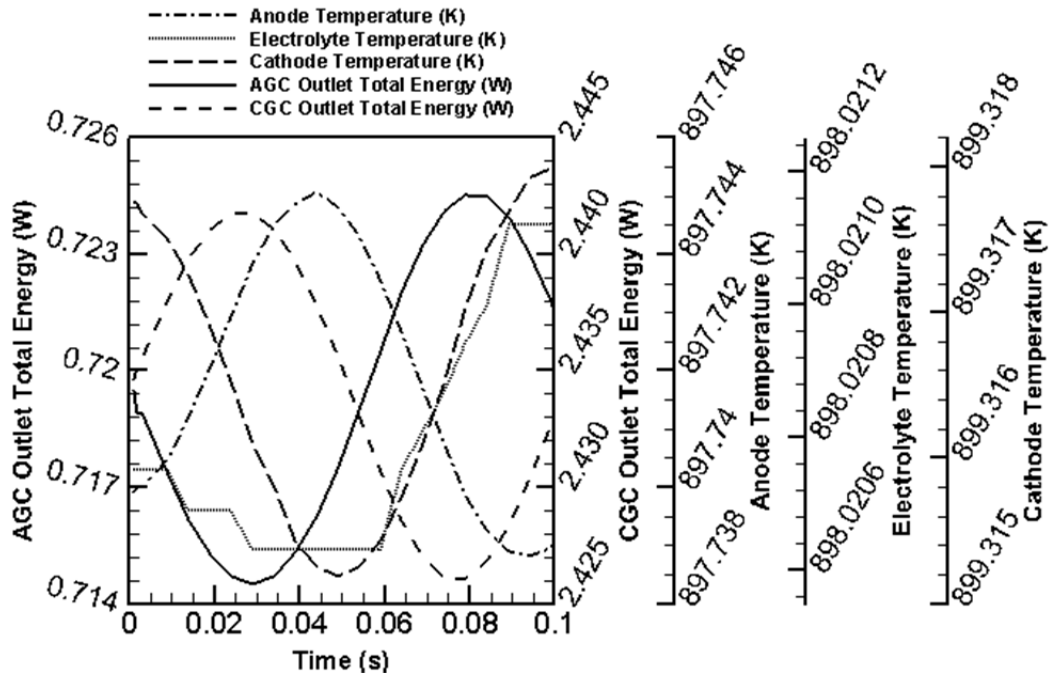
Anode Temperature (K)
Electrolyte Temperature (K)
Cathode Temperature (K)
AGC Outlet Total Energy (W)
CGC Outlet Total Energy (W)
AGC Outlet Total Energy (W)
0.726
0.723
0.72
0.717
0.714
0
0.02
0.04
0.06
0.08
0.1
Time (s)
2.445
2.440
2.435
2.430
2.425
CGC Outlet Total Energy (W)
897.746
897.744
897.742
897.74
897.738
Anode Temperature (K)
898.0212
898.0210
898.0208
898.0206
Electrolyte Temperature (K)
899.318
899.317
899.316
899.315
Cathode Temperature (K)

(a) 10 Hz

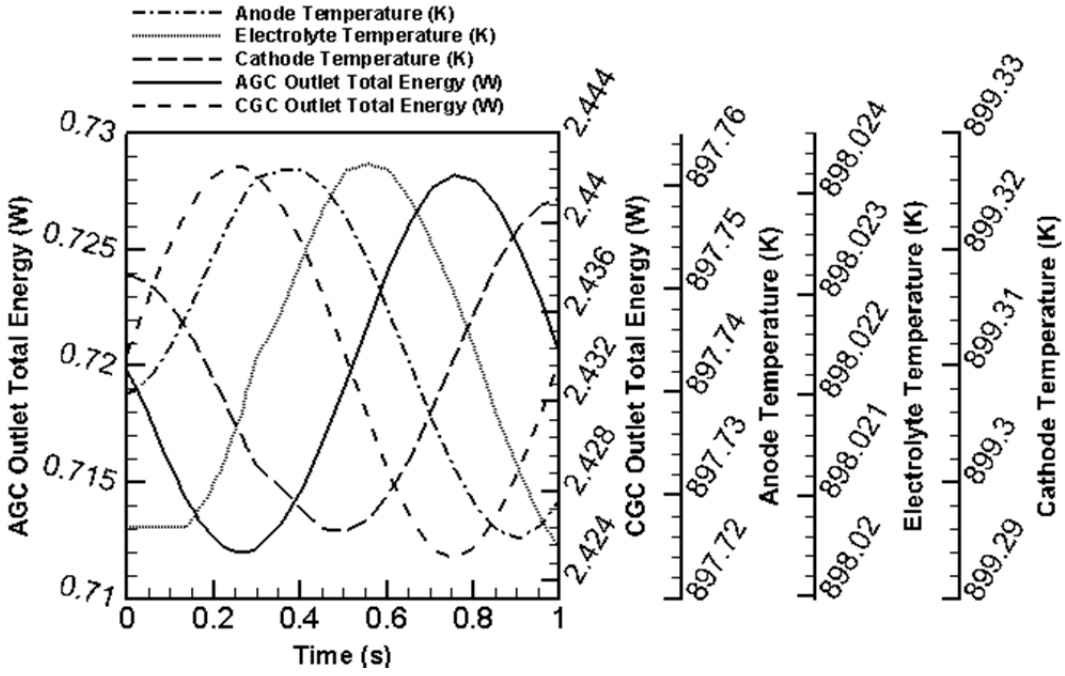
Anode Temperature (K)
Electrolyte Temperature (K)
Cathode Temperature (K)
AGC Outlet Total Energy (W)
CGC Outlet Total Energy (W)
AGC Outlet Total Energy (W)
0.73
0.725
0.72
0.715
0.71
0
0.2
0.4
0.6
0.8
1
Time (s)
2.444
2.44
2.436
2.432
2.428
2.424
CGC Outlet Total Energy (W)
897.76
897.75
897.74
897.73
897.72
Anode Temperature (K)
898.024
898.023
898.022
898.021
898.02
Electrolyte Temperature (K)
899.33
899.32
899.31
899.3
899.29
Cathode Temperature (K)

(b) 1 Hz

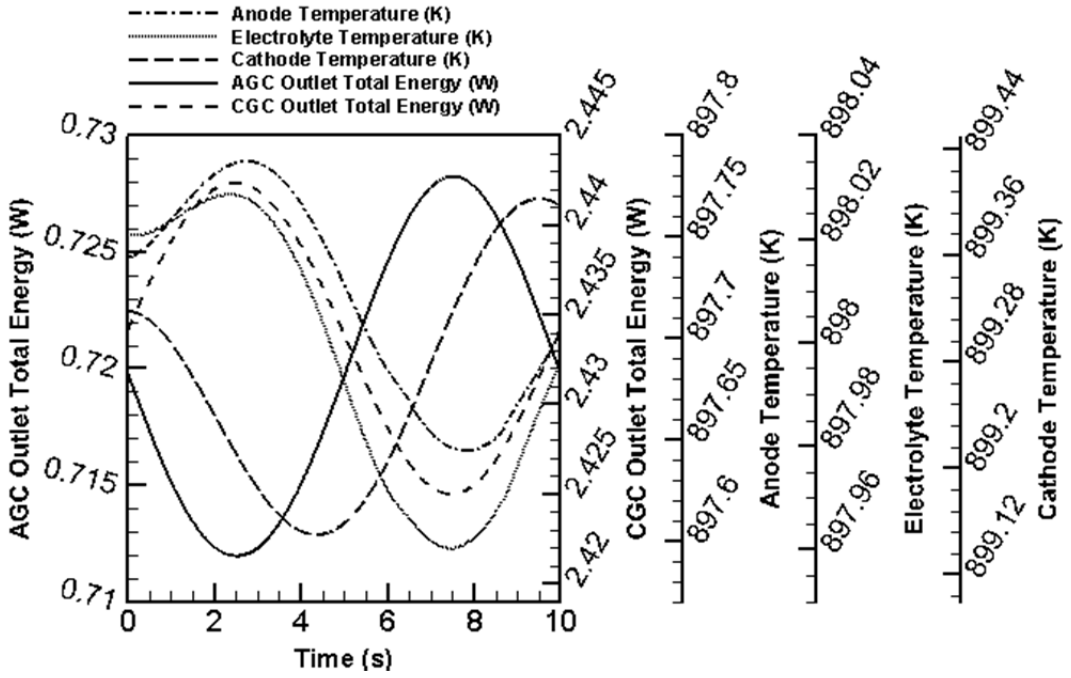

(c) 0.1 Hz

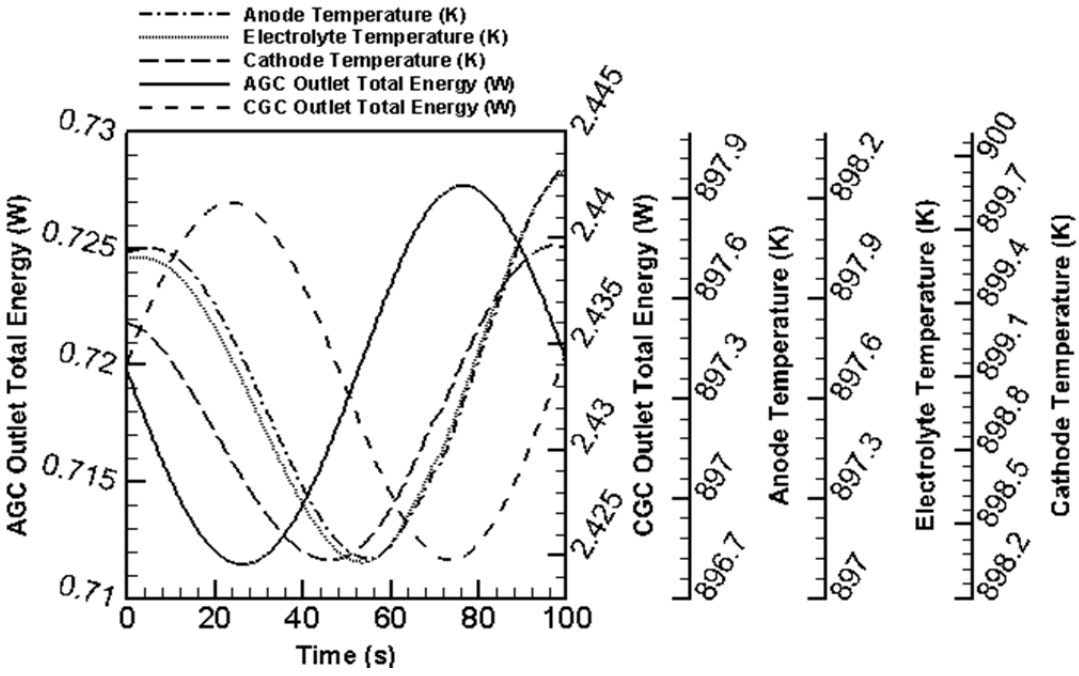

(d) 0.01 Hz

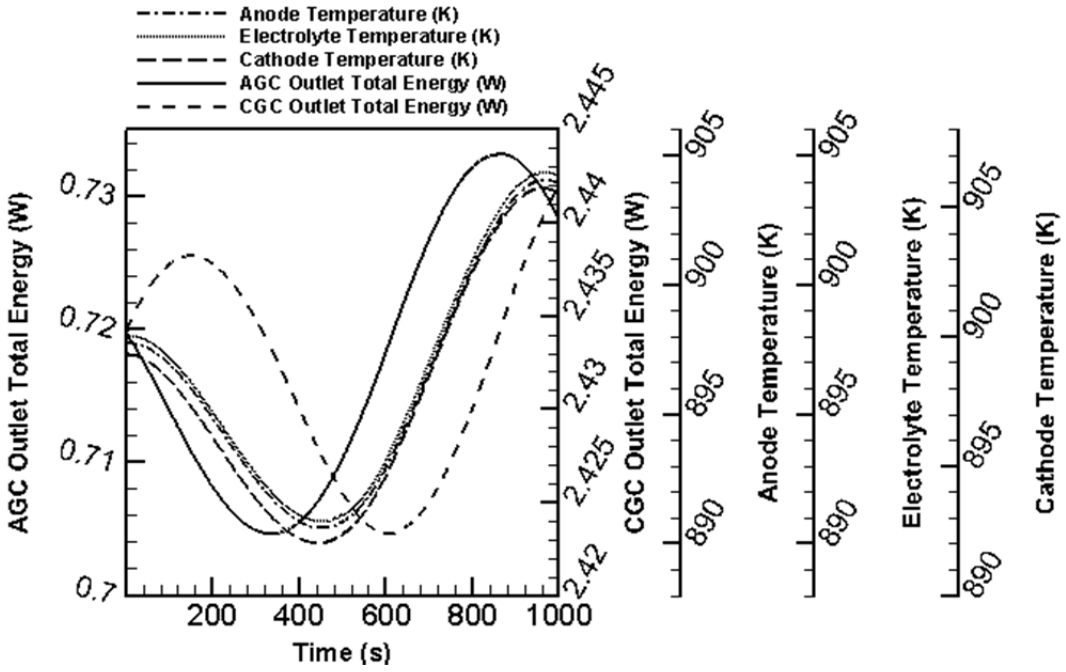

(e) 0.001 Hz

Figure 6.20: Dynamic response of electrolyte and electrodes' temperature and outlet energy corresponding to sinusoidal voltage perturbation during one sinusoidal cycle and over a wide range of impedance frequencies (10.0-0.001 Hz).

It may be observed that there is more complexity in the dynamic responses corresponding to the energy transport process. First of all, the electrolyte temperature does not exhibit exactly a sinusoidal shape at high frequencies (10 Hz and 1 Hz in Figures 6.20a and 6.20b). This simply indicates the fact that the heat conduction process in the electrolyte has the largest time scale and hence is the slowest thermal process in the unit cell. One may associate this with the heat conductivity or the heat capacity of the electrolyte. However, the sluggishness of this process can only be justified by Equation (6.15) which shows the largest value for the electrolyte time scale. Nonetheless, as the impedance frequency decreases, the electrolyte temperature dynamic response recovers the sinusoidal shape. Additionally, there are obvious phase shifts in all frequencies (Figure 6.20a-6.20d) for the four variables dynamic responses. Therefore, another simulation was carried out to examine the dynamic response with a much smaller frequency (0.001 Hz). The results are then presented in Figure 6.20e. Even at this small frequency, the

thermal characteristics of the unit cell do not show a rapid response to the voltage perturbation. Also, the local and bulk values of the investigated variables and parameters demonstrate different phase shifts indicating their different characteristic time scales. The phase shifts can be predicted to disappear at frequencies under 0.0005 Hz. This conclusion reveals the large time scale of the energy transport process to be 2500 sec. This great hindrance of the dynamic response, in comparison with the mass and charge transport processes, is primarily because of the high thermal capacity of the fuel cell. This finding can be beneficial for the design of the control systems for MCFC hybrid plants.

6.6.5 Extended Dynamic Response

So far, Figures 6.18, 6.19 and 6.20 have shown that the majority of the chemical and physical processes in an MCFC occur in the first second of the operation. Only the energy transport takes a longer time to reach its local equilibrium. Therefore, the same impedance simulation was extended for 20 cycles at a frequency of 10 Hz to study the dynamic responses of the various processes. This large frequency is required to capture the transient period. However, for the sake of comparison, only a few variables are selected for the extended-time study. Results are summarized in Figure 6.21a-6.21d.

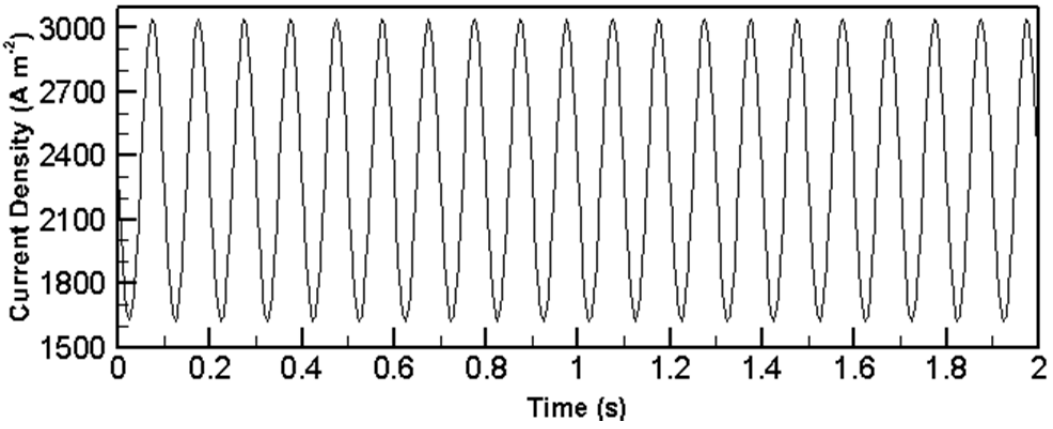

(a)

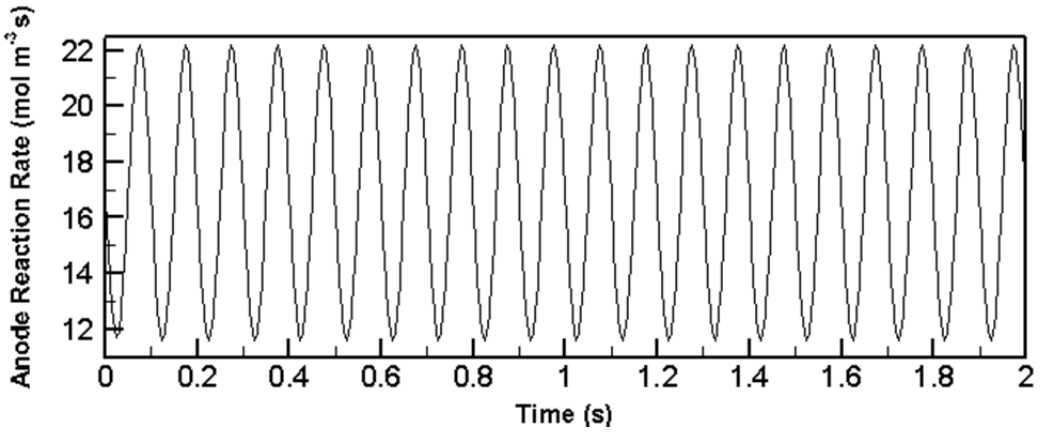

(b)

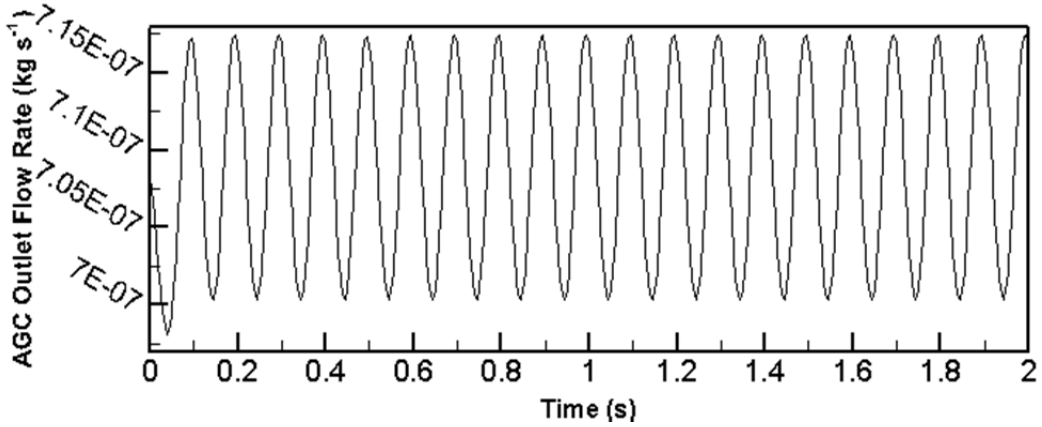

(c)

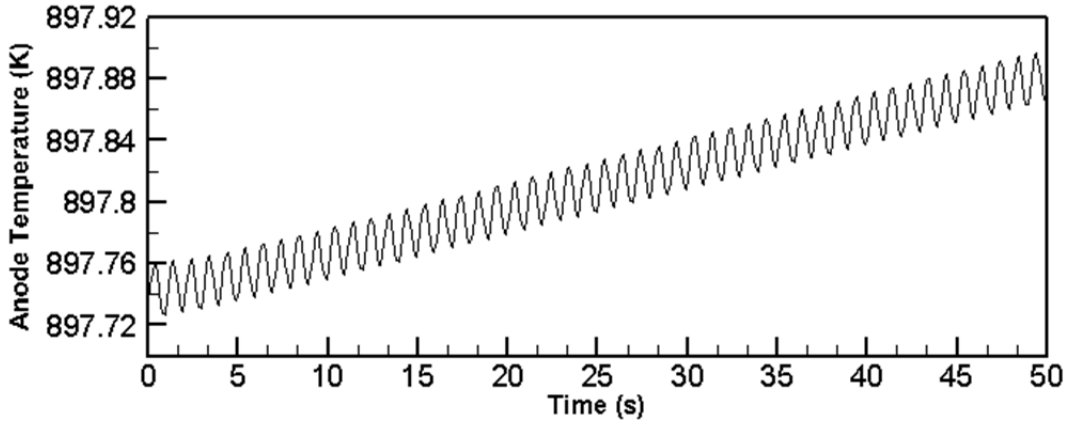

(d)

Figure 6.21: Time-extended dynamic response of a) average current density (at 10 Hz), b) anode reaction rate (at 10 Hz), c) AGC outlet mass flow rate (at 10 Hz) and d) anode temperature (at 1 Hz).

It may be observed that the cell average current density (Figure 6.21a) and anode reaction rate (Figure 6.21b) respond to the voltage fluctuation instantaneously without any obvious phase shift. On the other hand, the response of the AGC outlet mass flow rate (Figure 6.21c) is relatively slower. A 0.2 sec transition time is required for the outlet flow rate to reach the steady state condition. The last part of Figure 6.21 (d) demonstrates the anode temperature response for the first 50 cycles at the impedance frequency of 1 Hz. This lower frequency is necessary because the energy transport process is a much slower process. Figure 6.21d shows that the oscillation amplitude of the anode temperature increases instantly, and has a continuous growing trend throughout the operation time. This simulation was further continued for the next 1000 sec and the same rising trend was observed. Due to the enormous number of cycles over the extended operation time, the resulting graph is neither readable nor helpful. Thus, it is not included in this document.

In its place, a new simulation, with a linear voltage change in the beginning phase of the operation, was carried out and the results are demonstrated in Figure 6.22.

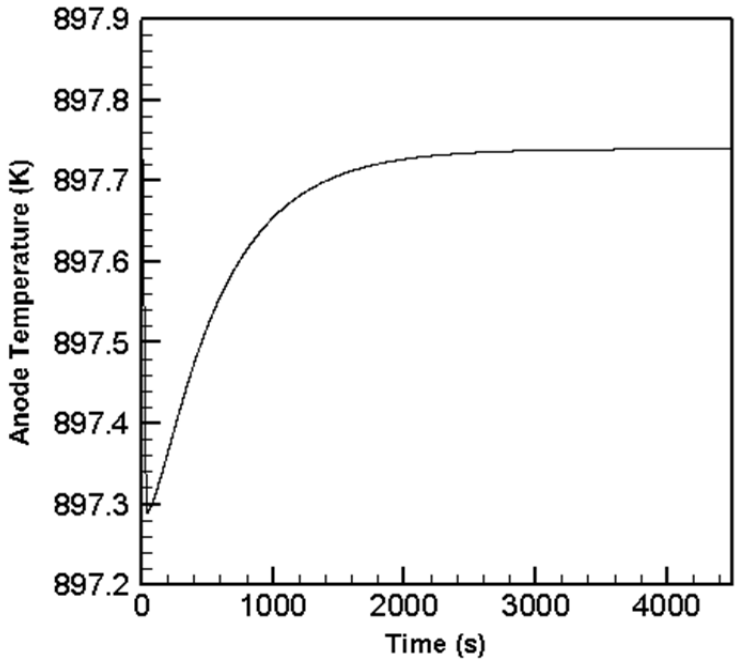

Figure 6.22: Linear dynamic response of the anode temperature to a small change (0.05 V) in the operating voltage.

This figure shows the anode temperature variation over a time period of 4500 sec. It confirms the previous conclusion (from Figure 6.20e) that the transition period of the energy transport process is about 2500 sec.

6.7 Start-Up Process Analysis

The presented mathematical model in this thesis not only evaluates the time scales of various transport processes in molten carbonate fuel cells, but also predicts the non-uniform distribution of field variables at any time of cell operation. In the previous section, it was found that MCFCs undergo physical and electrochemical processes with a wide range of time scales (from under milliseconds up to hours). On the other hand, MCFCs consist of components with a variety of length scales (from under millimetres up to centimeters). This combination of various spatial and temporal scales makes it tremendously difficult to conduct in-situ measurements. The most important advantage of a reliable numerical simulation over an actual experiment is that data such as the flow velocity, temperature, pressure and concentration can be measured precisely with a high temporal and spatial resolution. It would be either unfeasible or extremely difficult to obtain such detailed information in a real experiment.

Hence, this section provides a more detailed insight into the local variations of interdependent field variables in MCFC components at specified operating conditions. Some of the variables (e.g. average current density) are presented in steady state condition because of their slight variations. Table 6.2 summarizes the operating conditions and parameters utilized in the simulation cases.

Table 6.2: Operating conditions utilized for the start-up simulation.

Parameter	**Value**
Inlet molar fraction of hydrogen at AGC inlet	0.69
Inlet molar fraction of water vapour at AGC inlet	0.14
Inlet molar fraction of carbon dioxide at AGC inlet	0.17
Inlet molar fraction of carbon dioxide at CGC inlet	0.30
Inlet molar fraction of oxygen at CGC inlet	0.15
Inlet temperature (K)	853
Electrolyte filling degree in anode (mm)	0.31
Electrolyte filling degree in cathode (mm)	0.42
Operating cell voltage (V)	0.70
Operating absolute pressure (Pa)	101,325

6.7.1 Gas Flow Field

The heat and mass transfer processes are closely coupled to the gas flow behavior. Thus, the gas flow field needs to be understood. In Figure 6.23, the distribution of the gas phase gauge pressure and the flow streamlines are demonstrated at Plane 4 (in Figure 6.1). It may be seen that the anodic gaseous mixture flows from the anode towards the AGC. In addition, the gauge pressure declines as we move upwards.

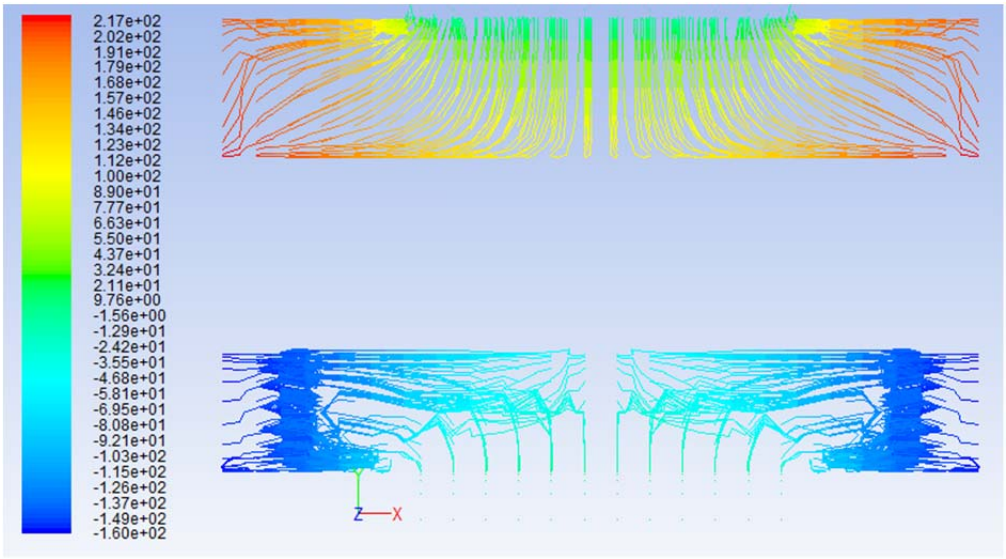

Figure 6.23: Pressure distribution (Pa) and flow stream lines within the simulated MCFC (anode and cathode only) at x-y cross section at Plane 4 at steady state.

This trend can be justified by taking into account the sink and source terms of the various gaseous species. For one mole of hydrogen consumed, one mole of carbon dioxide and one mole of water vapor are produced. Therefore, the accumulation of mass is higher within the anode which in turn leads to higher pressures and the above streamlines. In contrast, in the cathode side, the flow direction is from the CGC towards the cathode. The reason is that in the cathode, oxygen and carbon dioxide are depleted and no species is generated. Consequently, pressure drops through the cathode layer more significantly.

6.7.2 Transport of Gas Species

In accordance with Table 4.5, it is clear that all of the various source terms are directly related to the electrochemical reaction rates, evaluated by the Butler-Volmer equation. In addition, according to Equations (4.38) and (4.39), the rates of electrochemical reactions are strongly dependent on the local distribution of molar fractions. Therefore, it is very important to have an accurate prediction of the components molar fraction distribution in molten carbonate fuel cells.

Figures 6.24 to 6.28 show the start-up evolution of the species molar fraction distribution corresponding to the electrodes and gas channels. By now, it is understood that the time scales of species transport processes are on the order of 1 s. Therefore, in order to investigate the transient spatial distribution of molar fractions, six different cross sections are chosen (Planes 1, 2, 3, 4, 5 and 6 in Figure 6.1) and results are presented at 0.001 s, 0.01 s, 0.1 s, 1.0 s and 10 s.

6.7.2.1 Transport of Hydrogen

Figure 6.24 shows a slice plot view of the molar fraction distribution of hydrogen in the anode and anode gas channel. The x, y and z axis represent the width, height and length of the simulated molten carbonate fuel cell, respectively. The fuel gas flows from the right side of the figure towards the left. Then, hydrogen diffuses from the boundary under the gas channel (gas channel/anode interface) into the anode and then through the anode domain mainly due to a concentration gradient.

First of all, it is clear that the non-uniformity in the molar fraction is not considerable at t = 0.001 s (Figure 6.24a). However, in the gas channel inlet, some variations are observable. These changes are due to the inlet adjustments. An interesting result of Figure 6.24 is that until t = 0.1 s, the molar fraction of reactant increases along the gas channel, while the reverse was expected. One can justify this by considering the time scale analysis results in section 6.6. Accordingly, the anode electrochemical reaction time scale is much smaller than the species transport time scale. Consequently, the electrochemical reaction occurs instantly by consuming the reactant (hydrogen) which leads to a depletion in the molar fraction. Nonetheless, the hydrogen distribution finds a different pattern after t = 0.1 s (Figures 6.24c and 6.24d).

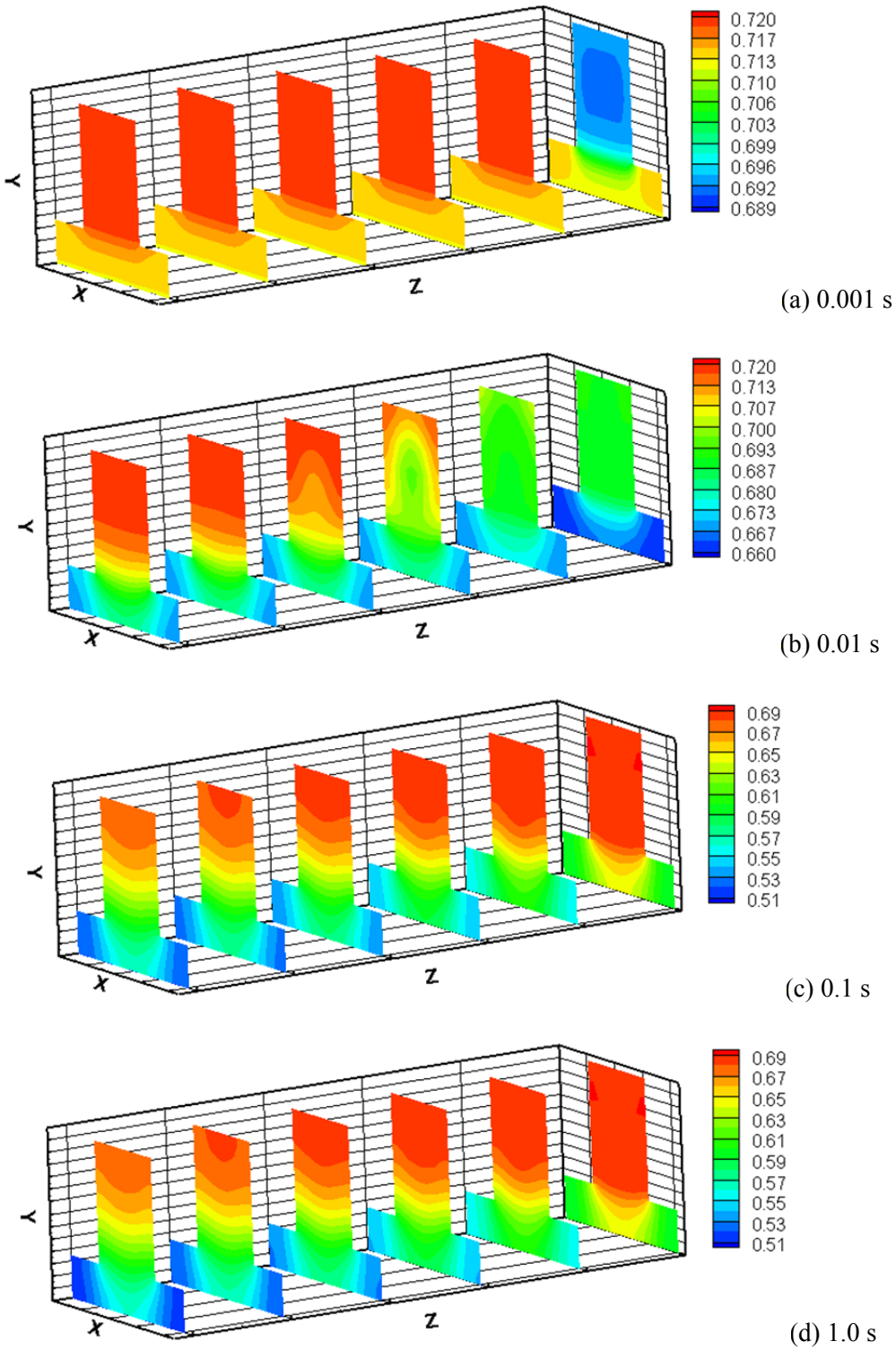

Figure 6.24: Transient variation of the hydrogen molar fraction at cross-sectional planes (z = 0 cm, z = 1 cm, z = 2 cm, z = 3 cm, z = 4 cm, z = 5 cm) within the anode and anode gas channel at 0.7 V: (a) t = 0.001 s, (b) t = 0.01 s, (c) t = 0.1 s, and (d) t = 1.0 s.

The reason is that both processes (electrochemical reaction and species transport) reach their local dynamic equilibrium after t = 0.1 s and the required amount of hydrogen for the electrochemical reaction is supplied. Since the electrochemical reaction takes place only within the electrode, the molar fraction of the electrode is lower in comparison with the gas channel. It may also be observed that the molar fraction within the anode is higher under the gas channel.

6.7.2.2 Transport of Water Vapour

The transport of water vapor (and carbon dioxide) in the anode and AGC is interconnected with the transport of hydrogen. In theory, there is one mole of water vapor produced for each mole of hydrogen molecules being consumed. Figure 6.25 illustrates the transient variation of the water vapor in the anode and AGC.

Similar to the hydrogen gas transport (Figure 6.25a), at t = 0.001 s, it is found that the water vapor molar fraction slightly increases at the inlet part of the gas channel because of the instantaneous electrochemical reaction and hence production of water vapor. At t = 0.1 s, when the gas transport reaches the steady state situation, it is expected to have higher values of the water vapor molar fraction under the gas channel. Nevertheless, the simulation results, represented in Figure 6.25, demonstrate the opposite. Inspecting the mass transport process and the electrochemical reaction rate can easily unveil the reason. After the instantaneous electrochemical reactions, when the water vapor molecules are generated, they need to be transferred to the AGC and then move towards the AGC outlet. This process takes a longer time for the water vapor molecules that reside at the sides of the anode electrode. The reason is that they have to pass a longer path to reach the anode/AGC interface boundary. Therefore, the mass transport process becomes the dominant and limiting factor in the whole process. This explanation emphasises the fact that the diffusion coefficient plays a crucial role for the gradient of gaseous species in the electrode.

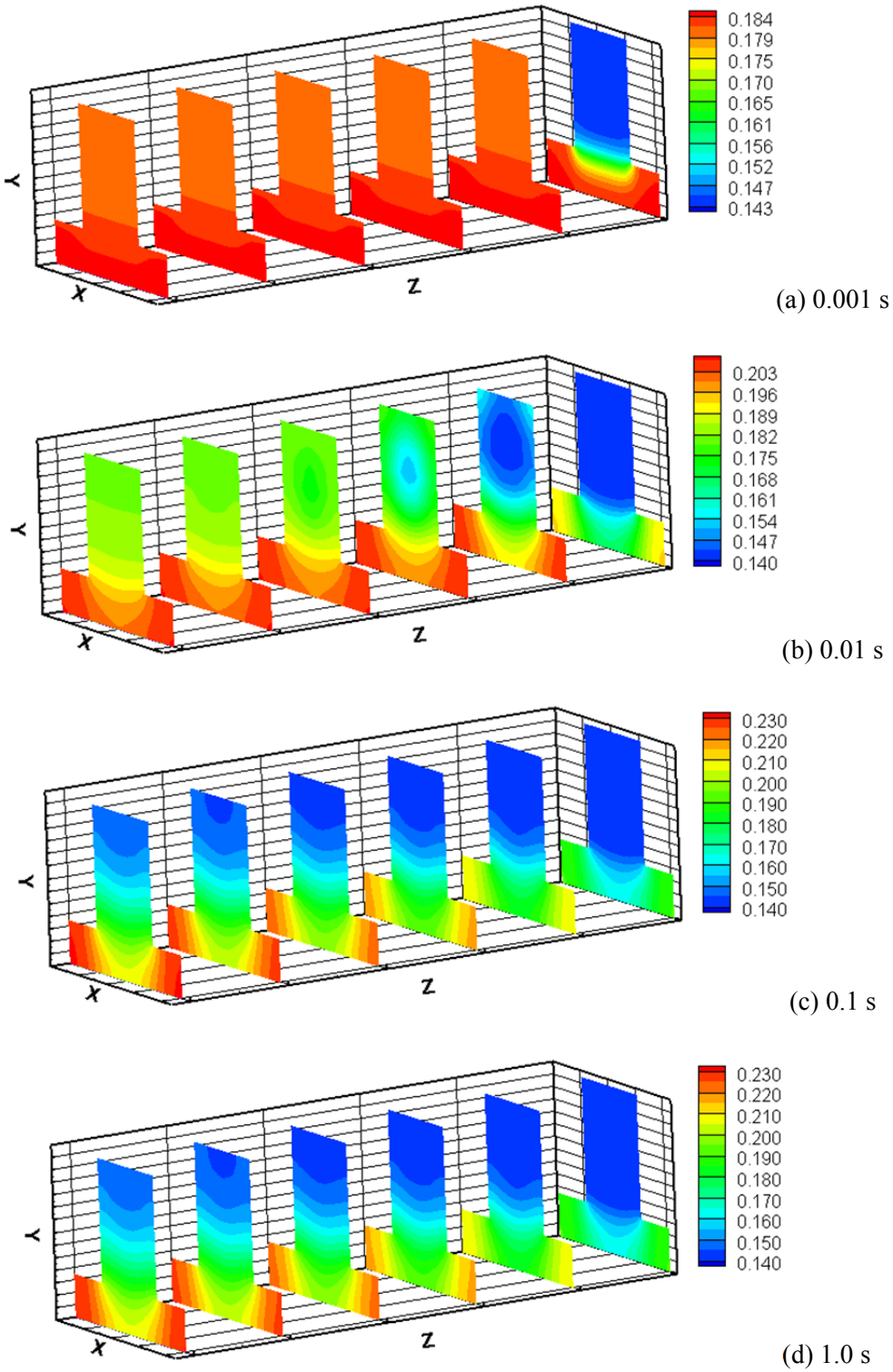

Figure 6.25: Transient variation of the water vapor molar fraction at cross-sectional planes (z = 0 cm, z = 1 cm, z = 2 cm, z = 3 cm, z = 4 cm, z = 5 cm) within the anode and anode gas channel at 0.7 V: (a) t = 0.001 s, (b) t = 0.01 s, (c) t = 0.1 s, and (d) t = 1.0 s.

6.7.2.3 Transport of Carbon Dioxide

Figures 6.26 shows a slice plot view of the molar fraction distribution of carbon dioxide in the anode and anode gas channel. Figure 6.27 also demonstrates the carbon dioxide distribution on the other side of the electrolyte, within the cathode gas channel and cathode.

Carbon dioxide is the only gaseous species that exists in both electrodes. It is a required reactant for the oxygen reduction reaction within the cathode which produces the carbonate ions. The carbonate ions migrate through the electrolyte layer towards the anode and combine with hydrogen, and as a result generate carbon dioxide. This process underlines the conservation of carbon dioxide. For one mole of carbon dioxide consumed in the cathode sub-domain, one mole of carbon dioxide is released in the anode sub-domain. Part (d) in Figures 6.26 and 6.27 is presented at t = 1.0 s when the mass transport process achieves its steady state situation. The former shows the molar fraction increasing from 0.17 up to 0.24 while the latter suggests the molar fraction decreasing from 0.30 down to 0.23. This result clearly suggests that the volume-averaged rates of the carbon dioxide production and consumption within the anode and cathode must be identical. In other words, the magnitudes of the anodic and cathodic volumetric current densities are the same.

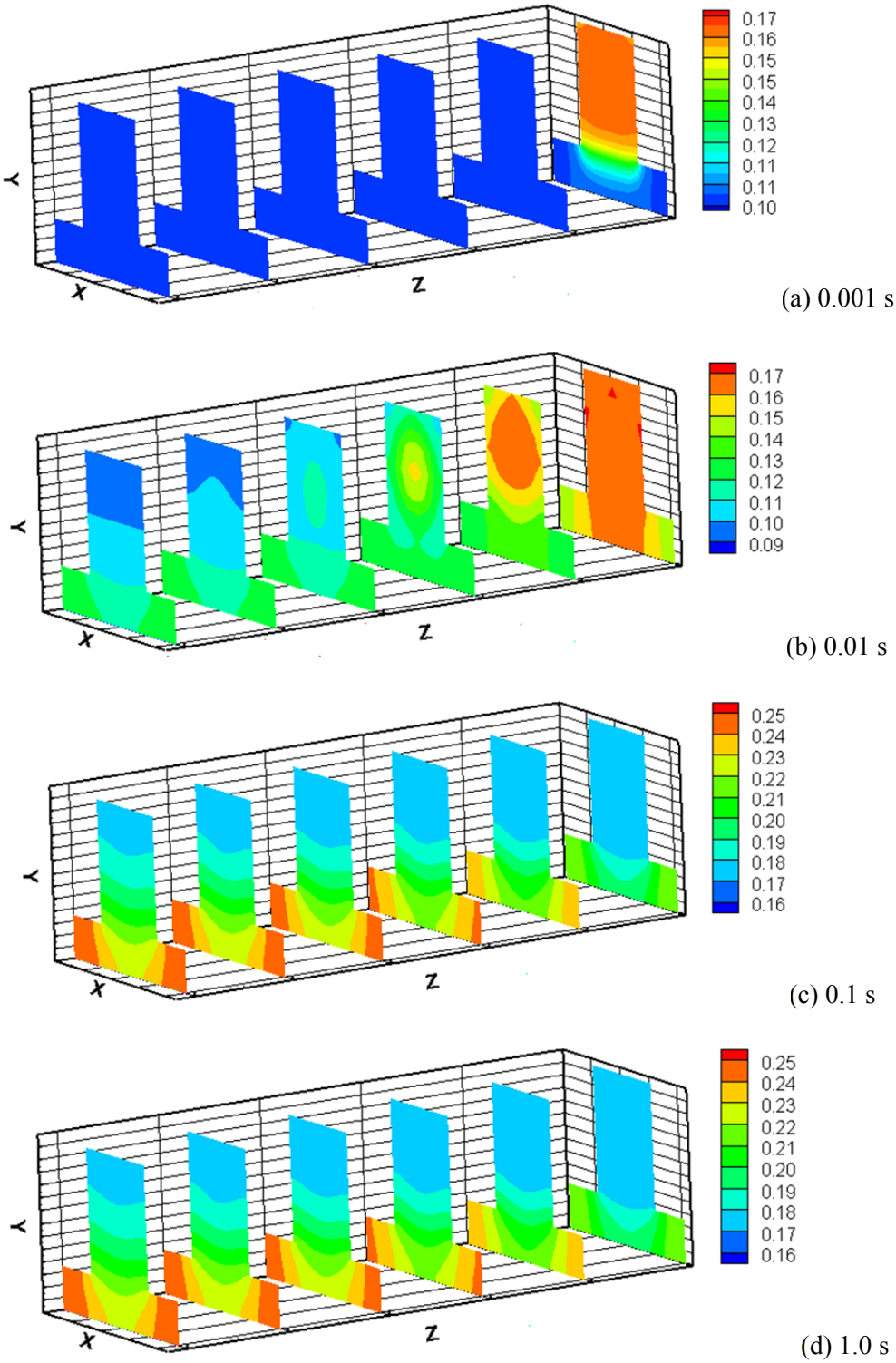

Figure 6.26: Transient variation of the carbon dioxide molar fraction at cross-sectional planes (z = 0 cm, z = 1 cm, z = 2 cm, z = 3 cm, z = 4 cm, z = 5 cm) within the anode and anode gas channel at 0.7 V: (a) t = 0.001 s, (b) t = 0.01 s, (c) t = 0.1 s, and (d) t = 1.0 s.

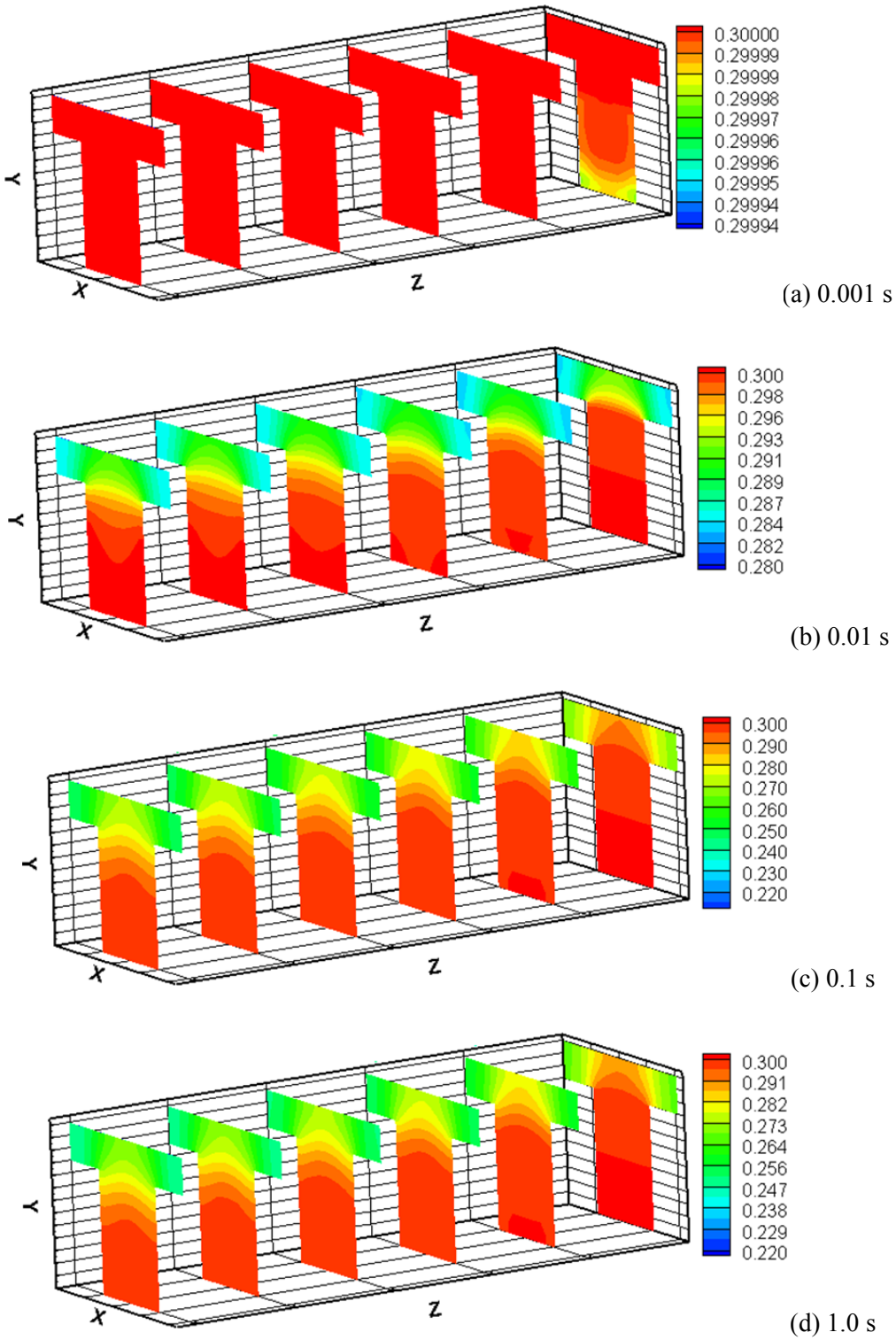

Figure 6.27: Transient variation of the carbon dioxide molar fraction at cross-sectional planes (z = 0 cm, z = 1 cm, z = 2 cm, z = 3 cm, z = 4 cm, z = 5 cm) within the cathode and cathode gas channel at 0.7 V: (a) t = 0.001 s, (b) t = 0.01 s, (c) t = 0.1 s, and (d) t = 1.0 s.

6.7.2.4 Transport of Oxygen

A cross-sectional distribution of oxygen molar fraction in the cathode and cathode gas channel is shown in Figure 6.28. Oxygen is consumed within the cathode, and so, its molar fraction decreases all the way from the channel inlet to outlet during the whole period. This is similar to the transient variation of the hydrogen molar fraction at the anode side (Figure 6.24). In addition, it can be seen that the molar fraction of oxygen decreases, from bottom to top of the respective sub-plots. This is due to the cathode reaction zone wherein the oxygen reduction reaction takes place. However, the rate of decline in the oxygen molar fraction is smaller compared to the carbon dioxide molar fraction (Figure 6.27). This observation agrees with the theory that induces half mole of oxygen being depleted per one mole of carbon dioxide being consumed.

An important outcome of this three-dimensional study is that the gas transport process is a fully three-dimensional process. It is difficult to predict this behaviour without having a 3D model. Clearly, the gradient in species molar fractions is observed along the thickness, width and length of the MCFC. However, larger variations can be seen along the y-direction which is attributed to the small thickness of the electrodes.

6.7.3 Transport of Electric Charge

In section 6.6, it was established that the electric charge transport has a very small time scale (10^{-6} – 10^{-4} s), pointing to the fact that this process occurs almost instantaneously. Thereby, the electric charge transport process reaches its steady state condition in the beginning of the fuel cell operation, and hence, the transient transport behavior has been neglected in this thesis. In fact, the corresponding results have an identical pattern at any operating time mentioned in section 6.7.2. Therefore, the results shown in this subsection are taken from t = 100 s which resemble the steady state simulation results.

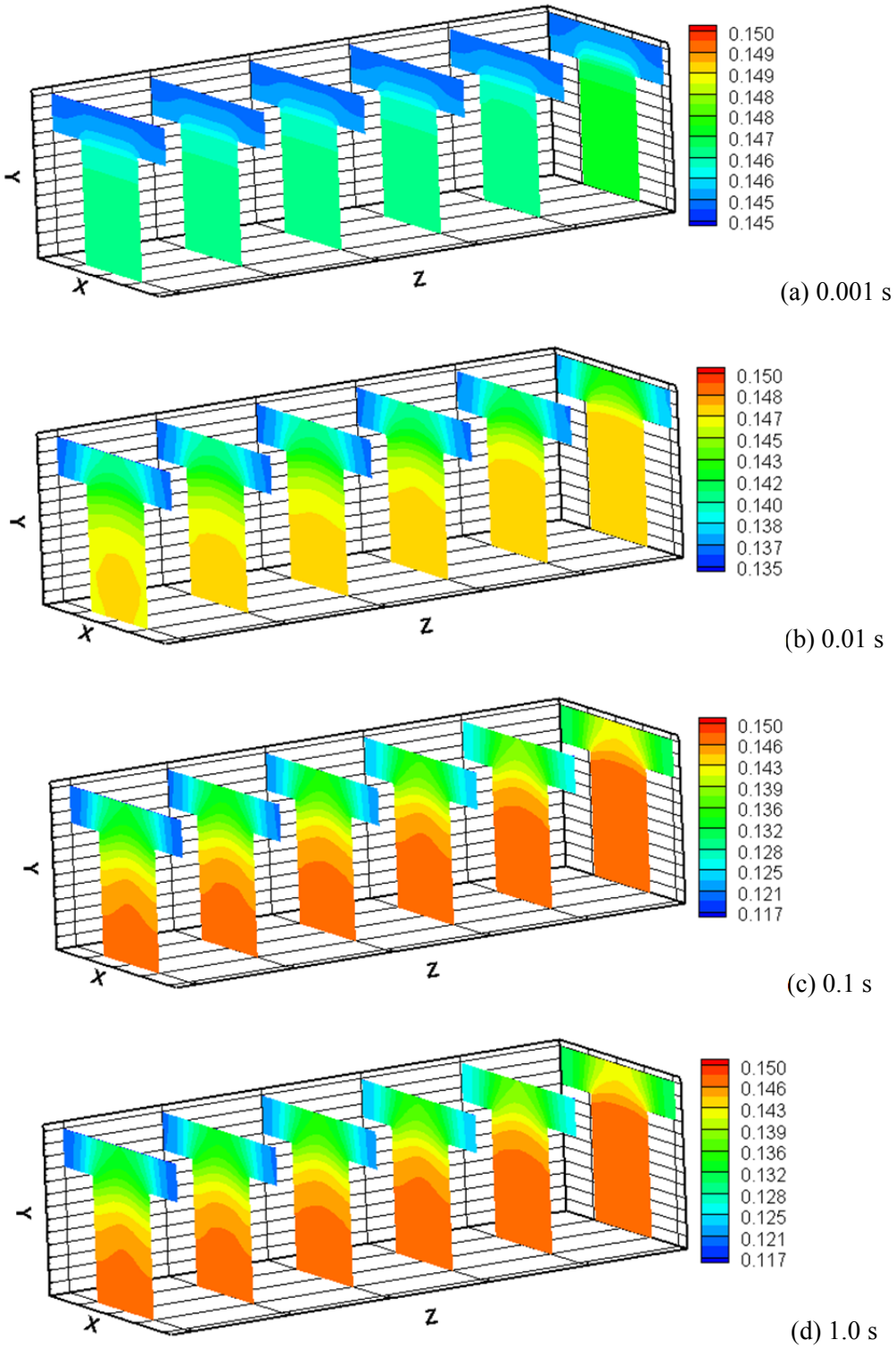

Figure 6.28: Transient variation of the oxygen molar fraction at cross-sectional planes (z = 0 cm, z = 1 cm, z = 2 cm, z = 3 cm, z = 4 cm, z = 5 cm) within the cathode and cathode gas channel at 0.7 V: (a) t = 0.001 s, (b) t = 0.01 s, (c) t = 0.1 s, and (d) t = 1.0 s.

6.7.3.1 Distribution of Electronic Potential

A 2D steady-state contour plot, demonstrating the distribution of the electronic potential at z = 0.03 cm (Plane 4 in Figure 6.1), is shown in Figure 6.29. Parts (a) and (b) represent the anode and cathode part of this plot. The horizontal-axis represents the width while the vertical-axis represents the thickness of the electrode.

Part (a) of this figure illustrates that the magnitude of the electronic potential increases as we move from the top to the bottom of the anode. This simply verifies the direction of the current flow which is from the bottom to the top of the anode electrode. In fact, the generation of the electrons in the anode triple-boundary phases causes the electronic potential gradient, and hence the over-potential which turns to a driving force for the electron transport process. Moreover, the distribution of the electronic potential exhibits a non-uniformity along the thickness and width of the anode. This can be attributed to the simultaneous transport and production of electrons in the anode electrode. It can also be seen that the electronic potential has the minimum value under the land and the maximum occurs under the gas channel. Besides, there is an obvious region under the gas channel with almost uniform distribution. In other words, as we move from the sides towards the center of the anode, the electronic potential gradient along the thickness (y-direction) decreases and finally vanishes in the center. This non-uniformity can be justified by taking into consideration the direction of the current flow. The generated electrons have to leave the anode zone in order to complete the current cycle. However, they cannot leave through the gas channel/electrode interface, because there is no electron-conductor medium in the gas channel. Therefore, the only viable option is to move towards the land. Consequently, it is seen that the potential varies more significantly under the land than under the channel.

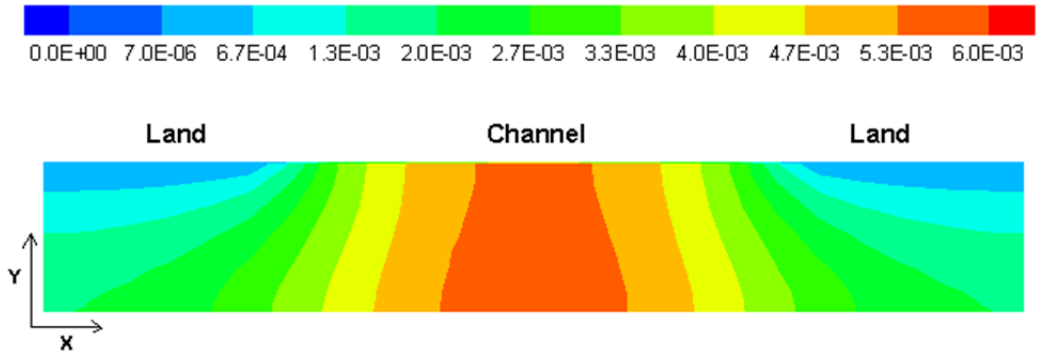

(a)

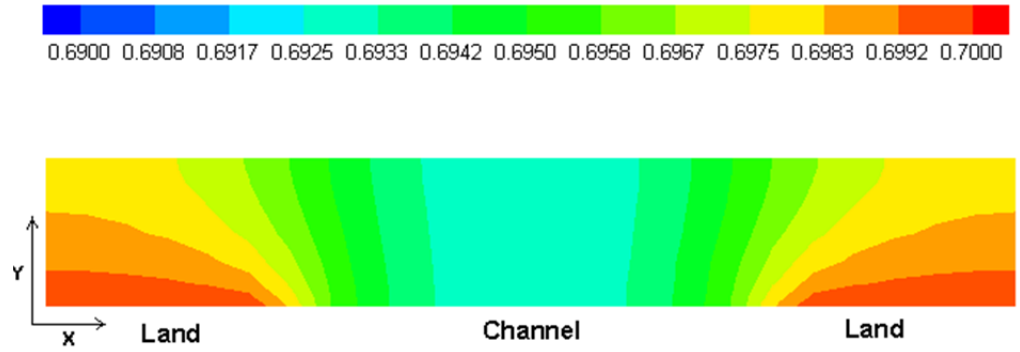

(b)

Figure 6.29: 2D slice plot showing the distribution of the electronic potential, ϕ_s (V), at Plane 4: (a) anode, (b) cathode. The operating voltage is 0.7 V.

Figure 6.29b, shows the electronic potential distribution in the cathode sub-domain. In contrast to the anode (Figure 6.29a) sub-domain, the electronic potential becomes maximal at the land and reduces as we move towards the cathode/electrolyte interface. It can be concluded that the current flow direction in the cathode is from the electrode towards the electrolyte. On the other hand, similar to the anode zone, the electronic potential variation under the channel is not detectable.

6.7.3.2 Distribution of Ionic Potential

Unlike the electronic potential, the ionic potential is present in the electrolyte. In fact, all three domains (anode, electrolyte and cathode) are ion-conducting materials. Therefore, Figure 6.30 shows a 2D contour plot of the ionic potential distribution within the anode (a), electrolyte (b) and cathode (c).

First of all, it is obvious that the variation of the ionic potential through the whole domain is much higher than the variation of electronic potential (Figure 6.29). The magnitude of the ionic potential becomes maximal in the cathode and decreases as we move towards the electrolyte and then anode. In addition, the ionic potential gradients are obvious along the thickness, while the horizontal variations are negligible. This is in contrast to the electronic potential (Figure 6.29). It is also interesting to see that there are three different potential distribution patterns within the anode, electrolyte and cathode. For instance, the variations within the electrolyte sub-domain (Figure b) are almost linear. The ionic potential declines from the cathode/electrolyte interface towards the electrolyte/anode interface. This linearity spreads out into a region of the anode which is closer to the electrolyte. However, the corresponding contours demonstrate a curvature at the top section of the anode. Finally, the cathode sub-domain consists of a constant-potential region accompanied by a region with linear potential variation.

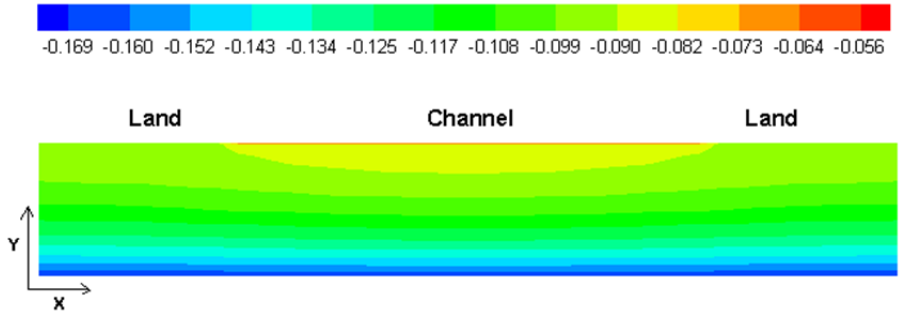

(a)

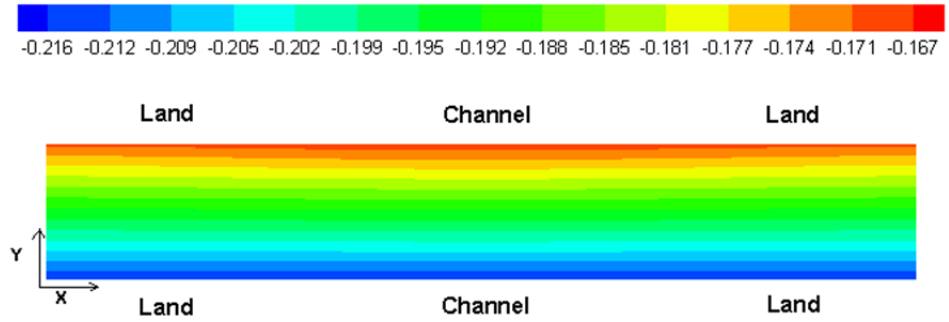

(b)

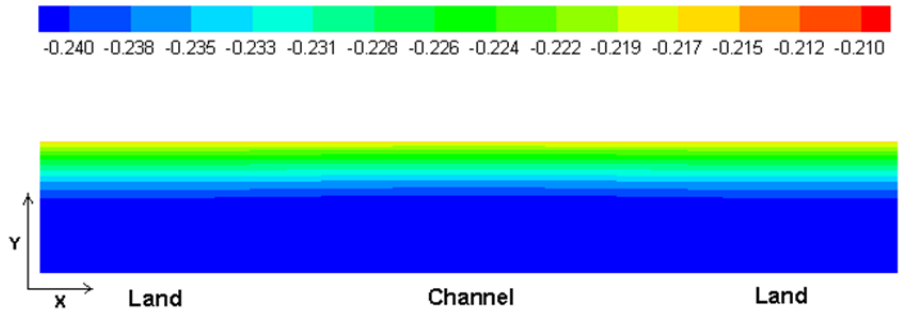

(c)

Figure 6.30: 2D slice plot showing the distribution of the ionic potential, ϕ_e (V), at Plane 4: (a) anode, (b) electrolyte, (c) cathode. The operating voltage is 0.7 V.

6.7.3.3 Distribution of Current Density

When the electrons and ions diffuse through the solid electrodes and liquid electrolyte, two types of current flow (A) occur, namely the electronic current flow and ionic current flow. By dividing these values by the cross-sectional area that they flow through, a new variable is obtained, named current density (A m^{-2}). Thereby, in a molten carbonate fuel cell, electronic current density (J_s) and ionic current density (J_e) are caused by the diffusion of the electrons and carbonate ions through the solid electrodes and liquid electrolyte. Here, s and e represent the medium that the current flows through, solid electrode and electrolyte.

It should be noted that current density is a vector quantity and only the transverse component (y-direction) contributes to the power output. Hence, in this study, only the y-component is presented. The transverse components of the current densities are evaluated after each iteration (or time step in transient simulation) by:

$$J_s^y = -\sigma \frac{\partial \phi_s}{\partial y} \tag{6.16}$$

$$J_e^y = \kappa \frac{\partial \phi_e}{\partial y} \quad . \tag{6.17}$$

The total current density at each point is simply the summation of the electronic and ionic current density. Thereby, it is calculated by:

$$J^y = J_s^y + J_e^y \quad . \tag{6.18}$$

The above variables represent the local current densities. Apparently, in the anode and cathode, both the electronic and ionic currents coexist. In contrast, the electrolyte conducts only the ionic current.

Figure 6.31 shows a 2D contour plot, demonstrating the electronic, ionic and total current density distribution within the anode sub-domain at z = 0.03 cm (Plane 4 in Figure 6.1) for the operating voltage of 0.7 V (or approximately at 2000 A m^{-2}). It can be seen that there is a wide range of variation in electronic current density in the anode (Figure a). Accordingly, the

electronic current density at the electrolyte/anode interface is zero which means there is no electron flow through this boundary. The same pattern applies to the anode/channel interface. On the contrary, the area under the land exhibits higher current densities. Specifically, there are two spots at the corners which represent the maximum electronic current density. The reason for this non-uniform distribution can be disclosed if one considers the direction of the flow of electrons. It was previously shown that the electrons move from the bottom of the anode towards the upper sides. The electrons residing under the gas channel cannot enter the gas channel. Therefore, they choose the closest conducting part to move through, which is the small region at the corners (at the land). Consequently, this area receives additional electrons compared to the other part of the land. This means that a higher amount of current flows through a constant surface area which leads to a higher current density.

Figure 6.31b illustrates the ionic current density distribution within the anode. It is clear that the non-uniformity is decreased in comparison with the electronic current density (Figure 30a). The only reason is that carbonate ions are consumed at the triple-phase boundaries within the anode sub-domain and cannot pass the upper boundaries. Thus, the ionic current density at the anode/channel interface as well as the land area is zero. As we go down towards the electrolyte, the ionic current density increases and finds its maximum value at the electrolyte/anode interface. Unlike Figure 6.31a, variations exist only in the y-direction. However, the parameter of interest in fuel cells is the total current density which is shown in Figure 6.31c. It may be observed that the only region with zero current density is at the anode/channel interface. The majority of the anode sub-domain lies within the 1,000-3,500 A m^{-2} range, with an average current density of 2,000 A m^{-2}.

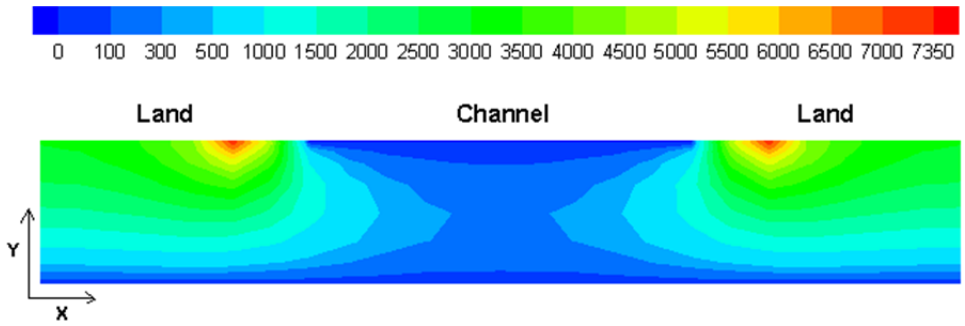

(a)

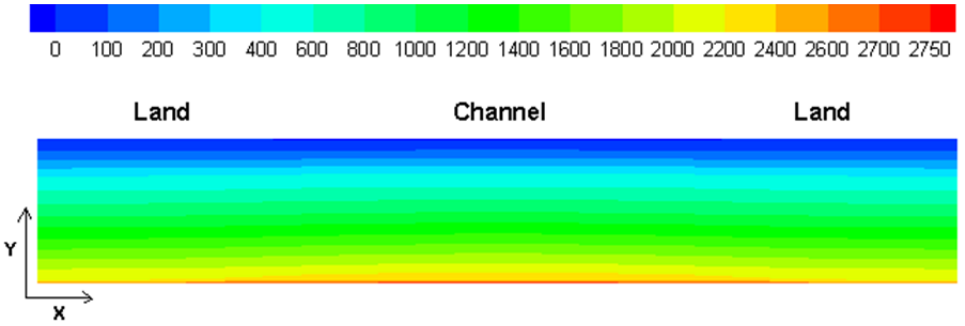

(b)

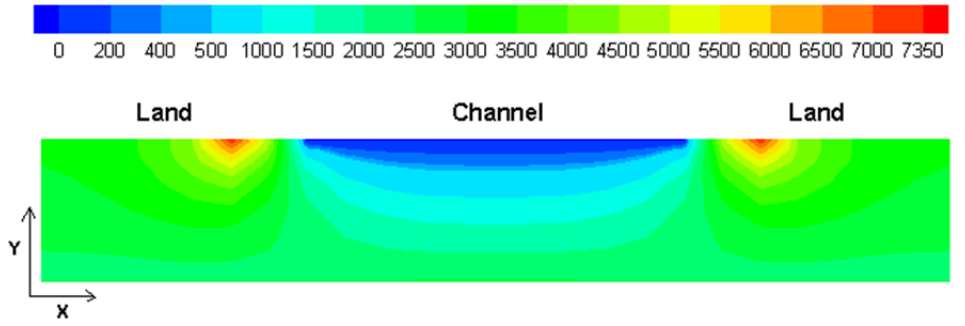

(c)

Figure 6.31: Distribution of the transverse component of the average current density, J^y (A m^{-2}), in anode, at Plane 4: (a) electronic current density, J_s^y, (b) ionic current density, J_e^y, and (c) total current density, $J^y = J_s^y + J_e^y$. The operating voltage is 0.7 V.

Figure 6.32 shows a 2D contour plot, demonstrating the electronic, ionic and total current density distribution within the cathode sub-domain at z = 0.03 cm (Plane 4 in Figure 6.1) for an operating voltage of 0.7 V (or approximately at 2000 A m^{-2}). All three current densities show behaviour similar to the anode current densities. According to Figure 6.32a, the electronic current density increases from the electrolyte/cathode interface towards the cathode gas channel and finds its maximum value at the land area. Obviously, electrons are not allowed to penetrate the electrolyte. As a result, the electronic current density is zero at the electrolyte/cathode interface. In addition, because no electrons can be supplied into the cathode area through the channel/cathode interface, the region under the gas channel shows the lowest electronic current density.

In contrast, the distribution of the ionic current density (Figure 6.32b) is opposite to that of the electronic current density. It declines from the electrolyte/cathode interface towards the gas channel and drops to zero at the lower boundaries of the cathode sub-domain.

The total current density within the cathode sub-domain is also shown in Figure 6.32c which demonstrates a distribution similar to Figure 6.31c. Another reason for the higher current density at the corners, in comparison with the rest of the land area, could be due to the reactants availability. Clearly, the molar fraction of the reactants is higher at the corners which in turn can produce more current.

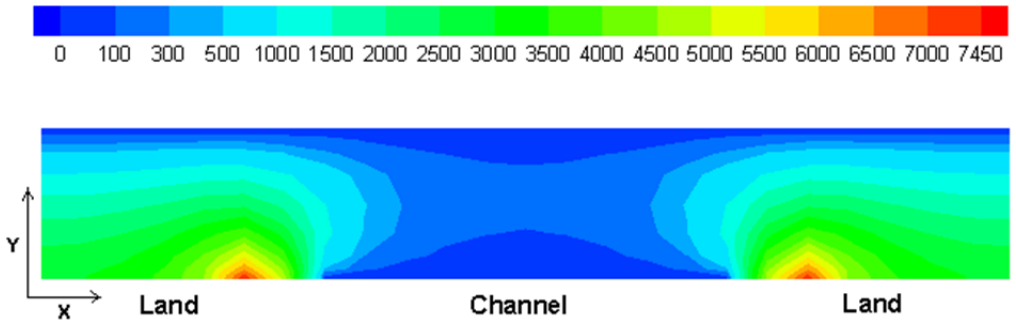

(a)

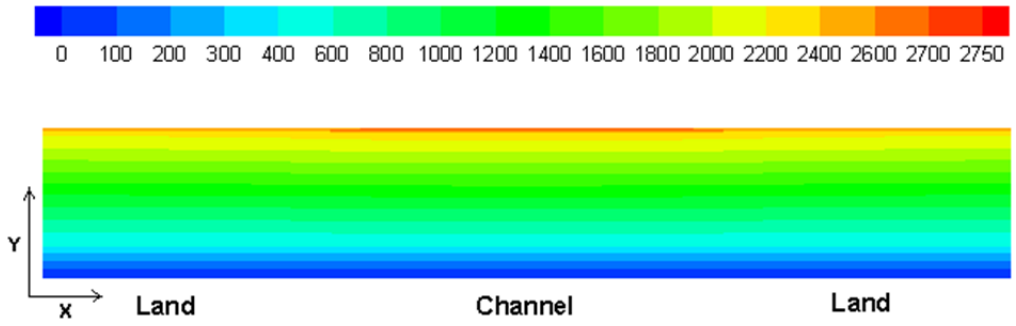

(a)

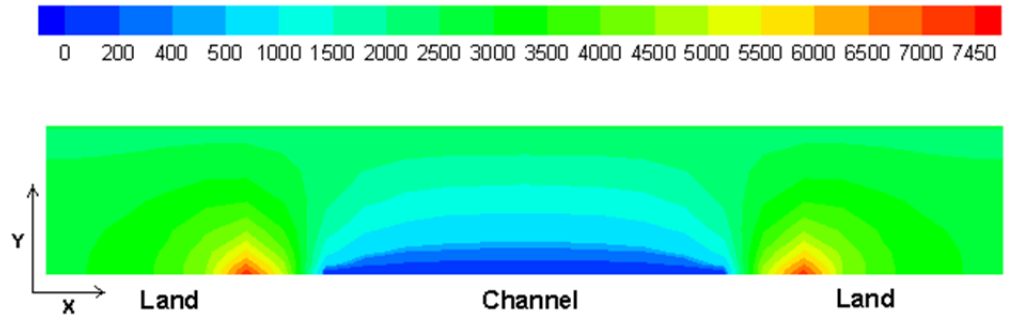

(c)

Figure 6.32: Distribution of the transverse component of the average current density, J^y (A m^{-2}), in cathode, at Plane 4: (a) electronic current density, J_s^y, (b) ionic current density, J_e^y, and (c) total current density, $J^y = J_s^y + J_e^y$. The operating voltage is 0.7 V.

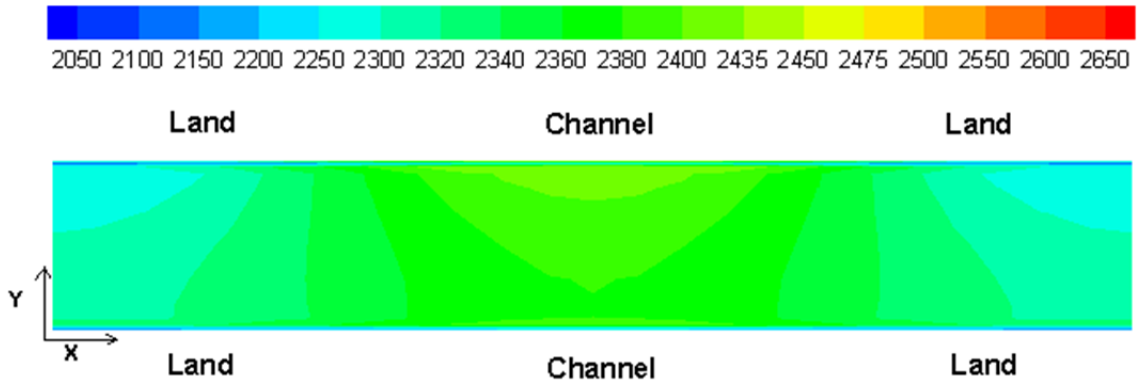

Figure 6.33: Distribution of the transverse component of the average current density, J^y (A m^{-2}), in electrolyte, at Plane 4. The operating voltage is 0.7 V.

6.7.3.4 Electrochemical Reaction Rates

Figure 6.34 demonstrates the volumetric current density across the anode (Figure 6.34a) and cathode (Figure 6.34b) at an operating cell voltage of 0.7 V. It was previously shown (Chapter 4) that the volumetric current density can be used to find the rate of electrochemical reactions. It may be observed that the variation of the electrochemical reaction rates along the length (z-direction) of the fuel cell is not considerable. Even though some small changes can be seen within the cathode, the anode layer shows a completely constant rate. In contrast, the reaction rates show a non-uniform profile along the width (x-direction) of the unit cell, especially as we move from the electrode/electrolyte interface towards the gas channels. However, the highest variations occur along the thickness (y-direction). These observations explain the fact that the electrochemical reaction is a two-dimensional process with more variation along the thickness. Increasing the thickness provides higher active surface area, and hence higher reaction rate, but may lead to larger ohmic loss which is not desirable. This implies that the electrode thickness is a crucial design parameter.

Figures 6.34a and 6.34b show that the distribution of the volumetric current density is more broadly distributed from the interface adjacent to the electrolyte throughout the electrode. The highest values of the reaction rates occur at the electrode/electrolyte interface for both electrodes (anode/electrolyte and cathode/electrolyte interfaces). This might be because of the potential difference (or over-potential) at these boundaries which drives the electrochemical reactions in the electrodes faster.

On the other hand, it is known that for any kind of reaction mechanism, the electrochemical reaction rate is related to the reactant availability. The Butler-Volmer formulation is derived based on this fact. By looking back to Figures 6.24 to 6.28, it is obvious that the molar fraction of the reactants decrease from gas channel towards the electrolyte while the reaction rate exhibits the opposite behaviour/trend. This simply suggests that the electrochemical reaction rate is controlled by the over-potential, not by the reactants' molar fraction. In other words, over-potential plays a more significant role. This can be explained by the Butler-Volmer equation which has an almost linear relation to the molar fractions while it uses the over-potential in exponential form.

6.7.3.5 Distribution of Over-potential

Figure 6.35 demonstrates a contour plot of the over-potential distribution within the anode (Figure 6.35a) and cathode (Figure 6.35b) of the simulated MCFC at an operating cell voltage of 0.7 V. The over-potential is the driving force for the occurrence of the electrochemical reactions. Figure 6.35a shows that, within the anode layer, the over-potential ranges from 0.07 to 0.17 V. Therefore, there is roughly a 0.1 V change along the thickness. On the other hand, Figure 6.35b exhibits a narrower range, from -0.13 to -0.175 V. In addition, it can be seen that the average magnitude of the over-potential is higher in the cathode compared to the anode.

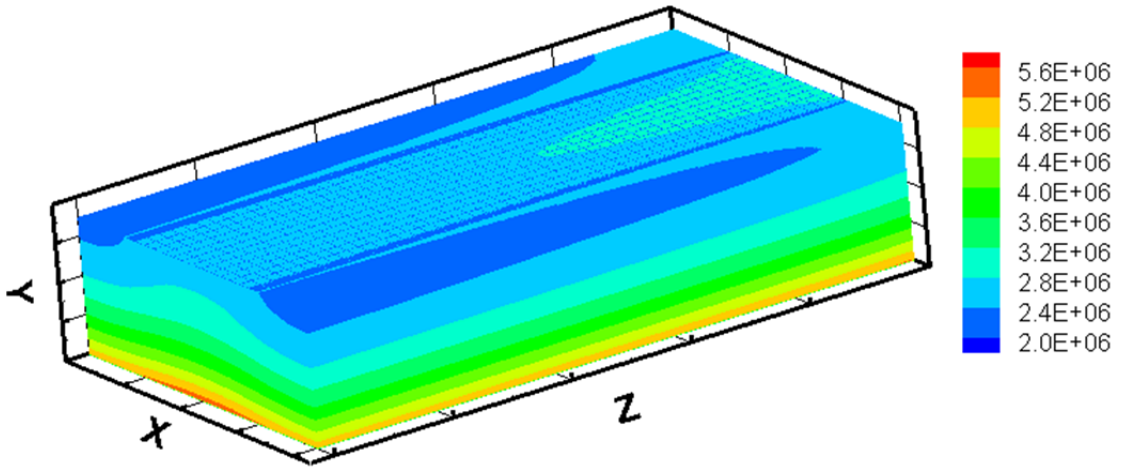

(a)

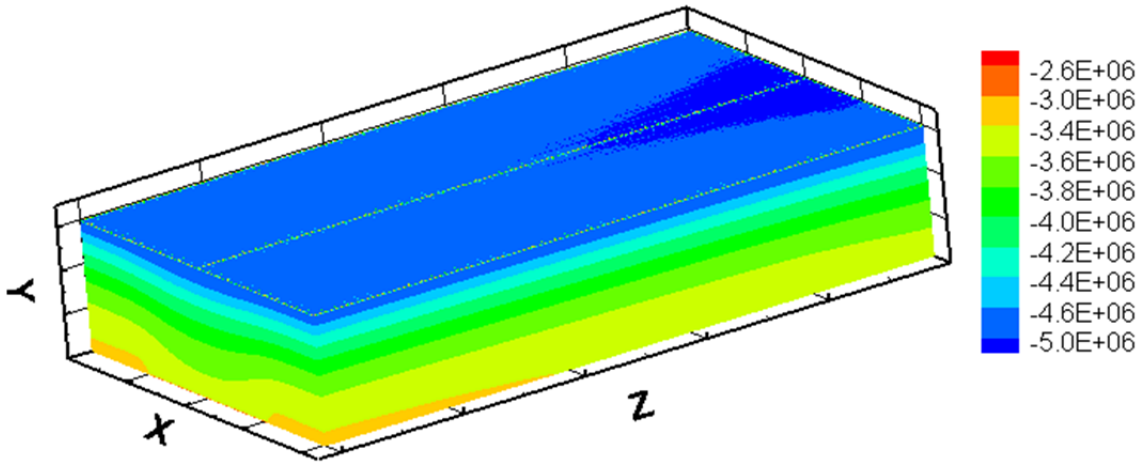

(b)

Figure 6.34: Distribution of the volumetric current density, R_i (A m^{-3}), within the: (a) anode (R_a), (b) cathode (R_c). It is related to the electrochemical reaction rate by: R_i/nF. The operating voltage is 0.7 V.

Consequently, it may be understood that the anodic reaction can take place with smaller values of the over-potential while the cathodic reaction requires higher over-potential. This helps to realize the bigger tendency towards reaction occurrence within the anode. This finding can justify the difference in reactant molar fractions within the anode and cathode in the early stage

of fuel cell operation (at t = 0.001 s) in Figures 6.24a and 6.27a. Clearly, Figure 6.24a suggests that the hydrogen molar fraction within the anode drops approximately 0.03 from the inlet towards the outlet while this change for carbon dioxide within the cathode (Figure 6.27a) is only 0.0001. Obviously, the variation within the anode is two orders of magnitude larger than within the cathode. Therefore, the hydrogen oxidation reaction can occur faster in comparison with the oxygen reduction reaction and a very small over-potential is adequate to start the reaction.

6.7.4 Transport of Heat Energy

To further evaluate the start-up process of the simulated MCFC, an analysis of the temperature distribution within the various components of the fuel cell is conducted. Therefore, the transient variation of the local temperature, along the three directions of the cell is demonstrated in Figure 6.36.

The energy transport process is the most complex process of the MCFC. Unlike the other phenomena that occur inside an MCFC, the energy transport is the only process that takes place within all sub-domains and crosses the interface boundaries. Additionally, as elucidated in the dynamic response analysis (section 6.6.4), the energy transport is the slowest process with a large time scale. For this reason, a larger time frame (0.1 s – 1000 s) is chosen to analyze this process. It is also influenced by the thermal conductivity and the specific heat capacity of the gaseous and solid materials. Furthermore, the various mechanisms of heat generation or consumption have a significant impact on the temperature distribution. Therefore, for the interpretation of the Figure 6.36 all these factors need to be considered.

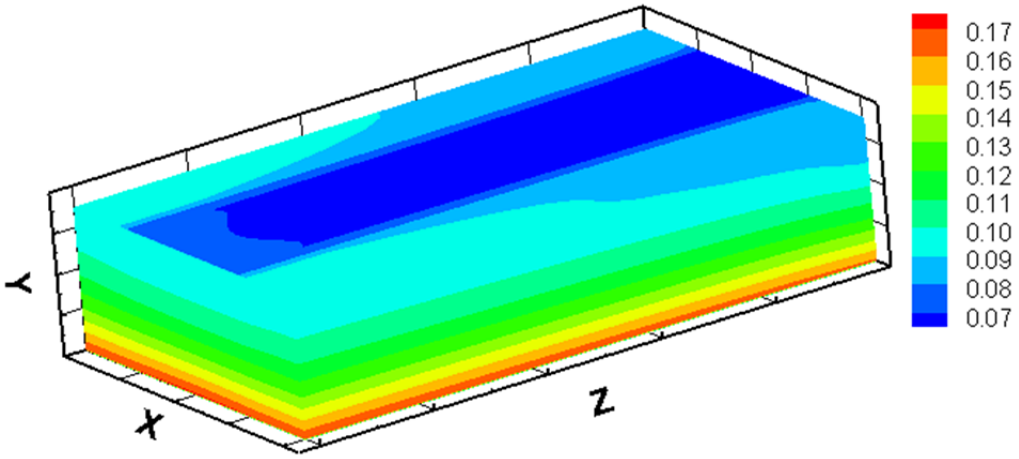

(a)

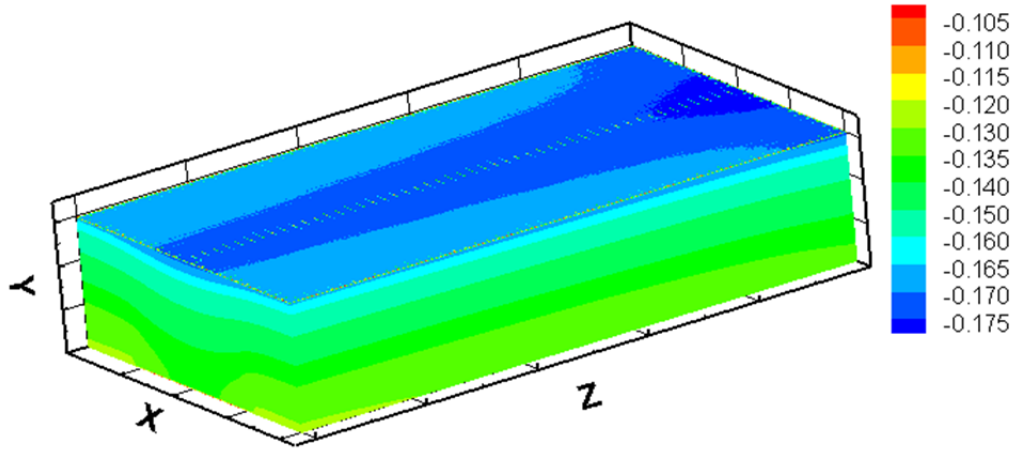

(b)

Figure 6.35: Distribution of the over-potential, η (V), within the: (a) anode (η_a), (b) cathode (η_c).The operating voltage is 0.7 V.

First of all, it can be seen that the gas channel temperature is not significantly altered in the first three parts (Figures 6.36a, 6.36b, 6.36c). In other words, the amount of heat, transferred from the electrode-electrolyte assembly to the gas channels, in the first 10 s of the cell operation, is not significant. In addition, it is clear that the gaseous mixture at the cathode side has a relatively higher temperate in comparison with the anode side. Nevertheless, this pattern is

changed after some time (Figures 6.36d and 6.36e). Clearly, the anode gas shows a higher temperature. One may conclude that the reversible and irreversible heat generation and consumption mechanisms of the cathode and anode are dominant in the first 10 s while the heat conduction from the solid materials to the gas phase is not considerable. However, after about 10 s, the effect of heat conduction gradually increases which in turn elevates the gas temperature.

It may be understood that the cathode sub-domain shows the highest temperature at any time during the cell operation. The temperature difference between the cathode and other components is constantly increased during the operation time. As previously stated (in Chapter 4), three kinds of heat sources exist within the MCFC electrodes, namely the reversible heat due to the electrochemical reactions, irreversible or activation heat generation, and ohmic (or joule) heating. The activation and ohmic heating seem to have approximately the same impact within the anode and cathode because of their similar electric conductivity and voltage losses. This fact does not apply to the reversible heat as the anodic electrochemical reaction is an endothermic process while the cathodic reaction is exothermic. However, this is not the only reason for the temperature difference between the cathode and anode. It is important to consider the effects of thermal conductivity and specific heat capacity. Nickel oxide has the lowest thermal conductivity (0.9 W m^{-1} K^{-1}) among the MCFC components which hinders the heat conduction throughout the cathode sub-domain. On the other hand, the specific heat capacity has the same order of magnitude for the anode, cathode and electrolyte materials (~ 4000 – 4500 J kg^{-1} K^{-1}). In essence, it becomes clear that the heat conductivity plays a major role in the thermal management of the molten carbonate fuel cell. Increasing the thermal conductivity of the cathode material will facilitate the process of heat transport throughout the cell. This may also be accomplished by lowering the effects of heat conduction by means of a cathode material with a smaller thickness.

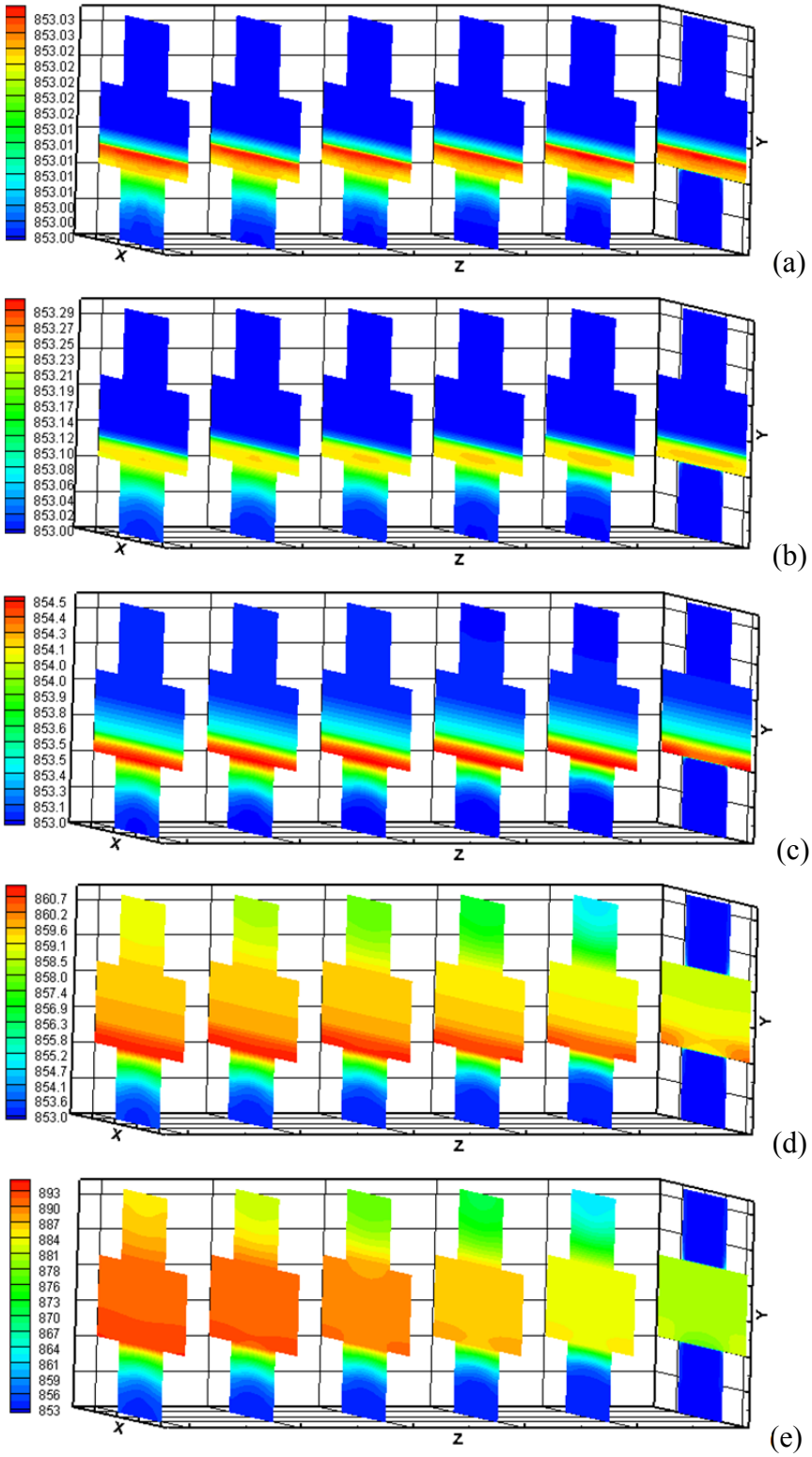

Figure 6.36: Transient variation of the temperature at cross-sectional planes (z = 0 cm, z = 1 cm, z = 2 cm, z = 3 cm, z = 4 cm, z = 5 cm) within the gas channels, electrolyte and electrodes at 0.7 V: (a) t = 0.1 s, (b) t = 1.0 s, (c) t = 10 s, (d) t = 100 s, and (e) t = 1000 s.

Figure 6.36 also demonstrates that the energy transport process within the MCFC can be considered two-dimensional. No significant variation can be seen along the width (x-direction) because of its small scale. Even though the height of the cell is small also, there are different materials along y-direction with different properties. Therefore, the temperature variation cannot be neglected. The temperature variation along the fuel cell length shows the highest change, about 6 K.

6.8 Thermodynamic Analysis

In this section, a number of parametric studies were conducted in detail with the intention of estimating the performance of the molten carbonate fuel cell at different operating conditions. Using equations provided earlier, energy and exergy efficiencies of the unit cell were obtained. In addition, the entropy generation is investigated in some cases. In general, molar fractions of hydrogen, water vapour and carbon dioxide were considered to be 0.72, 018 and 0.1, respectively. Likewise, oxygen and carbon dioxide molar fractions were chosen to be 0.33 and 0.67. Anodic and cathodic gas flow rates are 1.66 mol h^{-1} and 2.04 mol h^{-1}, respectively, unless otherwise stated. The variations of cell energy and exergy efficiencies at different operating temperature (ranging from 883 K to 963 K) are presented in Figure 6.37.

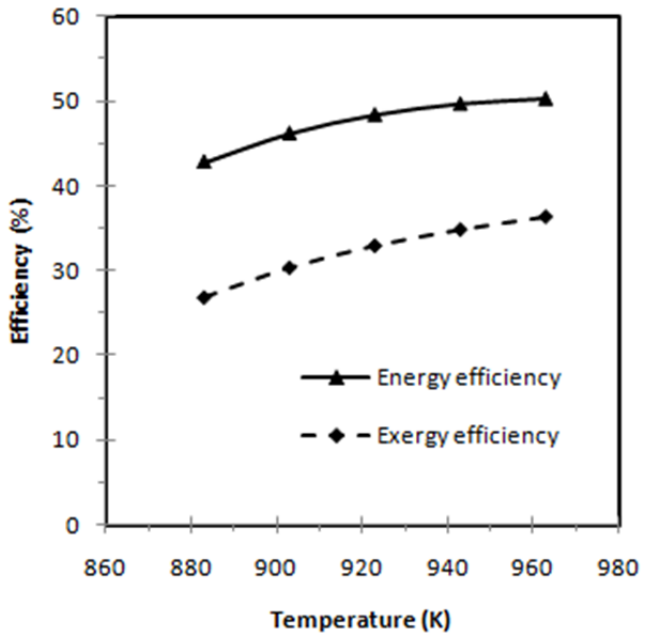

Figure 6.37: Variations of cell energy and exergy efficiencies at different operating temperature.

Figure 6.37 is obtained based on an operating current density of 4000 A m^{-2} and atmospheric pressure. This figure shows that energy efficiency of the unit cell varies from 42.8% to 50.5% while the exergy efficiency remains in the range of 26.8% to 36.3%. The dissimilarity of the two aforementioned efficiencies is caused by internal irreversibilities. Perceptibly, the activation, ohmic and concentration polarizations are the major source of irreversiblities and, hence, exergy destroyed inside the fuel cell assembly. As a result, the destroyed exergy diminishes the exergy efficiency of the MCFC. However, it is apparent that both energy and exergy efficiencies increase with rising temperature. This effect can be justified by the fact that an increase in operating temperature reduces the irreversible losses (irreversibility) of the fuel cell, which in turn augments both energy and exergy efficiencies. Furthermore, as it may be observed from Figure 6.37, even though both efficiencies increase with temperature, a sharper trend takes place at lower temperatures, with a flatter shape at higher temperatures. In fact, the unit cell total losses and the total input energy and exergy are the origin of this alteration in the efficiency trends. Clearly, Equations (4.95), (4.96) and (4.97) illustrate that as temperature increases, the activation, ohmic and concentration losses (hence total polarization) drop. The higher the temperature reaches, the smaller the irreversibilities are. In contrast, escalating the temperature results in a constant increase of energy and exergy supplied to the unit cell while the net power output of the cell reaches a maximum and then declines. As a consequent, efficiencies are expected to decrease. There always seems to be a trade off between the effect of ohmic losses and supplied energy and exergy.

Figure 6.38, presents the effect of current density (ranging from 1000 to 5000 A m^{-2}) on energy and exergy efficiencies. For this case, the operating temperature and pressure were set to 883K and 2 atm, respectively. It may be observed that both energy and exergy efficiencies initially increase at lower current densities up to the point when they attain their maximum values and ultimately decrease with the increase in current density. In terms of energy and exergy efficiencies, the optimum current density occurs around 4000 A m^{-2}. At the optimum current density, 58.7 % energy efficiency and 35.5 % exergy efficiency were achieved. Since the operating temperature is considered to be constant, any change in both efficiencies can be attributed to the net power output of the MCFC which is a function of cell operating voltage and current density. The voltage-current density curve has an increasing-decreasing trend which concludes a similar fashion in both efficiencies.

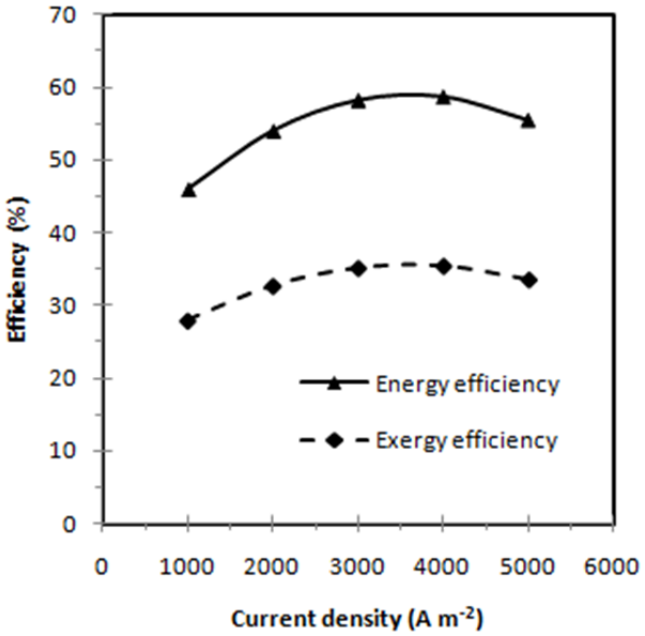

Figure 6.38: Variations of cell energy and exergy efficiencies at different current densities.

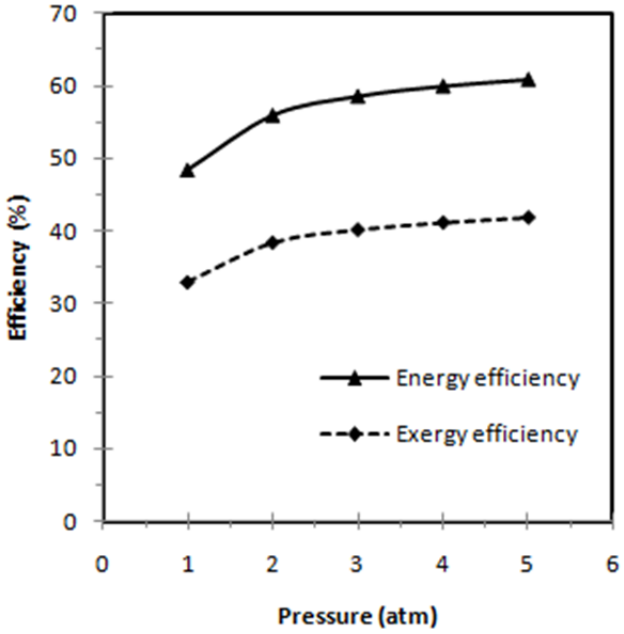

Figure 6.39: Variations of cell energy and exergy efficiencies at different operating pressure.

The effects of operating pressure (1 to 5 atm) on energy and exergy efficiencies of the studied MCFC are illustrated in Figure 6.39. In this parametric study, the operating temperature and current density were considered to be 923 K and 4000 A m^{-2}. With the increase of pressure, both the energy and exergy efficiencies of the cell are enhanced. This is realistic since as pressure increases, an extensive drop in irreversible losses occurs. In particular, anode and cathode over-potentials move to lower values at higher pressures. To be more specific, the molar concentration of hydrogen at the anodic triple-phase boundary, and oxygen and carbon dioxide at the cathodic triple-phase boundary increase with operating pressure. As a consequence, the irreversible losses of anode and cathode decrease, which in turn improve the performance of the MCFC. Nevertheless, both efficiencies increase faster at operating pressures below 3 atm and they tend to have a smoother change above this pressure.

Figure 6.40 describes how the variation of anode/cathode gas flow ratio can affect the efficiencies of an MCFC. The unit cell is assumed to operate at 923 K, atmospheric pressure and 4000 A m^{-2}. Results show that an increase in this stoichiometric ratio lessens the energy and exergy efficiencies of the unit cell. These changes are considerable for energy efficiency rather than exergy efficiency. Moreover, it may be observed from Figure 6.40 that, as this ratio grows past unity, both efficiencies decrease with a gentle slope. In addition, both efficiencies have their peak value when the molar flow rate of the oxidant entering the cathode gas channel is higher than the fuel molar flow rate which enters the anode gas channel.

Table 6.3 summarizes the value of the unit cell entropy generation at different operating temperature and pressure. As it may be seen from this table, an increase in operating temperature decreases the entropy generation in the unit cell.

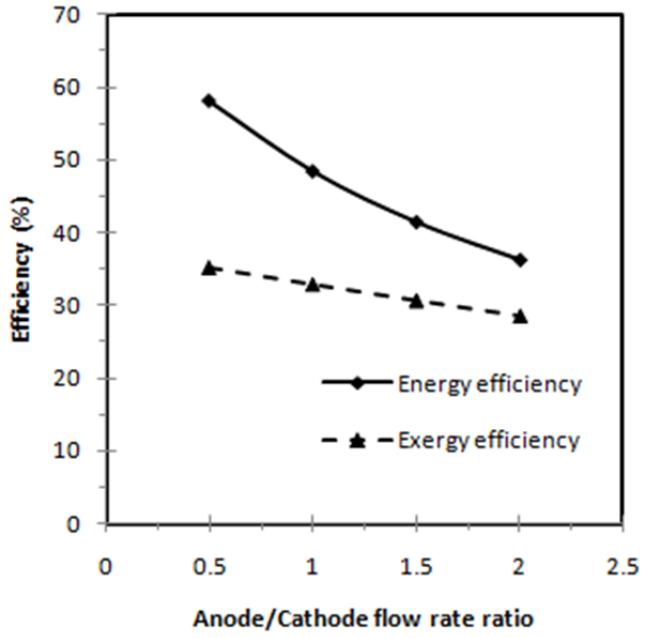

Figure 6.40: Variations of cell energy and exergy efficiencies at different anode/cathode flow rate ratios.

This effect can be acceptable by noting the fact that entropy generation is a function of cell irreversibilities in terms of activation and ohmic polarization. These irreversibilities are considerably reduced with the increase of operating temperature, which in turn cause a drop in the entropy generation. Likewise, higher operating pressures result in lower irreversibilities and hence entropy generation.

Table 6.3: Variations of entropy generation at different operating temperature and pressures.

Temperature (K)	**Entropy Generation ($J\ mol^{-1}\ K^{-1}$)**	**Pressure (atm)**	**Entropy Generation ($J\ mol^{-1}\ K^{-1}$)**
883	26.2	1	19.7
903	22.6	2	15.8
923	19.7	3	13.6
943	17.4	4	12.9
963	15.4	5	12.4

Chapter 7

Conclusions and Recommendations

7.1 Conclusions

Molten carbonate fuel cells undergo physical and electrochemical processes with a wide range of time scales (from under milliseconds up to hours). Additionally, MCFCs consist of components with a variety of length scales (from under millimetres up to centimeters). This combination of various spatial and temporal scales makes it tremendously difficult to conduct in-situ measurements. In this research, a detailed multi-component, multi-dimensional, transient mathematical model was presented for molten carbonate fuel cells. The presented model is the most complete MCFC model to-date. This predictive model was basically developed by a comprehensive inclusion of various physical, chemical and electrochemical processes that occur within the different components of MCFCs. In essence, it is a set of partial differential equations that satisfies the conservation of mass, momentum, electronic charge, ionic charge and energy. One of the novelties of the present model is its treatment of the porous electrodes wherein the effects of electrolyte filling degree is considered. The utilized modeling assumptions, approaches, boundary conditions and initial conditions were illustrated. The system of partial differential equations was discretized and solved using the finite volume based commercial software, ANSYS FLUENT 12.0.1. To handle the divergence difficulties, a set of under-relaxation techniques was developed. The programming language C was employed to develop an in-house code in order to add several capabilities and customize various model parameters and properties. Further, the developed model was validated with multiple experimental and numerical data available in the open literature, and good agreements were achieved.

Next, an investigation was performed to compare the available cathode reaction mechanisms. In fact, polarization curves for the porous lithiated NiO cathode are very often reported with a linear slope over a wide potential range. However, the MCFC behaviour at higher oxidant utilization, when the mass transfer becomes dominant, is mostly overlooked. Therefore, in this study, the two most common cathode mechanisms were utilized to compare their prediction capabilities at high current densities. The following concluding remarks are drawn from this study:

- Both peroxide and superoxide mechanisms predict the linear region of the polarization curve accurately. This occurs for low and moderate voltage losses, or low to moderate cathode gas utilizations.
- Both mechanisms show a concave, upward tendency for the cathode reaction rate as the carbon dioxide mole fraction is decreased when the current density increases.
- None of these mechanisms show a downward bent in the polarization curve.
- The negative exponent of the carbon-dioxide mole fraction is identified to be the cause of larger reaction rates at lower O_2 mole fractions.
- A larger negative exponent for the cathode reaction rate of the peroxide mechanism (as compared to the superoxide mechanism) creates a larger divergence from the linearity in the polarization curve.
- Using positive exponents for the carbon-dioxide in the cathode reaction rate would probably result in obtaining a good fit to the experimental data at high current densities.
- At extreme conditions (high voltage losses), the local current density at the cathode corners declines by a factor of 2.
- At high voltage drops, the cathode electrochemical reaction occurs mainly under the gas channel and partially in a small location close to the gas channel.
- The lack of reactants at high current densities (or high utilizations) is the source of all non-uniformity and performance deterioration.

As a next step, a sinusoidal impedance approach was employed to identify the characteristic time scales for the major dynamic transport processes. Thus, the electrochemical reactions, charge transport, mass transport and energy transport processes were analyzed to find the cell response during a sinusoidal voltage change over a wide range of impedance frequencies. The following results were obtained:

- The corresponding time scales are verified with distinctive orders of magnitudes.
- The most important physical and electrochemical processes occur in the first second of the fuel cell operation.
- The anodic and cathodic electrochemical reactions along with the charge transport process are found to be the fastest processes in the unit cell with time scales of about 10^{-6}-10^{-4} sec.
- The time scale of the gas transport process is evaluated to be on the order of 1 sec, while the energy transport process exhibited a time scale larger than 1000 sec.

Additionally, the presented model was further used to analyze the MCFC start-up process. Hence, the local variation of the interdependent field variables within MCFC components was provided by three-dimensional contour plots at different operating times. It was concluded that:

- The variation of the electronic potential is mostly along the thickness and width of the anode. The land area contains the minimum value while the maximum occurs under the gas channel.
- As we move from the sides towards the center of the anode, the electronic potential gradient along the thickness (y-direction) decreases and finally vanishes in the center.
- The potential varies more significantly under the land than under the channel.
- The variation of the ionic potential through the whole domain is much higher than the variation of electronic potential.
- The anode land area exhibits higher electronic current densities. Specifically, there are two spots at the corners which exhibit maximum electronic current density.
- As we move towards the electrolyte, the ionic current density increases and finds its maximum value at the electrolyte/anode interface.

- The cathode electronic current density increases from the electrolyte/cathode interface towards the cathode gas channel and finds its maximum value at the land area. The ionic current density is opposite to that of the electronic current density.
- The reaction rates show a non-uniform profile along the width (x-direction) of the unit cell, especially as we move from the electrode/electrolyte interface towards the gas channels. However, the highest variations occur along the thickness (y-direction).
- The electrochemical reaction is a two-dimensional process with more intensity along the thickness.
- Increasing the thickness provides higher active surface area and hence higher reaction rate, but may lead to larger ohmic loss which is not desirable. This implies that the electrode thickness is a crucial design parameter.
- The highest values of the reaction rates occur at the electrode/electrolyte interface for both electrodes (anode/electrolyte and cathode/electrolyte interfaces).
- The amount of heat transferred from the electrode-electrolyte assembly to the gas channels in the first 10 s of the cell operation, is not significant.
- The gaseous mixture at the cathode side has a relatively higher temperate in comparison with the anode side. After this time, the anode gas shows a higher temperature.
- The reversible heat generation and consumption mechanisms of the cathode and anode are dominant in the first 10 s while the heat conduction from the solid materials to the gas phase is not considerable. However, after this time, the effect of the heat conduction process gradually increases which in turn elevates the gas temperature.
- The temperature difference between the cathode and other components is constantly increased during the operation time and finally reaches a steady-state value.
- The activation and ohmic heating seem to have approximately the same impact within the anode and cathode because of their similar electric conductivity and voltage loss. This fact does not apply to the reversible heat generation as the anodic electrochemical reaction is an endothermic process while the cathodic reaction is exothermic.
- The heat conductivity plays a major role in the thermal management of the molten carbonate fuel cell. Increasing the thermal conductivity of the cathode material will facilitate the process of heat transport throughout the cell. This may also be accomplished

by lowering the effects of the heat conduction process by means of a cathode material with a smaller thickness.

In addition, a thermodynamic model is utilized to examine energy efficiency, exergy efficiency and entropy generation of a MCFC. Some parametric studies are performed and the following results are obtained:

- By changing the operating temperature from 883 K to 963 K, the energy efficiency of the unit cell varies from 42.8 % to 50.5 % while the exergy efficiency remains in the range of 26.8 % to 36.3%.
- Both efficiencies initially rise at lower current densities up to a point when they attain their maximum values and ultimately decrease with the increase of current density.
- With an increase of pressure, both the energy and exergy efficiencies of the cell grow.
- An increase in this anode/cathode flow ratio lessens the energy and exergy efficiencies of the unit cell.
- Higher operating pressure and temperature decrease the unit cell entropy generation.

7.2 Recommendations

The results obtained from this thesis research also suggest several areas for future studies, as summarized below:

- The presented model could help to expand the knowledge of, and be applied to, Electrochemical Impedance Spectroscopy (EIS) studies of MCFC cells for a better understanding of some of the fundamental phenomena such as voltage losses that can occur in such a system;
- The results from this research can be employed to perform thermal-stress analysis, to determine the stress and strain in materials and structures subjected to temperature variations;

- The developed model can be extended to a full 3D-dimensional stack model that would allow simulations of larger systems in various transient operation scenarios such as start-up, shut-down and purging;
- The developed model could also be used to conduct a performance analysis and investigate the effects of various gas flow configurations such as co-flow, counter-flow and cross-flow configurations;
- Using a high performance computing network (e.g. SHARCNET) would allow simulation of system behaviour during start-up from room-temperature;
- Thermal management of the MCFC could be aided by identifying and comparing the most significant heat losses within the anode, cathode and electrolyte;
- The mathematical model could further be enhanced to consider the effects of liquid electrolyte flow into the electrodes and gas flow into the electrolyte;
- The model could also be extended to multi-phase mode wherein the mass transport (oxygen, hydrogen, carbon dioxide, water) is considered in both gaseous mixture and liquid electrolyte.

Appendices

Appendix A

Code Development

The commercial used software, ANSYS FLUENT 12.0.1, does not have built-in modules for the non-standard governing equations for electronic charge and carbonate ionic charge. In order to add the simulation capability of the electric charges, two user-defined scalar (UDS) equations are defined for the electronic potential and ionic potential. In addition, the programming language C is used to develop several codes in order to define various source terms for mass, momentum, species, energy, electronic potential and ionic potential equations. This is performed using the user defined functions (UDF) capability of ANSYS FLUENT 12.0.1. In a similar way, boundary conditions, model parameters, material properties and empirical correlations are customized. Furthermore, the developed under-relaxation schemes which are stated in section 5.4, are applied to the model using UDF coding. A very short review of the ANSYS FLUENT macros which are used in the code development, are summarized in this appendix. In addition, a sample code that was used for a typical simulation will be presented in Appendix B.

- **DEFINE_SOURCE**

DEFINE_SOURCE is a general macro which is used to specify custom source terms for the different types of solved transport equations in ANSYS FLUENT including mass, momentum, species, energy, electronic potential and carbonate ion potential.

DEFINE SOURCE (UDF name, c, t, dS, eqn)

{

real source ;

... ;

source =... ;

...;

dS [eqn] =... ;

return source ;

}

- **DEFINE_ADJUST**

DEFINE_ADJUST is a general-purpose macro which is used to adjust or modify ANSYS FLUENT variables that are not passed as arguments. For instance, they are used to modify the physical properties, hook-up the source terms of conservation equations for each zone and employ under relaxation schemes.

```
DEFINE_ADJUST (UDF name, d)
{
    ... ;
    real zone_ID = ... ;
    ... ;
        cell_t c;
        Thread *t = Lookup_Thread (d, zone ID);

        thread_loop_c (t, d)
                {
                        if (FLUID_THREAD_P(t))
                        begin_c_loop (c, t)
                                {
                                ... ;
                                }
                        end_c_loop (c , t)
                }
}
```

- **DEFINE_PROFILE**

DEFINE_PROFILE macro is used to define a custom boundary profile that varies as a function of spatial coordinates or time. This macro is used for boundary conditions such as: over-potential, mass flux and temperature.

```
DEFINE PROFILE (UDF name, t, i)
{
    face_t f ;
    begin_f_loop (f , t)
        {
            ... ;
                F_PROFILE (f , t , i) =... ;
                ... ;
        }
    end_f_loop (f , t)
}
```

- **DEFINE_DIFFUSIVITY**

DEFINE_DIFFUSIVITY is used to specify the diffusivity for the species transport equations (mass diffusivity) and for UDS transport equations.

```
DEFINE DIFFUSIVITY (UDF name, c, t, i)
{
        int Zone_ID ;
        Zone_ID = THREAD_ID (t ) ;
        if (i = = UDS_1)
                {
                   ... ;
                        diffusivity = ... ;
                        ... ;
                }
    ... ;
        return diffusivity ;
}
```

- **DEFINE_EXECUTE_AT_END**

DEFINE_EXECUTE_AT_END is used to calculate the current density vector. This macro is executed at the end of an iteration in a steady state run, or at the end of a time step in a transient run.

```
DEFINE_EXECUTE_AT_END (UDF name)
{
        Domain * d ;
        Thread * t ;
        cell_t c ;
        d = Get_Domain (1)
        thread_loop_c (t , d)
                {
                        Zone_ID = THREAD ID (t) ;
                        Begin_c_loop_all (c , t)
                                {
                                        ... ;
                                        if ( Zone_ID = = AGC_LEFT)     ... ;
                                        ... ;
                                }
                        end_c_loop_all (c , t)
                }
}
```

- **DEFINE_INIT**

DEFINE_INIT is a general-purpose macro, used to specify a set of initial values for the solution. A DEFINE INIT function is executed once per initialization and is called immediately after the default initialization is performed by the solver. Since it is called after the flow field is initialized, it is typically used to set initial values of flow quantities.

```
DEFINE_INIT (UDF name, d)
{
        Thread * t ;
        cell_t c ;
        thread_loop_c (t , d)
                {
                        Zone_ID = THREAD ID (t) ;
                        Begin_c_loop_all (c , t)
                                {
                                        ... ;
                                        if ( Zone_ID = = AGC_LEFT)     ... ;
                                        ... ;
                                }
                        end_c_loop_all (c , t)
                }
}
```

Appendix B

Sample MCFC-Model Code

```
/*----------------------------------------------------------------------*/

/*                Molten Carbonate Fuel Cell Model Code                 */
/*                          Three-Dimensional                           */
/*                  Developed by MASOUD YOUSEF RAMANDI                  */
/*                       PhD Thesis: 2009-2012                          */
/*              Faculty of Engineering and Applied Science              */
/*            UNIVERSITY OF ONTARIO INSTITUTE OF TECHNOLOGY             */

/*----------------------------------------------------------------------*/


/*1=====================================================================*/
/*                         Inclusion Directives:                       */
/*  Allow definitions of ANSYS FLUENT-provided macros and functions    */
/*           to be included during the compilation process             */
/*=====================================================================*/

#include "udf.h"
#include "sg.h"
#include "mem.h"
#include "stdio.h"
#include "math.h"

/*=====================================================================*/
/*                              Enumeration:                           */
/*           Defines which SPECIES, UDS or UDM to be used              */
/*=====================================================================*/

enum
{
  i_h2,         /*0 Hydrogen*/
  i_o2,         /*1 Oxygen*/
  i_co2,      /*2 Carbon Dioxide*/
  i_h2o,      /*3 Water Vapor*/
  i_n2,         /*4 Nitrogen*/
  NUM_SPECIES
};

enum
{
  Ve,         /*0 Electronic Potential (V)*/
  Vi,         /*1 Ionic Potential (V)*/
  NUM_UDS
};
```

```
enum
{
  Eta,
  Ri,
  S_rev,
  S_act,
  S_ohm,
  S_react,
  Je_x,
  Je_y,
  Je_z,
  Ji_x,
  Ji_y,
  Ji_z,
  AAA,
  BBB,
  CCC,
  NUM_UDM
};

/*=====================================================================*/
/*                            Zone IDs:                                */
/*             Corresponding to different case file                    */
/*=====================================================================*/

#define ID_A 37
#define ID_E 38
#define ID_C 39
#define ID_AGC 36
#define ID_CGC 40

#define ID_AGCin 10107
#define ID_CGCin 10112

/*=====================================================================*/
/*                       Model Parameter Values                        */
/*=====================================================================*/
#define pi 3.14159265
#define amp 0.1
#define freq 10

#define ACT_AREA_A 270000
#define ACT_AREA_C 300000

#define REF_EXCH_CURR_A 20
#define REF_EXCH_CURR_C 7.5

#define MW_H2 0.002
#define MW_H2O 0.018
#define MW_O2 0.032
#define MW_CO2 0.044
#define MW_N2 0.028

#define STOCH_H2 -1
#define STOCH_H2O 1
#define STOCH_O2 -0.5
```

```
#define STOCH_CO2_A 1
#define STOCH_CO2_C -1

#define Rev_Pot 1.02
#define NO_ELEC 2
#define Faraday 96485
#define Uni_Gas_Cons 8.314

#define POR_A 0.52
#define POR_C 0.62
#define POR_AGC 1.00
#define POR_CGC 1.00

#define E_Cond_A 1300
#define E_Cond_C 1300
#define E_Cond_AGC 0.0000000000000001
#define E_Cond_CGC 0.0000000000000001

#define I_Cond_A 140
#define I_Cond_C 140
#define I_Cond_E 140
#define I_Cond_AGC 0.0000000000000001
#define I_Cond_CGC 0.0000000000000001

#define Bta_a 0.5
#define Bta_c 0.5

#define c1 0.5
#define c2 0.5
#define go2 0.625
#define gco2 -0.75

#define Fill_A 0.31
#define Fill_C 0.42
#define Fill_E 0.5
#define Fill_AGC 0.0
#define Fill_CGC 0.0

#define Perm_A 1e-12
#define Perm_C 1e-12

#define Y_H2_in 0.16
#define Y_H2O_in 0.36
#define Y_CO2a_in 0.48
#define Y_CO2c_in 0.40
#define Y_O2_in 0.14

#define X_H2a_in 0.69
#define X_O2a_in 0.00
#define X_CO2a_in 0.17
#define X_H2Oa_in 0.14

#define X_H2c_in 0.00
#define X_O2c_in 0.147
#define X_CO2c_in 0.30
#define X_H2Oc_in 0.0
```

```
#define Delta_S_A -161.6
#define Delta_S_C 216.2

#define T_in 853
#define Pout 1
#define mFlow_A 0.000000637
#define mFlow_C 0.00000647

static float urf_T=0.90;
static float urf_s=0.99;
static int MY_COUNTER=1;

#define Cell_Volt 0.7

/*======================================================================*/
/*                    Variable Parameter Functions                      */
/*======================================================================*/

/*------------------------Reversible Potential, V--------------------*/

double Get_E_r()
{
  double E0 = 1.2723-2.7645*0.0001*T_in;
  double exp =
pow(Pout,0.5)*X_H2a_in*X_CO2c_in*pow(X_O2c_in,0.5)/(X_CO2a_in*X_H2Oa_in);
  double E00 = ((Uni_Gas_Cons*T_in)/(NO_ELEC*Faraday))*log(exp);
  double Er = E0 + E00;
/*Message("\nEr = %g\n", Er);*/
  return Er;
}
/*-------------------------Filling Degree ()-------------------------*/

double Get_Fill_D(Thread *t)
{
  double fill;
  int Zone_ID=THREAD_ID(t);
    if (Zone_ID==ID_A) fill=Fill_A;
    else if (Zone_ID==ID_C) fill=Fill_C;
    else if (Zone_ID==ID_AGC) fill=Fill_AGC;
    else if (Zone_ID==ID_CGC) fill=Fill_CGC;
  return fill;
}
/*----------------------Intristic Porosity ()----------------------*/

double Get_Porosity(Thread *t)
{
  double porosity;
  int Zone_ID=THREAD_ID(t);
  if (Zone_ID==ID_A) porosity=POR_A;
  else if (Zone_ID==ID_C) porosity=POR_C;

/*   Channel can be porous (depends on the type of the distributor)  */

  else if (Zone_ID==ID_AGC) porosity=POR_AGC;
  else if (Zone_ID==ID_CGC) porosity=POR_CGC;
  else porosity=1.0;
  return porosity;
```

```
}
/*----------------Effective Permeability, 1/m2 ()--------------------*/

double Get_K_A(cell_t c, Thread *t)
{
  return Perm_A*pow((Get_Porosity(t)*(1-Get_Fill_D(t))),1.5);
}

double Get_K_C(cell_t c, Thread *t)
{
  return Perm_C*pow((Get_Porosity(t)*(1-Get_Fill_D(t))),1.5);
}
/*-------------Effective Electronic Conductivity, S/m ()-------------*/

double Get_E_Cond(Thread *t)
{
  double e_conductivity;
  int Zone_ID=THREAD_ID(t);
  if (Zone_ID==ID_A) e_conductivity=E_Cond_A*pow((1-Get_Porosity(t)),1.0);

  else if (Zone_ID==ID_C) e_conductivity=E_Cond_C*pow((1-
Get_Porosity(t)),1.0);

/*Channel conductivity used to handle interior B.C. issue in 2D model*/

  else if (Zone_ID==ID_AGC) e_conductivity=E_Cond_AGC;
  else if (Zone_ID==ID_CGC) e_conductivity=E_Cond_CGC;
  return e_conductivity;
}
/*-----------------Effective Ionic Conductivity, S/m ()--------------*/

double Get_I_Cond(Thread *t)
{
  double i_conductivity;
  int Zone_ID=THREAD_ID(t);
  if (Zone_ID==ID_A)
i_conductivity=I_Cond_A*pow((Get_Porosity(t)*Get_Fill_D(t)),1.5);

  else if (Zone_ID==ID_C)
i_conductivity=I_Cond_C*pow((Get_Porosity(t)*Get_Fill_D(t)),1.5);

  else if (Zone_ID==ID_E) i_conductivity=I_Cond_E*pow(Fill_E,1.5);

/*Channel conductivity used to handle interior B.C. issue in 2D model*/

  else if (Zone_ID==ID_AGC) i_conductivity=I_Cond_AGC;
  else if (Zone_ID==ID_CGC) i_conductivity=I_Cond_CGC;
  return i_conductivity;
}


/*------------------------Inlet Mass fractions----------------------*/

double Yin_A(int i)
{
  double y;
  double Y_H2=Y_H2_in;
```

```
  double Y_H2O=Y_H2O_in;
  double Y_CO2a=Y_CO2a_in;
  if (i==0) y=Y_H2;
  else if (i==2) y=Y_CO2a;
  else if (i==3) y=Y_H2O;
  return y;
}

double Yin_C(int i)
{
  double y;
  double Y_O2=Y_O2_in;
  double Y_CO2c=Y_CO2c_in;
  if (i==1) y=Y_O2;
  else if (i==2) y=Y_CO2c;
  return y;
}
/*------------------------Inlet Mole fractions-----------------------*/

double Xin_A(int i)
{
  double x;
  double X_H2a=X_H2a_in;
  double X_O2a=X_O2a_in;
  double X_CO2a=X_CO2a_in;
  double X_H2Oa=X_H2Oa_in;
  if (i==0) x=X_H2a;
  else if (i==1) x=X_O2a;
  else if (i==2) x=X_CO2a;
  else if (i==3) x=X_H2Oa;
  return x;
}

double Xin_C(int i)
{

  double x;
  double X_H2c=X_H2c_in;
  double X_O2c=X_O2c_in;
  double X_CO2c=X_CO2c_in;
  double X_H2Oc=X_H2Oc_in;
  if (i==0) x=X_H2c;
  else if (i==1) x=X_O2c;
  else if (i==2) x=X_CO2c;
  else if (i==3) x=X_H2Oc;
  return x;

}
/*-------------------------Cell Voltage,V----------------------------*/

double Cell_V()
{
  double v=Cell_Volt;
  return v;
}
/*-----Butler_Volmer Volumetric Current Density,A/m3 (Boden 2006)----*/
```

```
double RR_A(cell_t c, Thread *t)
{
  double
MW_MIX_A=1/((C_YI(c,t,0)/MW_H2)+(C_YI(c,t,2)/MW_CO2)+(C_YI(c,t,3)/MW_H2O));
  double X_H2=C_YI(c,t,0)*MW_MIX_A/MW_H2;
  double X_CO2_A=C_YI(c,t,2)*MW_MIX_A/MW_CO2;
  double X_H2O=1-(X_CO2_A+X_H2);

  double
Coeff_A=ACT_AREA_A*REF_EXCH_CURR_A*pow((X_H2a_in*Pout),(0.5*Bta_a))*pow((X_H2
Oa_in*Pout),(0.5*(1-Bta_a)))*pow((X_CO2a_in*Pout),(0.5*(1-Bta_a)));

  double Exp_1 = pow((X_H2/X_H2a_in),0.5)*exp((1-
Bta_a)*Faraday*C_UDMI(c,t,1)/(Uni_Gas_Cons*C_T(c,t)));

  double Exp_2 = (X_CO2_A/X_CO2a_in)*pow((X_H2/X_H2a_in),(-
0.5))*(X_H2O/X_H2Oa_in)*exp(-
(1+Bta_a)*Faraday*C_UDMI(c,t,1)/(Uni_Gas_Cons*C_T(c,t)));

  double Ra = Coeff_A*(Exp_1-Exp_2);
C_UDMI(c,t,11)=Coeff_A;
C_UDMI(c,t,12)=Exp_1;
C_UDMI(c,t,13)=Exp_2;
  return Ra;
}

double RR_C(cell_t c, Thread *t)
{

  double
MW_MIX_C=1/((C_YI(c,t,1)/MW_O2)+(C_YI(c,t,2)/MW_CO2)+(C_YI(c,t,3)/MW_H2O)+(C_
YI(c,t,4)/MW_N2));
  double X_O2=C_YI(c,t,1)*MW_MIX_C/MW_O2;
  double X_CO2_C=C_YI(c,t,2)*MW_MIX_C/MW_CO2;
  double X_H2O_C=C_YI(c,t,3)*MW_MIX_C/MW_H2O;
  double X_N2=1-(X_CO2_C+X_O2+X_H2O_C);

  double
Coeff_C=ACT_AREA_C*REF_EXCH_CURR_C*pow((X_O2c_in*Pout),go2)*pow((X_CO2c_in*Po
ut),gco2);

  double Exp_1 = pow((X_CO2_C/X_CO2c_in),(-
2))*exp(c1*Faraday*C_UDMI(c,t,1)/(Uni_Gas_Cons*C_T(c,t)));

  double Exp_2 = pow((X_CO2_C/X_CO2c_in),(-
1))*pow((X_O2/X_O2c_in),(0.5))*exp(-
c2*Faraday*C_UDMI(c,t,1)/(Uni_Gas_Cons*C_T(c,t)));


  double Rc = Coeff_C*(Exp_1-Exp_2);
C_UDMI(c,t,11)=Coeff_C;
C_UDMI(c,t,12)=Exp_1;
C_UDMI(c,t,13)=Exp_2;

  Rc = MIN(0,Rc);

  return Rc;
```

```
}

/*======================================================================*/
/*                            DEFINE Macros                             */
/*======================================================================*/

/*--------------------------Initialization--------------------------*/
DEFINE_INIT(MCFC_Initialization,d)
{
Thread *t ;
cell_t c ;
int Zone_ID;
int i;
Message(" \n\n Start initialization... \n\n");
thread_loop_c(t,d)
{
  Zone_ID=THREAD_ID(t);

  begin_c_loop_all(c,t)
  {
    C_T(c,t) = T_in;

    if (Zone_ID==ID_AGC || Zone_ID==ID_AGCin)
    {
    if (FLUID_THREAD_P(t))
    C_YI(c,t,0)=Yin_A(0);
    C_YI(c,t,1)=0;
    C_YI(c,t,2)=Yin_A(2);
    C_YI(c,t,3)=Yin_A(3);
    C_YI(c,t,4)=0.0;
    C_UDSI(c,t,0)=0.0;
    C_UDSI(c,t,1)=0.0;
    }

    if (Zone_ID==ID_A)
    {
    if (FLUID_THREAD_P(t))
    C_YI(c,t,0)=Yin_A(0);
    C_YI(c,t,1)=0;
    C_YI(c,t,2)=Yin_A(2);
    C_YI(c,t,3)=Yin_A(3);
    C_YI(c,t,4)=0.0;
    C_UDSI(c,t,0)=0.0;
    C_UDSI(c,t,1)=-0.01;
    }


    else if(Zone_ID==ID_CGC || Zone_ID==ID_CGCin)
    {
    C_YI(c,t,0)=0.0;
    C_YI(c,t,1)=Yin_C(1);
    C_YI(c,t,2)=Yin_C(2);
    C_YI(c,t,3)=0.0;
    C_UDSI(c,t,0)=0.0;
    C_UDSI(c,t,1)=0.0;
    }
```

```
    else if(Zone_ID==ID_C)
    {
    C_YI(c,t,0)=0.0;
    C_YI(c,t,1)=Yin_C(1);
    C_YI(c,t,2)=Yin_C(2);
    C_YI(c,t,3)=0.0;
    C_UDSI(c,t,0)=Cell_V();
    C_UDSI(c,t,1)=-0.09;
    }

    else if(Zone_ID==ID_E)
    {
    C_UDSI(c,t,1)=0.0;
    }
  }
  end_c_loop_all(c,t)
}
Message(" Initialization is done. \n\n");
}
/*-----------------------------Porosity-------------------------------*/

DEFINE_PROFILE(porosity,t,i)
{
  cell_t c;
  begin_c_loop(c,t)
  {
    C_PROFILE(c,t,i)=Get_Porosity(t)*(1-Get_Fill_D(t));
  }
  end_c_loop(c,t)
}
/*--------------------Electronic Conductivity------------------------*/

DEFINE_DIFFUSIVITY(Elec_Cond, c, t, i)
{
  float Cond;
  Cond=Get_E_Cond(t);
      return Cond;
}
/*-----------------------Ionic Conductivity--------------------------*/

DEFINE_DIFFUSIVITY(Ion_Cond, c, t, i)
{
  float Cond;
  Cond=Get_I_Cond(t);
      return Cond;
}

/*-------------Effective Mass Diffusivity, m2/s ()-------------*/

DEFINE_DIFFUSIVITY(diff_specOLD, c, t, i)
{
  double D;
  int Zone_ID=THREAD_ID(t);

  double p_op = RP_Get_Real("operating-pressure");
  double p = C_P(c,t);
```

```
  double p_ref = 101325;
  p += p_op;

  if (i==0)
  {
    if (Zone_ID == ID_A || Zone_ID == ID_C)
D=0.000016*(C_T(c,t)/298)*(p_ref/p)*pow((Get_Porosity(t)*(1-
Get_Fill_D(t))),1.5);
    else D=0.000056*(C_T(c,t)/298)*(p_ref/p);
  }

  if (i==1)
  {
    if (Zone_ID == ID_A || Zone_ID == ID_C)
D=0.000016*(C_T(c,t)/298)*(p_ref/p)*pow((Get_Porosity(t)*(1-
Get_Fill_D(t))),1.5);
    else D=0.000056*(C_T(c,t)/298)*(p_ref/p);
  }

  if (i==2)
  {
    if (Zone_ID == ID_A || Zone_ID == ID_C)
D=0.000016*(C_T(c,t)/298)*(p_ref/p)*pow((Get_Porosity(t)*(1-
Get_Fill_D(t))),1.5);
    else D=0.000056*(C_T(c,t)/298)*(p_ref/p);
  }

  if (i==3)
  {
    if (Zone_ID == ID_A || Zone_ID == ID_C)
D=0.000016*(C_T(c,t)/298)*(p_ref/p)*pow((Get_Porosity(t)*(1-
Get_Fill_D(t))),1.5);
    else D=0.000056*(C_T(c,t)/298)*(p_ref/p);
  }

  if (i==4)
  {
    if (Zone_ID == ID_A || Zone_ID == ID_C)
D=0.000016*(C_T(c,t)/298)*(p_ref/p)*pow((Get_Porosity(t)*(1-
Get_Fill_D(t))),1.5);
    else D=0.000056*(C_T(c,t)/298)*(p_ref/p);
  }

return D;
}

/*----------------------Viscous Resistance, m2----------------------*/

DEFINE_PROFILE(Visc_Res_A,t,i)
{
  cell_t c;
  begin_c_loop(c,t)
  {
    C_PROFILE(c,t,i)=1/Get_K_A(c,t);
  }
  end_c_loop(c,t)
}
```

```
DEFINE_PROFILE(Visc_Res_C,t,i)
{
  cell_t c;
  begin_c_loop(c,t)
  {
    C_PROFILE(c,t,i)=1/Get_K_C(c,t);
  }
  end_c_loop(c,t)
}
/*----------------------B.C.: Outlet Pressure, atm-------------------*/

DEFINE_PROFILE(Outlet_P,t,i)
{
  face_t f;
  begin_f_loop(f,t)
  {
    F_PROFILE(f,t,i)=(Pout-1)*101325;
  }
  end_f_loop(f,t)
}

/*----------------------B.C.: Inlet Temperature, K-------------------*/

DEFINE_PROFILE(Inlet_T,t,i)
{
  face_t f;
  begin_f_loop(f,t)
  {
    F_PROFILE(f,t,i)=T_in;
  }
  end_f_loop(f,t)
}
/*----------------------B.C.: Inlet Mole Fraction--------------------*/

DEFINE_PROFILE(Inlet_Xi_A,t,i)
{
  face_t f;
  double x;
  if (i==0) x=Xin_A(0);
  else if (i==1) x=Xin_A(1);
  else if (i==2) x=Xin_A(2);
  else if (i==3) x=Xin_A(3);
    begin_f_loop(f,t)
    {
      F_PROFILE(f,t,i)=x;
    }
    end_f_loop(f,t)
}

DEFINE_PROFILE(Inlet_Xi_C,t,i)
{
  face_t f;
  double x;
  if (i==0) x=Xin_C(0);
  else if (i==1) x=Xin_C(1);
  else if (i==2) x=Xin_C(2);
```

```
  else if (i==3) x=Xin_C(3);
    begin_f_loop(f,t)
    {
      F_PROFILE(f,t,i)=x;
    }
    end_f_loop(f,t)
}
/*------------------B.C.: Inlet Mass Flow Rate, kg/s-----------------*/

DEFINE_PROFILE(Mass_Flow_A,t,i)
{
  face_t f;
  begin_f_loop(f,t)
  {
    F_PROFILE(f,t,i)=Pout*mFlow_A;
  }
  end_f_loop(f,t)
}

DEFINE_PROFILE(Mass_Flow_C,t,i)
{
  face_t f;
  begin_f_loop(f,t)
  {
    F_PROFILE(f,t,i)=Pout*mFlow_C;
  }
  end_f_loop(f,t)
}

/*--------------------B.C.: Operating Cell Voltage-------------------*/

DEFINE_PROFILE(Cell_Voltage,t,i)
{
  face_t f;
  begin_f_loop(f,t)
  {
    F_PROFILE(f,t,i)=Cell_V();
  }
  end_f_loop(f,t)
}


DEFINE_PROFILE(Cell_Vol_step,t,i)
{
  face_t f;
  double flow_time = CURRENT_TIME;
  begin_f_loop(f,t)
  {
  if (flow_time < 1.0) F_PROFILE(f,t,i)=Cell_V();
  else   if (flow_time < 3.0) F_PROFILE(f,t,i)=Cell_V()+0.05;
  else F_PROFILE(f,t,i)=Cell_V()-0.05;
  }
  end_f_loop(f,t)
}

DEFINE_PROFILE(Cell_V_Sinusoidal,t,i)
{
```

```
   face_t f;
   double time = CURRENT_TIME;
   begin_f_loop(f,t)
   {
     F_PROFILE(f,t,i)=Cell_V()+amp*sin(2*pi*freq*time);
   }
   end_f_loop(f,t)
}

/*------------Under-relaxation & freezing N2 mass fraction-----------*/

DEFINE_ADJUST(MCFC_adjust,d)
{
   Thread *t;
   cell_t c;
   MY_COUNTER += 1;
urf_s += 0.002;
urf_T += 0.001;
urf_s = MIN(1,urf_s);
urf_T = MIN(1,urf_T);
/*Message("\nurf_s = %g\n", urf_s);*/
/*Message("\nurf_T = %g\n", urf_T);*/

/*           Update values based on the under-relaxed values         */

   thread_loop_c(t,d)
   {
   begin_c_loop_all(c,t)
   {
     double T = C_T(c,t);
     int Zone_ID = THREAD_ID(t);

/*      freezing the nitrogen mass fraction to zero at anode side    */

   if (Zone_ID == ID_A || Zone_ID == ID_AGC || Zone_ID == ID_AGCin)
C_YI(c,t,4)=0.0;

/*           Under-relaxation of the rxn rate & overpotentials       */

   if (Zone_ID == ID_A)
   {
   C_UDMI(c,t,1) += urf_s*((C_UDSI(c,t,0)-C_UDSI(c,t,1))-
C_UDMI(c,t,1));

   C_UDMI(c,t,0) += urf_s*(RR_A(c,t)-C_UDMI(c,t,0));
   }

   if (Zone_ID == ID_C)
   {
   C_UDMI(c,t,1) += urf_s*((C_UDSI(c,t,0)-C_UDSI(c,t,1)-Get_E_r())-
C_UDMI(c,t,1));

   C_UDMI(c,t,0) += urf_s*(RR_C(c,t)-C_UDMI(c,t,0));
   }

   if (Zone_ID == ID_AGC || Zone_ID == ID_CGC || Zone_ID == ID_E)
   {
```

```
   C_UDMI(c,t,0)=0;
   }

   }
   end_c_loop_all(c,t)
   }
}

/*-------------------Hydrogen Source Term: kg/m3.s-------------------*/

DEFINE_SOURCE(SOURCE_H2,c,t,dS,eqn)
{
   double S_h2 = 0.0;
   S_h2 = (STOCH_H2*MW_H2*C_UDMI(c,t,0))/(NO_ELEC*Faraday);
   dS[eqn] = 0.0;
   return S_h2;
}
/*-----------------Water Vapor Source Term: kg/m3.s-----------------*/

DEFINE_SOURCE(SOURCE_H2O,c,t,dS,eqn)
{
   double S_h2o = 0.0;
   S_h2o = (STOCH_H2O*MW_H2O*C_UDMI(c,t,0))/(NO_ELEC*Faraday);
   dS[eqn] = 0.0;
   return S_h2o;
}
/*---------------Carbon Di-Oxide Source Term: kg/m3.s----------------*/

DEFINE_SOURCE(SOURCE_CO2, c, t, dS, eqn)
{
   double S_co2 = 0.0;
   int Zone_ID = THREAD_ID(t);
   if (Zone_ID == ID_A)
S_co2=(STOCH_CO2_A*MW_CO2*C_UDMI(c,t,0))/(NO_ELEC*Faraday);
   if (Zone_ID == ID_C) S_co2=-
(STOCH_CO2_C*MW_CO2*C_UDMI(c,t,0))/(NO_ELEC*Faraday);
   dS[eqn] = 0.0;
   return S_co2;
}
/*-------------------Oxygen Source Term: kg/m3.s--------------------*/

DEFINE_SOURCE(SOURCE_O2, c, t, dS, eqn)
{
   double S_o2 = 0.0;
   S_o2 =-(STOCH_O2*MW_O2*C_UDMI(c,t,0))/(NO_ELEC*Faraday);
   dS[eqn] = 0.0;
   return S_o2;
}
/*--------------------Mass Source Term: kg/m3.s--------------------*/

DEFINE_SOURCE(SOURCE_MASS, c, t, dS, eqn)
{
   double S_mass = 0.0;
   int Zone_ID = THREAD_ID(t);
   if (Zone_ID == ID_A)
   {
```

```
  S_mass=(STOCH_H2*MW_H2+STOCH_H2O*MW_H2O+STOCH_CO2_A*MW_CO2)*C_UDMI(c,t,0)/(
NO_ELEC*Faraday);
  }
  else if (Zone_ID == ID_C)
  {
    S_mass=-
(STOCH_O2*MW_O2+STOCH_CO2_C*MW_CO2)*C_UDMI(c,t,0)/(NO_ELEC*Faraday);
  }
  else if (Zone_ID == ID_AGC || Zone_ID == ID_CGC) S_mass = 0.0;

  else S_mass = 0.0;

  dS[eqn] = 0.0;
  return S_mass;
}

/*--------------Electronic Potential Source Term: A/m3---------------*/

DEFINE_SOURCE(SOURCE_Ve, c, t, dS, eqn)
{
  double S_Ve = 0.0;
  int Zone_ID = THREAD_ID(t);
  if (Zone_ID == ID_A) S_Ve = C_UDMI(c,t,0);
  if (Zone_ID == ID_C) S_Ve = C_UDMI(c,t,0);
  dS[eqn] = 0.0;
  return S_Ve;
}

/*-----------------Ionic Potential Source Term: A/m3-----------------*/

DEFINE_SOURCE(SOURCE_Vi, c, t, dS, eqn)
{
  double S_Vi = 0.0;
  int Zone_ID = THREAD_ID(t);
  if (Zone_ID == ID_A) S_Vi = C_UDMI(c,t,0);
  if (Zone_ID == ID_C) S_Vi = C_UDMI(c,t,0);
  dS[eqn] = 0.0;
  return S_Vi;
}

/*--------------------Energy Source Term: J/m3.s--------------------*/

DEFINE_SOURCE(SOURCE_ENERGY,c,t,dS,eqn)
{
  double S_energy = 0.0;
  double heat_rev, heat_act, heat_ohm;
  double T = C_T(c,t);
  int Zone_ID = THREAD_ID(t);

  double NV_VEC(Je), NV_VEC(Ji);
ND_SET(Je[0], Je[1], Je[2], C_UDMI(c,t,2), C_UDMI(c,t,3), C_UDMI(c,t,4));
ND_SET(Ji[0], Ji[1], Ji[2], C_UDMI(c,t,5), C_UDMI(c,t,6), C_UDMI(c,t,7));

  if (Zone_ID == ID_A)
  {
    heat_rev = T*Delta_S_A*fabs(C_UDMI(c,t,0))/(NO_ELEC*Faraday);
```

```
    heat_act = fabs(C_UDMI(c,t,1)*C_UDMI(c,t,0));
    heat_ohm = NV_MAG2(Je)/C_UDSI_DIFF(c,t,0)+NV_MAG2(Ji)/C_UDSI_DIFF(c,t,1);
  }

  else if (Zone_ID == ID_C)
  {
    heat_rev = T*Delta_S_C*fabs(C_UDMI(c,t,0))/(NO_ELEC*Faraday);
    heat_act = fabs(C_UDMI(c,t,1)*C_UDMI(c,t,0));
    heat_ohm = NV_MAG2(Je)/C_UDSI_DIFF(c,t,0)+NV_MAG2(Ji)/C_UDSI_DIFF(c,t,1);
  }
  else if (Zone_ID == ID_E)
  {
    heat_rev = 0.0;
    heat_act = 0.0;
    heat_ohm = NV_MAG2(Ji)/C_UDSI_DIFF(c,t,1);
  }

  S_energy = heat_rev + heat_act + heat_ohm;
  dS[eqn] = 0.0;
  return urf_T*S_energy;
}


/*-----Calculation of current densities and source terms at end------*/

DEFINE_EXECUTE_AT_END(MCFC_At_End)

{
Domain *d;
Thread *t;
cell_t c;
d = Get_Domain(1);


thread_loop_c(t,d)
{
int Zone_ID = THREAD_ID(t);

    begin_c_loop_all(c,t)
    {

double T = C_T(c,t);



double NV_VEC(Je), NV_VEC(Ji);
ND_SET(Je[0], Je[1], Je[2], C_UDMI(c,t,2), C_UDMI(c,t,3), C_UDMI(c,t,4));
ND_SET(Ji[0], Ji[1], Ji[2], C_UDMI(c,t,5), C_UDMI(c,t,6), C_UDMI(c,t,7));


if (Zone_ID == ID_A || Zone_ID == ID_AGC || Zone_ID == ID_AGCin)
C_YI(c,t,4)=0.0;

    if (Zone_ID == ID_A)
    {
```

```
     C_UDMI(c,t,2) += urf_s*(-C_UDSI_G(c,t,0)[0]*C_UDSI_DIFF(c,t,0)-
C_UDMI(c,t,2));

     C_UDMI(c,t,3) += urf_s*(-C_UDSI_G(c,t,0)[1]*C_UDSI_DIFF(c,t,0)-
C_UDMI(c,t,3));


     if (C_UDMI(c,t,3) < min_err || C_UDMI(c,t,3) > max_err) C_UDMI(c,t,3)=0;


     C_UDMI(c,t,4) += urf_s*(-C_UDSI_G(c,t,0)[2]*C_UDSI_DIFF(c,t,0)-
C_UDMI(c,t,4));

     C_UDMI(c,t,5) += urf_s*(+C_UDSI_G(c,t,1)[0]*C_UDSI_DIFF(c,t,1)-
C_UDMI(c,t,5));

     C_UDMI(c,t,6) += urf_s*(+C_UDSI_G(c,t,1)[1]*C_UDSI_DIFF(c,t,1)-
C_UDMI(c,t,6));


     if (C_UDMI(c,t,6) < min_err || C_UDMI(c,t,6) > max_err) C_UDMI(c,t,6)=0;


     C_UDMI(c,t,7) += urf_s*(+C_UDSI_G(c,t,1)[2]*C_UDSI_DIFF(c,t,1)-
C_UDMI(c,t,7));

     C_UDMI(c,t,8) = T*Delta_S_A*fabs(C_UDMI(c,t,0))/(NO_ELEC*Faraday);

     C_UDMI(c,t,9) = fabs(C_UDMI(c,t,1)*C_UDMI(c,t,0));

     C_UDMI(c,t,10) = NV_MAG2(Je)/C_UDSI_DIFF(c,t,0) +
NV_MAG2(Ji)/C_UDSI_DIFF(c,t,1);
     }

     else if (Zone_ID == ID_C)
     {
     C_UDMI(c,t,2) += urf_s*(-C_UDSI_G(c,t,0)[0]*C_UDSI_DIFF(c,t,0)-
C_UDMI(c,t,2));

     C_UDMI(c,t,3) += urf_s*(-C_UDSI_G(c,t,0)[1]*C_UDSI_DIFF(c,t,0)-
C_UDMI(c,t,3));



     if (C_UDMI(c,t,3) < min_err || C_UDMI(c,t,3) > max_err) C_UDMI(c,t,3)=0;


     C_UDMI(c,t,4) += urf_s*(-C_UDSI_G(c,t,0)[2]*C_UDSI_DIFF(c,t,0)-
C_UDMI(c,t,4));

     C_UDMI(c,t,5) += urf_s*(+C_UDSI_G(c,t,1)[0]*C_UDSI_DIFF(c,t,1)-
C_UDMI(c,t,5));

     C_UDMI(c,t,6) += urf_s*(+C_UDSI_G(c,t,1)[1]*C_UDSI_DIFF(c,t,1)-
C_UDMI(c,t,6));
```

```
     if (C_UDMI(c,t,6) < min_err || C_UDMI(c,t,6) > max_err) C_UDMI(c,t,6)=0;



     C_UDMI(c,t,7) += urf_s*(+C_UDSI_G(c,t,1)[2]*C_UDSI_DIFF(c,t,1)-
C_UDMI(c,t,7));

     C_UDMI(c,t,8) = T*Delta_S_C*fabs(C_UDMI(c,t,0))/(NO_ELEC*Faraday);

     C_UDMI(c,t,9) = fabs(C_UDMI(c,t,1)*C_UDMI(c,t,0));

     C_UDMI(c,t,10) = NV_MAG2(Je)/C_UDSI_DIFF(c,t,0) +
NV_MAG2(Ji)/C_UDSI_DIFF(c,t,1);

     }

     else if (Zone_ID == ID_E)
     {
     C_UDMI(c,t,0)=0.0;

     C_UDMI(c,t,2) = 0.0;
     C_UDMI(c,t,3) = 0.0;
     C_UDMI(c,t,4) = 0.0;

     C_UDMI(c,t,5) += urf_s*(+C_UDSI_G(c,t,1)[0]*C_UDSI_DIFF(c,t,1)-
C_UDMI(c,t,5));

     C_UDMI(c,t,6) += urf_s*(+C_UDSI_G(c,t,1)[1]*C_UDSI_DIFF(c,t,1)-
C_UDMI(c,t,6));

     C_UDMI(c,t,7) += urf_s*(+C_UDSI_G(c,t,1)[2]*C_UDSI_DIFF(c,t,1)-
C_UDMI(c,t,7));


     C_UDMI(c,t,8) = 0.0;
     C_UDMI(c,t,9) = 0.0;

     C_UDMI(c,t,10) = NV_MAG2(Ji)/C_UDSI_DIFF(c,t,1);
     }


     else if (Zone_ID == ID_AGC || Zone_ID == ID_CGC)
     {
     C_UDMI(c,t,0)=0.0;

     C_UDMI(c,t,2) = 0.0;
     C_UDMI(c,t,3) = 0.0;
     C_UDMI(c,t,4) = 0.0;
     C_UDMI(c,t,5) = 0.0;
     C_UDMI(c,t,6) = 0.0;
     C_UDMI(c,t,7) = 0.0;
     C_UDMI(c,t,8) = 0.0;
     C_UDMI(c,t,9) = 0.0;

     C_UDMI(c,t,10) = 0.0;
     }
```

```
    }
    end_c_loop_all(c,t)

  }
}

/*------------Alternative Mass Diffusivity--------------------*/

DEFINE_DIFFUSIVITY(diff_species, c, t, i)
{
  double D;
  double DEN;
  double D02;
  double D03;
  double D23;
  double D12;
  double D14;
  double D24;
  int Zone_ID=THREAD_ID(t);

  double p_op = RP_Get_Real("operating-pressure");
  double p = C_P(c,t);

  double p_ref = 101325;
  p += p_op;


if (Zone_ID == ID_A || Zone_ID == ID_AGC)
{
  double
MW_MIX_A=1/((C_YI(c,t,0)/MW_H2)+(C_YI(c,t,2)/MW_CO2)+(C_YI(c,t,3)/MW_H2O));
  double X_H2=C_YI(c,t,0)*MW_MIX_A/MW_H2;
  double X_CO2_A=C_YI(c,t,2)*MW_MIX_A/MW_CO2;
  double X_H2O=1-(X_CO2_A+X_H2);

  D02 = 0.0000550*(C_T(c,t)/298)*(p_ref/p)*pow((Get_Porosity(t)*(1-
Get_Fill_D(t))),1.5);
  D03 = 0.0000915*(C_T(c,t)/298)*(p_ref/p)*pow((Get_Porosity(t)*(1-
Get_Fill_D(t))),1.5);
  D23 = 0.0000162*(C_T(c,t)/298)*(p_ref/p)*pow((Get_Porosity(t)*(1-
Get_Fill_D(t))),1.5);
  D12 = 0.0000140*(C_T(c,t)/298)*(p_ref/p)*pow((Get_Porosity(t)*(1-
Get_Fill_D(t))),1.5);
  D14 = 0.0000180*(C_T(c,t)/298)*(p_ref/p)*pow((Get_Porosity(t)*(1-
Get_Fill_D(t))),1.5);
  D24 = 0.0000160*(C_T(c,t)/298)*(p_ref/p)*pow((Get_Porosity(t)*(1-
Get_Fill_D(t))),1.5);

  if (i==0)
  {
    DEN = X_CO2_A/D02+X_H2O/D03;
    D = (1-X_H2)/(DEN);
  }

  if (i==1)
```

```
   {
     D = 0.0001;
   }

   if (i==2)
   {
     DEN = X_H2/D02+X_H2O/D23;
     D = (1-X_CO2_A)/(DEN);
   }

   if (i==3)
   {
     DEN = X_H2/D03+X_CO2_A/D23;
     D = (1-X_H2O)/(DEN);
   }

   if (i==4)
   {
     D = 0.0001;
   }

}


if (Zone_ID == ID_C || Zone_ID == ID_CGC)

{

   double
MW_MIX_C=1/((C_YI(c,t,1)/MW_O2)+(C_YI(c,t,2)/MW_CO2)+(C_YI(c,t,3)/MW_H2O)+(C_
YI(c,t,4)/MW_N2));
   double X_O2=C_YI(c,t,1)*MW_MIX_C/MW_O2;
   double X_CO2_C=C_YI(c,t,2)*MW_MIX_C/MW_CO2;
   double X_H2O_C=C_YI(c,t,3)*MW_MIX_C/MW_H2O;
   double X_N2=1-(X_CO2_C+X_O2+X_H2O_C);

   D02 = 0.0000550*(C_T(c,t)/298)*(p_ref/p)*pow((Get_Porosity(t)*(1-
Get_Fill_D(t))),1.5);
   D03 = 0.0000915*(C_T(c,t)/298)*(p_ref/p)*pow((Get_Porosity(t)*(1-
Get_Fill_D(t))),1.5);
   D23 = 0.0000162*(C_T(c,t)/298)*(p_ref/p)*pow((Get_Porosity(t)*(1-
Get_Fill_D(t))),1.5);
   D12 = 0.0000140*(C_T(c,t)/298)*(p_ref/p)*pow((Get_Porosity(t)*(1-
Get_Fill_D(t))),1.5);
   D14 = 0.0000180*(C_T(c,t)/298)*(p_ref/p)*pow((Get_Porosity(t)*(1-
Get_Fill_D(t))),1.5);
   D24 = 0.0000160*(C_T(c,t)/298)*(p_ref/p)*pow((Get_Porosity(t)*(1-
Get_Fill_D(t))),1.5);

   if (i==0)
   {
     D = 0.0001;
   }


   if (i==1)
   {
```

```
    DEN = X_CO2_C/D12+X_N2/D14;
    D = (1-X_O2)/(DEN);
  }

  if (i==2)
  {
    DEN = X_O2/D12+X_N2/D24;
    D = (1-X_CO2_C)/(DEN);
  }

  if (i==3)
  {
    DEN = X_O2/D12+X_N2/D24;
    D = (1-X_H2O_C)/(DEN);
  }

  if (i==4)
  {
    DEN = X_O2/D14+X_CO2_C/D24;
    D = (1-X_N2)/(DEN);
  }


}

return D;
}



/******************New Mass Diffusivity***********************/

/*------------Alternative Mass Diffusivity---------------------*/

DEFINE_DIFFUSIVITY(diff_sp_new, c, t, i)
{
  double D;
  double DEN;
  double D01;
  double D02;
  double D03;
  double D04;
  double D12;
  double D13;
  double D14;
  double D23;
  double D24;
  double D34;

  int Zone_ID=THREAD_ID(t);

  double p_op = RP_Get_Real("operating-pressure");
  double p = C_P(c,t);
  double p_ref = 101325;
  p += p_op;
```

```
if (Zone_ID == ID_A || Zone_ID == ID_AGC || Zone_ID == ID_C || Zone_ID ==
ID_CGC)

{


  double
MW_MIX=1/((C_YI(c,t,0)/MW_H2)+(C_YI(c,t,1)/MW_O2)+(C_YI(c,t,2)/MW_CO2)+(C_YI(
c,t,3)/MW_H2O)+(C_YI(c,t,4)/MW_N2));

  double X_H2 = C_YI(c,t,0)*MW_MIX/MW_H2;
  double X_O2 = C_YI(c,t,1)*MW_MIX/MW_O2;
  double X_CO2 = C_YI(c,t,2)*MW_MIX/MW_CO2;
  double X_H2O = C_YI(c,t,3)*MW_MIX/MW_H2O;
  double X_N2 = 1-(X_H2+X_O2+X_CO2+X_H2O);

  D01 = 0.000070*(C_T(c,t)/298)*(p_ref/p)*pow((Get_Porosity(t)*(1-
Get_Fill_D(t))),1.5);
  D02 = 0.0000550*(C_T(c,t)/298)*(p_ref/p)*pow((Get_Porosity(t)*(1-
Get_Fill_D(t))),1.5);
  D03 = 0.0000915*(C_T(c,t)/298)*(p_ref/p)*pow((Get_Porosity(t)*(1-
Get_Fill_D(t))),1.5);
  D04 = 0.0000680*(C_T(c,t)/298)*(p_ref/p)*pow((Get_Porosity(t)*(1-
Get_Fill_D(t))),1.5);


  D12 = 0.0000140*(C_T(c,t)/298)*(p_ref/p)*pow((Get_Porosity(t)*(1-
Get_Fill_D(t))),1.5);
  D13 = 0.0000244*(C_T(c,t)/298)*(p_ref/p)*pow((Get_Porosity(t)*(1-
Get_Fill_D(t))),1.5);
  D14 = 0.0000180*(C_T(c,t)/298)*(p_ref/p)*pow((Get_Porosity(t)*(1-
Get_Fill_D(t))),1.5);


  D23 = 0.0000162*(C_T(c,t)/298)*(p_ref/p)*pow((Get_Porosity(t)*(1-
Get_Fill_D(t))),1.5);
  D24 = 0.0000160*(C_T(c,t)/298)*(p_ref/p)*pow((Get_Porosity(t)*(1-
Get_Fill_D(t))),1.5);


  D34 = 0.0000242*(C_T(c,t)/298)*(p_ref/p)*pow((Get_Porosity(t)*(1-
Get_Fill_D(t))),1.5);


  if (i==0)
  {
    DEN = X_O2/D01 + X_CO2/D02 + X_H2O/D03 + X_N2/D04;
    D = (1-X_H2)/(DEN);
  }

  if (i==1)
  {
    DEN = X_H2/D01 + X_CO2/D12 + X_H2O/D13 + X_N2/D14;
    D = (1-X_O2)/(DEN);
  }

  if (i==2)
```

```
  {
    DEN = X_H2/D02 + X_O2/D12 + X_H2O/D23 + X_N2/D24;
    D = (1-X_CO2)/(DEN);
  }

  if (i==3)
  {
    DEN = X_H2/D03 + X_O2/D13 + X_CO2/D23 + X_N2/D34;
    D = (1-X_H2O)/(DEN);
  }

  if (i==4)
  {
    DEN = X_H2/D04 + X_O2/D14 + X_CO2/D24 + X_H2O/D34;
    D = (1-X_N2)/(DEN);
  }

}
return D;
}
```

References

1. Dincer, I., "Environmental and sustainability aspects of hydrogen and fuel cell systems", International Journal of Energy Research, Vol. 31, pp. 29-55, 2007.

2. European Commission, "Hydrogen energy and fuel cells, a vision for the future", Belgium, 2003.

ec.europa.eu/research/fch/pdf/hlg_vision_report_en.pdf (accessed September 10th, 2010).

3. Energy Information Administration. World energy outlooks 2007. Preprint 99-43, (SFB 359), Energy Information Administration, February 2007.

4. Dincer, I., "Renewable energy and sustainable development: a crucial review", Renewable & Sustainable Energy Reviews, Vol. 4, pp. 157-175, 2000.

5. Zegers, P., "Fuel cell commercialization: The key to a hydrogen economy", Journal of Power Sources, Vol. 154, pp. 497-502, 2006.

6. Clean Energy State Alliance, "Fuel cell technology, a clean, reliable source of stationary power", U.S.A. 2010. http://www.cleanerenergystates.org/Publications/CESA_FC_Tech_Overview_060410LR.pdf (accessed August 3rd, 2010).

7. Appleby, A., J., "From Sir William Grove to today: Fuel cells and the future", Journal of Power Sources, Vol. 29, pp. 3-11, 1990.

8. Tseung, A., C., C., "Past, present and future of fuel cells", Battery Bimonthly, Vol. 32, pp. 130-132, 2002.

9. Li, X., Principles of fuel cells, Taylor & Francis, New York, 2005.

10. Hirschenhofer, J., H., Stauffer, D., B., Engleman, R., R., Klett, M., G., Fuel cell handbook, DOE/NETL-2002/1179 (DE-AM26-99FT40575), U.S.A.

11. Williams, M., Fuel cell handbook, EG&G technical services, U.S.A., 2004.

12. Sundmacher, K., Kienle, A., Pesch, H., J., Berndt, J., F., Huppmann, J., Molten carbonate fuel cell-Modeling, analysis, simulation and control, WILEY-VCH Verlag GmbH & Co. KGaA, Germany, 2007.

13. Adams, V., W., "The potential of fuel cells to reduce energy demands and pollution from U.K. transport sector", PhD thesis, The Open University, U.K., 1998.

14. Ketelaar, J., A., A., Broers, G., H., J., "Solubility of oxygen in molten carbonates", Journal of The Electrochemical Society, Vol. 113, pp. 404-409, 1966.

15. Boers, G., H., J., Ketelaar, J., A., A., "High temperature fuel cells", Industrial and Engineering Chemistry, Vol. 52, pp. 303-306, 1960.

16. Gorin, E., Recht, H., L., "Fuel cells", Chemical Engineering Progress, Vol. 55, pp. 51-58, 1959.

17. Gorin, E., Recht, H., L., "Nature of the electrode process", Industrial and Engineering Chemistry, Vol. 52, pp. 306-308, 1960.

18. Lurie, R., M., "A laboratory demonstration fuel cell", Journal of Scientific Instruments, Vol. 42, pp. 131-138, 1965.

19. Bannochie, J., G., "Laboratory demonstration fuel cell", Journal of Scientific Instruments, Vol. 41, pp. 644-668 pp. 94, 1960.

20. Hong, S., G., "Wetting characteristics and performance of molten carbonate fuel cell electrode", PhD thesis, Graduate College of the Illinois Institute of Technology, Chicago, 2002.

21. Edwards P. P., et al., "Hydrogen and fuel cells: Towards a sustainable energy future", Energy Policy, Vol. 36, pp. 4356-4362, 2008.

22. European Commission, JRC Scientific and Technical Reports, "International status of molten carbonate fuel cell (MCFC) technology", Netherlands, 2008.

http://publications.jrc.ec.europa.eu/repository/bitstream/111111111/6319/1/mcfc_status.pdf (accessed September 12th, 2010).

23. Larminie, J., Dicks, A., Fuel cell systems explained, John Wiley & Sons Ltd, England, 2003.

24. Appleby, A., J., Foulkes, F., R., Fuel cell handbook, Van Nostrand Reinhold, New York, U.S.A, 1989.

25. Gasik, M., Materials for fuel cells, Woodhead Publishing Limited, U.K., 2008.

26. Biedenkopf, P., Bischoff, M., M., Wochner, T., "Corrosion phenomena of alloys and electrode materials in molten carbonate fuel cells", Mater. Corrosion, Vol. 51, pp. 287-302, 2000.

27. Dave, B., B., "Oxygen reduction in lithium carbonate melt: determination of electrode kinetic and mass transfer parameters", PhD thesis, Texas A&M University, Texas, U.S.A, 1991.

28. Basu, S., Recent trends in fuel cell science and technology, Springer, New Delhi, India, 2007.

29. Yuh, C., Y., Selman, J., R., "Porous-electrode modelling of the molten-carbonate-fuel-cell electrodes", Journal of Electrochemical Society, Vol. 139, pp. 1373-1379, 1992.

30. Austin, L., G., Ariet,, M., Walker, R., D., Wood, G., B., Comyn, R., H., "Simple-pore and thin-film models of porous gas diffusion electrodes" Industrial & Engineering Chemistry Fundamentals, Vol. 4, pp. 321-326, 1965.

31. Will, F., G., Daniel, D., J., B., "Significance of electrolyte films for performance of porous hydrogen electrodes", Journal of Electrochemical Society, Vol. 119, pp. 933-937, 1969.

32. Srinivas, S., Hurwitz, H., D., "Theory of a thin film model of porous gas-diffusion electrodes", Electrochimica Acta, Vol. 12, pp. 495-500, 1967.

33. Albright, L., F., Cobb, Jr., J., T., “Effect of peroxidation and meniscus shape on hydrogen platinum anode of molten-carbonate fuel cell”, Electrochemical Society Journal, Vol. 115, pp. 2-6, 1968.

34. Iczkowski, R., P., “Mechanism of the hydrogen gas diffusion electrode”, Vol. 111, pp. 1078-1086, 1964.

35. Burshtein, R., C., Markin, V., X., Psheniohnikov, A., G., Chismdagev, V., A., Chirkov, Y., G., “The relationship between structure and electrochemical properties of porous gas electrodes”, Electrochimica Acta, Vol. 9, pp. 773-787, 1964.

36. Grens, E., A., “Analysis of operation of porous gas electrodes with two superimposed scales of pore structure”, Vol. 5, pp. 542-547, 1966.

37. Brown, R., Horve, L., A., “Infinite meniscus assumption in porous electrode theory”, Journal of The Electrochemical Society, Vol. 113, pp. C-197-C201, 1966.

38. Giner, J., Hunter, C., “Mechanism of operation of Teflon-bonded gas diffusion electrode-A mathematical model”, Journal of The Electrochemical Society, Vol. 116, pp. 1124-1128, 1969.

39. Yuh, C., Y., Selman, J., R., “Polarization of the molten carbonate fuel cell anode and cathode”, Journal of Electrochemical Society, Vol. 131, pp. 2062-2069, 1984.

40. Wilemski, G., “Simple porous electrode models for molten carbonate fuel cells”, Journal of The Electrochemical Society, Vol. 130, pp. 117-121, 1983.

41. Kunz, H., R., Bergoli, L., J., Szymanski, T., “A homogeneous/agglomerate model for molten carbonate fuel cell cathodes”, Journal of Electrochemical Society, Vol. 131, pp. 2815-2821, 1984.

42. Jewulski, J, Suski, L., “Model of the isotropic anode in the molten carbonate fuel cell”, Journal of Applied Electrochemistry, Vol. 14, pp. 135-143, 1984.

43. Jewulski, J, “Process modelling in the porous molten carbonate fuel cell (MCFC) cathode”, Journal of Applied Electrochemistry, Vol. 16, pp. 643-653, 1986.

44. Lee, G., L., Selman, J., R., Plomp, L., “Comparison of MCFC cathode materials by porous-electrode performance modeling”, Journal of The Electrochemical Society, Vol. 140, pp. 390-396, 1993.

45. Fontes, E., Lagergren, C., Simonsson, D., “Mathematical-modeling of the MCFC cathode”, Electrochimica Acta, Vol. 38, pp. 2669-2682, 1993.

46. Prins-Jansen, J., A., Hemmes, K., De Wit, H., W., “An extensive treatment of the agglomerate model for porous electrodes in molten carbonate fuel cells-I. Qualitative analysis of the steady-state model”, Electrochimica Acta, Vol. 42, pp. 3585-3600, 1997.

47. Fontes, E., Fontes, M., Simonsson, D., “Effects of different design parameters on the performance of MCFC cathodes”, Electrochimica Acta, Vol. 41, pp. 1-13, 1996.

48. Fontes, E., Lagergren, C., Lindbergh, G., Simonsson, D., “Influence of gas phase mass transfer limitations on molten carbonate fuel cell cathodes”, Journal of Applied Electrochemistry, Vol. 27, pp. 1149-1156, 1997.

49. Fehribach, J., D., Prins-Jansen, J., A., Hemmes, K., De Wit, J., H., W., Call, F., W., “On modelling molten carbonate fuel-cell cathodes by electrochemical potentials”, Journal of Applied Electrochemistry, Vol. 30, pp. 1015-1021, 2000.

50. Fehribach, J., D., Hemmes, K., “Estimation for polarization losses in molten carbonate fuel cell cathodes”, Journal of Electrochemical Society, Vol. 148, pp. A783-A787, 2001.

51. Fehribach, J., D., “Diffusion-reaction-conduction processes in porous electrodes: the electrolyte wedge problem”, European Journal of Applied Mathematics, Vol. 12, pp. 77-96, 2001.

52. Subramanian, N., Haran, B., S., Ganesan, P., White, R., E., Popov, B., N., “Analysis of molten carbonate fuel cell performance using a three-phase homogeneous model”, Journal of The Electrochemical Society, Vol. 150, pp. A46-A56, 2003.

53. Subramanian, N., Haran, B., S., White, R., E., Popov, B., N., “Fuel cell mathematical model of a MCFC”, Journal of The Electrochemical Society, Vol. 150, pp. A1360-A1367, 2003.

54. Berg, P., Findlay, J., “Comment on “Analysis of molten carbonate fuel cell performance using a three-phase homogeneous model” [J. Electrochem. Soc., 150, A46 (2003)]”, Journal of The Electrochemical Society, Vol. 157, pp. S13-S13, 2010.

55. Hao, H., Zhang, H., Weng, S., Su, M., “Dynamic numerical simulation of a molten carbonate fuel cell”, Journal of Power Sources, Vol. 161, pp. 849-855, 2006.

56. Fermegila, M., Cudicio, A., De Simon, G., Longo, G., Pricl, S., “Process simulation for molten carbonate fuel cells”, Fuel Cells, Vol. 5, pp. 66-79, 2005.

57. Lukas, M., D., Lee, K., Y., “Model-based analysis for the control of molten carbonate fuel cell systems”, Fuel Cells, Vol. 5, pp. 115-125, 2005.

58. He, W., Chen, Q., “Three-dimensional simulation of a molten carbonate fuel cell stack under transient conditions”, Journal of Power Sources, Vol. 73, pp. 182-192, 1998.

59. Lukas, M., D., Lee, K., Y., Ghezel-Ayagh, H., 1999 “Development of a stack simulation model for control study on direct reforming molten carbonate fuel cell power plant”, IEEE Trans. Energy Convers., Vol. 14, pp. 1651–1657, 1999.

60. Lukas, M., D., Lee, K., Y., Ghezel-Ayagh, H., “Modeling and cycling control of carbonate fuel cell power plants”, Control Eng. Pract., Vol. 10, pp. 197–206, 2002.

61. Zhang, H., Weng, S., Su, M., Zhang, W., “Control performance study on the molten carbonate fuel cell hybrid systems”, Journal of Fuel Cell Science and Technology, Vol. 7, pp. 061006-1-061006-8, 2010.

62. Grillo, O., Magistri, L., and Massardo, A., F., “Hybrid systems for distributed power generation based on pressurization and heat recovering of an existing 100 kW molten carbonate fuel cell”, Journal of Power Sources, Vol. 115, pp. 252–267, 2003.

63. Au, S., F., McPhail, S., J., Woudstra, N., Hemmes, K., "The influence of operating temperature on the efficiency of a combined heat and power fuel cell plant", Journal of Power Sources, Vol. 122, pp. 37–46, 2003.

64. Rashidi, R., Berg, P., Dincer, I., "Performance investigation of a combined MCFC system", International Journal of Hydrogen Energy, Vol. 34, pp. 4395-4405, 2009.

65. Shen, C., Cao, G., Y., Zhu, X., J., "Nonlinear modeling of MCFC stack based on RBF neural networks identification", Simulation Modelling Practice and Theory, Vol. 10, pp. 109-119, 2002.

66. Heidebrecht, P., Sundmacher, K., "Molten carbonate fuel cell (MCFC) with internal reforming: model-based analysis of fuel cell dynamics", Chemical Engineering Science, Vol. 58, pp. 1029-1036, 2003.

67. Heidebrecht, P., Sundmacher, K., "Dynamic model of a cross-flow molten carbonate fuel cell with direct internal reforming", Journal of The Electrochemical Society, Vol. 152, pp. A2217-A2228, 2005.

68. He, W., Chen, Q., "Three-dimensional simulation of a molten carbonate fuel cell stack using computational fluid dynamics technique", Journal of Power Sources, Vol. 55, pp. 25-32, 1995.

69. He, W., Chen, Q., "Three-dimensional simulation of a molten carbonate fuel cell stack under transient conditions", Journal of Power Sources, Vol. 73, pp. 182-192, 1998.

70. Yoshiba, F., Ono, N., Izaki, Y., Watanabe, T., Abe, T., "Numerical analysis of the internal conditions of a molten carbonate fuel cell stack: comparison of stack performances for various gas flow types", Journal of Power Sources, Vol. 71, pp. 328-336, 1998.

71. Yoshiba, F., Abe, T., Watanabe, T., "Numerical analysis of molten carbonate fuel cell stack performance: diagnosis of internal condition using cell voltage profiles", Journal of Power Sources, Vol. 87, pp. 21-27, 2000.

72. Hirata, H., Nakagaki, T., Hori, M., “Effect of gas channel height on gas flow and gas diffusion in a molten carbonate fuel cell stack”, Journal of Power Sources, Vol. 83, pp. 41-49, 1999.

73. Koh, J., H., Kang, B., S., Lim, H., C., “Effect of various stack parameters on temperature rise in molten carbonate fuel cell stack operation”, Journal of Power Sources, Vol. 91, pp. 161-171, 2000.

74. Koh, J., H., Seo, H., K., Yoo, Y., S., Lim, H., C., “Consideration of numerical simulation parameters and heat transfer models for a molten carbonate fuel cell stack”, Chemical Engineering Journal, Vol. 87, pp. 367-379, 2002.

75. Koh, J., H., Seo, H., K., Lee, C., G., Yoo, Y., S., Lim, H., C., “Pressure and flow distribution in internal gas manifolds of a fuel-cell stack”, Journal of Power Sources, Vol. 115, pp. 54-65, 2003.

76. Bittanti, S., Canevese, S., De Marco, A., Errigo, A., Prandoni, V., “Molten carbonate fuel cell dynamic modeling”, Journal of Fuel Cell Science and Technology, Vol. 4, pp. 283-293, 2007.

77. Lee, S., Y., Lim, H., C., Chung, G., Y., “Studies on the modeling of a molten carbonate fuel cell (MCFC) 5 kW class stack”, Korean Journal of Chemical Engineering, Vol. 27, pp. 487-493, 2010.

78. Park, H., K., Lee, Y., R., Kim, M., H., Chung, G., Y., Nam, S., W., Hong, S., A., Lim, T., H., Lim, H., C., “Studies of the effects of the reformer in an internal-reforming molten carbonate fuel cell by mathematical modeling”, Journal of Power Sources, Vol. 104, pp. 140-147, 2002.

79. Kim, M., H., Park, H., K., Chung, G., Y., Lim, H., C., Nam, S., W., Lim, T., H., Hong, A., A., “Effect of water-gas shift reaction on simulated performance of a molten carbonate fuel cell”, Journal of Power Sources, Vol. 104, pp. 245-252, 2002.

80. Ma, Z., Jeter, S., M., Abdel-Khalik, A., I., “Modeling the transport processes within multichannel molten carbonate fuel cells”, International Journal of Hydrogen Energy, Vol. 28, pp. 85-97, 2003.

81. Yoo, M., J., Kim, D., P., Chung, G., Y., Lim, H., C., “Studies on the numerical modeling of the butterfly-type unit molten carbonate fuel cell”, Journal of Fuel Cell Science and Technology, Vol. 3, pp., 327-332, 2006.

82. Wee, J., H., Lee, K., Y., “Simulation of the performance for the direct internal reforming molten carbonate fuel cell. Part I: Distribution of temperatures, energy transfer and current density”, International Journal of Energy Research, Vol. 30, pp. 599-618, 2006.

83. Wee, J., H., Lee, K., Y., “Simulation of the performance for the direct internal reforming molten carbonate fuel cell. Part II: Comparative distributions of reaction rates and gas compositions”, International Journal of Energy Research, Vol. 30, pp. 619-631, 2006.

84. Lee, Y., R., Kim, I., G., Chung, G., Y., Lee, C., G., Lim, H., C., Lim, T., H., Nam, S., W., Hong, S., A., “Studies on the initial behaviours of the molten carbonate fuel cell”, Journal of Power Sources, Vol. 137, pp.9-16, 2004.

85. Lukas, M., D., Lee, K., Y., Ghezel-Ayaghb, H., “Modeling and cycling control of carbonate fuel cell power plants”, Control Eng. Pract, Vol. 10, pp. 197–206, 2002.

86. Pfafferodt, M., Heidebrecht, P., Sundmacher, K., Würtenberger, U., Bednarz, M., “Multiscale simulation of the indirect internal reforming unit (IIR) in a molten carbonate fuel cell (MCFC)”, Industrial Engineering Chemistry Research, Vol. 47, pp. 4332-4341, 2008.

87. Brouwer, J., Jabbari, F., Leal, E., M., Orr, Trevor, “Analysis of a molten carbonate fuel cell: Numerical modeling and experimental validation”, Journal of Power Sources, Vol. 158, pp. 213-224, 2006.

88. Lee, C., G., Kang, B., S., Seo, H., K., Lim, H., C., “Effect of gas-phase transport in molten carbonate fuel cell”, Journal of Electroanalytical Chemistry, Vol. 540, pp. 169-188, 2003.

89. Arato, E., Bosio, B., Massa, R., Parodi, F., “Optimisation of the cell shape for industrial MCFC stacks”, Journal of Power Sources, Vol. 86, pp. 302-308, 2000.

90. Silveira, J., L., Leal, E., M., Ragonha Jr., L., F., “Analysis of a molten carbonate fuel cell: cogeneration to produce electricity and cold water”, Energy, Vol. 26, pp. 891-904, 2001.

91. Varbanov, P., Klemes, J., Shah, R., K., Harmanjeet, S., “Power cycle integration and efficiency increase of molten carbonate fuel cell system”, Journal of Fuel Cell Science and Technology, Vol. 3, pp. 375-383, 2006.

92. Kang, B., S., Koh, J., H., Lim, H., C., “Effects of system configuration and operating condition on MCFC system efficiency”, Journal of Power Sources, Vol. 108, pp. 232-238, 2002.

93. Rashidi, R., Dincer, I., Berg, P., “Energy and exergy analysis of a hybrid molten carbonate fuel cell system”, Journal of Power Sources”, Vol. 185, pp., 1107-1114, 2008.

94. Musa, A., Steeman, H., J., Paepe, M., D., “Performance of internal and external reforming molten carbonate fuel cell systems”, Journal of Fuel Cell Science and Technology, Vol. 4, pp., 65-71, 2007.

95. Verda, V., Nicolin, F., “Thermodynamic and economic optimization of a MCFC-based hybrid system for the combined production of electricity and hydrogen”, International Journal of Hydrogen Energy”, Vol. 35, pp., 794-806, 2010.

96. Campanari, S., “Carbon dioxide separation from high temperature fuel cell power plants”, Journal of Power Sources, Vo. 112, pp. 273-289, 2002.

97. Guo, Z., L., Zhao, T., S., “Lattice Boltzmann model for incompressible flows through the porous media”, Physical Review, Vol. 66, pp. 036304-1 – 036304-9, 2002.

98. Kang, Q., Zhang, D., Chen, S., He, X., “Lattice Boltzmann simulation of chemical dissolution in porous media”, Physical Review, Vol. 65, pp. 036318-1 – 036304-8, 2002.

99. Ponce Dawson, S., Chen, S., Doolen, G., D., “Lattice Boltzmann computations for reaction-diffusion equations”, Journal of Chemical Physics, Vol. 98, pp., 1514-1523, 1993.

100. Kumar, R., Nivarthi, S., S., Davis, H., T., Kroll, D., M., Maier, R., S., “Application of the lattice Boltzmann method to study flow and dispersion in channels with and without expansion and contraction geometry”, International Journal for Numerical Methods in Fluids, Vol. 31, pp. 801-819, 1999.

101. You-Sheng, X., Yang, L., Guo-Xianq, H., “Using digital imaging to characterize threshold dynamic parameters on porous media based on lattice Boltzmann method”, Chinese Physics Letters, Vol. 21, pp. 2454-2457, 2004.

102. Xu, Y., S., Liu, Y., Xu, X., Z., Huang, G., X., “Lattice Boltzmann simulation on molten carbonate fuel cell performance”, Journal of The Electrochemical Society, Vol. 153, pp. A607-A613, 2006.

103. Prins-Jansen, J., A., Fehribach, J., D., Hemmes, K., de With, H., W., “A three-phase homogeneous model for porous electrodes in molten-carbonate fuel cells”, Journal of Electrochemical Society, Vol. 143, No. 5, pp. 1617-1628, 1996.

104. Bird, R., B., Stewart, W., E., Lightfoot, E., N., Transport phenomena, New York, John Wiley & Sons, 1960.

105. Ye, Q., Nguyen, T., V., “Three-dimensional simulation of liquid water distribution in a PEMFC with experimentally measured capillary functions”, Journal of The Electrochemical Society, Vol. 154, pp. B1242-B1251, 2007.

106. Boden, A., Lindbergh, G., “A model for mass transfer of molten alkali carbonate mixtures applied to the MCFC”, Journal of The Electrochemical Society, Vol. 153, pp. A2111-A2119, 2006.

107. Findlay, J., E., “Mass transport in the cathode electrode of a molten carbonate fuel cell”, Masters Thesis, University of Ontario Institute of Technology, 2009.

108. Nield, D., A., Bejan, A., Convection in porous media, 2nd ed., Springer, New York, 1999.

109. Yu, L., J., Ren, G., P., Jiang, X., M., Yuan, J., Q., Cao, G., Y., "Experiment and numerical simulation on the performance of a kW-scale molten carbonate fuel cell stack", Brazilian Journal of Chemical Engineering, Vol. 24, No. 04, pp. 523-533, 2007.

110. Jiao, K., "Experimental and modelling studies of cold start processes in proton exchange membrane fuel cells", PhD Thesis, University of Waterloo, 2011.

111. Promislow, K., Chang, P., Haas, H., Wetton, B., "Two-phase unit cell model for slow transients in polymer electrolyte membrane fuel cells", Journal of The Electrochemical. Society, Vol, 155, No. 7, pp. A494-A504, 2008.

112. Bear, J., Bachmat, Y., Introduction to Modeling of Transport Phenomena in Porous Media, Kluwer, Dordrecht, The Netherlands, 1991.

113. Ang, P., G., P., Sammells, A., F., "Influence of electrolyte composition on electrode kinetics in molten carbonate fuel cell", Journal of Electrochemical Society, Vol. 127, pp.1287-1294, 1980.

114. Wu, H., "Mathematical modeling of transient transport phenomena in PEM fuel cells", PhD thesis, University of Waterloo, Waterloo, Canada, 2009.

115. Verda, V., Sciacovelli, A., "Design improvement of circular molten carbonate fuel cell stack through CFD Analysis", Applied Thermal Engineering, Vol. 31, pp. 2740-2748, 2011.

116. Wang, C., Y., "Fundamental models for fuel cell engineering", Chemical Reviews, Vol. 104, No. 12, pp. 4727-4766, 2004.

117. Prins-Jansen, J., A., "Cathodes in molten carbonate fuel cells, mathematical modelling and experimental characterization", PhD Thesis, Delft University, 1996.

118. Haynes, W., M., ed., CRC handbook of chemistry and physics, 91st Edition, CRC Press/Taylor and Francis, Internet Version 2011.

119. Yoshiba, F., "Numerical analysis of the single electrode heat effect in molten carbonate fuel cells: temperature analysis of the electrolyte plate by applying irreversible thermodynamics", International Journal of Energy Research, Vol. 28, pp. 1361-1377, 2004.

120. Versteeg, H., K., Malalasekera, W., An introduction to computational fluid dynamics the finite volume method, John Wiley & sons Inc, New York, 1995.

121. ANSYS ICEM 12.0.1 User's Guide, Ansys Inc., 2009.

122. ANSYS FLUENT 12.0.1 User's Guide, Ansys Inc., 2009.

123. Wu, H., "Mathematical modelling of transient transport phenomena in PEM fuel cells", PhD Thesis, University of Waterloo, 2011.

124. Lee, C., Kim, D., Lim, H.,"Electrode reaction characteristcs under pressurized conditions in a molten carbonate fuel cell", Journal of Electrochemical Society, Vol. 154, pp. B396-B404, 2007.

125. Shi, J., Xue, X., "CFD analysis of a novel symmetrical planar SOFC design with micro-flow channels", Chemical Engineering Journal, Vol. 163, pp. 119-125, 2010.

126. Shi, J., Xue, X., "CFD analysis of a symmetrical planar SOFC with hetrogeneous electrode properties", Electrochemical Acta, Vol. 55, pp. 5263-5273, 2010.

127. Kazim, A., Liu, H., T., Forges, P., "Modeling of performance of PEM fuel cells with conventional and interdigitated flow fields", Journal of Applied Electrochemistry, Vol. 29, pp. 1409-1416, 1999.

128. Wu, H., Berg, P., Li, X., "Modeling of PEMFC transients with finite-rate phase-transfer processes", Journal of Electrochemical Society, Vol. 157, pp. B1-B12, 2010.

129. Wu, H., Li, X., Berg, P., “Numerical analysis of dynamic processes in fully humidified PEM fuel cells”, International Journal of Hydrogen Energy, Vol. 32, pp. 2022-2031, 2007.

130. Heidebrecht, P., “Modelling, Analysis and Optimisation of a Molten Carbonate Fuel Cell with Direct Internal Reforming (DIR-MCFC)”, PhD Thesis, Otto-von-Guericke University Magdeburg, 2004.

131. Dincer I., Rosen M. A., Exergy, energy, environment and sustainable development, Elsevier, 2007

132. Hussain, M., M., Baschuk, J., J., Li, X., Dincer, I., “Thermodynamic analysis of a PEM fuel cell power system”, International Journal of Thermal Sciences, Vol. 44, pp. 903-911, 2005.

133. Chan, S., H., Low, C., F., Ding, O., L., “Energy and exergy analysis of simple solid-oxide fuel-cell power systems”, Journal of Power Sources, Vol. 103, pp. 188-200, 2002.